

**Experimental Investigation of Saltwater Intrusion  
Dynamics in Porous Media Under the  
Influence of Beach Slope and Tidal Conditions**

*Thesis submitted to the  
Indian Institute of Technology Kharagpur  
for Award of the Degree*

*of*

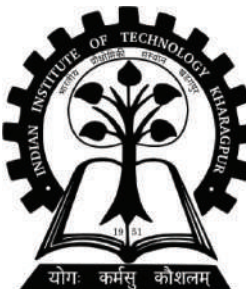
**Doctor of Philosophy**

*by*

**Chitaranjan Dalai**

Under the Guidance of

**Dr. Anirban Dhar**



**SCHOOL OF WATER RESOURCES**

**INDIAN INSTITUTE OF TECHNOLOGY KHARAGPUR**

**August 2021**

©2021 Chitaranjan Dalai. All rights reserved.



## APPROVAL OF THE VIVA-VOCE BOARD

Date: 30/08/2021

Certified that the thesis entitled **Experimental Investigation of Saltwater Intrusion Dynamics in Porous Media Under the Influence of Beach Slope and Tidal Conditions** submitted by **Chitaranjan Dalai** to the Indian Institute of Technology Kharagpur, for the award of the degree of Doctor of Philosophy has been accepted by the external examiners and that the student has successfully defended the thesis in the viva-voce examination held today.

**Dr. H. P Reddy**

Dept. of Civil Engg.

Member of the DSC

**Dr. Bhabagrahi Sahoo**

School of Water Resources

Member of the DSC

**Dr. Manoj K. Tiwari**

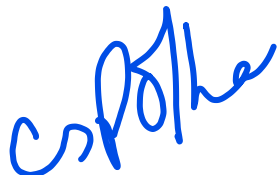
School of Water Resources

Member of the DSC

**Dr. Anirban Dhar**

Department of Civil Engineering

Supervisor



**Prof. C.S.P. Ojha**

External Examiner

**Prof. A. K. Gupta**

Chairman, DSC



## **CERTIFICATE**

This is to certify that the thesis entitled **Experimental Investigation of Saltwater Intrusion Dynamics in Porous Media Under the Influence of Beach Slope and Tidal Conditions**, submitted by **Chitaranjan Dalai** to Indian Institute of Technology Kharagpur, is a record of bonafide research work under my supervision and I consider it worthy of consideration for the award of the degree of Doctor of Philosophy of the Institute.

**Dr. Anirban Dhar**

Associate Professor

Department of Civil Engineering

Indian Institute of Technology Kharagpur

Date: 30/08/2021

Place: IIT Kharagpur



## Acknowledgment

I want to express my sincere gratitude to my advisor Dr. Anirban Dhar for his excellent guidance and constant encouragement. His immense knowledge, motivation, dedication to research, and patience to tolerate a novice like me have inspired me. He has supported me throughout my thesis with his patience and knowledge while allowing me the room to work in my way.

Special thanks to my members of my Doctoral Scrutiny Committee (DSC). I would also like to extend appreciation to the Head, Civil Engineering Department, IIT Kharagpur, for providing the laboratory facilities in the department.

I extend my sincere thanks and regards to all Professors in the School of Water Resources for their support and help throughout my stay in campus.

Everything is meaningless without my parents and my brother. I received their continuous support, motivation, and unconditional love in this journey. Their undoubted faith in me has been the pillars of my strength. I dedicate this thesis to them.

I would also thank my friends for providing invaluable help, continued support, who made my stay here a memorable one. I am also thankful to the Mr. Debasish Ghosh of Hydraulic and Water Resources Engineering Laboratory.

**Chitaranjan Dalai**



## DECLARATION

I certify that

- a. The work contained in the thesis is original and has been done by myself under the general supervision of my supervisor.
- b. The work has not been submitted to any other Institute for any degree or diploma.
- c. I have followed the guidelines provided by the Institute in writing the thesis.
- d. I have conformed to the norms and guidelines given in the Ethical Code of Conduct of the Institute.
- e. Whenever I have used materials (data, theoretical analysis, and text) from other sources, I have given due credit to them by citing them in the text of the thesis and giving their details in the references.
- f. Whenever I have quoted written materials from other sources, I have put them under quotation marks and given due credit to the sources by citing them and giving required details in the references.

Chitaranjan Dalai



## List of Journal Publication(s)

1. **Dalai, C.**, Munusamy, S.B., and Dhar, A. “Experimental and numerical investigation of saltwater intrusion dynamics on sloping sandy beach under static seaside boundary condition” *Flow Measurement and Instrumentation*, 75, 101794, 2020.



## 2. Fingering effect:

The fingering effect, also known as "saltwater fingering" or "gravity current fingering," occurs when a denser fluid, such as saltwater, intrudes into a lighter fluid, such as freshwater, in a non-uniform manner. Instead of forming a smooth interface, the denser fluid penetrates the lighter one in finger-like patterns due to the interplay of buoyancy and fluid dynamics.

## 3. The G-channel in RGB (Red, Green, Blue) image analysis:

refers to the green component of an image. Utilizing the G-channel involves extracting and analyzing information primarily from the green color channel to study specific features or patterns within an image. This technique is often employed in image processing applications, such as vegetation analysis or object detection, where green components convey significant information.

## Abstract

Saltwater intrusion (SWI) in coastal aquifers is a critical hydro-environmental problem. The intrusion of saltwater in freshwater aquifers occurs due to variable-density flow in porous media. The conceptual understanding of saltwater intrusion dynamics is important from the aquifer management point of view. The current research quantifies the influence of beach slope and tidal conditions on saltwater dynamics in single and multilayered porous media. A series of experiments were performed in a 2D *Sand Box Model* (longitudinal & vertical). Ten experimental cases (5 + 5) were considered corresponding to single-layered porous media under static and tidal saltwater side boundary conditions. Similarly, Ten experimental cases were considered corresponding to multilayered porous media. Locally available *Clean Sand* was utilized as aquifer material in two experimental cases. However, Grade-I IS Sand was used for all other cases (20 experiments). *Bentonite* was used for the low permeability layer. *Rohdamine B* was utilized as the saltwater tracer. Time-varying porewater pressure values and images were recorded/captured during the experiments. Experimental and numerical analyses showed that the movement rate and volume of the saltwater wedge (i.e., saltwater-freshwater interface toe length) decrease with the increase in beach slope (e.g.,  $\alpha = 15^\circ$  to  $\alpha = 30^\circ$ ). The fingering effect was prominent for flatter slopes. A G-Channel (of R-G-B) based image analysis technique was utilized to identify the saltwater-freshwater interface and concentration gradient from the experimental images. The 50% concentration isolines obtained from the numerical simulations were matched with the interfaces obtained from the image analysis. A narrow mixing zone was observed for the current set of experiments. Upper saline plume (USP) developed for all experimental cases for unconfined layer in single and multilayered systems under tidal saltwater side boundary conditions. The extent of the upper saline plume was dependent on the freshwater flux. The vertical SGD gap ( $\zeta_0$ ) decreases with an increase in beach face slope, whereas the SWI toe length increases. Tracer injection technique was utilized to identify the Submarine groundwater discharge (SGD) pathways. Non-dimensional groups were also identified for both tidal and static conditions. The saltwater-freshwater interface toe length and submarine groundwater discharge gap values depend on beach slope. Flow stability was determined on the basis of Rayleigh number ( $R_a^* = 150$  to  $250$  or  $750$ ).

## 4. The upper saline plume:

refers to the upper layer of a saltwater intrusion in an estuary or coastal aquifer. It occurs when denser saltwater intrudes into the freshwater, forming a distinct layer above the underlying freshwater.

## 5. The vertical SGD (Submarine Groundwater Discharge) gap:

denoted by  $\zeta_0$ , represents the vertical separation between the seafloor and the groundwater table or the level of the submarine groundwater discharge.



# Contents

<b>Title Page</b>	<b>i</b>
<b>Certificate of Approval</b>	<b>iii</b>
<b>Certificate</b>	<b>v</b>
<b>Acknowledgment</b>	<b>vii</b>
<b>Declaration</b>	<b>ix</b>
<b>List of Journal Publication(s)</b>	<b>xi</b>
<b>Abstract</b>	<b>xiii</b>
<b>1 Introduction</b>	<b>1</b>
1.0 Background . . . . .	1
1.1 Motivation . . . . .	4
1.2 Objectives of the Thesis . . . . .	5
1.3 Outline of the Thesis . . . . .	5
<b>2 Experimental Design &amp; Methodology</b>	<b>7</b>
2.0 Overview . . . . .	7

2.1	Instrumentation	7
2.1.1	Sand Box Model	7
2.1.2	Tidal Mechanism	9
2.1.3	Pressure Transducer	10
2.1.4	Data Acquisition System	12
2.1.5	Digital Camera	12
2.1.6	Peripheral Apparatus	13
2.2	Material Characterization	17
2.2.1	Porous Materials/Aquifer Materials	17
2.2.2	Tracer for Saltwater	22
2.3	Summary	29
<b>3</b>	<b>Laboratory Experiments on Saltwater Movement Under Static Saltwater Boundary Condition</b>	<b>31</b>
3.0	Overview	31
3.1	Experiments with Clean Sand	32
3.2	Numerical Simulation Model	35
3.2.1	Initial and Boundary Conditions	38
3.3	Basic Image Analysis	40
3.4	Analytical Solution	42
3.5	Results and Discussion	44
3.5.1	Pore Water Pressure Measurement	48
3.5.2	Comparison with Analytical Solution	49
3.5.3	Saltwater Circulation	52
3.5.4	Freshwater Flow Patterns	53

3.6	Summary	56
<b>4</b>	<b>Influence of Beach Slope on Saltwater Movement in Single Layer Under Static and Tidal Conditions</b>	<b>57</b>
4.0	Overview	57
4.1	Single Layer Under Static Condition	58
4.1.1	Experimental Method	58
4.1.2	Numerical Simulation Model	64
4.1.3	G-Channel Based Image Analysis	67
4.1.4	Results and Discussion	72
4.2	Single Layer Under Tidal Condition	82
4.2.1	Experimental Method	82
4.2.2	Numerical Simulation Model	86
4.2.3	G-Channel Based Image Analysis	88
4.2.4	Results and Discussion	88
4.3	Summary	100
<b>5</b>	<b>Influence of Beach Slope on Saltwater Movement in Multi-Layered Porous Media Under Static and Tidal Conditions</b>	<b>101</b>
5.0	Overview	101
5.1	Experimental Details	102
5.1.1	Static Experimental Setup	102
5.1.2	Tidal Experimental Setup	104
5.2	Numerical Modelling Method	104
5.2.1	Static Numerical Simulations	106
5.2.2	Tidal Numerical Simulations	108

5.3	G-Channel Based Image Analysis . . . . .	110
5.4	Results and Discussion . . . . .	110
5.4.1	Pore Water Pressure Measurement . . . . .	120
5.4.2	Comparison with Analytical Expression . . . . .	124
5.4.3	Freshwater Flow Patterns . . . . .	128
5.5	Summary . . . . .	132
<b>6</b>	<b>Dimensional Analysis of Saltwater Intrusion Experiments</b>	<b>133</b>
6.0	Overview . . . . .	133
6.1	Buckingham $\Pi$ -Theorem . . . . .	133
6.2	Single Layered Under Static Condition . . . . .	134
6.3	Layered Under Static Condition . . . . .	138
6.3.1	Unconfined Layer Under Static Condition . . . . .	140
6.3.2	Confined Layer Under Static Condition . . . . .	142
6.4	Parameters Under Tidal Condition . . . . .	145
6.5	Single Layered Under Tidal Conditions . . . . .	147
6.5.1	Toe Length for Tidal Condition . . . . .	147
6.5.2	SGD Gap for Tidal Condition . . . . .	148
6.6	Layered Under Tidal Conditions . . . . .	148
6.6.1	Toe Length for Unconfined Layer . . . . .	151
6.6.2	SGD Gap for Unconfined Layer . . . . .	152
6.6.3	Toe Length for Confined Layer . . . . .	153
6.6.4	SGD Gap for Confined Layer . . . . .	154
6.7	Summary . . . . .	155

<b>7 Overview and Conclusions</b>	<b>157</b>
7.1 Overview . . . . .	157
7.2 Conclusions . . . . .	160
7.3 Recommendations for Future Work . . . . .	162



# List of Tables

2.1	Relevant Porous Material Properties and BIS Codes . . . . .	19
2.2	Physical Properties of Aquifer Materials . . . . .	20
3.1	Configurations for Clean Sand Experiments . . . . .	32
3.2	Numerical Parameters Used for Clean Sand Experiments . . . . .	40
3.3	Submarine Groundwater Discharge (SGD) Gap and Saltwater-Freshwater Interface Toe Length for <i>CASE – 1/S</i> . . . . .	51
3.4	Submarine Groundwater Discharge (SGD) Gap and Saltwater-Freshwater Interface Toe Length for <i>CASE – 2/S</i> . . . . .	51
4.1	Configurations for Experiments with Single Layered Porous Media Under Static Saltwater Side Boundary Condition . . . . .	58
4.2	Numerical Parameters Used for Experiments with Single Layered Porous Media Under Static Saltwater Side Boundary Condition . . .	65
4.3	Submarine Groundwater Discharge (SGD) Gap and Saltwater-Freshwater Interface Toe Length for Experiments with Single Layered Porous Media Under Static Saltwater Side Boundary Condition . . . . .	79
4.4	Configurations for Experiments with Single Layered Porous Media Under Tidal Saltwater Side Boundary Condition . . . . .	83
4.5	Numerical Parameters Used for Experiments with Single Layered Porous Media Under Tidal Saltwater Side Boundary Condition . . .	88

4.6	Submarine Groundwater Discharge (SGD) Gap and Saltwater-Freshwater Interface Toe Length for Experiments with Single Layered Porous Media Under Tidal Saltwater Side Boundary Condition . . . . .	97
5.1	Configurations for Experiments with Multilayered Porous Media Under Static Saltwater Side Boundary Condition . . . . .	103
5.2	Configurations for Experiments with Multilayered Porous Media Under Tidal Saltwater Side Boundary Condition . . . . .	105
5.3	Numerical Parameters Used for Experiments with Multilayered Porous Media Under Static and Tidal Saltwater Side Boundary Conditions	110
5.4	Submarine Groundwater Discharge (SGD) Gap and Saltwater-Freshwater Interface Toe Length for Experiments with Multilayered Porous Media Under Static Saltwater Side Boundary Condition . . . . .	125
5.5	Submarine Groundwater Discharge (SGD) Gap and Saltwater-Freshwater Interface Toe Length for Experiments with Multilayered Porous Media Under Tidal Saltwater Side Boundary Condition . . . . .	127
6.1	Dimensional and Non-Dimensional Variables Used In Dimensional Analysis of Single Layered System Under Static Saltwater Side Boundary Condition . . . . .	135
6.2	Numerical Toe Length Calculation for Single Layered System Under Static Saltwater Side Boundary Condition . . . . .	137
6.3	Experimental Toe Length Calculation for Single Layered System Under Static Saltwater Side Boundary Condition . . . . .	137
6.4	Numerical SGD Gap Calculation for Single Layered System Under Static Saltwater Side Boundary Condition . . . . .	138
6.5	Experimental SGD Gap Calculation for Single Layered System Under Static Saltwater Side Boundary Condition . . . . .	138
6.6	Dimensional and Non-Dimensional Variables Used In Dimensional Analysis of Multilayered System Under Static Saltwater Side Boundary Condition . . . . .	139

6.7	Numerical Toe Length Calculation for Unconfined Layer Under Static Saltwater Side Boundary Condition . . . . .	140
6.8	Experimental Toe Length Calculation for Unconfined Layer Under Static Saltwater Side Boundary Condition . . . . .	141
6.9	Numerical SGD Gap Calculation for Unconfined Layer Under Static Saltwater Side Boundary Condition . . . . .	141
6.10	Experimental SGD Gap Calculation for Unconfined Layer Under Static Saltwater Side Boundary Condition . . . . .	142
6.11	Numerical Toe Length Calculation for Confined Layer Under Static Saltwater Side Boundary Condition . . . . .	142
6.12	Experimental Toe Length Calculation for Confined Layer Under Static Saltwater Side Boundary Condition . . . . .	143
6.13	Numerical SGD Gap Calculation for Confined Layer Under Static Saltwater Side Boundary Condition . . . . .	143
6.14	Experimental SGD Gap Calculation for Confined Layer Under Static Saltwater Side Boundary Condition . . . . .	143
6.15	Non-Dimensional Variables Used In Dimensional Analysis of Single Layered System Under Tidal Saltwater Side Boundary Condition . .	146
6.16	Numerical Toe Length Calculation for Single Layered System Under Tidal Saltwater Side Boundary Condition . . . . .	148
6.17	Experimental Toe Length Calculation for Single Layered System Under Tidal Saltwater Side Boundary Condition . . . . .	148
6.18	Numerical SGD Gap Calculation for Single Layered System Under Static Saltwater Side Boundary Condition . . . . .	149
6.19	Experimental SGD Gap Calculation for Single Layered System Under Static Saltwater Side Boundary Condition . . . . .	149
6.20	Non-Dimensional Variables Used In Dimensional Analysis of Multi-layered System Under Tidal Saltwater Side Boundary Condition . .	150
6.21	Numerical Toe Length Calculation in Unconfined Layer Under Tidal Saltwater Side Boundary Condition . . . . .	151

6.22 Experimental Toe Length Calculation in Unconfined Layer Under Tidal Saltwater Side Boundary Condition . . . . .	151
6.23 Numerical SGD Gap Calculation in Unconfined Layer Under Tidal Saltwater Side Boundary Condition . . . . .	152
6.24 Experimental SGD Gap Calculation in Unconfined Layer Under Tidal Saltwater Side Boundary Condition . . . . .	152
6.25 Numerical Toe Length Calculation in Confined Layer Under Tidal Saltwater Side Boundary Condition . . . . .	153
6.26 Experimental Toe Length Calculation in Confined Layer Under Tidal Saltwater Side Boundary Condition . . . . .	153
6.27 Numerical SGD Gap Calculation in Confined Layer Under Tidal Saltwater Side Boundary Condition . . . . .	154
6.28 Experimental SGD Gap Calculation in Confined Layer Under Tidal Saltwater Side Boundary Condition . . . . .	154
7.1 Configurations for Experiments with Single Layered Porous Media Under Static and Tidal Saltwater Side Boundary Conditions . . . .	158
7.2 Configurations for Experiments with Multilayered Porous Media Under Static and Tidal Saltwater Side Boundary Conditions . . . .	159

# List of Figures

1.1	Schematic Representation of Multilayered Coastal Aquifer with Driving Forces . . . . .	2
2.1	<i>Sand Box Model:</i> a Pictorial Representation of Experimental Setup and b Schematic Representation of Experimental Setup. . . . .	8
2.2	Tidal Control Mechanism a Tidal Mechanism and b Control Panel .	10
2.3	Pressure Transducers and Data Acquisition System . . . . .	11
2.4	UEILogger 300— A: Network Connectors, B: USB Port, C: SD Card Slot, D: RS-232 Port, E: I/O Board/Layer Slots, F: I/O Layer Status LEDs, G: Sync Connector, H: Start/Reset Button, I: Communication Status LEDs, J: Power Connectors . . . . .	12
2.5	Digital Single Lens Reflex (DSLR) Camera (Nikon d5100) . . . . .	13
2.6	Variable Speed Peristaltic Pump (PP-50VX). . . . .	13
2.7	Calibration of Peristaltic Pump . . . . .	14
2.8	Conductivity, Temperature and Depth (CTD) Diver . . . . .	15
2.9	Calibration of CTD Diver . . . . .	16
2.10	Experimental Porous Materials . . . . .	17
2.11	SEM Micrographs and EDX Spectrums of Clean Sand . . . . .	18
2.12	SEM Micrographs and EDX Spectrums of Grade-I IS Sand . . . . .	18
2.13	SEM Micrographs and EDX Spectrums of Bentonite Clay . . . . .	19

2.14	Grain Size Distribution of Clean Sand . . . . .	20
2.15	Grain Size Distribution of Grade-I IS Sand . . . . .	21
2.16	Molecular Structure of Rhodamine B . . . . .	22
2.17	Molecular Structure of Indigo Carmine . . . . .	22
2.18	Molecular Structure of Methyl Orange . . . . .	22
2.19	Transmittance ( $T = I/I_0$ ) of Light by Aqueous Solution. . . . .	23
2.20	Absorption Spectra of Rhodamine B, Indigo Carmine, Methyl Orange in Aqueous Solution . . . . .	24
2.21	Absorption Spectra of Commercial Food Dye in Aqueous Solution .	25
2.22	Absorption Spectra of Dyes in Aqueous Solutions at Different Concentration Levels with Clean Sand . . . . .	26
2.23	Absorption Spectra of Dyes in Aqueous Solutions at Different Concentration Levels with Grade-I IS Sand . . . . .	27
2.24	Dye Adsorption Performance (Adsorbent Dose = 10 g/l, Dye Concentration = 10 mg/l) . . . . .	27
2.25	Salt Wedge and Saltwater-Freshwater Interface for Rhodamine-B in IS Sand . . . . .	28
2.26	Salt Wedge and Saltwater-Freshwater Interface for Food Dye in IS Sand . . . . .	28
3.1	Schematic Representation of the Sand Box Model for Clean Sand Experiments . . . . .	33
3.2	Observed Time Varying Conductivity Profiles at Saltwater Reservoir (Zone - A) . . . . .	36
3.3	Soil Water Retention Curves . . . . .	37
3.4	Initial Pressure Distribution for CASE - 1/S . . . . .	38
3.5	Boundary Conditions Used in Numerical Simulation for Clean Sand Experiments . . . . .	39

3.6 A Multidimensional Array of Colour Information . . . . .	41
3.7 Development of Saltwater Wedge with Time in <i>CASE – 1/S</i> (First Column: Experimental Images; Second Column: Output of Basic Image Analysis, The Color Maps Indicate $\bar{C}_{i,j}$ ). All dimensions are in mm. . . . .	43
3.8 Development of Saltwater Wedge with Time in <i>CASE – 2/S</i> (First Column: Experimental Images; Second Column: Output of Basic Image Analysis, The Color Maps Indicate $\bar{C}_{i,j}$ ). All dimensions are in mm. . . . .	44
3.9 Conceptual Representation of Two-dimensional Saltwater-freshwater Interface in Sloping Beach Aquifer . . . . .	44
3.10 Development of Saltwater-freshwater Interface with Time in <i>CASE – 1/S</i> [First Column: Output of Basic Image Analysis, The Color Maps Indicate $\bar{C}_{i,j}$ ; Second Column: Numerical Simulation (0.5-Concentration Isoline); Third Column: Overlap of Numerical Simulation and Basic Image Analysis Outputs]. All dimensions are in mm. . . . .	46
3.11 Development of Saltwater-freshwater Interface with Time in <i>CASE – 2/S</i> [First Column: Output of Basic Image Analysis, The Color Maps Indicate $\bar{C}_{i,j}$ ; Second Column: Numerical Simulation (0.5-Concentration Isoline); Third Column: Overlap of Numerical Simulation and Basic Image Analysis Outputs]. All dimensions are in mm. . . . .	47
3.12 Comparison Between Time Varying Observed and Numerically Simulated Pressure Head Data in <i>CASE – 1/S</i> . . . . .	49
3.13 Comparison Between Time Varying Observed and Numerically Simulated Pressure Head Data in <i>CASE – 2/S</i> . . . . .	49
3.14 Saltwater-freshwater Interface in <i>CASE – 1/S</i> . (Red Line: FEFLOW Simulation Results; Blue Line: Experimental Results Obtained from Basic Image Analysis) . . . . .	50
3.15 Saltwater-freshwater Interface in <i>CASE – 2/S</i> . (Red Line: FEFLOW Simulation Results; Blue Line: Experimental Results Obtained from Basic Image Analysis) . . . . .	50

3.16	Time Varying Experimental Tracer Movement in Saltwater Wedge Under Quasi Steady Condition for <i>CASE – 1/S</i> . . . . .	52
3.17	Time Varying Numerical Tracer Movement in Saltwater Wedge Under Quasi Steady Condition for <i>CASE – 1/S</i> . . . . .	53
3.18	Time Varying Experimental Tracer Movement in Freshwater Zone Under Quasi Steady Condition for <i>CASE – 1/S</i> . . . . .	54
3.19	Time Varying Numerical Tracer Movement in Freshwater Zone Under Quasi Steady Condition for <i>CASE – 1/S</i> . . . . .	55
4.1	Schematic Representation Experimental Setup with Single Layered Porous Media Under Static Saltwater Side Boundary Condition . .	59
4.2	Green Rectangular Box and Experimental Beach Slope for <i>CASE – 3A/S</i> . . . . .	60
4.3	Green Rectangular Box and Experimental Beach Slope for <i>CASE – 3B/S</i> . . . . .	61
4.4	Green Rectangular Box and Experimental Beach Slope for <i>CASE – 3C/S</i> . . . . .	62
4.5	Green Rectangular Box and Experimental Beach Slope for <i>CASE – 3D/S</i> . . . . .	63
4.6	Observed Time Varying Salinity Profiles at Saltwater Reservoir ( <i>Zone – A</i> ) . . . . .	64
4.7	Boundary Conditions Used in Numerical Simulation for Experiments with Single Layered Porous Media Under Static Saltwater Side Condition . . . . .	66
4.8	Detailed Steps of G-Channel Matrix Subtraction . . . . .	68
4.9	Detailed Steps of G-Channel Based Image Analysis: (a) Identification of Saltwater-Freshwater Interface, (b) Filtered Saltwater-Freshwater Interface Obtained from 10% Winsorized Mean , (c) Concentration Distribution . . . . .	70

4.10 Development of Saltwater Wedge with Time in <i>CASE-3A/S</i> [First Column: Experimental Images; Second Column: Output of G-Channel Based Image Analysis; Third Column: Numerical Simulation (0.5-Concentration Isoline), The Color Maps Indicate Concentration]. All dimensions are in <i>mm</i> . . . . .	73
4.11 Development of Saltwater Wedge with Time in <i>CASE – 3B/S</i> [First Column: Experimental Images; Second Column: Output of G-Channel Based Image Analysis; Third Column: Numerical Simulation (0.5-Concentration Isoline), The Color Maps Indicate Concentration]. All dimensions are in <i>mm</i> . . . . .	74
4.12 Development of Saltwater Wedge with Time in <i>CASE-3C/S</i> [First Column: Experimental Images; Second Column: Output of G-Channel Based Image Analysis; Third Column: Numerical Simulation (0.5-Concentration Isoline), The Color Maps Indicate Concentration]. All dimensions are in <i>mm</i> . . . . .	75
4.13 Development of Saltwater Wedge with Time in <i>CASE – 3D/S</i> [First Column: Experimental Images; Second Column: Output of G-Channel Based Image Analysis; Third Column: Numerical Simulation (0.5-Concentration Isoline), The Color Maps Indicate Concentration]. All dimensions are in <i>mm</i> . . . . .	76
4.14 Comparison Between Time Varying Observed and Numerically Simulated Pressure Head Data . . . . .	78
4.15 Saltwater-freshwater Interface for Experiments with Single Layered Porous Media Under Static Saltwater Side Boundary Condition (Red Line: FEFLOW Simulation Results; Blue Line: Experimental Results Obtained from G-Channel Based Image Analysis) . . . . .	80
4.16 SGD Flow Pathways for Experiments with Single Layered Porous Media Under Static Saltwater Side Boundary Condition . . . . .	81
4.17 Schematic Representation Experimental Setup with Single Layered Porous Media Under Tidal Saltwater Side Boundary Condition . . . . .	84
4.18 Observed Time Varying Salinity Profiles at Saltwater Reservoir ( <i>Zone-A</i> ) . . . . .	85

4.19 Boundary Conditions Used in Numerical Simulation for Experiments with Single Layered Porous Media Under Tidal Saltwater Side Condition. . . . .	87
4.20 Development of Saltwater Wedge with Time in <i>CASE – 3A/T</i> [First Column: Experimental Images; Second Column: Output of G-Channel Based Image Analysis; Third Column: Numerical Simulation, The Color Maps Indicate Concentration]. All dimensions are in <i>mm</i> . . . . .	90
4.21 Development of Saltwater Wedge with Time in <i>CASE – 3B/T</i> [First Column: Experimental Images; Second Column: Output of G-Channel Based Image Analysis; Third Column: Numerical Simulation, The Color Maps Indicate Concentration]. All dimensions are in <i>mm</i> . . . . .	91
4.22 Development of Saltwater Wedge with Time in <i>CASE – 3C/T</i> [First Column: Experimental Images; Second Column: Output of G-Channel Based Image Analysis; Third Column: Numerical Simulation, The Color Maps Indicate Concentration]. All dimensions are in <i>mm</i> . . . . .	92
4.23 Development of Saltwater Wedge with Time in <i>CASE – 3D/T</i> [First Column: Experimental Images; Second Column: Output of G-Channel Based Image Analysis; Third Column: Numerical Simulation, The Color Maps Indicate Concentration]. All dimensions are in <i>mm</i> . . . . .	93
4.24 Comparison Between Time Varying Observed and Numerically Simulated Pressure Head Data . . . . .	94
4.25 Observed Time Varying Pore-Water Pressure Head . . . . .	95
4.26 Saltwater-freshwater Interface for Experiments with Single Layered Porous Media Under Tidal Saltwater Side Boundary Condition (Red Line: FEFLOW Simulation Results; Blue Line: Experimental Results Obtained from G-Channel Based Image Analysis) . . . . .	98
4.27 SGD Flow Pathways for Experiments with Single Layered Porous Media Under Tidal Saltwater Side Boundary Condition . . . . .	99

5.1	Schematic Representation Experimental Setup with Multilayered Porous Media Under Static Saltwater Side Boundary Condition . . . . .	103
5.2	Observed Time Varying Salinity Profiles at Saltwater Reservoir ( <i>Zone-A</i> ) . . . . .	104
5.3	Schematic Representation Experimental Setup with Multilayered Porous Media Under Tidal Saltwater Side Boundary Condition . . . . .	105
5.4	Observed Time Varying Salinity Profiles at Saltwater Reservoir ( <i>Zone-A</i> ) . . . . .	106
5.5	Boundary Conditions Used in Numerical Simulation for Experiments with Multilayered Porous Media Under Static Saltwater Side Condition . . . . .	107
5.6	Boundary Conditions Used in Numerical Simulation for Experiments with Multilayered Porous Media Under Tidal Saltwater Side Condition . . . . .	109
5.7	Development of Saltwater Wedge with Time in <i>CASE-4A/S</i> [First Column: Experimental Images; Second Column: Output of G-Channel Based Image Analysis; Third Column: Numerical Simulation, The Color Maps Indicate Concentration]. All dimensions are in <i>mm</i> . . . . .	112
5.8	Development of Saltwater Wedge with Time in <i>CASE-4B/S</i> [First Column: Experimental Images; Second Column: Output of G-Channel Based Image Analysis; Third Column: Numerical Simulation, The Color Maps Indicate Concentration]. All dimensions are in <i>mm</i> . . . . .	113
5.9	Development of Saltwater Wedge with Time in <i>CASE-4C/S</i> [First Column: Experimental Images; Second Column: Output of G-Channel Based Image Analysis; Third Column: Numerical Simulation, The Color Maps Indicate Concentration]. All dimensions are in <i>mm</i> . . . . .	114

5.10 Development of Saltwater Wedge with Time in <i>CASE – 4D/S</i> [First Column: Experimental Images; Second Column: Output of G-Channel Based Image Analysis; Third Column: Numerical Sim- ulation, The Color Maps Indicate Concentration]. All dimensions are in mm. . . . .	115
5.11 Development of Saltwater Wedge with Time in <i>CASE – 4A/T</i> [First Column: Experimental Images; Second Column: Output of G-Channel Based Image Analysis; Third Column: Numerical Sim- ulation, The Color Maps Indicate Concentration]. All dimensions are in mm. . . . .	116
5.12 Development of Saltwater Wedge with Time in <i>CASE – 4B/T</i> [First Column: Experimental Images; Second Column: Output of G-Channel Based Image Analysis; Third Column: Numerical Sim- ulation, The Color Maps Indicate Concentration]. All dimensions are in mm. . . . .	117
5.13 Development of Saltwater Wedge with Time in <i>CASE – 4C/T</i> [First Column: Experimental Images; Second Column: Output of G-Channel Based Image Analysis; Third Column: Numerical Sim- ulation, The Color Maps Indicate Concentration]. All dimensions are in mm. . . . .	118
5.14 Development of Saltwater Wedge with Time in <i>CASE – 4D/T</i> [First Column: Experimental Images; Second Column: Output of G-Channel Based Image Analysis; Third Column: Numerical Sim- ulation, The Color Maps Indicate Concentration]. All dimensions are in mm. . . . .	119
5.15 Comparison Between Time Varying Observed and Numerically Sim- ulated Pressure Head Data . . . . .	121
5.16 Observed Time Varying Pore-Water Pressure Head . . . . .	122
5.17 Comparison Between Time Varying Observed and Numerically Sim- ulated Pressure Head Data . . . . .	123
5.18 Saltwater-freshwater Interface for Experiments with Multilayered Porous Media Under Static Saltwater Side Boundary Condition (Red Line: FEFLOW Simulation Results; Blue Line: Experimental Re- sults Obtained from G-Channel Based Image Analysis) . . . . .	126

5.19	Saltwater-freshwater Interface for Experiments with Multilayered Porous Media Under Static Saltwater Side Boundary Condition (Red Line: FEFLOW Simulation Results; Blue Line: Experimental Results Obtained from G-Channel Based Image Analysis) . . . . .	128
5.20	SGD Flow Pathways for Experiments with Multilayered Porous Media Under Static Saltwater Side Boundary Condition . . . . .	130
5.21	SGD Flow Pathways for Experiments with Multilayered Porous Media Under Tidal Saltwater Side Boundary Condition . . . . .	131
6.1	Single Layered Unconfined Aquifer Under Static Saltwater Side Boundary Condition . . . . .	134
6.2	Multilayered Aquifer Under Static Saltwater Side Boundary Condition	139
6.3	Single Layered Unconfined Aquifer Under Tidal Saltwater Side Boundary Condition . . . . .	146
6.4	Multilayered System Under Tidal Saltwater Side Boundary Condition	149



# List of Algorithms

1	G-Channel Based Image Analysis . . . . .	71
---	--	----



# Chapter 1

## Introduction

### 1.0 Background

Worldwide coastal zones are highly populated ones (MOEFCC, 2017). Saltwater intrusion in coastal aquifers is a critical hydro-environmental problem (Llopis-Albert and Pulido-Velazquez, 2014; Post and Werner, 2017; Kim and Yang, 2018; Zhang et al., 2019). The intrusion of saltwater (Figure 1.1) in freshwater aquifer occurs due to variable-density flow (Holzbecher, 1998) in porous media. Saltwater density is higher than the density of freshwater. High-density saltwater generates a large concentration gradient in the saltwater-freshwater interface (SWI) zone. Density stratification across the SWI alters the flow dynamics and mass transport in porous media. This flow dynamics generate a landward force. Freshwater flux or submarine groundwater discharge quasi-dynamically maintains the saltwater-freshwater interface and the nutrient balance in the sea. This saltwater-freshwater interface can be conceptualized using a) sharp interface approach (no mixing zone) and b) diffused interface approach (wide mixing zone). Hydrostatic balance of saltwater-freshwater interface under sharp interface approximation was first defined by Ghyben and Herzberg (Diersch, 2013). Sharp interface approximation was used in large number of studies, e.g., Reilly and Goodman (1985), Bear (1999), and Cheng and Ouazar (1999). However, a sharp interface between two miscible fluids (saltwater and freshwater) cannot exist in reality. Diffused interface approach is required for better representation of the saltwater-freshwater transition zone. Henry (1964) and Pinder and Cooper Jr (1970) started the use of density-dependent diffused interface approach for coastal problems. Analytical and numerical models with sharp interface approximation are computationally less expensive compared to diffused interface models. Pumping patterns, beach slope, tidal dynamics, and sea-level rise influence the saltwater-freshwater interface. Physically consistent and stable/unstable multiple flow patterns are possible under variable

density conditions. The situation becomes worse in the presence of tidal oscillations. Density-driven flow in porous media remains one of the challenging problems owing to its inherent non-linearity and limited availability of analytical solutions or availability of standard or field data set (Simpson and Clement, 2003). Thus a conceptual understanding of saltwater intrusion dynamics is important from the aquifer management point of view.

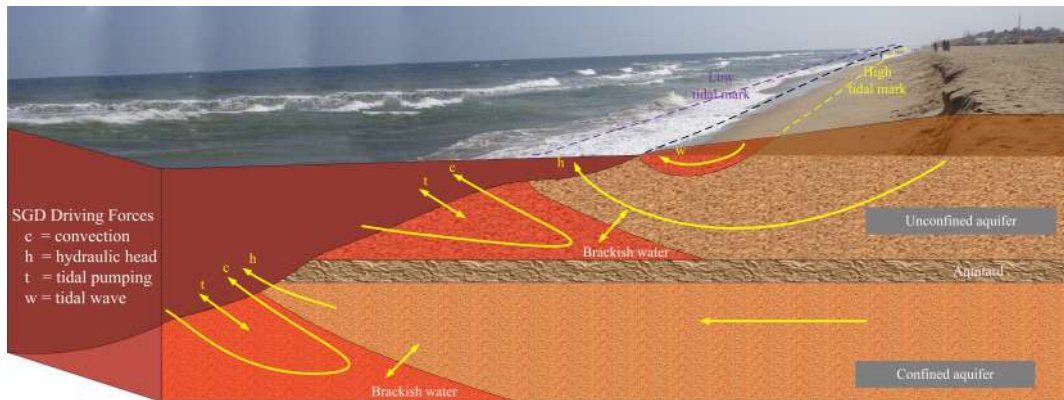


Figure 1.1: Schematic Representation of Multilayered Coastal Aquifer with Driving Forces

Field observations are mostly scattered information and are limited by cost. Point data do not provide sufficient information about the dynamics and flow patterns in coastal aquifers. In recent years, different in-situ observation-based methods were proposed to identify the fluid dynamics of density-dependent flows (Souza and Voss, 1987; Kim et al., 2007; MacAllister et al., 2018). Experimental investigation can provide scientific and systematic information on freshwater-saltwater interface and flow pattern under geometric, kinematic, and dynamic similitude conditions. Moreover, experimental quantification is necessary to evaluate the performance of mathematical/numerical models in the context of robust and reliable engineering solutions. Laboratory-scale experiments were widely used to investigate the behaviour of saltwater interface (Schincariol and Schwartz, 1990; Zhang et al., 2002; Goswami and Clement, 2007; Konz et al., 2008, 2009b, a; Chang and Clement, 2013; Dose et al., 2014; Mehdizadeh et al., 2014). These studies mostly focused on the dispersive mixing zone while solving the variants of the Henry problem (Werner et al., 2013). Experiments were performed under confined or unconfined, steady-state or transient conditions under controlled temperature, pressure, and hydraulic gradient. A large number of studies considered one dimensional (1D) saltwater dynamics experiments (Hassanizadeh and Leijnse, 1995; Schotting et al., 1999; Watson et al., 2002; Jiao and Hötzl, 2004). However, saltwater-freshwater interface identification is not possible from 1D experiments. Two-dimensional (Goswami and Clement, 2007; Abdoulhalik and Ahmed, 2018) or

1. Image Analysis:  
Involves obtaining concentrations through visual interpretation of images. This technique utilizes digital image processing to analyze features.

2. Gamma Radiation technique:  
this method is employed to assess soil or subsurface properties by measuring the intensity of gamma rays emitted by naturally occurring radioactive isotopes, providing information about soil composition and contamination.

3. Nuclear magnetic Resonance imaging:  
MRI can be applied to investigate subsurface structures, soil properties, or fluid distribution. The technique relies on the behavior of atomic nuclei, particularly hydrogen protons, in a magnetic field. When exposed to radiofrequency pulses, these nuclei emit signals that are processed to create detailed cross-sectional images, providing valuable information about the composition and spatial distribution of substances within a sample.

## 1.0. BACKGROUND

3

three-dimensional (Pearl et al., 1993; Oswald and Kinzelbach, 2004; Oswald et al., 2007) *Sand Box Models* are preferred as the shape of the saltwater-freshwater interface is scale-dependent. Two-dimensional (2D) *Sand Box Models* was utilized for the current study over three-dimensional (3D) model considering the ease in a) instrumentation (Non intrusive measurement) and b) visualization. Under controlled conditions, i.e., known boundary conditions, initial conditions, and porous material properties, repeatability of the experiments can be ensured. Most of the studies in literature considered vertical beach face for saltwater intrusion experiments (Konz et al., 2008; Lu et al., 2019; Mehdizadeh et al., 2020; Wu et al., 2020). Previous studies either used vertical saltwater boundary or homogenous configuration to understand the density-dependent flow process. Vertical beach face is very rare under natural conditions. The density gradient at a non-vertical sloping boundary plays a vital role in changing the hydraulic gradient and contaminant transport across the SWI. Only a few studies included the sloping beach face (Zhang et al., 2001; Kuan et al., 2012; Shen et al., 2020) and layered media (Mehdizadeh et al., 2014; Shi et al., 2018; Abdoulhalik et al., 2020). However, experimental quantification of the beach slope effect was not studied. The multilayered coastal aquifers are commonly encountered in real settings. Layer heterogeneity dictates the intra and inter-layer mass transfer. Previous saltwater intrusion studies (Ketabchi et al., 2014; Liu et al., 2014; Dose et al., 2014; Mehdizadeh et al., 2014, 2017; Strack and Ausk, 2015) considered layered configurations to represent subsurface heterogeneous conditions. Experimental investigations (Abdoulhalik and Ahmed, 2017b; Strack and Ausk, 2015) showed that layered heterogeneity controls the saltwater-freshwater interface toe location. Saltwater dynamics in sloping beach multilayered porous media were not studied with/without tidal conditions.

Quantification studies can be designed based on head and concentration. Pore-water pressure measurement can provide head values. Concentrations were usually obtained from image analysis (Schincariol and Schwartz, 1990; Swartz and Schwartz, 1998; Zhang et al., 2001), gamma radiation technique (Oostrom et al., 1992), or nuclear magnetic resonance imaging technique (Oswald and Kinzelbach, 2004). Tracer studies require colour dye for visualization purposes. Image analysis can be considered a semi-quantitative method. Previous studies (Schincariol and Schwartz, 1990; Swartz and Schwartz, 1998; Zhang et al., 2001) were based on monochromatic images. These images do not provide sufficient information on the saltwater-freshwater mixing zone Zhang et al. (2001). High resolution coloured images can provide concentration variation information with small measurement errors Konz et al. (2008). Concentration isolines can be checked against the processed images.

The previous works focused on the position, shape, and thickness of the saltwater-freshwater transition zone for density-dependent flow in porous media. The convective saltwater circulation phenomenon (Oz et al., 2015) was not studied in detail. The convective fingering effect is another phenomenon not observed in the previous vertical boundary studies. It is well known that variable density flows in porous media can become unstable (Dentz et al., 2006). The occurrence of fingering is caused by flow instabilities due to differences in viscosity and density values between two miscible fluids. Instabilities and fingering develop when a denser fluid lies above the lighter fluid (Manickam and Homsy, 1995; Wooding et al., 1997; Simmons et al., 2001; Diersch and Kolditz, 2002). Viscous fingers develop and can be visualized in the form of corrugated interface (Schincariol et al., 1994). The fingers propagate rapidly until they reach a stable convective flow regime. The results of density-coupled groundwater flow simulations were typically represented in terms of concentration isolines (Lee and Cheng, 1974; Volker and Rushton, 1982; Simpson and Clement, 2004) or vector plots of the groundwater velocity (Mehnert and Jennings, 1985; Simmons and Narayan, 1997). Saltwater circulation patterns cannot be determined from these types of information. Circulation patterns in steady-state mixed convection problems can be identified from the streamline plots. The density-driven circulation can be conceptually divided into two consecutive processes: (i) flow of high-density fluid (in the counterclockwise direction) towards low-density fluid due to density gradient, and (ii) upward flow of low-density fluid towards the free surface of the interface. Moreover, a limited number of studies are available on circulation patterns in density-dependent flows (Oz et al., 2015).

2. Density Dependent circulation:  
This difference in density creates a vertical density gradient.

In the Northern Hemisphere, due to the Coriolis effect, this downward flow tends to deviate and form a counterclockwise circulation pattern.

As the denser fluid sinks, it creates a space that needs to be filled. This vacancy triggers the less dense fluid above to rise due to its buoyancy.

## 1.1 Motivation

Literature review on saltwater dynamics in porous media revealed that most experimental studies utilized density-dependent flow in porous media with vertical beach face under static and tidal saltwater side boundary conditions. Vertical beach face does not represent the natural coastal aquifer condition. There is a need for quantification of influence of beach slope on saltwater dynamics in single and multilayered porous media. The obtained results can be verified with standard numerical code(s). Non-intrusive measurement techniques (e.g., pore-water pressure, image analysis) can be employed for quantitative, semi-quantitative, and qualitative analysis. Only a few studies included pressure sensor data acquisition in experiments. The tracer-based experimental study can be utilized for capturing time-varying images. However, no standard framework is available for experimental image analysis for saltwater dynamics in porous media. There is scope for

Dimensional Analysis is Crucial for Quantifying Scale Effects:

Complexity Reduction: Physical systems often involve multiple variables with different dimensions (e.g., length, time, mass). Dimensional analysis combines these variables into dimensionless groups, reducing the number of independent parameters and simplifying the analysis.

Similitude: Non-dimensional parameters allow for comparison of systems of different sizes that are geometrically, kinematically, and dynamically similar. This makes it possible to predict the behavior of full-scale systems based on smaller-scale experiments or models.

2. Pressure Transducers  
pressure transducer placed on the container would sense this change in pressure and send out a corresponding electrical signal.

## 1.2. OBJECTIVES OF THE THESIS

5

the development of methodology for experimental image analysis. Moreover, no study is available on the experimental identification of submarine groundwater discharge pathways. Hence, there is a need for tracer injection study in the freshwater zone. Moreover, a Dimensional Analysis study is required to identify suitable non-dimensional parameters to quantify the scale effect. The current Thesis is aimed at addressing the aforementioned gaps.

## 1.2 Objectives of the Thesis

The main objective is to investigate the influence of varying beach slopes on the saltwater dynamics in porous media under static and tidal boundary conditions. The specific objectives of this Thesis are:

- To experimentally investigate the saltwater dynamics in single and multilayered systems under static and tidal conditions.
- To develop an image analysis technique to quantify the concentration gradient in porous media.
- To quantify the saltwater dynamics through numerical analysis and direct pressure measurement method with pressure transducers.
- To quantify the influence of beach slope on saltwater movement.

## 1.3 Outline of the Thesis

The Thesis consists of seven chapters, including this introductory chapter. The present chapter introduces the fundamentals of the saltwater intrusion process, including previous works, motivation, objectives of the Thesis. However, relevant literature for individual topics is included in respective chapters.

Chapter 2 is devoted to the experimental design and methodology. Detailed descriptions of instrumentation and material characterization are also presented.

Chapter 3 deals with experimental conceptualization under static condition. It also includes a basic image analysis method. Pore-water measurement, numerical simulation, and analytical solution are used for quantitative analysis. Circulation patterns in saltwater wedge and freshwater zones are also included.

Chapter 4 presents laboratory-scale experimental observations with varying beach slopes in single-layered porous media under static and tidal saltwater side

boundary conditions. A novel G-Channel based image analysis technique is presented. Submarine groundwater discharge pathways are also included.

Chapter 5 presents laboratory-scale experimental observations with varying beach slopes in multilayered porous media under static and tidal saltwater side boundary conditions. Submarine groundwater discharge pathways are also included.

Chapter 6 includes Dimensional Analysis for both single and multilayered porous media under static and tidal saltwater side boundary conditions. Expressions for saltwater-freshwater interface toe length and submarine groundwater discharge gaps are presented.

In Chapter 6, an overview of this study, conclusions, and recommendations for further work are presented.

**1. Peristaltic pumps:**

sometimes called hose pumps or tube pumps, are a unique type of positive displacement pump that use rollers or a rotor to squeeze a flexible tube, propelling the fluid inside along a specific path. Imagine squeezing a toothpaste tube – that's essentially how a peristaltic pump works, but with much more control and precision.

**2. CTD DRIVER**

Collects Conductivity (salinity), Temperature, and Depth data in the ocean. A driver is a software component that allows a computer system to communicate with a specific hardware device, like the CTD instrument in this case. The CTD driver manages data communication between the CTD and the computer software that will analyze the collected data.

# Chapter 2

## Experimental Design & Methodology

### 2.0 Overview

This Chapter focuses on the basics of experimental design. There are two major components in the experimental design, a) instrumentation and b) material characterization. The use of higher precision instruments can eliminate instrumentation errors. However, selecting proper material can eliminate/ reduce errors in the inherent assumptions used in the controlled experiments. In this Thesis, a two-dimensional (2D) *Sand Box Model* was utilized for conducting the physical experiments. Both instrumentation and material selection (including characterization) are discussed in detail.

### 2.1 Instrumentation

The experimental instrumentation can be divided into five parts/ units a) Sand Box Model, b) Tidal Mechanism, c) Pressure Transducer, d) Data Acquisition System, and e) Digital Camera. Moreover, Peristaltic Pump and Conductivity Temperature, and Depth (CTD) Diver were also utilized for the experiments.

#### 2.1.1 Sand Box Model

The *Sand Box Model* was utilized to study variable density currents in both confined and unconfined hydraulic conditions. The frame structure of the experimental setup is made of stainless steel. It is 3.0 m long, 1.0 m high, and 0.02 m wide and resting on three iron frame bases (Figure 2.1). The width of the setup is very small compared to other two dimensions to ensure the 2D flow in the vertical

cross section (Cartwright et al., 2004; Goswami and Clement, 2007; Luyun Jr et al., 2011; Kuan et al., 2012; Zhou et al., 2016; Yu et al., 2019a).

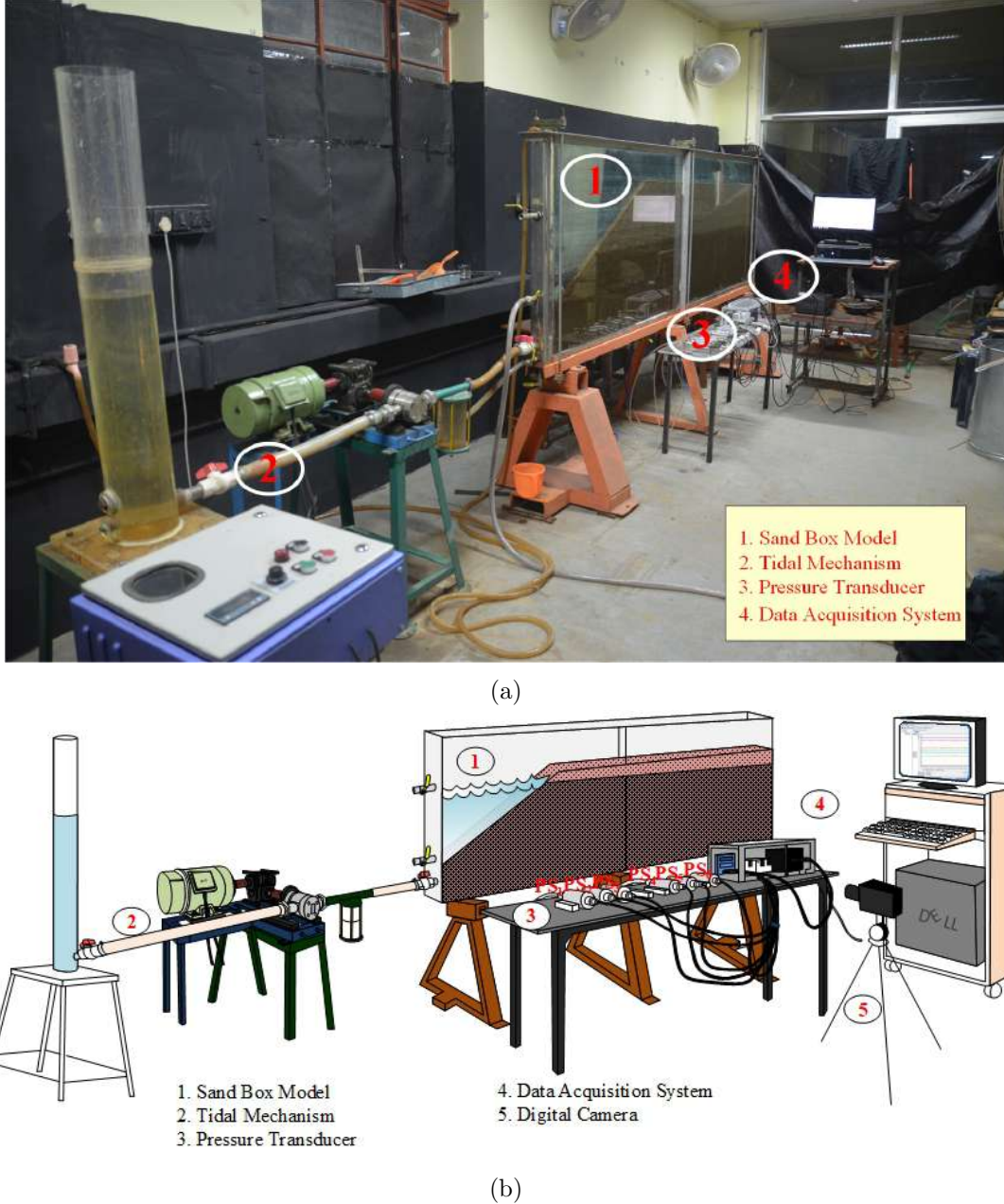


Figure 2.1: *Sand Box Model*: a Pictorial Representation of Experimental Setup and b Schematic Representation of Experimental Setup.

The *Sand Box Model* is made of two glass plates of 180 mm thickness parallelly placed at a distance of 0.02 m. Two water reservoirs (each 50 mm length) are available at both ends. The right reservoir is used to feed (flux condition) freshwater flow to the system. Constant head condition is maintained in the left reservoir (filled with saltwater). An overflow outlet pipe (5 mm diameter) is placed at the height of 0.64 m from the model's base. **Stainless steel mesh (0.1 mm opening)** separates both the reservoirs from the middle sand box zone. The top of the setup is in

Brushless DC motor:  
Unlike brushed DC motors that use brushes to contact the rotor and generate sparks, Rotodyne motors have electronically controlled commutation, offering smoother operation, longer lifespan, and reduced maintenance needs.

High torque and displacement: Compared to conventional DC motors, Rotodyne motors deliver significantly higher torque and displacement per unit size, making them ideal for applications requiring powerful and compact solutions.

High efficiency

## 2.1. INSTRUMENTATION

9

direct contact with the atmosphere representing an unconfined aquifer condition. The bottom part of the setup has 18 flow controlling outlets, including one each at the bottom of the end reservoirs. The backside of the glass wall has 59 openings (8 mm diameter) for taking pressure measurements and injection-extraction of fluid.

### 2.1.2 Tidal Mechanism

The tidal mechanism was designed to impose a periodic head boundary condition at the left side of the *Sand Box Model*. It has four sub-units i) Water Column, ii) Flexible Pipe Connector, iii) Rotodyne DC Motor, iv) Control System.

Figure 2.2 shows different components of the Tidal Mechanism. This mechanism produces a linear periodic water level variation. The Rotodyne DC motor transfers saltwater from the column to the *Sand Box Model* through a flexible pipe connector in the forward cycle. In the backward cycle, water from *Sand Box Model* gets transferred to the saltwater column. This forward-backward (direction) motion of Rotodyne DC motor and its duration are automatically controlled by the *Control System*. A potentiometer circuit controls the rotational speed (rpm: revolutions per minute) of the DC motor. Therefore, water level variations (amplitude of fluctuations) of different periodicity could be imposed by changing the speed of the motor. High and low tide levels can be generated from the clockwise and anti-clockwise rotation of the motor. Two switches are available as a backup to initiate the cycle (direction) change in case of *micro switch failure* (automatic).

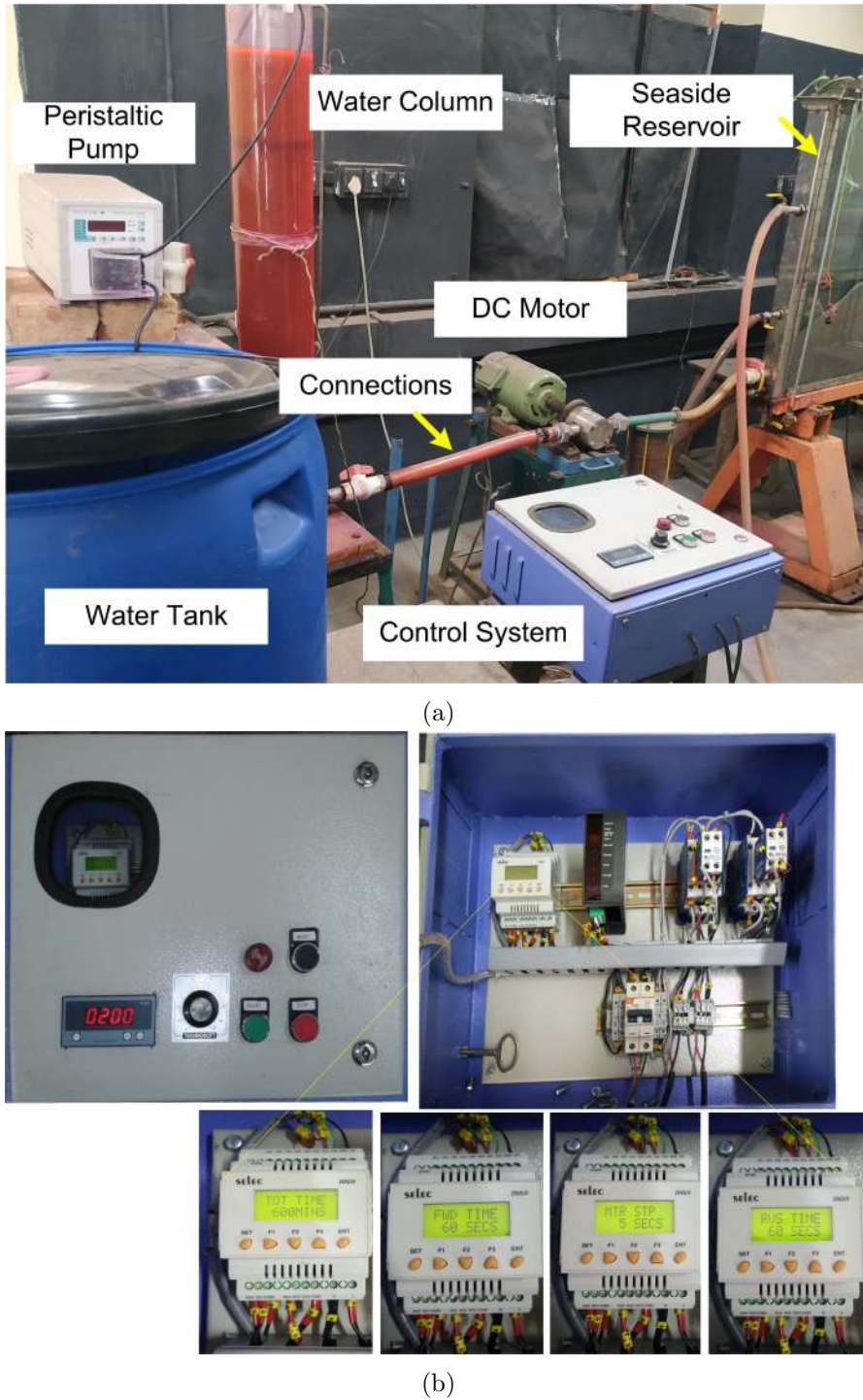


Figure 2.2: Tidal Control Mechanism a Tidal Mechanism and b Control Panel

### 2.1.3 Pressure Transducer

Pressure Transducers were used to measure the pore water pressure developed within the saturated porous medium. Pore water pressure refers to the pressure of water held or trapped between the inter-particle gaps. Under phreatic or unconfined condition, the pore water pressure is hydrostatic. Porewater pressure increases with salinity. Effective overpressure was estimated from the pore water

pressure by subtracting the hydrostatic component from it. Under confined or non-hydrostatic pressure conditions, porewater pressure was directly used to estimate the piezometric head. Water table wave information was extracted from the pressure transducer measurements. Forces generated due to buoyancy and capillary effects generally oppose each other. Buoyancy originates from the density difference between the brine phase and the fresh water phase, and points toward the upward direction. Capillary pressure is a function of the pore size. It opposes the movement of brine in response to buoyancy or other forces.

**2. Relation between effective overpressure and pore water pressure:**

**Effective Overpressure Calculation:** In hydrostatic conditions, pore water pressure increases linearly with depth due to the weight of the water column above. To determine the effective overpressure, which reflects pressure beyond this hydrostatic component, you subtract the hydrostatic pressure from the measured pore water pressure.

**Piezometric Head Estimation:** In confined or non-hydrostatic conditions, the hydrostatic assumption doesn't hold, and pore water pressure doesn't strictly follow a linear relationship with depth. Under these circumstances, the measured pore water pressure itself can be directly used to estimate the piezometric head, as it reflects the total hydraulic potential at that point.

**1. PSI gauge pressure:**

PSI gauge pressure is a measurement of pressure relative to the surrounding atmospheric pressure. PSI stands for pounds per square inch. It's an imperial unit of pressure, where one PSI is equal to the force of one pound exerted on an area of one square inch.

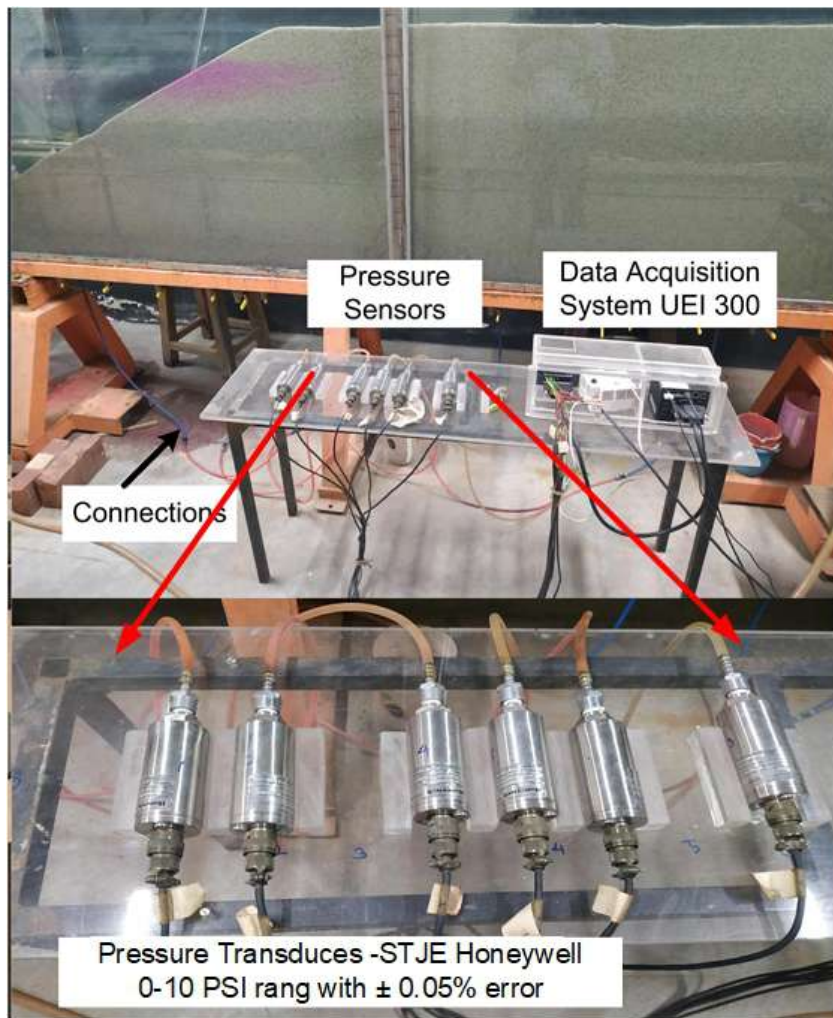


Figure 2.3: Pressure Transducers and Data Acquisition System

Pore water pressure was captured by Super TJE ultra-precision pressure transducers (STJE AP111) from Honeywell. The pressure transducers (with cylindrical stainless steel casing of 50 mm diameter and 64 mm high) can measure up to 10 psi gauge (psi gauge pressure) with an accuracy of  $\pm 0.05\%$ . This is equivalent to 7.0319 m water head with an accuracy of  $\pm 0.0035$  m. Each externally mounted pressure transducers were connected to the openings (8 mm diameter) present in the rear glass wall of *Sand Box Model* through a flexible rubber tube (8 mm diam-

eter). The data sampling frequency used in the present study was 20 *Hz* to avoid instrument response time-related issues.

### 2.1.4 Data Acquisition System

Data Acquisition (DAQ) System was used to acquire data from the pressure transducers. Pressure transducers send pore water pressure equivalent electrical signals to DAQ. DAQ supplies power to the transducer. After signal conditioning, the transducer signal is passed to the analog input board. The analog input board (UEILogger 300, Figure 2.4) converts the conditioned analog voltage into a computer-readable digital format. The UEILogger is connected to a computer through an ethernet port. The raw data can be visualized and transferred from the UEILogger Graphical User Interface.

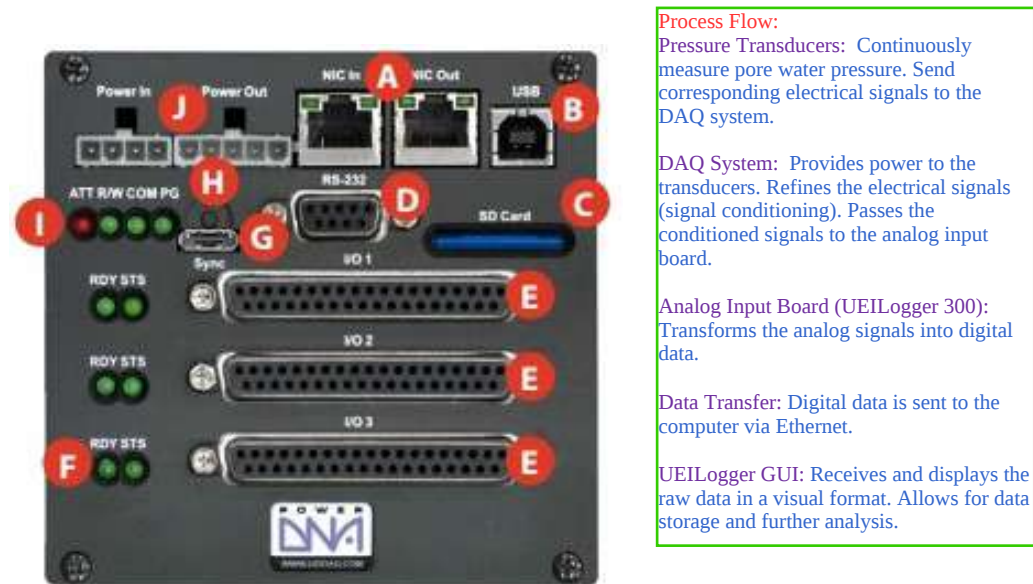


Figure 2.4: UEILogger 300— A: Network Connectors, B: USB Port, C: SD Card Slot, D: RS-232 Port, E: I/O Board/Layer Slots, F: I/O Layer Status LEDs, G: Sync Connector, H: Start/Reset Button, I: Communication Status LEDs, J: Power Connectors

### 2.1.5 Digital Camera

The Digital Single Lens Reflex (DSLR) camera Nikon d5100 was utilized for capturing time-varying experimental saltwater-fresh water interface movement visible from the front glass wall of the *Sand Box Model*. The camera mounted on a fixed tripod was placed centrally in front of the *Sand Box Model* at a distance of 1 *m* (Figure 2.1b). A wide-angle lens was used to overcome the space restriction. The recorded images show mild distortion toward the periphery of the frame. Distortion removal technique is discussed in Chapter 3. Images were capture using

the self capturing mode at an interval of 2 s to 2 min depending on the stage of saltwater-freshwater interface development.



Figure 2.5: Digital Single Lens Reflex (DSLR) Camera (Nikon d5100)

## 2.1.6 Peripheral Apparatus

Peristaltic Pump and CTD Diver were used for freshwater-saltwater supplies and conductivity-depth measurements, respectively.

### 2.1.6.1 Peristaltic Pump

Two *Peristaltic Pumps* were utilized for i) freshwater supply: to maintain freshwater flux at the right side boundary, and ii) saltwater supply: to maintain saltwater density at the left side boundary. A set of rotating rollers squeeze the tube to supply water at a constant flow rate. **Electrolab India make Peristaltic pumps of Model:PP-50VX were used** (Figure 2.6).



Figure 2.6: Variable Speed Peristaltic Pump (PP-50VX).

The flux was controlled by fixing the rotational speed (rpm: revolutions per minute) of the motor. It varies from 1 to 200 rpm. The pumps were individually calibrated to obtain the relationship between rotational speed and flow rate (Figure 2.7).

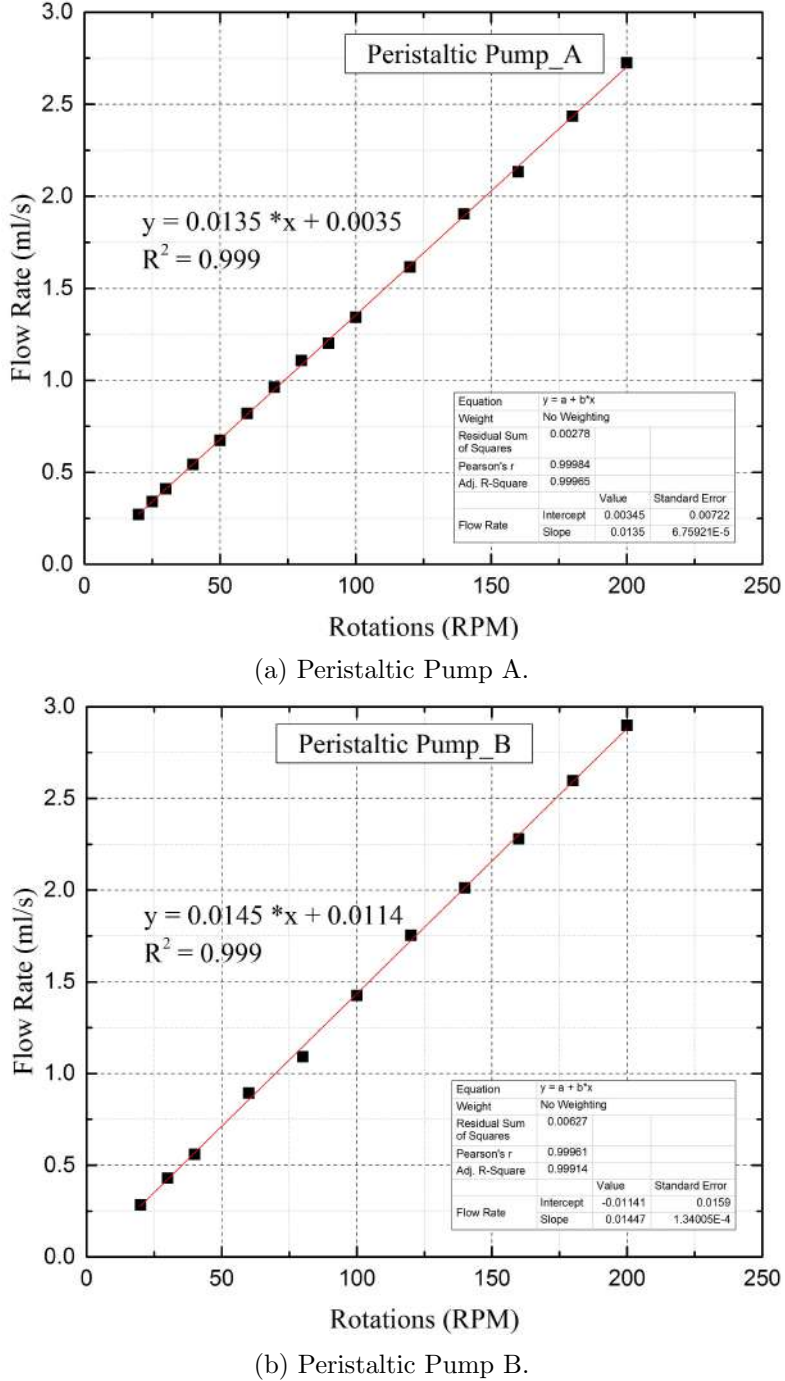


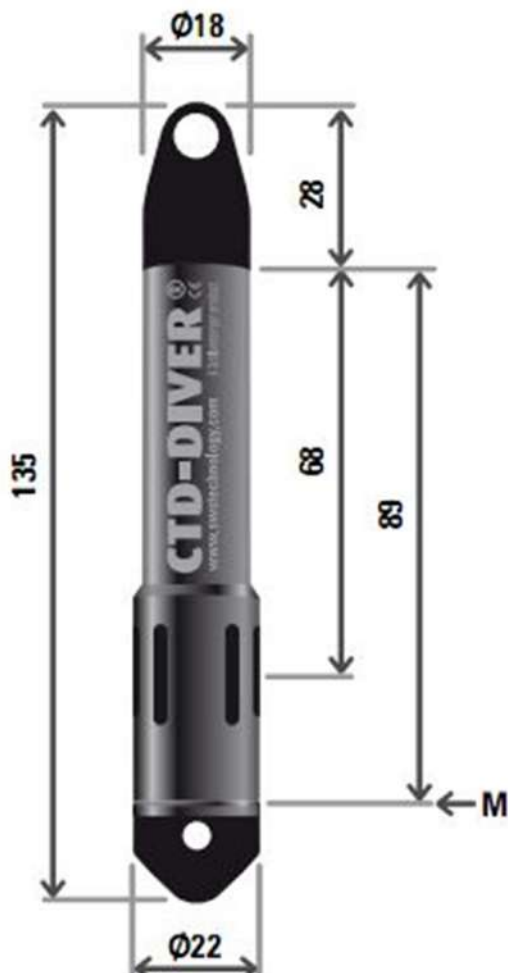
Figure 2.7: Calibration of Peristaltic Pump

### 2.1.6.2 Conductivity, Temperature and Depth (CTD) Diver

Two *CTD Divers* were utilized in i) water column: to monitor the time-varying saltwater density variation, and ii) left compartment of the *Sand Box Model*: to

monitor the time-varying saltwater density and water level variations. The CTD Diver Model: DI272 (Make: Schlumberger Water Services, Delft, Netherlands) measures absolute pressure, temperature, and conductivity of the water. CTD diver can operate in conductivity range of 0 to 120 mS/cm (equivalent to 0 mg/l to 76800 mg/l) with an accuracy of  $\pm 1\%$ . In the Thesis, sampling was performed at an interval of 15 milliseconds for 10-12 hours. Both the divers were calibrated based on known salt concentration values.

Scale 1:1



M = membrane  
Dimensions are expressed in mm.

Figure 2.8: Conductivity, Temperature and Depth (CTD) Diver

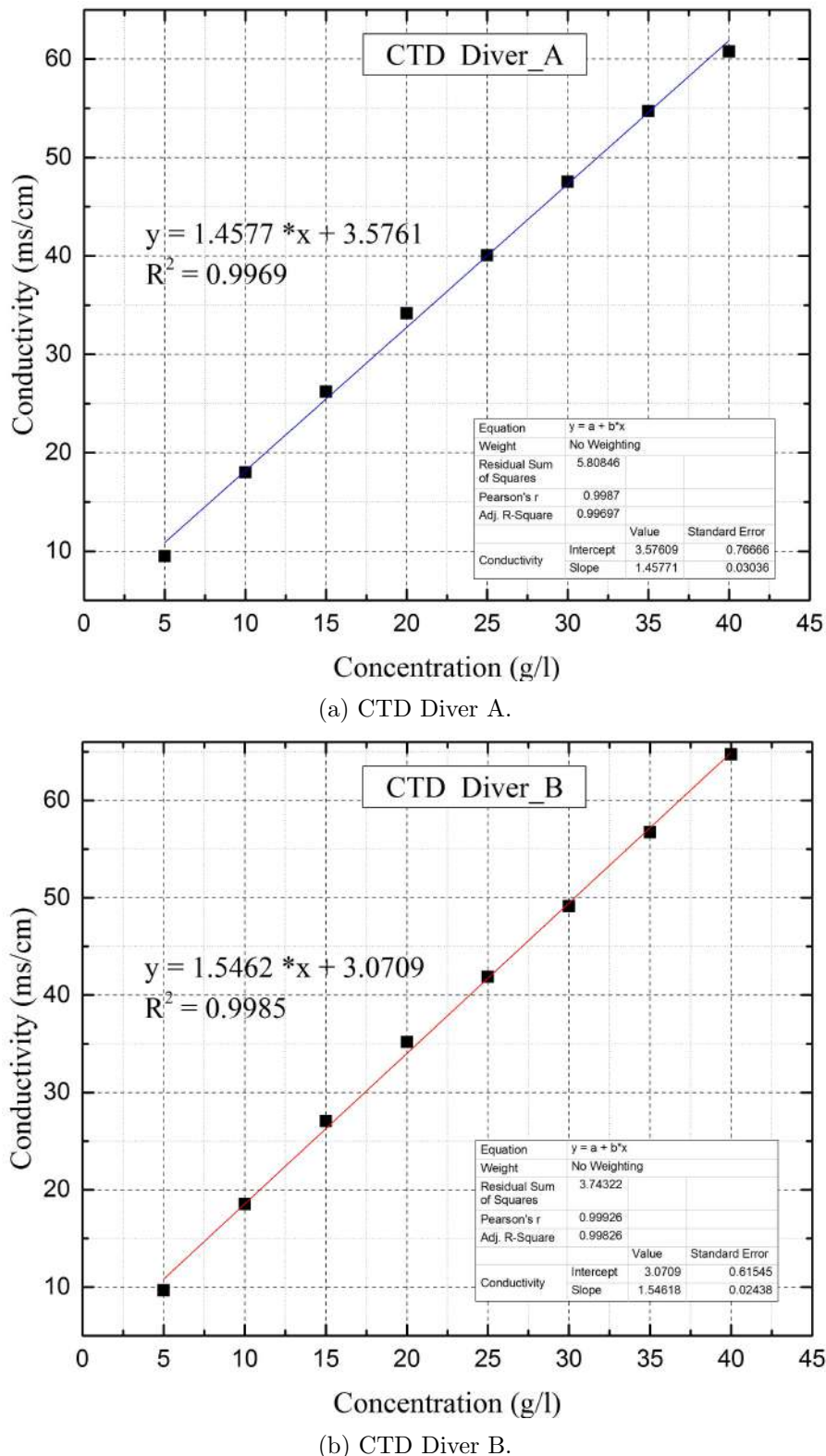


Figure 2.9: Calibration of CTD Diver

## 1. Standard Sand Indian

Grade 1:  
Bag of 25 Kg is made of local (French Source) natural silica sand (silica content higher than 98%), having a water content lower than 0.1 %. The constituent grains of this natural sand are uncrushed and of rounded form.

The standard sand is obtained from Ennore, Tamil Nadu, and is also known as Ennore sand.

## 2. Scanning Electron Microscope (SEM)

### Micrograph:

## Electron Beam

Instead of light, SEM uses a focused beam of high-energy electrons.

Scanning:

This beam scans across the surface of the sample in a raster pattern, like a TV screen.

Secondary Electrons (SE): These reveal the sample's topography, providing a 3D-like image of its surface features.

**Backscattered Electrons (BSE):** These tell about the composition of the sample, as denser areas scatter electrons more strongly, creating brighter regions in the image.

X-rays: These give information about the elemental composition of the sample.

### An EDX spectrum

is a type of analysis that reveals the elemental composition of a material. It works by bombarding the sample with an electron beam causing atoms to emit X-rays. Each element emits X-rays at specific energies, like a fingerprint, allowing identification and quantification.

**X-axis:** Shows the energy of the X-rays (keV).

Y-axis: Shows the number of X-rays detected at each energy level

## 2.2 Material Characterization

The *Material Characterization* can be divided into two parts/units a) Porous Materials/Aquifer Materials, and b) Tracer for Saltwater.

### 2.2.1 Porous Materials/Aquifer Materials

Three types of porous material i) Locally available clean Sand, ii) Grade-I Indian Standard sand (IS 650:1991), iii) Bentonite clay was used as aquifer/aquitard material in the *Sand Box Model*. Scanning Electron Microscope (SEM) Micro-

graph and Energy-dispersive X-ray (EDX) spectrum of *Clean Sand*, *Grade-I IS Sand*, and *Bentonite* are shown in Figures 2.11, 2.12, and 2.13, respectively. The SEM images at different magnifications indicate the presence of noticeable pores. Maximum pore space can be observed for *Bentonite*. This might cause an increase in the surface area and pore volume. The EDX analysis for *Clean Sand* indicates the presence of *Silica*, *Aluminum*, *Carbon*, *Oxygen*, *Iron*, and a small percentage of *Potassium*. However, EDX spectrum of *Grade-I IS Sand* shows *Silica*, *Aluminum*, *Oxygen*, and *Potassium*. Thus, it is evident that *Grade-I IS Sand* is free from organic impurities (indicated by *Carbon*). EDX spectrum of *Bentonite* shows the presence of *Silica*, *Oxygen*, *Iron*, and *Potassium*. *Clean Sand* was selected based on local availability. The clean Sand was washed with water to remove fine clay particles attached to the sand grains. The cleaned Sand was dried at room temperature. However, repeatability of the experimental results could be ensured with standard material. *Grade-I IS Sand* (IS 650:1991) was selected as porous material as it possesses standard physical characteristics. *Bentonite* was used as aquitard material for multilayered porous medium experiments.

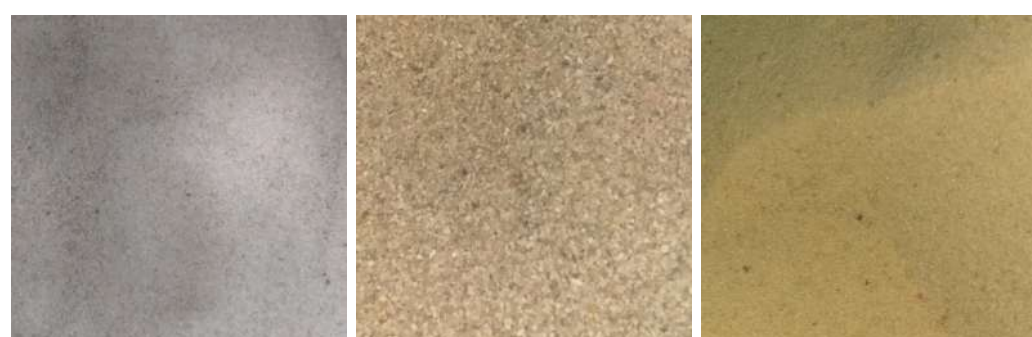
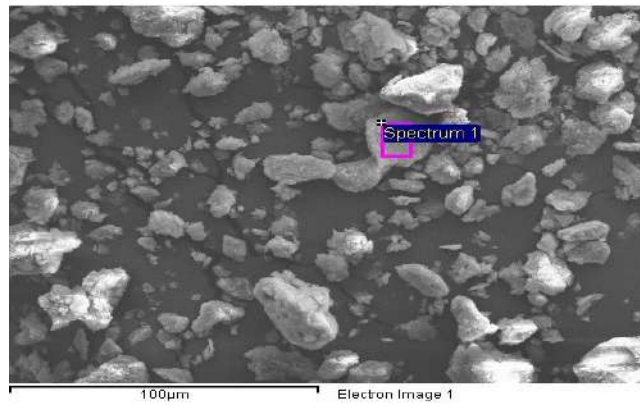
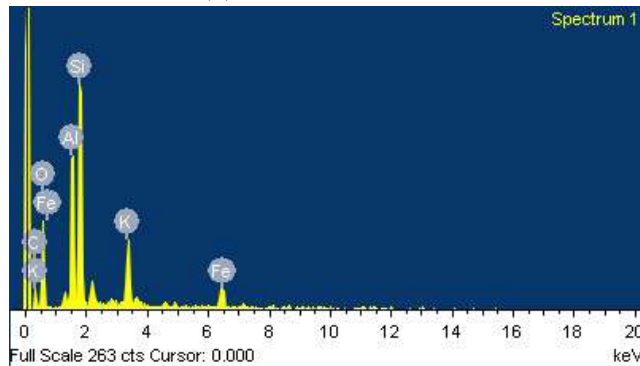


Figure 2.10: Experimental Porous Materials

Physical properties for the Sands were determined as per the methods prescribed in Bureau of Indian Standards codes (Table 2.1). The specific gravity,

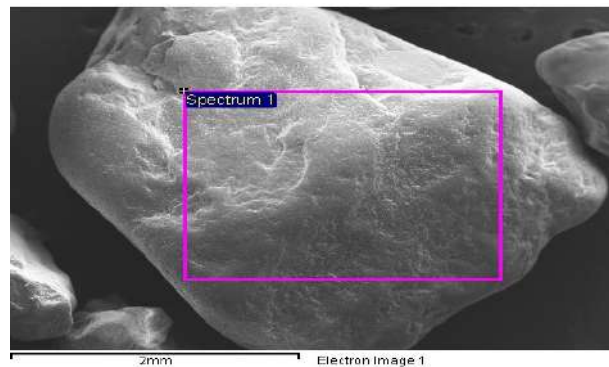


(a) SEM Micrographs

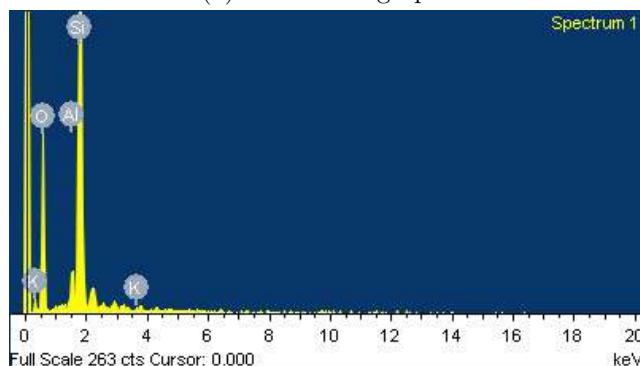


(b) EDX Spectrums

Figure 2.11: SEM Micrographs and EDX Spectrums of Clean Sand



(a) SEM Micrographs



(b) EDX Spectrums

Figure 2.12: SEM Micrographs and EDX Spectrums of Grade-I IS Sand

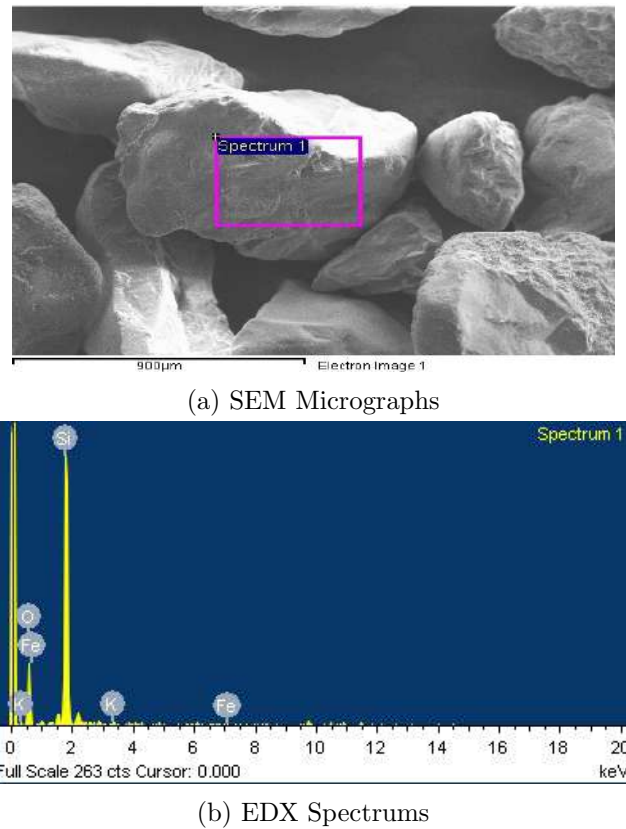


Figure 2.13: SEM Micrographs and EDX Spectrums of Bentonite Clay

mean grain size, coefficient of uniformity, coefficient of gradation, and hydraulic conductivity values for both *Clean Sand* and *Grade-I IS Sand* are summarized in Table 2.2. Grain size distribution plots for *Clean Sand* and *Grade-I IS Sand* are shown in Figures 2.14 and 2.15, respectively. The coefficient of uniformity and coefficient of gradation indicates that both the Sands are of uniform grade. However, hydraulic conductivity value is higher for Grade-I IS Sand compared to Clean Sand.

Table 2.1: Relevant Porous Material Properties and BIS Codes

Properties	IS Code
Grain size analysis	IS-2720 (Part 4):1985
Specific gravity	IS:2720(Part 4)-1985
Permeability	IS:2720(Part XVII)-1966
Indian Standard Sand	IS 650:1991

Table 2.2: Physical Properties of Aquifer Materials

Properties	Clean Sand	Grade-I IS Sand
Specific gravity (G)	2.65	2.67
Mean grain size, $D_{50}$ (mm)	1.025	1.124
Coefficient of uniformity, $C_u$	1.4	1.36
Coefficient of gradation, $C_c$	1.07	0.75
Permeability K (m/sec)	0.00017	0.00207

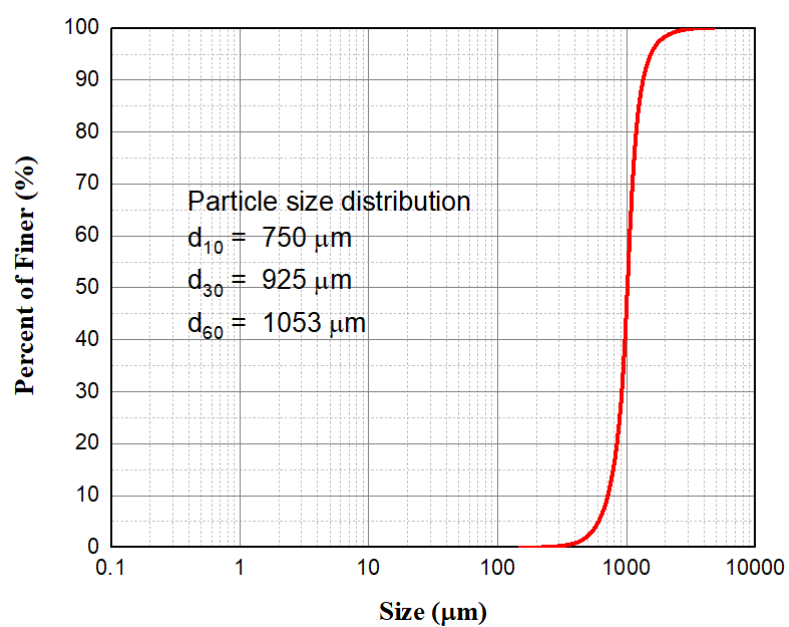


Figure 2.14: Grain Size Distribution of Clean Sand

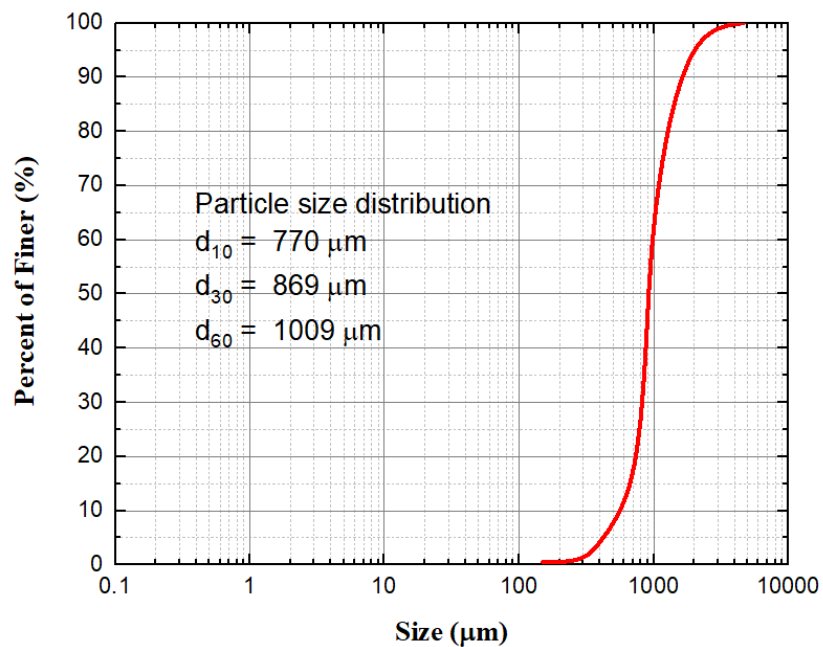


Figure 2.15: Grain Size Distribution of Grade-I IS Sand

### 2.2.2 Tracer for Saltwater

Saltwater ( $NaCl$ ) does not have any specific colour. Thus a suitable tracer is required to identify the saltwater-freshwater interface movement. The tracer will convect at the local seepage velocity. Moreover, the tracer should be buoyancy neutral. Thus, the tracer should be i) soluble in an aqueous solution, ii) non-reactive (low absorption), and iii) non-diffusive. Four Dyes [a natural or synthetic substance, Adegoke and Bello (2015)] were tested, e.g., i) Rhodamine-B (C.I. 45170, Basic Violet 10), ii) Indigo Carmine AR (C.I. 73015, Acid Blue 74), iii) Methyl Orange Indicator ACS (C.I. 13025, Acid Orange 52), iv) Commercial Food Dye(Neoteric DCBA Ideas).

1. Buoyancy neutral means that the tracer should have the same density as the medium it's moving through.

Diffused reflectance absorption spectra (DRS):

This is a spectroscopic technique that measures the light reflected by a sample after it interacts with the material.

Unlike traditional transmission spectroscopy, where light passes through the sample, DRS deals with scattered and reflected light.

DRS is valuable for analyzing opaque or highly scattering materials such as powders, films, and pigments.

Measuring the DRS provides information about the wavelengths of light that the sample absorbs.

Analyzing the absorption peaks in the spectra reveals details about the electronic structure and composition of the material.

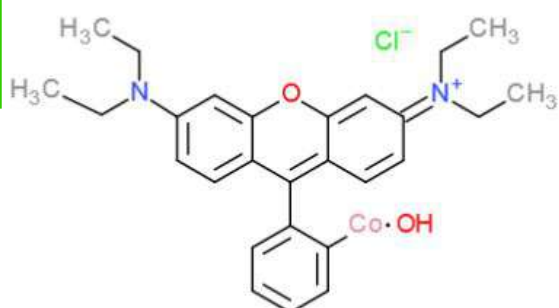


Figure 2.16: Molecular Structure of Rhodamine B



Figure 2.17: Molecular Structure of Indigo Carmine

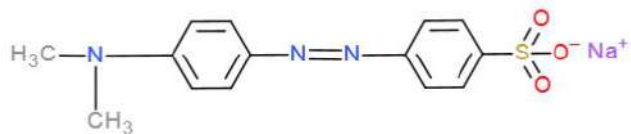


Figure 2.18: Molecular Structure of Methyl Orange

Molecular structure of first three dyes are shown in Figures 2.16, 2.17, and 2.18. If a dye dissociates into a positively charged ion in an aqueous solution is called cationic dye or basic dye. Otherwise, it is called anionic dye or acidic

dye in case of negatively charged ions. All four dyes are soluble in an aqueous solution. Rhodamine B is a cationic dye, whereas Indigo Carmine and Methyl Orange are acidic ones. Diffused reflectance absorption spectra (DRS) [with OR-3100 spectrophotometer (ORLAB)] were recorded to check the absorption characteristics. Ultraviolet-Visible (UV-vis) Spectroscopic measurements (in the range 380 to 720 nm) quantify the interaction of visible light with an aqueous solution of dye. This allows the determination of unknown solution concentration values. Transmittance is determined by taking the proportion of the intensity of light leaving the dye solution to the intensity of light entering the dye solution. Deionized water was used for preparing the aqueous solution for the tests.

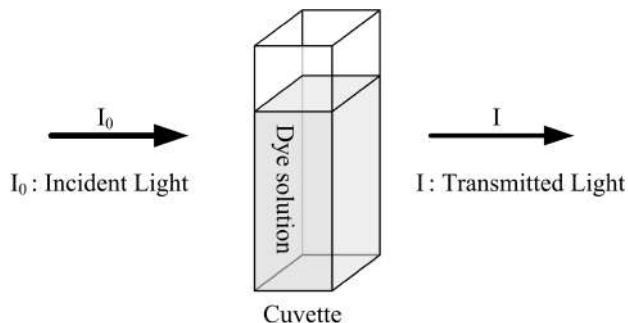


Figure 2.19: Transmittance ( $T = I/I_0$ ) of Light by Aqueous Solution.

Absorbance ( $A$ ) is calculated from the transmittance:

$$A = \log_{10} \left( \frac{1}{T} \right) \quad (2.1)$$

where  $T$  is transmittance of the light by dye solution. The absorption spectra is a plot of the absorbance of a sample (for a particular dye concentration) as a function of wavelength. Figures 2.20 and 2.21 show the absorbance spectra for different dyes in aqueous solution. Maximum absorption for dyes occur at different wavelengths.

*Beer's Law* plot is between absorbance and the known concentration of the solution. This plot can be utilized to determine the unknown concentration level corresponding to a known absorbance level. The amount of light absorbed at a specific wavelength is directly proportional to the concentration of the solution. Figures 2.20 and 2.21 show the *Beer's Law* plots for different dyes in aqueous solution. The present research focuses on saltwater dynamics in a porous medium (primarily in Sand). All the absorption experiment results shown in Figures 2.20 and 2.21 were performed without Sand. Absorption rate and amount varies for different dyes in presence of sand (Figures 2.22 and 2.23). Batch studies were carried out to measure the adsorption with 100 ml solution (mixed with 100 mg dye). Six different concentration levels were considered. Adsorption values were recorded us-

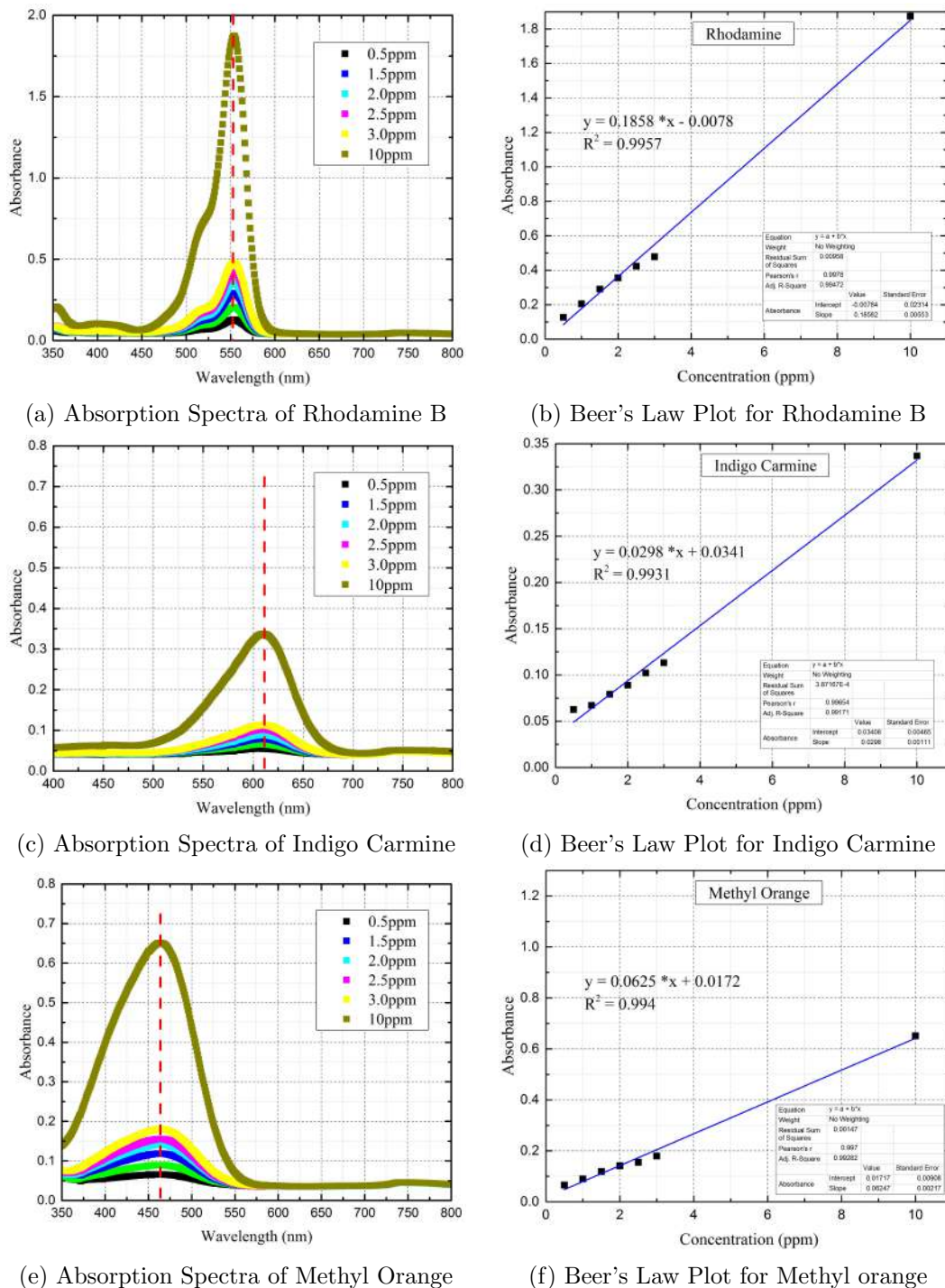
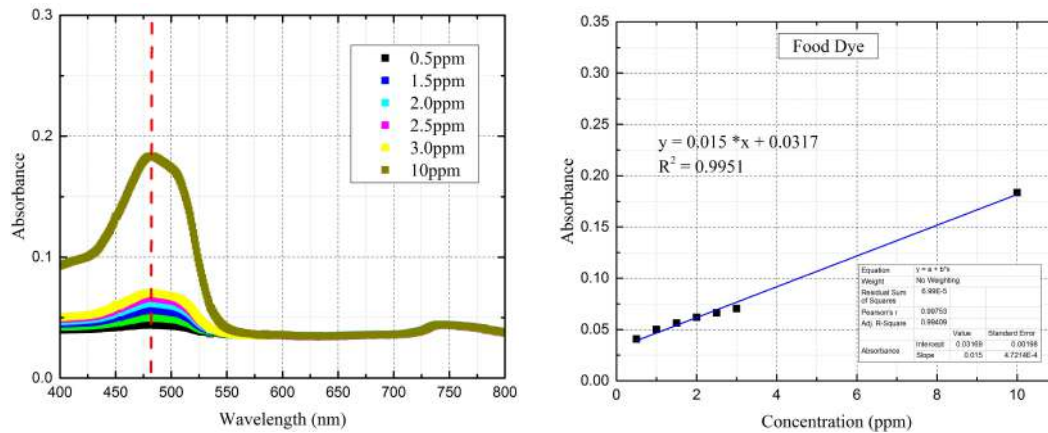


Figure 2.20: Absorption Spectra of Rhodamine B, Indigo Carmine, Methyl Orange in Aqueous Solution

ing OR-3100 spectrophotometer (ORLAB) corresponding to different wavelengths. The maximum absorbance values corresponding to different concentration levels are visible in Figure 2.22 and 2.23. The change in absorbance (with and without Sand) of the dye solution was used to calculate the dye concentration in solution



(a) Absorption Spectra of Commercial Food Dye in Aqueous Solution and (b) Beer's Law Plot for Commercial Food Dye

Figure 2.21: Absorption Spectra of Commercial Food Dye in Aqueous Solution and the percentage adsorption of the dye on Sand.

$$Dye\ Adsorption(\%) = \left(1 - \frac{C_f}{C_i}\right) \times 100 \quad (2.2)$$

where  $C_f$  and  $C_i$  are the initial and the final concentration values of the dye solution, respectively. From Figure 2.24, it is clear that adsorbed amount changes with dye. **Rhodamine-B** was identified as the most suitable dye for the current research with Sand.

*Diffusion* characteristics vary for different dyes in the presence of Sand. Moreover, the saltwater-freshwater interface is diffused in nature. A scaled version of *Sand Box Model* was utilized for visualization of the saltwater-freshwater interface in presence dye mixed saltwater. Porous material was placed in the middle compartment of the model. **Static saltwater (prepared by dissolving 35 g NaCl per liter of water)** head boundary condition was applied in the left compartment of the scaled model. The freshwater head was considered at the right side compartment. Development of saltwater wedge was observed for the experiments. The interface gets generated due to differences in the fluid densities (between saltwater and freshwater). All four dyes were tested under similar conditions. Figures 2.25 and 2.26 show the saltwater wedge and saltwater-freshwater interface in *IS Sand*. Both the dyes show similar results in terms of diffusion. However, **Rhodamine-B** was identified as the most suitable dye considering the better visualization effect.

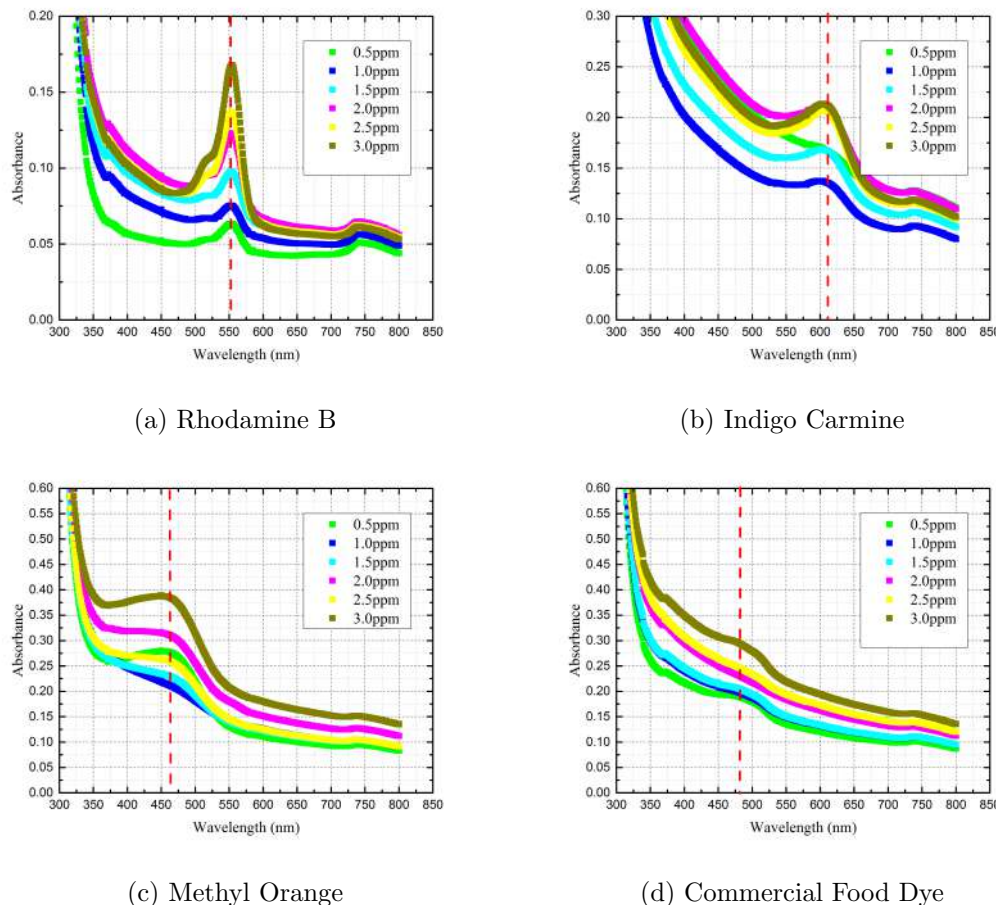


Figure 2.22: Absorption Spectra of Dyes in Aqueous Solutions at Different Concentration Levels with Clean Sand

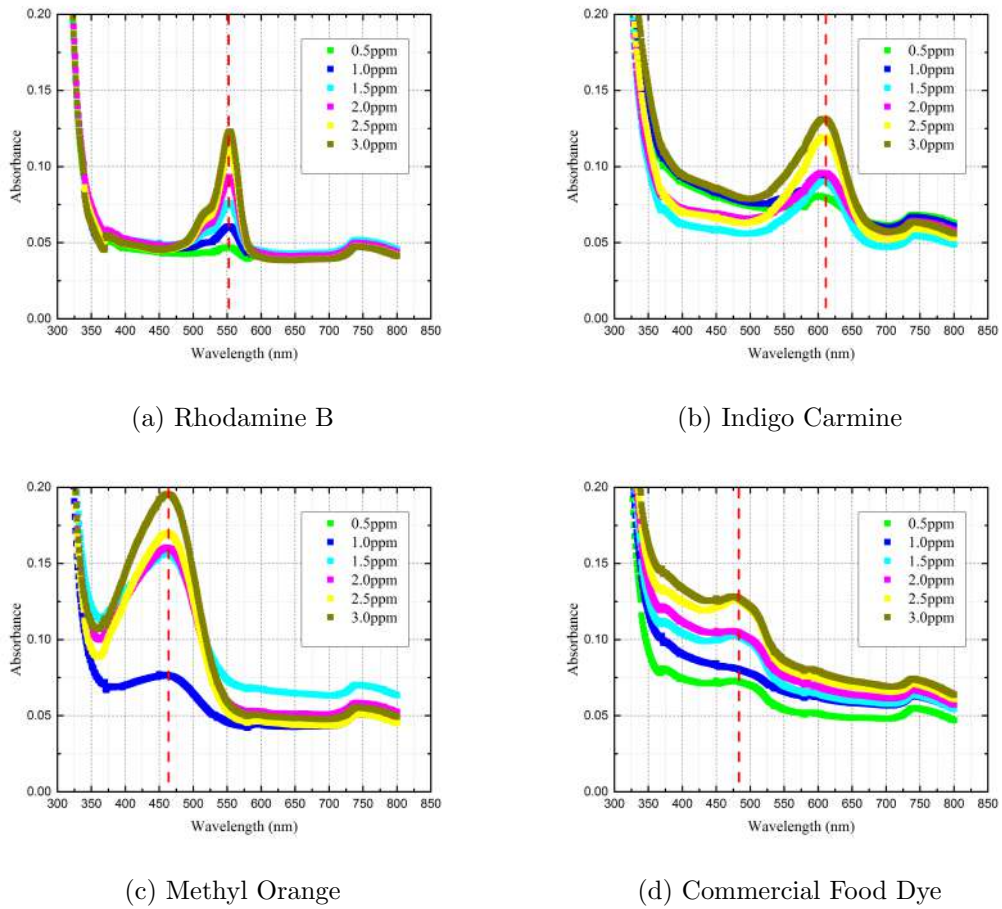


Figure 2.23: Absorption Spectra of Dyes in Aqueous Solutions at Different Concentration Levels with Grade-I IS Sand

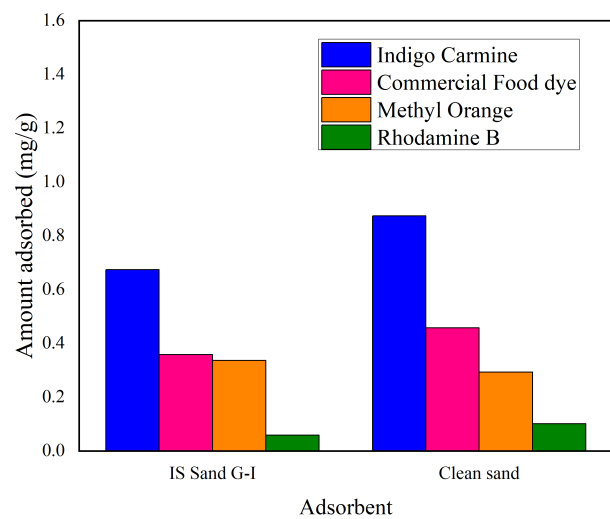


Figure 2.24: Dye Adsorption Performance (Adsorbent Dose = 10 g/l, Dye Concentration = 10 mg/l)



Figure 2.25: Salt Wedge and Saltwater-Freshwater Interface for Rhodamine-B in IS Sand



Figure 2.26: Salt Wedge and Saltwater-Freshwater Interface for Food Dye in IS Sand

## 2.3 Summary

In this Chapter, detailed descriptions of the experimental setups, peripheral apparatus, and material characteristics were provided. The details of the *Sand Box Model* used for laboratory-scale experiments were explained. The next chapter deals with the laboratory experiments on saltwater movement in single and multilayered porous media (Aquifer Material: Clean Sand) under static saltwater boundary conditions.



## Chapter 3

# Laboratory Experiments on Saltwater Movement Under Static Saltwater Boundary Condition

### 3.0 Overview

The previous Chapter covered the detailed descriptions of the experimental setup, peripheral apparatus, and material characteristics. The details of the *Sand Box Model* used for laboratory-scale experiments were also explained. A variable density flow experiment is an essential tool to test the reliability of numerical simulations under realistic geometric conditions. In recent years, different in-situ observation-based methods were proposed to identify the fluid dynamics of density-dependent flows (Souza and Voss, 1987; Kim et al., 2007; MacAllister et al., 2018). However, experimental quantification is necessary to evaluate the performance of mathematical/numerical models. The laboratory experiments are useful under known initial conditions, boundary conditions, and porous material properties over the field experiments. Laboratory scale *Sand Box Model* can be used as a useful instrument for flow visualization and in-situ measurements. Generally, one-dimensional experiments were performed to study the behavior of flow in porous media under the influence of saltwater (Schotting et al., 1997; Watson et al., 2002; Jiao and Hötzl, 2004; Flowers and Hunt, 2007). Few studies (Zhang et al., 2002; Goswami and Clement, 2007; Konz et al., 2008) considered laboratory-scale two-dimensional (2D) sandbox experiments for identifying the saltwater-freshwater interface. As per our knowledge, no experimental laboratory study is available on quantitative and qualitative analysis of saltwater dynamics in porous media. The present work considers both confined and unconfined configurations of porous media under sloping beach face conditions. This quantitative (porewater pressure

measurement) analysis captures the saltwater dynamics.

Initial laboratory experiments were carried out with *Clean Sand* to understand the saltwater dynamics in single (homogeneous) and stratified porous media (3 layered configuration including low-permeability strata) under static saltwater boundary conditions. The scaling effect was assessed indirectly by comparing the physical results with the numerically simulated values. It includes the study of flow circulation mechanisms in saltwater and freshwater zones within the porous media. The experimental configurations are presented in Table 3.1.

Table 3.1: Configurations for Clean Sand Experiments

Cases	Beach Slope	Material	Stratification	Tidal/ Static
<i>CASE - 1/S</i>	$15^0$	Clean Sand ( $d_{50} = 1.024 \text{ mm}$ )	No	Static
<i>CASE - 2/S</i>	$15^0$	Clean Sand ( $d_{50} = 1.024 \text{ mm}$ ) and Bentonite Clay	Yes (3 Layer)	Static

### 3.1 Experiments with Clean Sand

Experimental investigation was carried out with a two-dimensional *Sand Box Model* (Figure 3.1). Detailed description of *Instrumentation* is available in Chapter 2. However, *Tidal Mechanism* was not utilized for the *Initial Laboratory Experiments*. The right reservoir (*ZoneC*) was used to feed (flux condition) freshwater flow to the system. A constant head condition was maintained with the left reservoir (*ZoneA*, filled with saltwater) and overflow outlet pipe (5 mm diameter) placed at the height of 0.64 m from the model's base. Stainless steel mesh (0.1 mm opening) was used to separate both the reservoirs from the middle sandbox zone (*ZoneB*). The top of the setup is in direct contact with the atmosphere representing an unconfined aquifer condition. The bottom part of the setup has 18 flow controlling outlets, including one each at the bottom of the end reservoirs (*ZoneA* and *ZoneC*). The backside of the glass wall has 59 openings (8 mm diameter) for taking pressure measurements and injection-extraction of fluid. In the present study, six pressure transducers (STJE from Honeywell; *PS1* to *PS6*) were placed in a horizontal line 0.57 m above the floor. Screens were used to prevent the entry of porous material at the connection points between flexible pipes (to connect the pressure transducer and setup) and openings at the backside glass wall.

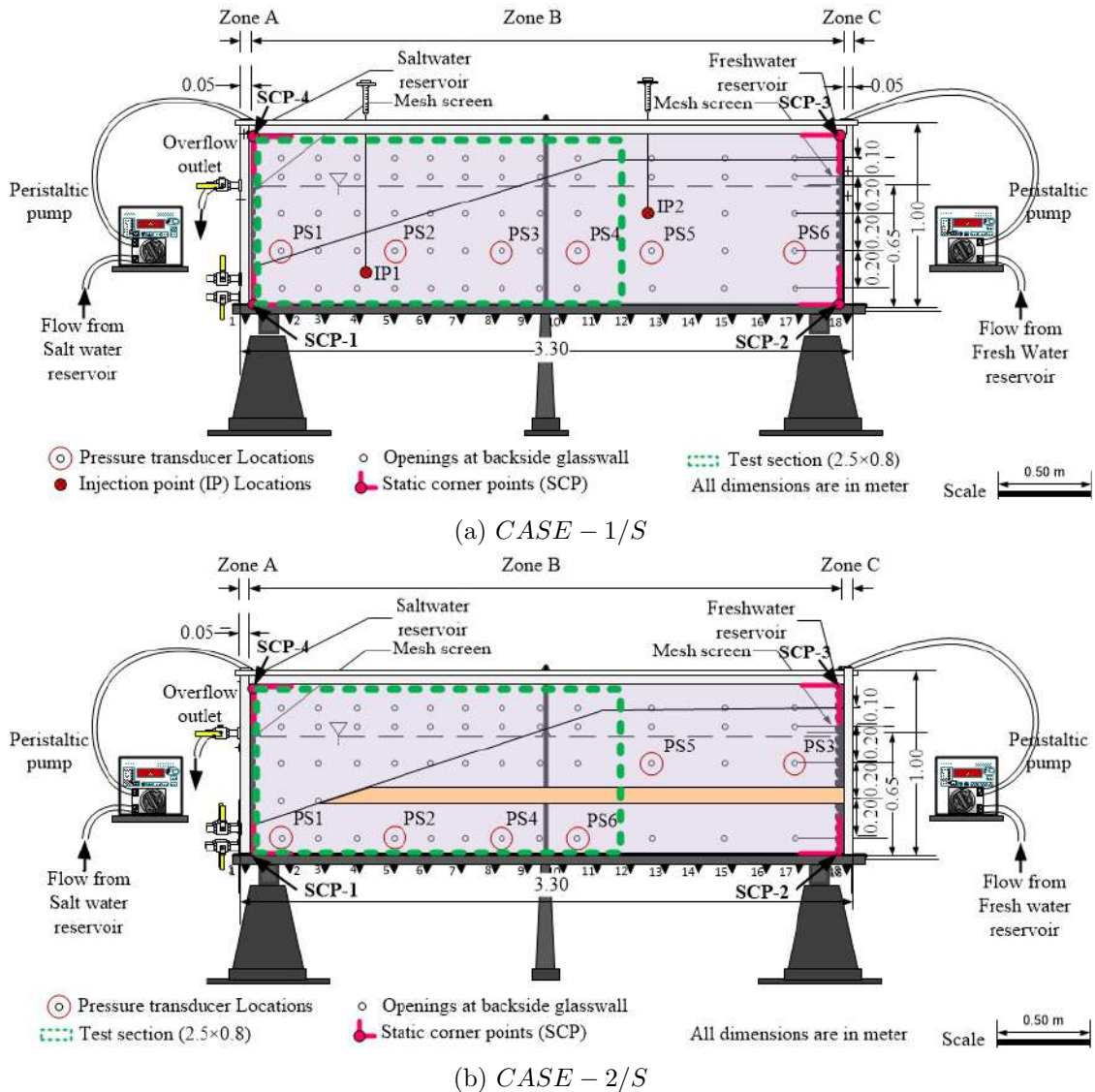


Figure 3.1: Schematic Representation of the Sand Box Model for Clean Sand Experiments

The *ZoneB* was packed with *Clean Sand* to represent illustrative unconfined coastal aquifer material (*CASE - 1/S*) with a sloping

beach surface (slope  $\approx 15^\circ$ ). A wet packing method similar to Ataie-Ashtiani et al. (1999) was adapted to obtain uniform sand packing with minimum entrapped air to satisfy a homogeneous isotropic condition. *Clean Sand* was placed in 15 layers of similar thickness. Each layer was carefully tamped down. The water was supplied to the end reservoirs (freshwater to *ZoneC* and saltwater to *ZoneA*). A silastic tube of 7 mm internal diameter was placed into the reservoirs to supply water through peristaltic pump ( PP-50vx from Electrolab) at the desired flow rate. Two peristaltic pumps ( max flow rate: 250.44 l/d) were utilized for the experimental purpose. Saltwater solution of volume 20 l was prepared prior to the experiments by dissolving commercial salt ( $NaCl$ ) into freshwater at a concentra-

tion of  $36.16 \text{ g/l}$  to achieve a density of  $1025 \text{ kg/m}^3$ . The density was measured digitally with a CTD Driver [ $D127 \times (DI272 50 \text{ m})$  from Schlumberger] and manually using mass/volume ratio. To distinguish the saltwater from the freshwater, *Rhodamine B* was used as a tracer (concentration of  $0.25 \text{ g/l}$ ) for saltwater. *Rhodamine B* was successfully applied as tracer in previous studies (Schincariol and Schwartz, 1990; Simmons et al., 2002; Werner et al., 2009; Shi et al., 2011).

In *CASE – 2/S* a  $0.03 \text{ m}$  thick low permeable layer (Bentonite clay) was considered at a distance  $0.22 \text{ m}$  from the bottom boundary as shown in Figure 3.1b. Bentonite clay layer thickness was maintained throughout the length of porous media. *Clean Sand* was utilized for both confined and unconfined layers.

All of the following steps were performed before starting the experiments:

1. Preparation of the saltwater solution.
2. Valve connecting the *Tidal Mechanism* was closed.
3. Bottom outlets were closed.
4. The aquifer was saturated up to a height of  $0.65 \text{ m}$  with freshwater.
5. Continuous supply of freshwater in *ZoneC* was ensured with peristaltic pump ( $120 \text{ rpm}$ , equivalent to  $6.00 \text{ m/d}$ ).
6. The outlet valve of *ZoneA* placed at a  $0.65 \text{ m}$  was opened to maintain the water level.
7. Pressure transducers were connected and calibrated.
8. Camera was started in self capturing mode along with the lighting arrangements.

Prior to the experiments, freshwater flow from the right side was allowed at a constant rate along with the constant freshwater head in the left sloping beach part to achieve a zero saltwater intrusion and aquifer material saturation conditions simultaneously. Excess water was drained through the overflow outlet situated on the left side of *ZoneA*. Thus the physical system got stabilized under freshwater flow conditions. After initial conditioning of the experimental setup, saltwater was introduced slowly in the *ZoneA* with a constant head of  $0.65 \text{ m}$  by using peristaltic pump. An excess amount of saltwater was supplied into the left reservoir to ensure flushing of freshwater floating at the surface (above sloping beach face) in *ZoneB*. The conductivity (density) in the saltwater reservoir was continuously monitored using a CTD Driver (Figure 3.2a). Initial fluctuations were observed

due to initial saltwater-freshwater mixing in the *Sand Box Model*. A 35000 mg/l saltwater concentration was maintained in *ZoneA* after initial period (Figure 3.2a, and 3.2b). The measurements for density-dependent flow experiments were taken only after stabilization of the density measurements. Figure 3.2a shows the starting point of the experiment. The experiments (*CASE – 1/S* and *CASE – 2/S*) were continued for 432000 s (12 h).

## 3.2 Numerical Simulation Model

FEFLOW (Diersch, 2013) was chosen as the numerical (finite-element) simulator. In the present work, variable density flow in two-dimensional vertical cross-section was modelled using variably saturated flow and transport equations. The flow and mass transport equations for FEFLOW (DHI-WASY, 2010) can be written as:

$$\varepsilon \frac{\partial s(\psi)}{\partial t} + s_0 s(\psi) \frac{\partial \psi}{\partial t} - \nabla \cdot \{K_r(s_e) K [\nabla \psi + (1 + \chi)e]\} = Q_s. \quad (3.1)$$

and

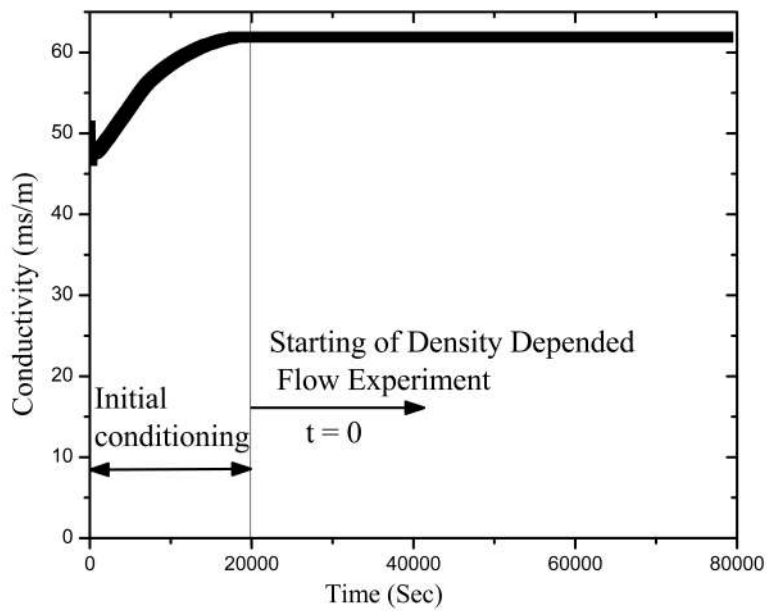
$$s(\psi) \frac{\partial C}{\partial t} + \{-K_r(s) K [\nabla \psi + (1 + \chi)e]\} \cdot \nabla C - \nabla \cdot [\varepsilon s(\psi) D \cdot \nabla C] = Q_s C. \quad (3.2)$$

where  $\varepsilon$  is the porosity;  $s(\psi)$  is the effective saturation which is a function of pressure head,  $\psi$  [L];  $s_0$  [ $L^{-1}$ ] is the specific storage due to medium compressibility;  $K_r(s)$ , the relative hydraulic conductivity, which is a function of saturation,  $s$ ;  $s_e$  is the effective saturation;  $K$  is the tensor of hydraulic conductivity for saturated medium;  $e$  is the gravitational units vector;  $\rho_s$  [ $ML^{-3}$ ] is the density of sources/sinks;  $Q_s$  [ $L^3 T^{-1}$ ] is the flow of sources/sinks;  $D$  is the hydrodynamic dispersion tensor;  $\chi$  is buoyancy coefficient,  $\chi = (\rho - \rho_0)/\rho_0$ ;  $\rho$  [ $ML^{-3}$ ] is the density of the fluid and can be expressed as:  $\rho = \rho_0 + C(\partial \rho / \partial C)$ , where  $\rho_0$  [ $ML^{-3}$ ] is the density of freshwater ( $1000 kg m^{-3}$ ),  $C$  [ $ML^{-3}$ ] is the total concentration of solute. Linear coupling relation was considered for Equations 3.1 and 3.2.

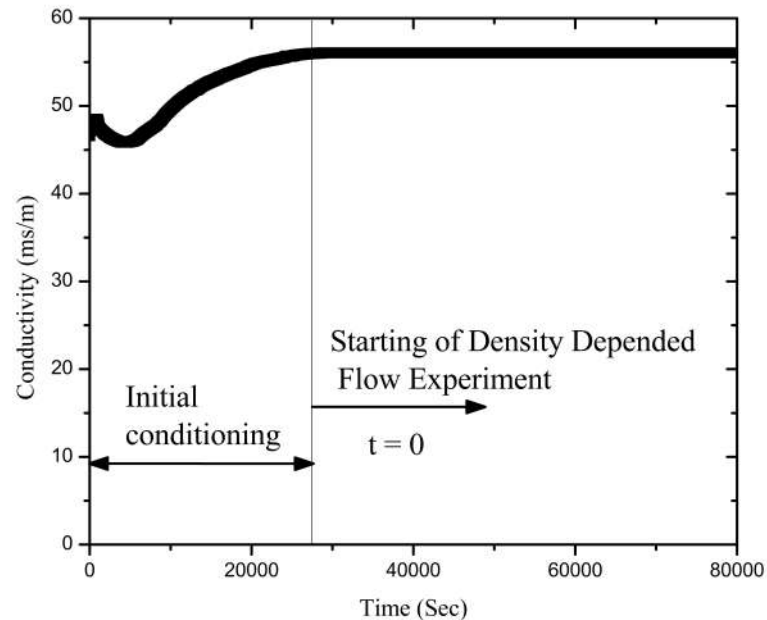
$$\frac{\rho}{\rho_0} = 1 + \chi C \quad (3.3)$$

The constitutive relationship between the hydraulic conductivity, soil saturation and capillary pressure head was prescribed by the van Genutchen model in Richard's equation for modeling of unsaturated-saturated flow (Mualem, 1976):

$$s(e) = \begin{cases} \frac{1}{[1 + |\alpha \psi|^n]^m}, & \psi < 0, \\ 1, & \psi \geq 0 \end{cases} \quad (3.4)$$



(a) CASE - 1/S



(b) CASE - 2/S

Figure 3.2: Observed Time Varying Conductivity Profiles at Saltwater Reservoir (Zone-A)

$$K_r(s_e) = s_e^{\frac{1}{2}} \{1 - [1 - s_e^{\frac{1}{m}}]^m\}^2, \quad (3.5)$$

$$s_e = \frac{s - s_r}{s_s - s_r}, \quad (3.6)$$

where  $s_r$  is the residual saturation and  $s_s$  is the maximum saturation;  $\alpha$  is the curve-fitting parameter;  $n$  is the pore size distribution index;  $m$  is a curve-fitting parameter (Mualem assumption) and  $m = 1 - 1/n$ . The water retention curves of the *Clean Sand* and *Grade-I IS Sand* were determined in the laboratory using an apparatus similar to Chetia and Sekharan (2015). In Figure 3.3, The five models, viz. Brooks and Corey (Brooks and Corey, 1964), van Genuchten (Van Genuchten, 1980), Kosugi's log-normal pore-size distribution (Kosugi, 1996), and Durner's bimodal pore-size distribution (Durner, 1994) were utilized to fit the experiment data.

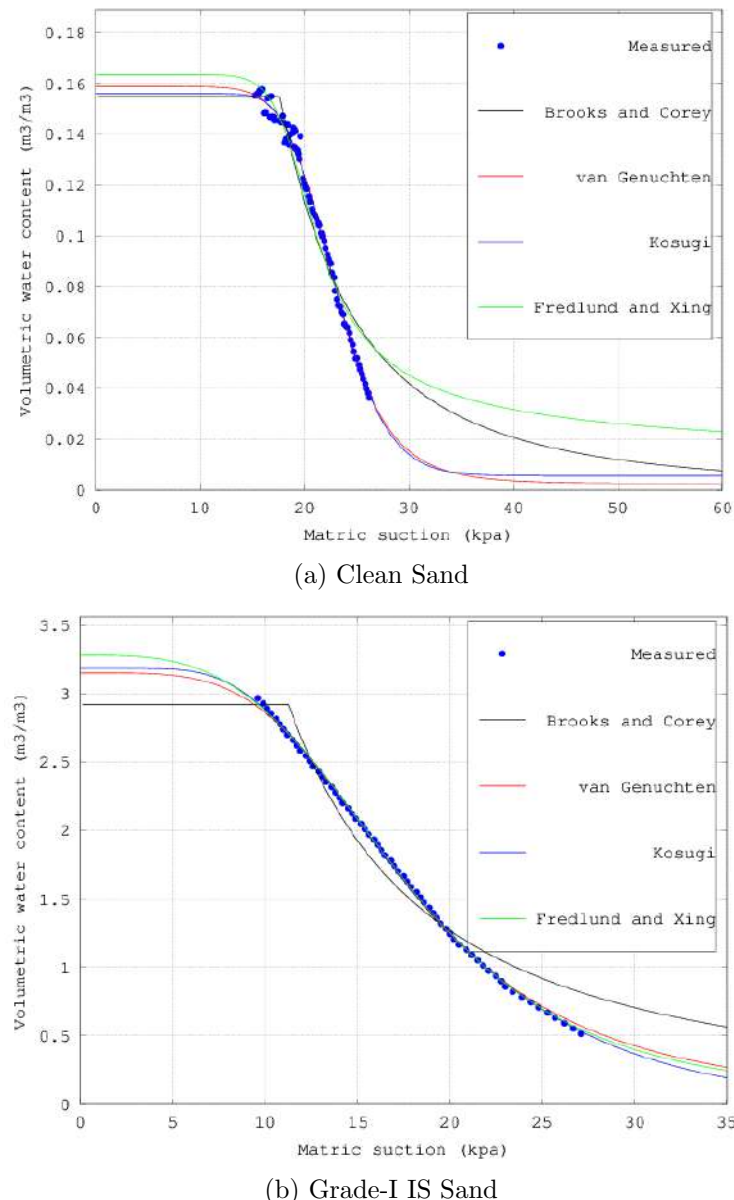


Figure 3.3: Soil Water Retention Curves

### 3.2.1 Initial and Boundary Conditions

The laboratory based physical model equivalent numerical domain (*CASE – 1/S* and *CASE – 2/S*), and relevant boundary conditions are shown in Figure 3.5.

Initial conditions for *CASE – 1/S* and *CASE – 2/S* were specified in terms of head and concentration values. At the beginning, the domain was saturated with freshwater at constant flux from the right side (freshwater concentration). Initial conditions were specified following the boundary conditions by running the simulation model under quasi-steady-state conditions (without saltwater). Figure 3.4 show the initial pressure distribution for *CASE – 1/S*.

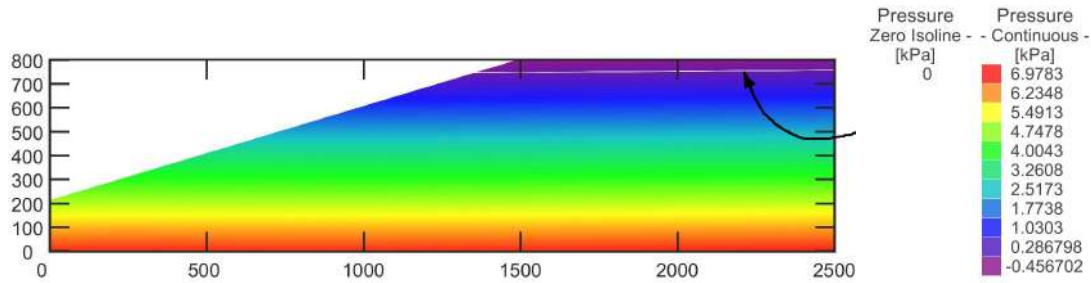


Figure 3.4: Initial Pressure Distribution for *CASE – 1/S*

Along the saltwater-side boundary ( $B_1 - C_1$  in *CASE – 1/S* and  $B_2 - F_2$  in *CASE – 2/S*) equivalent static freshwater head condition was applied. Concentration boundary conditions were assigned from the starting point (after stabilization of conductivity values) of the experiments. Initial free surface in porous media or water table ( $B_1 - F_1$  in *CASE – 1/S* and  $B_2 - I_2$  in *CASE – 2/S*) was identified from the quasi-steady-state run. Two types of boundary conditions were applied i) Dirichlet Boundary and ii) Neumann Boundary.

#### 3.2.1.1 Dirichlet Boundary Condition

The saltwater head equivalent hydrostatic boundary condition was specified along sloping boundary ( $B_1 - C_1$  in *CASE – 1/S* and  $B_2 - F_2$  in *CASE – 2/S*). Specified constant concentration (saltwater, 35000 mg/l) condition was applied along the sloping boundary. Individual nodes along the boundary were identified for specification of flow and concentration Dirichlet boundary conditions.

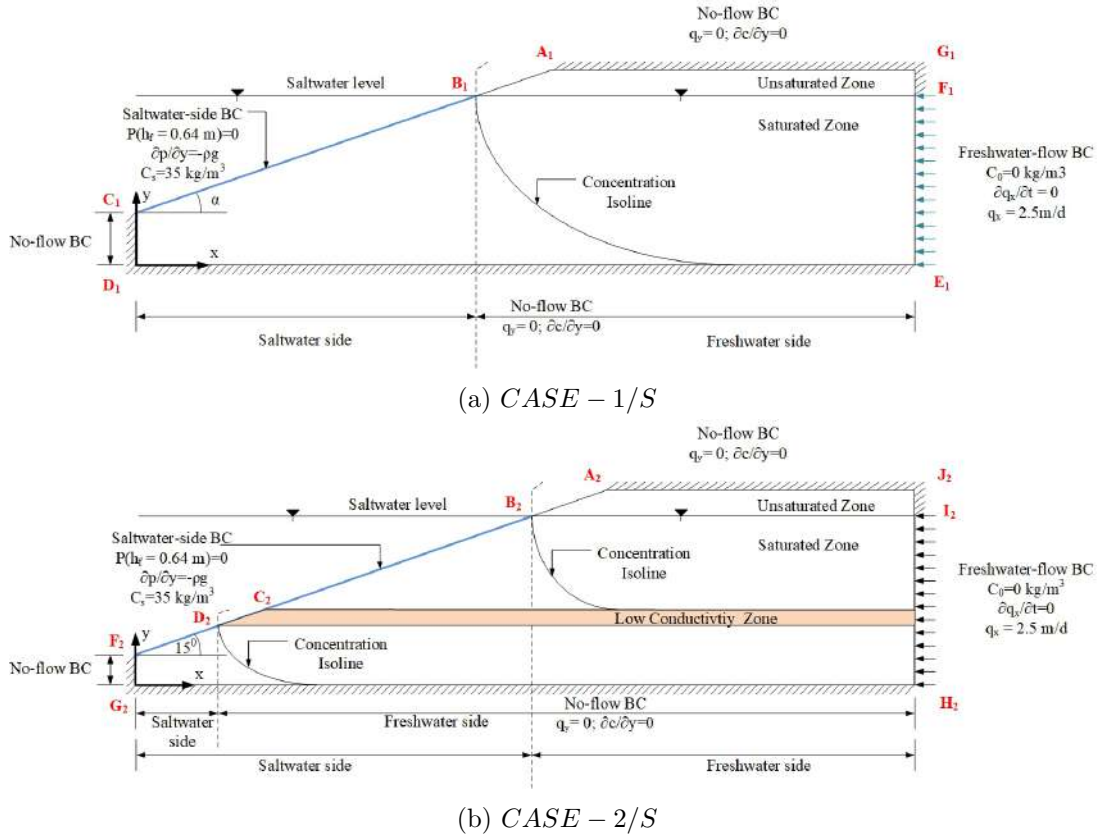


Figure 3.5: Boundary Conditions Used in Numerical Simulation for Clean Sand Experiments

### 3.2.1.2 Neumann Boundary Condition

Freshwater flow from right side ( $E_1 - F_1$  in  $CASE - 1/S$  and  $H_2 - I_2$  in  $CASE - 2/S$ ) was specified as Neumann flux type boundary condition. The peristaltic pump was used for creating the freshwater flux boundary condition. Top boundary ( $G_1 - A_1$  in  $CASE - 1/S$  and  $J_2 - A_2$  in  $CASE - 2/S$ ), bottom boundary ( $D_1 - E_1$  in  $CASE - 1/S$  and  $G_2 - H_2$  in  $CASE - 2/S$ ),

vertical face in saltwater side boundary ( $C_1 - D_1$  in  $CASE - 1/S$  and  $F_2 - G_2$  in  $CASE - 2/S$ ), and top vertical face in right side boundary ( $F_1 - G_1$  in  $CASE - 1/S$  and  $I_2 - J_2$  in  $CASE - 2/S$ ) were specified with zero Neumann condition for flow and mass transport (concentration).

An optimal element size of 0.004 m was obtained from the mesh convergence study. Meshes with finer and coarser spatial discretizations were tested to establish whether the above element size was adequate to provide numerically converged solutions. The longitudinal and transverse dispersivity values (0.004 m and 0.0004 m) were determined from the calibration process within the range reported in Abarca and Clement (2009). The hydraulic conductivity value was also determined from the calibration process within the range of clean sand (Freeze and Cherry, 1974).

Table 3.2: Numerical Parameters Used for Clean Sand Experiments

Parameters	Symbols	Value	Unit
Horizontal Length	L	3.1	m
Domain thickness	d	1.0	m
Porosity	$\epsilon$	0.38	-
Saltwater level	H	0.66	m
Freshwater density	$\rho_0$	1000	kg/m <sup>3</sup>
Saltwater density	$\rho_s$	1025	kg/m <sup>3</sup>
Saltwater concentration	$C_s$	35	kg/m <sup>3</sup>
Longitudinal dispersivity	$\beta_L$	0.004	m
Transverse dispersivity	$\beta_T$	0.0004	m
Molecular diffusion coefficient	D	$10^{-9}$	m <sup>2</sup> /s
Density Ratio	$\chi$	0.025	-
Hydraulic conductivity(Clean Sand)	$K_s$	420	m/d
Hydraulic conductivity(Bentonite)	$K_B$	0.00004	m/d

The molecular diffusion value of  $1 \times 10^{-9} \text{ m}^2 \text{s}^{-1}$  was used in the numerical simulations. The simulation parameter values are reported in Table 3.2. The uniform, homogeneous, isotropic hydraulic conductivity value was determined from the numerical model calibration process. The average hydraulic conductivity value of the saturated material was estimated as  $420 \text{ m/d}$ . An average porosity value of 0.38 was used.

### 3.3 Basic Image Analysis

A rectangular grid ( $0.10 \text{ m} \times 0.05 \text{ m}$ ) was marked on the frontal glass surface of the *Sand Box Model*. Instantaneous movement of saltwater was visually tracked within the physical grid marked on the glass surface. During the image acquisition process, points placed at four corners of the *ZoneB* (rectangular) were utilized as static control points. These static control points were used to define the scale and orientation of the all-digital images under a unique reference frame. Two Halogen Lights (1000 watt, SUNGUN photographic products) were placed on the front side of the experimental setup to ensure homogeneity of the light throughout the test section (*ZoneB*). A Digital Single-Lens Reflex (DSLR) camera (Nikon d5100) was placed centrally in front of the *Sand Box Model* at 1 m distance on a fixed tripod. Images were captured at 2 s time interval with the camera.

The acquired images were analyzed suitably with an image processing technique. In recent times, image analysis has emerged as a proxy measurement technique for physical experiments. A number studies are available on image analysis for solute transport

(Catania et al., 2008; Jaeger et al., 2009; Oates and Harvey, 2006; Olsson and Grathwohl, 2007; Werth et al., 2010; Zinn et al., 2004). However, these techniques are relatively complex in nature. Robinson et al. (2015) suggested that a light source placed at the backside for tracer experiment with relatively transparent glass beads can provide reasonably good results. The intensity of the light-transmitting through highly porous glass beads was uniform. In *Sand Box Model* light source cannot be placed at the backside due to the opaque nature of the material. Thus two *Halogen Lights* were provided from the front side.

In the present work, a simplified interface identification technique for saltwater intrusion in *Sand Box Model* is proposed. An image covers the complete area of the *Sand Box Model*. Image is a combined representation of number of pixels, and each pixel store the color information. A colour can be regarded as a mixture of basic colours, viz. Red (R), Green (G), Blue (B) with different Digital Number (DN) values Aeby et al. (1997). Image ( $Im_{Raw}$ ) stores colour (R-G-B) information in pixels. It is convenient to represent image as a multidimensional digital array ( $p_y \times p_x \times 3$ ). In the three-dimensional array represent, dimensions represent row, column, and colour. The raw image pixel data is represented in Figure 3.6. In concentration space for a single concentration value, there exist multiple combinations of R-G-B. The multiplicity exists due to the combined effect of tracer and sand color. Thus the specification of a single concentration value for a particular R-G-B cluster will provide misleading information (Richards and Richards, 1999).

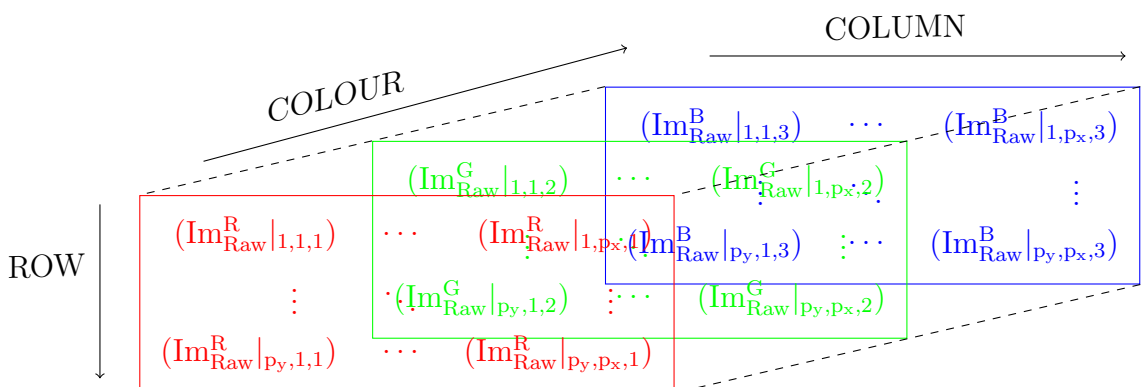


Figure 3.6: A Multidimensional Array of Colour Information

A mapping between concentration and color space requires an equivalent functional relationship. From pixel level image analysis (Figure 3.6), it was observed

**RGB Color Representation:**  
ImRaw images typically use the RGB color model, which creates a wide range of colors by combining three primary colors: Red, Green, and Blue. Each pixel in an RGB image stores intensity values for these three colors. These values typically range from 0 (no intensity) to 255 (full intensity).

**Multidimensional Array Structure:**  
To organize and access pixel information effectively, ImRaw images are represented as multidimensional digital arrays. The common structure is ( $p_y \times p_x \times 3$ ), where:  $p_y$  represents the number of pixels in the vertical direction (height).  $p_x$  represents the number of pixels in the horizontal direction (width). 3 represents the three color channels (Red, Green, Blue).

that saltwater-freshwater interface identification heavily depends on the difference of red (R) and green (G) colours. Thus pixel level modification was performed to obtain a concentration equivalent single value. The simplified expression can be written as

$$\bar{C}_{i,j} = 255 + [D_{i,j}^R - D_{i,j}^G] \quad (3.7)$$

where  $\bar{C}_{i,j}$  is converted pixel value applied to original image at pixel location  $(i, j)$  of image matrix.  $D_{i,j}^R$  and  $D_{i,j}^G$  are the digital number (DN) values for red and green colors at pixel location  $(i, j)$ , respectively.

Information regarding interface variation over vertical cross-section was extracted from the experimental images. Total 820 images were acquired at a 2 s time interval. The raw images were aligned and corrected with respect to the static control points. The cropped images corresponding to the test section were utilized for the next level of analysis. These images provide scattered/noisy information about the color distribution. Thus neighborhood averaged images were used for further analysis. Resulting images provided usable tracer movement information for comparison with physical and numerical results. Numerical saltwater-freshwater interface corresponds to 0.5 *isochlor* (half of the maximum concentration level) as a narrow mixing zone was observed for both the cases.

The processed images (Figures 3.7 and 3.8) provide the spatial distribution of tracer concentration at various times for both *CASE – 1/S* and *CASE – 2/S*. The results reveal that the concentration distribution evolves slowly over time. The interface movement was better captured through the processed images compared to experimental ones due to the representation in terms of the converted pixel value. These processed interface movement information were utilized for calibrating and validating by numerical simulation results.

### 3.4 Analytical Solution

Analytical solution of Strack (1976) is based on one-dimensional steady Dupuit interface flow in a vertical cross-section. It can be used to identify saltwater-freshwater interface toe location (Figure 3.9) in an unconfined single-layered configuration. However, the Submarine Groundwater Discharge (SGD) gap ( $\zeta_0$ ) cannot be determined from the solution of Strack (1976). Van der Veer (1977) provided a more robust solution. The main focus of this analysis is to quantify SGD gap through which the freshwater discharge occurs. In the present study Van der Veer (1977) solution was utilized with no recharge from the top. The horizontal distance between the extended point of saltwater-freshwater interface and sloping

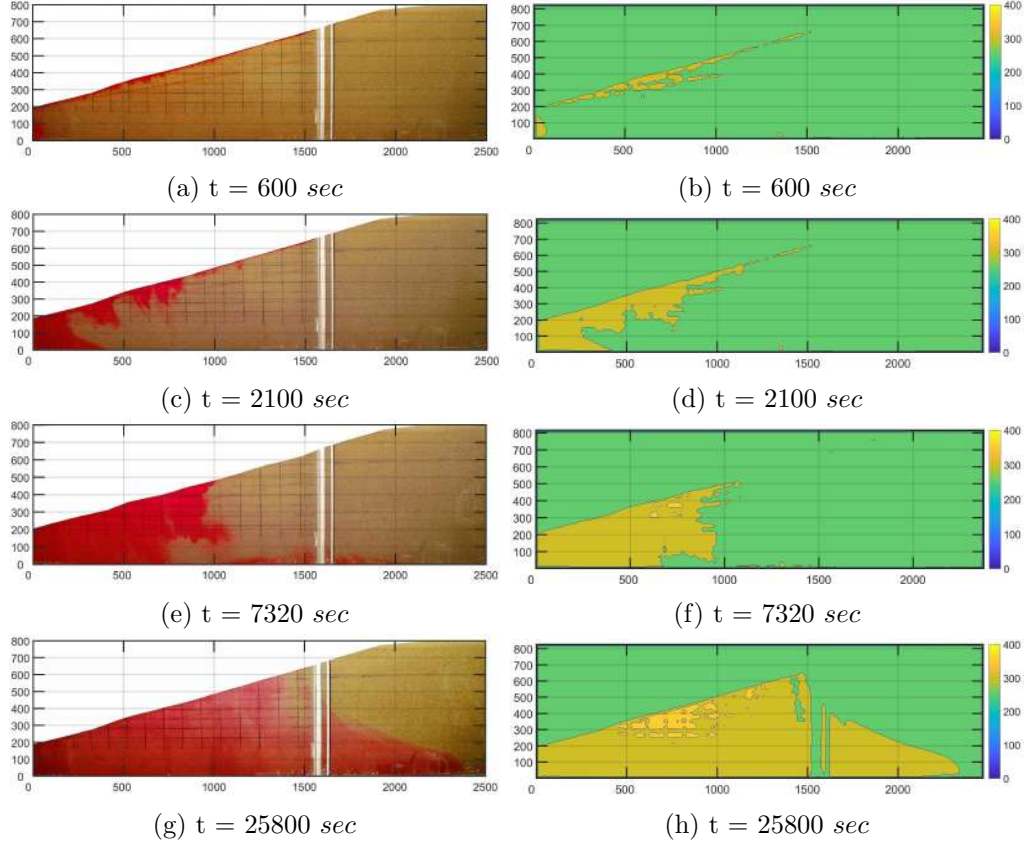


Figure 3.7: Development of Saltwater Wedge with Time in *CASE - 1/S* (First Column: Experimental Images; Second Column: Output of Basic Image Analysis, The Color Maps Indicate  $\bar{C}_{i,j}$ ). All dimensions are in mm.

beach face,  $l_e$ , can be calculated as

$$l_e = \frac{q^*}{2K} \left( \frac{1-\chi}{\chi} \right) \quad (3.8)$$

Saltwater-freshwater interface toe length,  $l_T$ , can be calculated as

$$l_T = \frac{\frac{H_U^2 \chi (\chi + 1)}{2q^*}}{\frac{K}{K}} - l_e \quad (3.9)$$

Submarine Groundwater Discharge (SGD) gap,  $\zeta_0$ , can be calculated as

$$\zeta_0 = \left[ \frac{2 \frac{q^*}{K} l_e}{\chi (\chi + 1)} \right]^{1/2} = \frac{q^*}{\chi K} \sqrt{\frac{1-\chi}{1+\chi}} \quad (3.10)$$

where  $q^*$  is the outflow of freshwater towards the saltwater;  $K$  is the coefficient of permeability;  $\chi$  is buoyancy coefficient,  $\chi = (\rho_s - \rho_0)/\rho_0$ ;  $\rho_s$  is the density of the

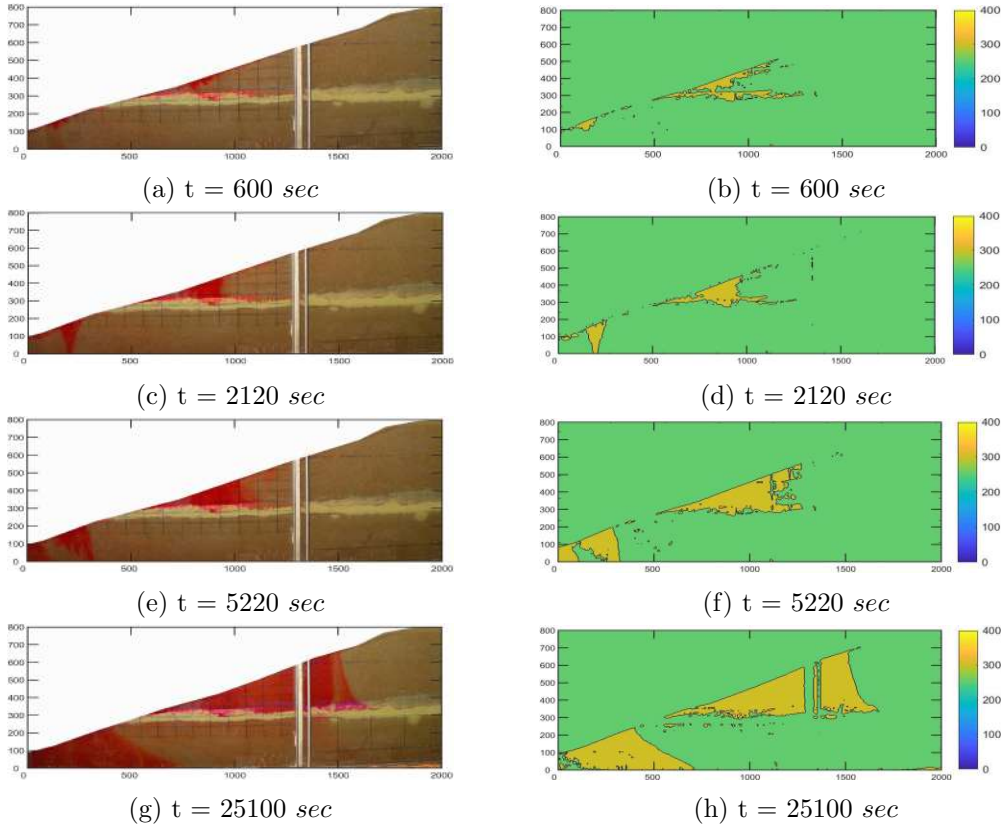


Figure 3.8: Development of Saltwater Wedge with Time in *CASE - 2/S* (First Column: Experimental Images; Second Column: Output of Basic Image Analysis, The Color Maps Indicate  $\bar{C}_{i,j}$ ). All dimensions are in mm.

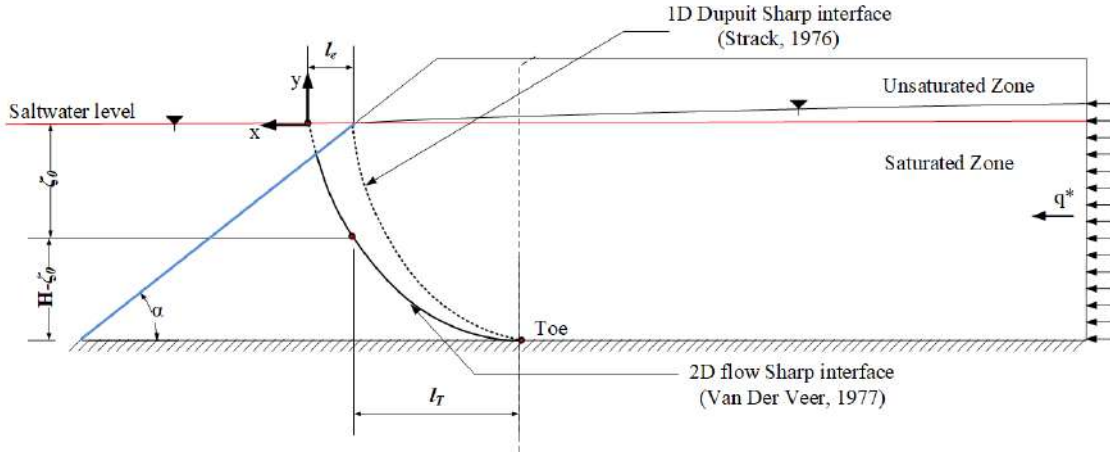


Figure 3.9: Conceptual Representation of Two-dimensional Saltwater-freshwater Interface in Sloping Beach Aquifer

saltwater.

### 3.5 Results and Discussion

Finite element method-based subsurface flow and transport model FEFLOW (Diersch, 2013) was utilized for numerical analysis. *Basic Image Analysis* was per-

formed based on the captured experimental photographs. Pressure data from the transducers were utilized for comparing the results obtained from numerical simulations. The analytical solution was also utilized for comparison of experimental and numerical values of *Toe Length* and *Submarine Groundwater Discharge Gap*.

**Convective Instabilities:** When a denser fluid (saline water in this case) moves through a lighter fluid (freshwater), convective instabilities can arise. These instabilities occur due to the density difference between the fluids, causing the denser fluid to sink and the lighter fluid to rise. These instabilities create turbulent mixing at the interface, which can lead to a greater vertical displacement of the interface than predicted by the simulation.

**Natural Medium Perturbations:** The presence of perturbations in the natural medium, such as uneven terrain or obstacles, can also contribute to the overprediction. These perturbations can disrupt the smooth flow of the fluids and further enhance the mixing at the interface, leading to increased vertical movement.

In *CASE – 1/S*, Figure 3.10 provides the comparison of processed images and numerical simulation results at different time periods. The combined Figures 3.10c, 3.10f, 3.10i, and 3.10l clearly show that the interface movements were reasonably captured by the numerical simulation model. The numerical simulation results over-predicted the interface movement in vertical direction (Figure 3.10 3.10f, 3.10i). Overprediction is due to the fact that convective instabilities occur during the travel of a heavier fluid (saline water) in the presence of a lighter fluid (freshwater) flow and under the perturbations of the natural medium (Schincariol et al., 1994).

In *CASE – 2/S*, Figure 3.11 indicates that the thickness of the low-permeability layer has a significant impact on saltwater front movement. The saltwater movement was separated by the thickness of low permeability layer. The upper portion of the low permeability layer can be conceptualized as an unconfined zone. Similarly, the lower part represents a confined zone. In the confined zone, *Saltwater-Freshwater Interface* movement was small compared to the upper portion due to the difference in freshwater movement.

Numerically, the saltwater front movement was better captured in the stratified case compared to the single layer configuration. Nevertheless, discrepancies exist between the experimental and simulated results. However, the numerical simulation failed to capture the local fingering effect visible in experiments during the initial period. It is a limitation of the numerical simulation model. The finger effect can be captured with a more complex model.

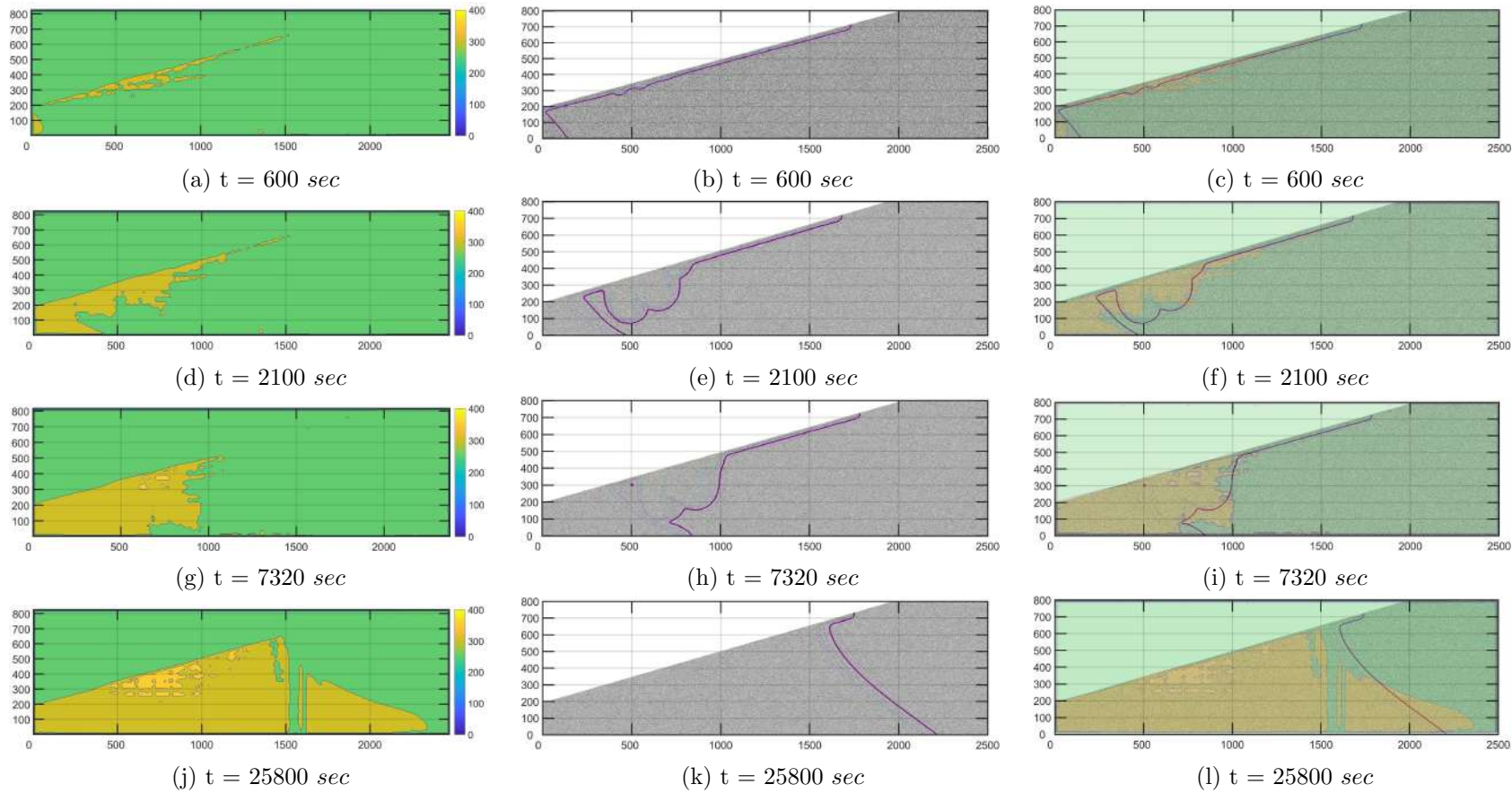


Figure 3.10: Development of Saltwater-freshwater Interface with Time in *CASE - 1/S* [First Column: Output of Basic Image Analysis, The Color Maps Indicate  $\bar{C}_{i,j}$ ; Second Column: Numerical Simulation (0.5-Concentration Isoline); Third Column: Overlap of Numerical Simulation and Basic Image Analysis Outputs]. All dimensions are in  $mm$ .

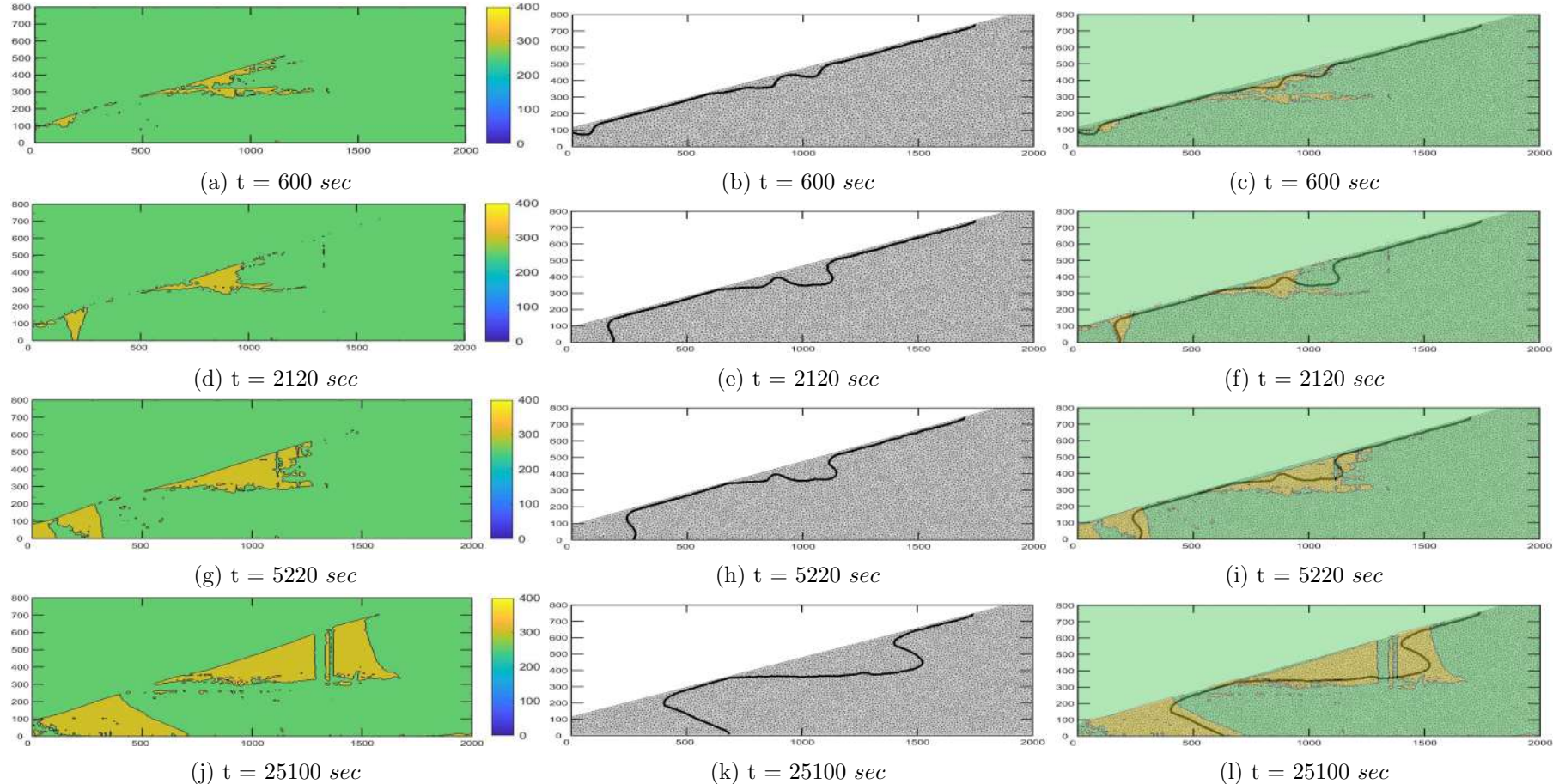


Figure 3.11: Development of Saltwater-freshwater Interface with Time in *CASE - 2/S* [First Column: Output of Basic Image Analysis, The Color Maps Indicate  $\bar{C}_{i,j}$ ; Second Column: Numerical Simulation (0.5-Concentration Isoline); Third Column: Overlap of Numerical Simulation and Basic Image Analysis Outputs]. All dimensions are in mm.

### 3.5.1 Pore Water Pressure Measurement

Front tracking is the most complex part of the saltwater intrusion problem. In general, the density of fluid gets influenced by temperature (density decreases when temperature increases) and pressure (density increases when pressure increases due to compressibility). Direct measurement of the hydraulic head is not practically feasible for non-hydrostatic, unsteady variation within the porous media. A limited number of studies (Kang et al., 2017) are available on the experimental determination of porewater pressure. The pore water pressure measurements were used as a latent variable for the hydraulic head. The pressure transducers were directly connected to the openings in the backside glass wall through a flexible tube (8 mm diameter). Averaging was performed on the porewater pressure data (acquired at 20 Hz frequency) to remove noise.

Pore water pressure can be directly measured using instruments like piezometers, while hydraulic head often needs to be inferred from other measurements like pore water pressure and elevation.

A latent variable is something that isn't directly measured but can be inferred from other related measurements. It acts like a hidden factor influencing the observed data.

Numerically simulated pressure head and experimental hydraulic head values were plotted to check the consistency of the obtained results. Figure 3.12 shows the plot corresponding *CASE – 1/S*. The plot shows a match of the results within 2 cm band for four pressure probes (*PS1*, *PS2*, *PS3*, *PS5*). The cluster outliers (*PS4* & *PS6*) are visible from the plot. Those outlier zones are considered to be a cluster of pressure transducer locations. *PS4* (Figure 3.1a) was placed just below the junction point between the sloping beach face and water level in the saltwater water zone. Density variation was the possible reason for this discrepancy as water moved out from the freshwater zone (Figure 3.18) through the junction point. Discrepancy in cluster *PS6* may be attributed to right boundary effect (Figure 3.1a). Freshwater flux was provided through the right boundary at a constant rate. During the experiment, a marginal rise in water level was observed at the right boundary. This leads to an overestimation of pore water pressure near the boundary.

The consistency check was also performed for *CASE – 2/S* (Figure 3.13). The plot shows a match of the results within 2 cm band for four pressure probes (*PS1*, *PS2*, *PS4*, *PS6*) placed below the low-permeability layer (in the confined zone). The cluster outliers (*PS3* & *PS5*) are visible from the plot. *PS3* was placed near to right boundary above the low permeable layer (Figure 3.1b). Variation in head value may be attributed to freshwater flux from the right side boundary. *PS5* (Figure 3.1b) was placed at the middle portion in the unconfined zone above the low permeability layer. Variation in compaction level in the unconfined zone was the possible reason for this variation.

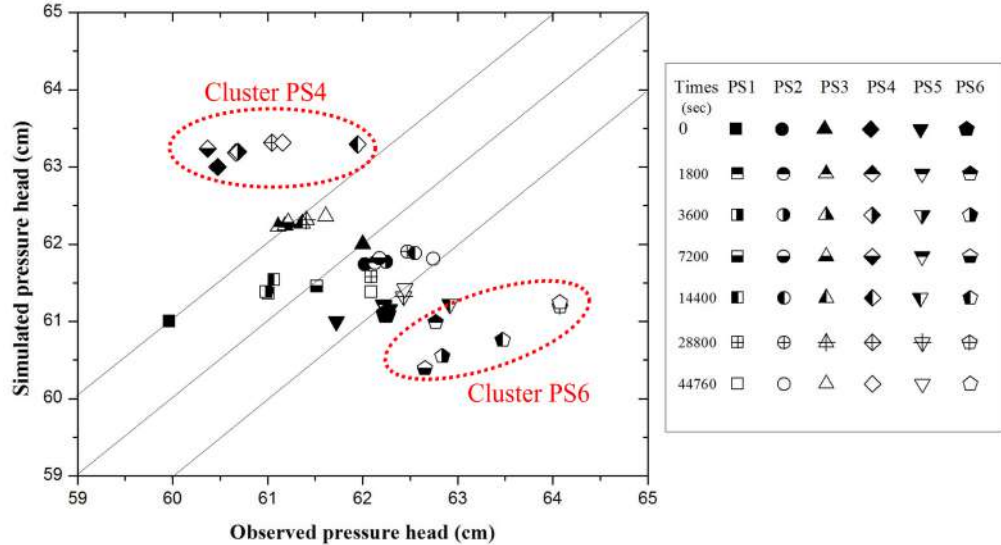


Figure 3.12: Comparison Between Time Varying Observed and Numerically Simulated Pressure Head Data in *CASE - 1/S*

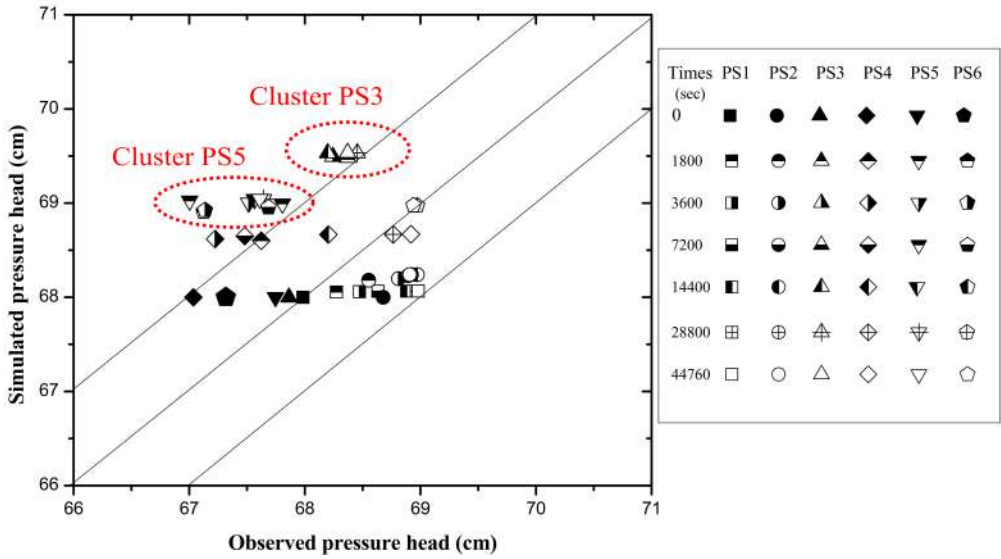


Figure 3.13: Comparison Between Time Varying Observed and Numerically Simulated Pressure Head Data in *CASE - 2/S*

### 3.5.2 Comparison with Analytical Solution

The 1D Van der Veer (1977) solution predicts interface for the infinitely thick 2D vertical cross-section under unconfined condition. Comparative analysis was performed with saltwater-freshwater interface corresponding to 50%-salinity line in FEFLOW and processed images. Saltwater-freshwater toe location ( $l_T$ ) and submarine groundwater discharge ( $zeta_0$ ) were determined analytically (Equations 3.9 and 3.10), numerically and experimentally. In *CASE - 1/S*, analytical (Van der Veer, 1977) values of  $l_T$  and  $zeta_0$  are 507 mm and 394 mm, respectively. However,  $l_T$  and  $zeta_0$  values are 143 mm and 394 mm for the upper unconfined zone in *CASE - 2/S*. Numerical and experimental values ( $l_T$  and  $zeta_0$ ) were compared for the confine zone in *CASE - 2/S*. In *CASE - 1/S* and *CASE - 2/S*, the

coefficient of permeability for *Clean Sand* and *Bentonite Clay* were estimated as  $K_s = 420 \text{ m/d}$  and  $K_B = 0.00004 \text{ m/d}$ , respectively. Figures 3.14 and 3.15 show saltwater-freshwater interface variations for *CASE – 1/S* and *CASE – 2/S*. The FEFLOW simulations under-predict the  $\zeta_0$  compared to the experimental value (Tables 3.3 and 3.4) for both the cases.

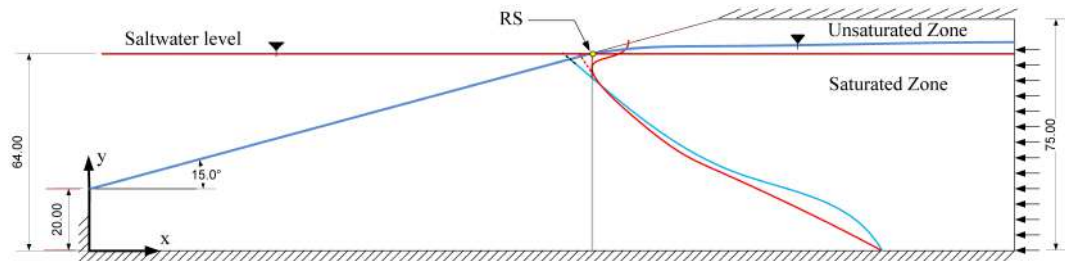


Figure 3.14: Saltwater-freshwater Interface in *CASE – 1/S*. (Red Line: FEFLOW Simulation Results; Blue Line: Experimental Results Obtained from Basic Image Analysis)

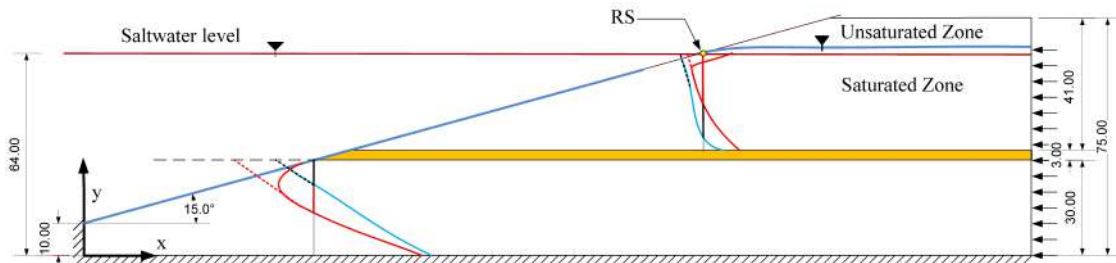


Figure 3.15: Saltwater-freshwater Interface in *CASE – 2/S*. (Red Line: FEFLOW Simulation Results; Blue Line: Experimental Results Obtained from Basic Image Analysis)

Table 3.3: Submarine Groundwater Discharge (SGD) Gap and Saltwater-Freshwater Interface Toe Length for *CASE – 1/S*

Case	Slope	Sand	$\zeta_o$ (mm)	$\ell_T$ (mm)	$\zeta_o$ (mm)	$\ell_T$ (mm)	$\zeta_{o-FEFLOW}/$
			Expt	Expt	FEFLOW	FEFLOW	$\zeta_{o-Expt}$
<i>CASE – 1/S</i>	$15^0$	Clean Sand $d_{50}=1.024\text{ mm}$	63.26	972.65	104.95	969.30	0.602

Table 3.4: Submarine Groundwater Discharge (SGD) Gap and Saltwater-Freshwater Interface Toe Length for *CASE – 2/S*

Case	Slope	Layer	Sand	$\zeta_o$ (mm)	$\ell_T$ (mm)	$\zeta_o$ (mm)	$\ell_T$ (mm)	$\zeta_{o-FEFLOW}/$
				Expt	Expt	FEFLOW	FEFLOW	$\zeta_{o-Expt}$
<i>CASE – 2/S</i>	$15^0$	Upper	Clean Sand $d_{50}=1.024\text{ mm}$	208.09	121.47	139.12	67.98	0.668
		Lower	3 cm thickness of low permeable layer	222.12	385.26	102.88	353.53	0.463

### 3.5.3 Saltwater Circulation under Quasi-Steady State Condition for CASE – 1/S

The saltwater circulation study was conducted before attaining the quasi-steady state condition in terms of movement of toe location. The external tracer was injected through the location *IP1* inside the saltwater wedge. A total 60 *ml* Fluorescein Sodium (Loba Chemie) liquid solution was injected (Figure 3.1a) at *IP1* (600 *mm*, 180 *mm*) with 2.1 *g* *NaCl* to maintain a density neutral condition within the saltwater wedge. The tracer plume movement was captured through photographs (Figure 3.16) taken at an interval of 2 *s*. These visual images revealed the saltwater circulation pattern within the saltwater wedge for the sloping beach portion in terms of tracer movement. The density difference between fluids produces convective flows. Moreover, inflowing freshwater creates a density gradient along with the diffused interface. The gradient of density introduces gravitational instabilities, which in turn facilitates a circular pattern within the system. The tracer dye follows the circulating fluid flow path (Figure 3.16).

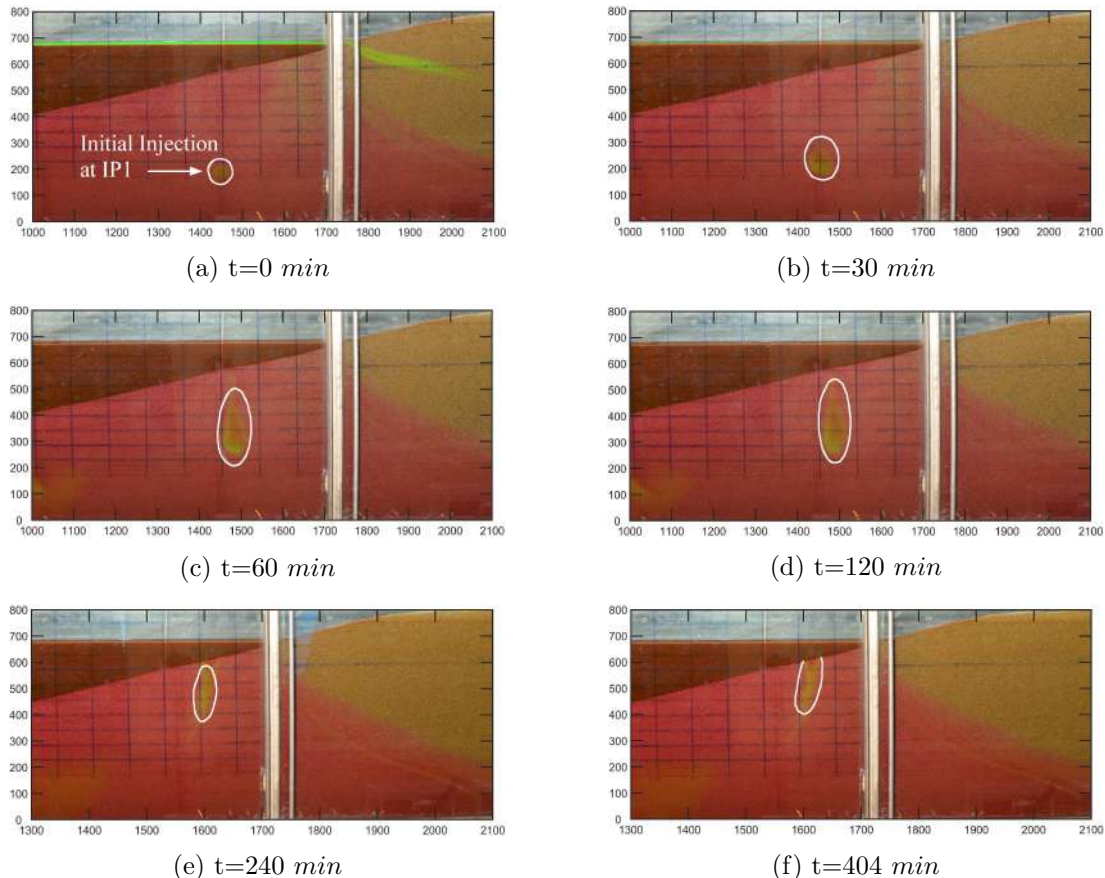


Figure 3.16: Time Varying Experimental Tracer Movement in Saltwater Wedge Under Quasi Steady Condition for CASE – 1/S

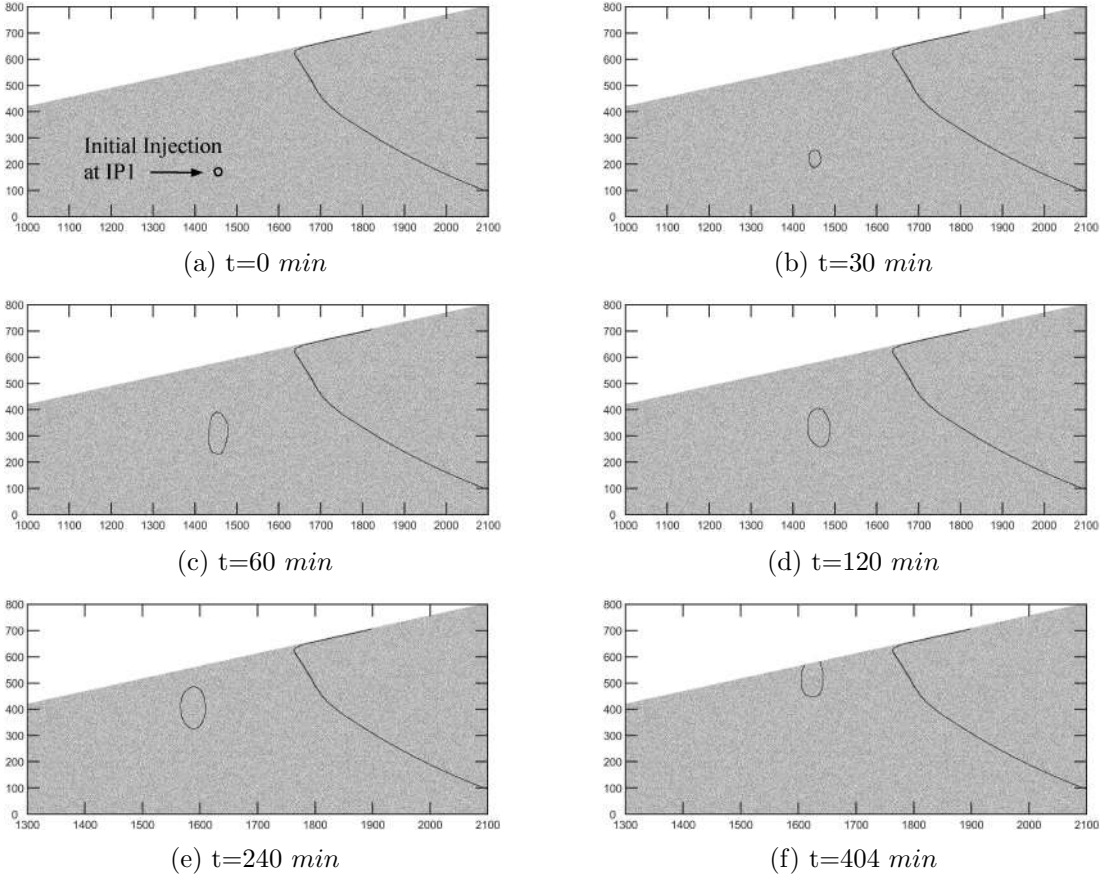


Figure 3.17: Time Varying Numerical Tracer Movement in Saltwater Wedge Under Quasi Steady Condition for  $CASE - 1/S$

### 3.5.4 Freshwater Flow Patterns Under Quasi-Steady State Condition for $CASE - 1/S$

Tracer was also injected at a uniform rate in the freshwater zone (Figure 3.1a) at the location  $IP2$  (2140 mm, 480 mm) to identify the flow pattern. A total 30 ml Fluorescein Sodium (Loba Chemie) liquid solution was injected (Figure 3.1a). Absorption rate in *Clean Sand* was minimal for this tracer (Sabatini and Austin, 1991). A uniform interval of 2 s was used for capturing photographs (Figure 3.18) of tracer movement. The tracer movement was recorded (starting from initial injection) till it reached the top of the saltwater surface (at the intersection point between the saltwater zone and sloping beach face). It is evident that freshwater particles move along the interface zone and rise due to the density difference between the saline and freshwaters.

Information regarding tracer movement over the vertical cross-section was extracted from the experimental images. Processed images (Figure 3.7) provide the spatial distribution of tracer concentrations at various times. The results reveal that the tracer distribution evolves slowly over time. The tracer movement was better captured through the processed images compared to experimental ones due

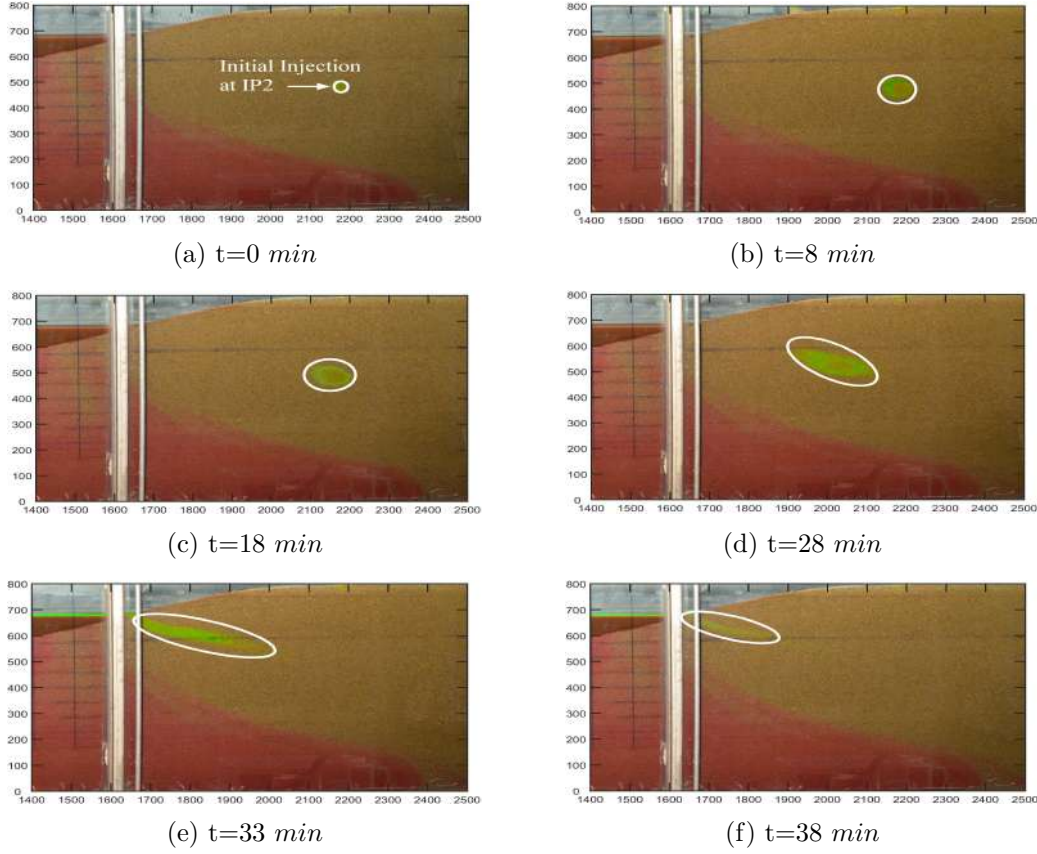


Figure 3.18: Time Varying Experimental Tracer Movement in Freshwater Zone Under Quasi Steady Condition for *CASE – 1/S*

to the representation in terms of the converted pixel values. These processed saltwater-freshwater interface movement information were utilized for calibrating and validating the numerical simulation results. The numerical simulation results for injection through *IP1* and *IP2* experimental are presented in Figures 3.19 and 3.17. The time evolution of injected tracer was captured through numerical simulation. The simulated tracer movement matches the experimental pattern. However, small discrepancies are present due to differences in dispersivity value.

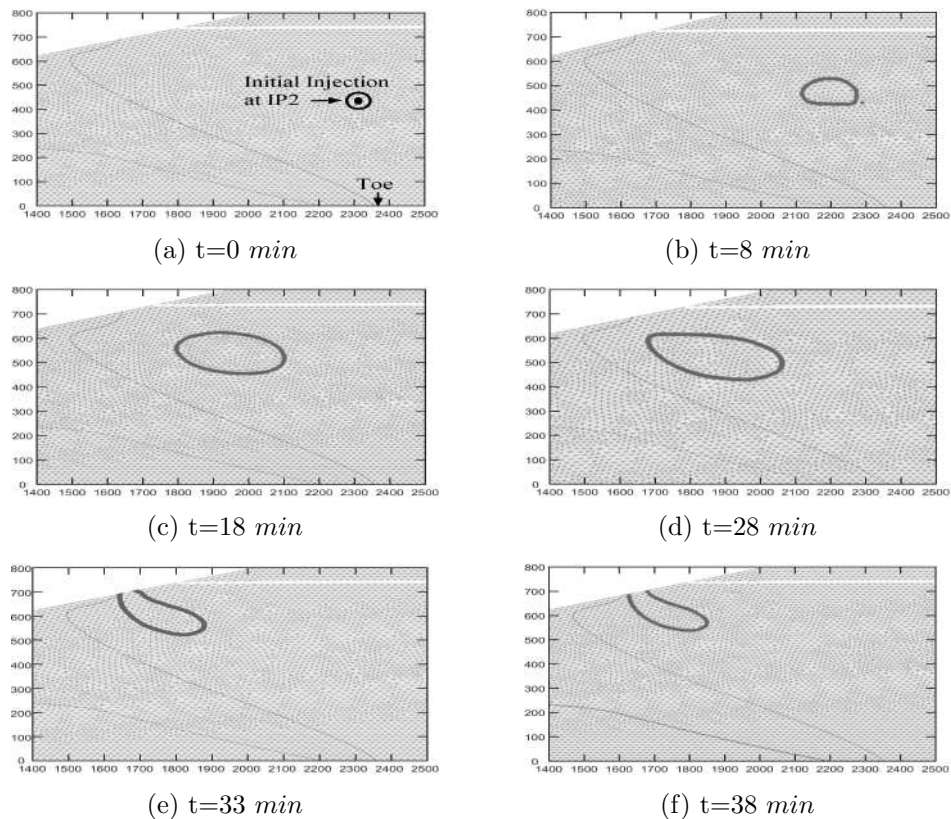


Figure 3.19: Time Varying Numerical Tracer Movement in Freshwater Zone Under Quasi Steady Condition for CASE - 1/S

## 3.6 Summary

This Chapter presented preliminary experiments with *Clean Sand* for single and multilayered porous media under static saltwater side boundary conditions. Flow circulation patterns in saltwater wedge and freshwater zone were also identified. The next Chapter presents quantification of the influence of beach slope on saltwater intrusion dynamics in a single-layered system under static and tidal boundary conditions.

## Chapter 4

# Influence of Beach Slope on Saltwater Movement in Single Layer Under Static and Tidal Conditions

## 4.0 Overview

The coastal aquifer boundary is generally non-vertical. The classical *Henry Problem* (Henry, 1960) considered a vertical coastal boundary due to difficulties in incorporating a sloping geometry in a finite difference model. Most of the previous laboratory tests were performed under vertical seaside boundary approximation, e.g., water table salinization (Nakagawa et al., 2005; Goswami and Clement, 2007; Oz et al., 2015), physical barrier system (Abdoulhalik et al., 2017; Armanuos et al., 2019) saltwater upconing (Werner et al., 2009; Jakovovic et al., 2016; Abdoulhalik and Ahmed, 2018). Process complexity increases with the sloping beach condition. Tide and wave forces create complex seaside boundary conditions (a combination of static and dynamic pressure head conditions). Laboratory scale sloping beach condition was considered in few studies only (Dalai et al., 2020; Shen et al., 2020; Kuan et al., 2019; Stoeckl et al., 2016; Sriapai et al., 2012). However, none of these studies had quantified the effect of beach slope on the *Saltwater-freshwater Interface* movement in porous media. Walther et al. (2017) presented a numerical investigation to qualitatively comment on the saltwater-freshwater mixing zone shift under beach slope variation. The current study focuses on the quantification of the impact of beach slope variation on *Saltwater-freshwater Interface* movement in the unconfined configuration under static and tidal saltwater side boundary conditions. Physical experiment, numerical analysis, image analysis, and analytical

solution were utilized for quantitative and qualitative analysis.

## 4.1 Influence of Beach Slope on Saltwater Movement in Single Layer Under Static Condition

The laboratory experiments were carried out with Grade I (1-2 mm) Indian Standard Sand (IS: 650-1991; Manufactured by Tamilnadu Minerals Limited) with varying beach slopes to understand the saltwater dynamics in single (homogeneous) layered porous media under static saltwater boundary conditions. The experimental configurations are presented in Table 4.1. Experiments also included the study of flow circulation in the freshwater zone within the porous media.

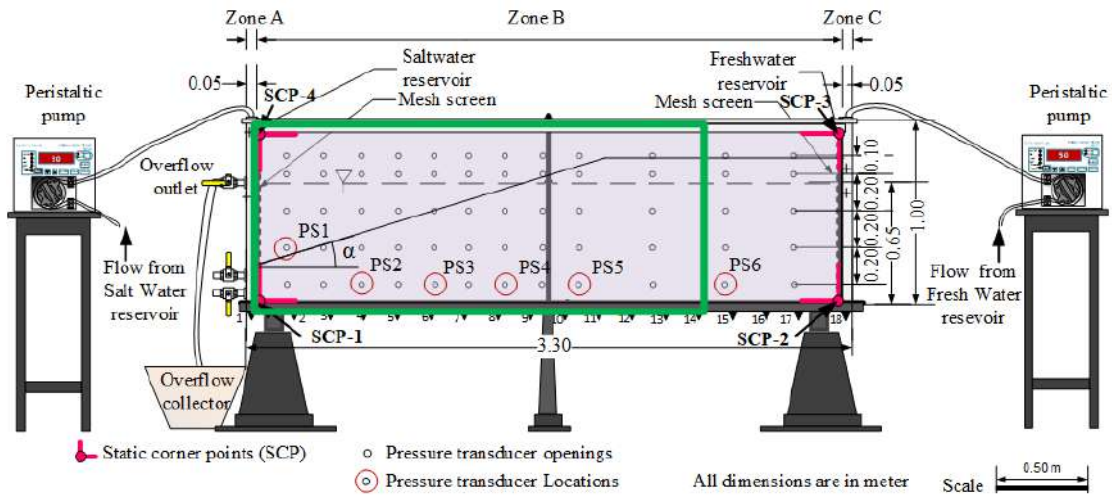
Table 4.1: Configurations for Experiments with Single Layered Porous Media Under Static Saltwater Side Boundary Condition

Cases	Beach Slope	Sand	Stratification	Tidal/ Static	Remarks
<i>CASE - 3A/S</i>	$15^0$	Grade I IS Sand $d_{50} = 1.12 \text{ mm}$	No	Static	-
<i>CASE - 3B/S</i>	$20^0$	Grade I IS Sand $d_{50} = 1.12 \text{ mm}$	No	Static	-
<i>CASE - 3C/S</i>	$25^0$	Grade I IS Sand $d_{50} = 1.12 \text{ mm}$	No	Static	-
<i>CASE - 3D/S</i>	$30^0$	Grade I IS Sand $d_{50} = 1.12 \text{ mm}$	No	Static	-

### 4.1.1 Experimental Method

Experiments were carried with the *Sand Box Model* described in *Section 3.1*. Same experimental steps were followed to obtain pressure head data under static saltwater boundary condition. Figure 4.1 shows the experimental setup. *Grade-I IS Sand* was used as the aquifer medium in the middle part of the *Sand Box Model* (*ZoneB*). In the present study, six pressure transducers (*PS1*, *PS2*, *PS3*, *PS4*, *PS5*, and *PS6*) were connected through 8 mm diameter openings of the back side glass wall for taking pressure measurements. Pressure measurements and images were recorded until the saltwater-freshwater interface reached the quasi steady state condition. Four cases with different slopes ( $15^0$ ,  $20^0$ ,  $25^0$ ,  $30^0$ ) were considered (Figures 4.2, 4.3, 4.4 and 4.5). The salinity in the saltwater

reservoir was continuously monitored as mentioned in *Section 3.1* using a CTD Diver (Figure 3.2a). Initial fluctuations were observed due to initial saltwater-freshwater mixing in the *Sand Box Model*. Approximately 35000 mg/l saltwater concentration was maintained in *Zone A* after initial period (Figures 4.6a, 4.6b, 4.6c, and 4.6d). The measurements for density dependent flow experiments were recorded only after stabilisation of the salinity measurements. Figure 4.6 shows the starting point for different experimental cases. The experiments (*CASE – 3A/S*, *CASE – 3B/S*, *CASE – 3C/S*, and *CASE – 3D/S*) were continued for 12 h to 15 h.



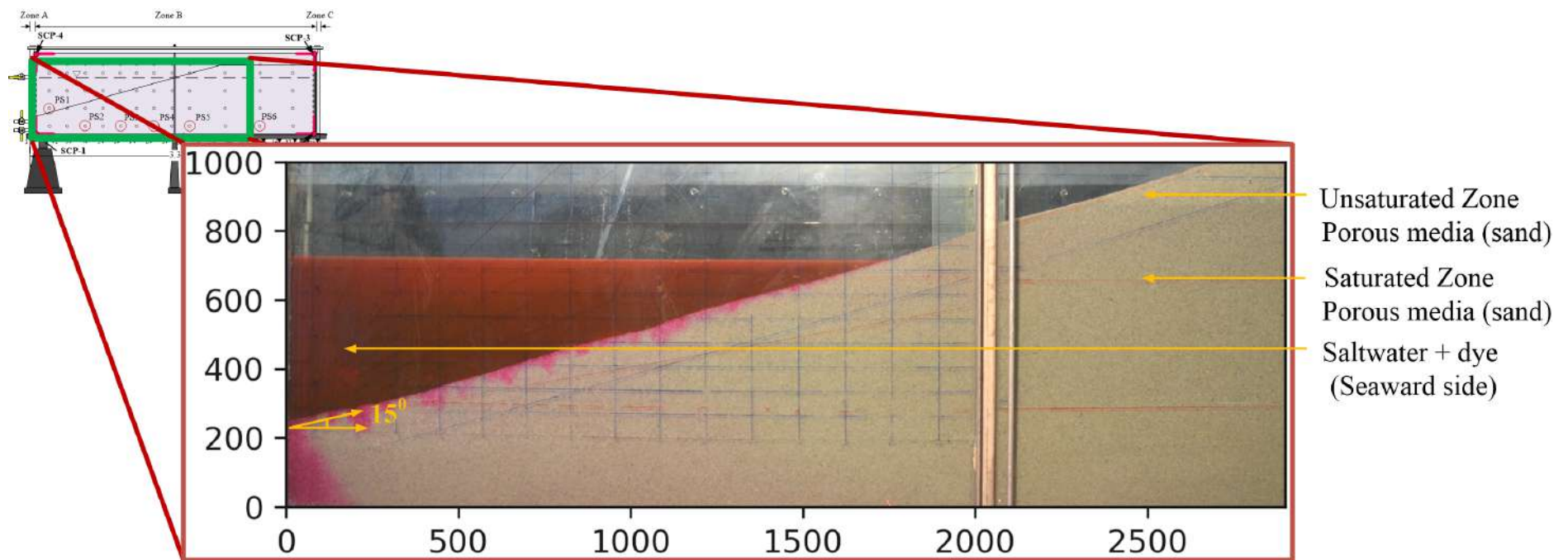
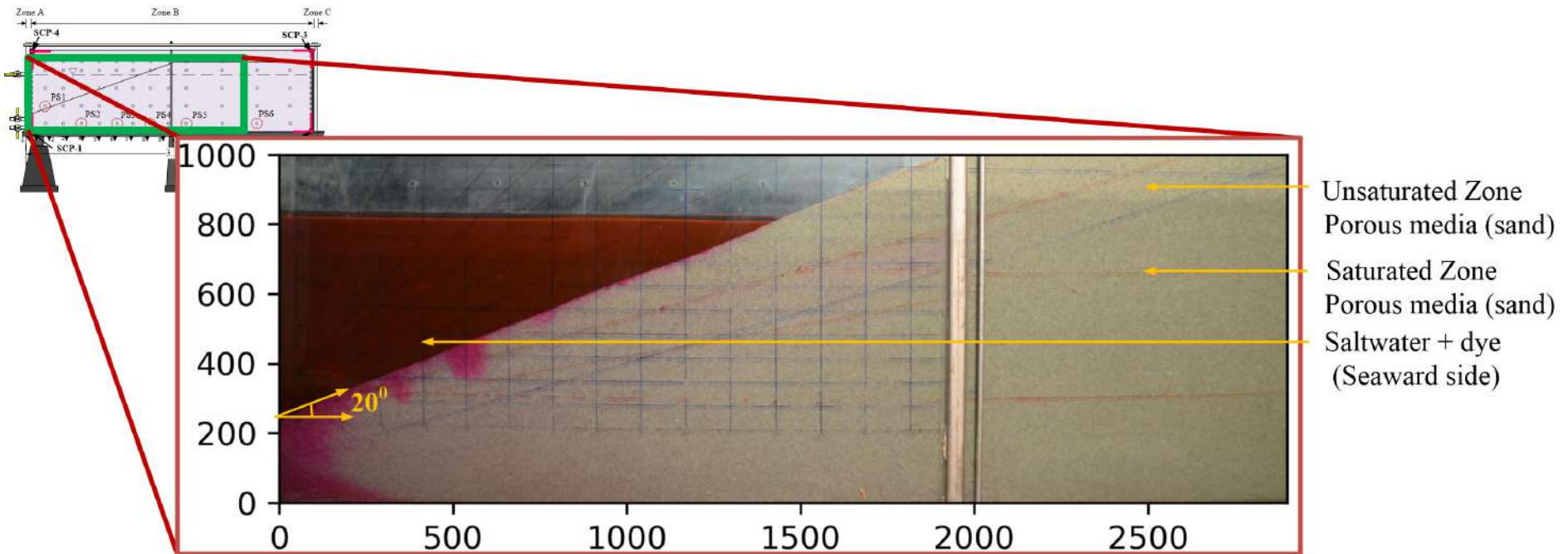


Figure 4.2: Green Rectangular Box and Experimental Beach Slope for CASE - 3A/S



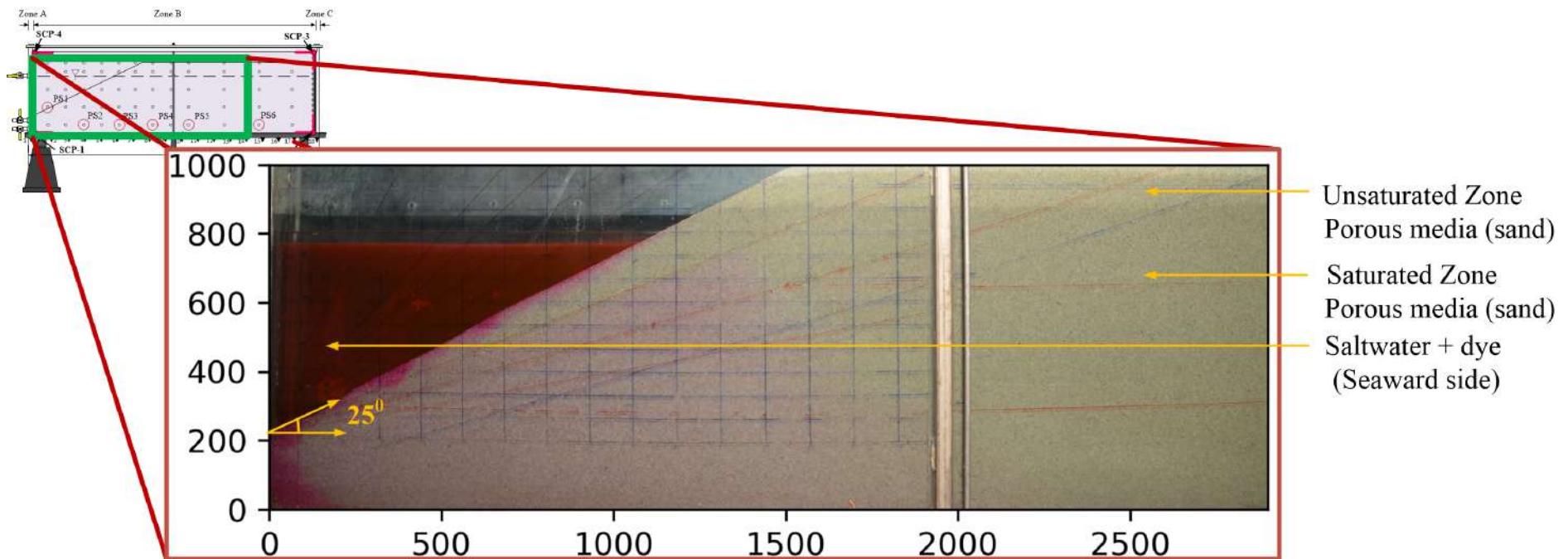


Figure 4.4: Green Rectangular Box and Experimental Beach Slope for CASE – 3C/S

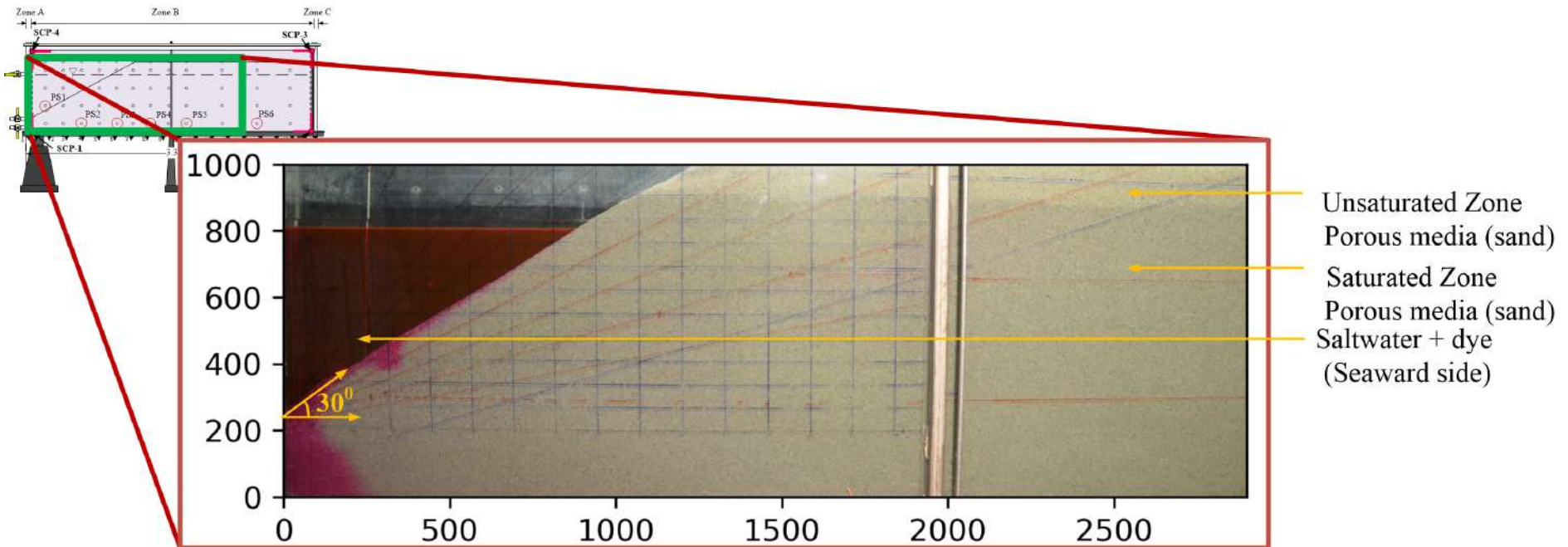


Figure 4.5: Green Rectangular Box and Experimental Beach Slope for *CASE – 3D/S*

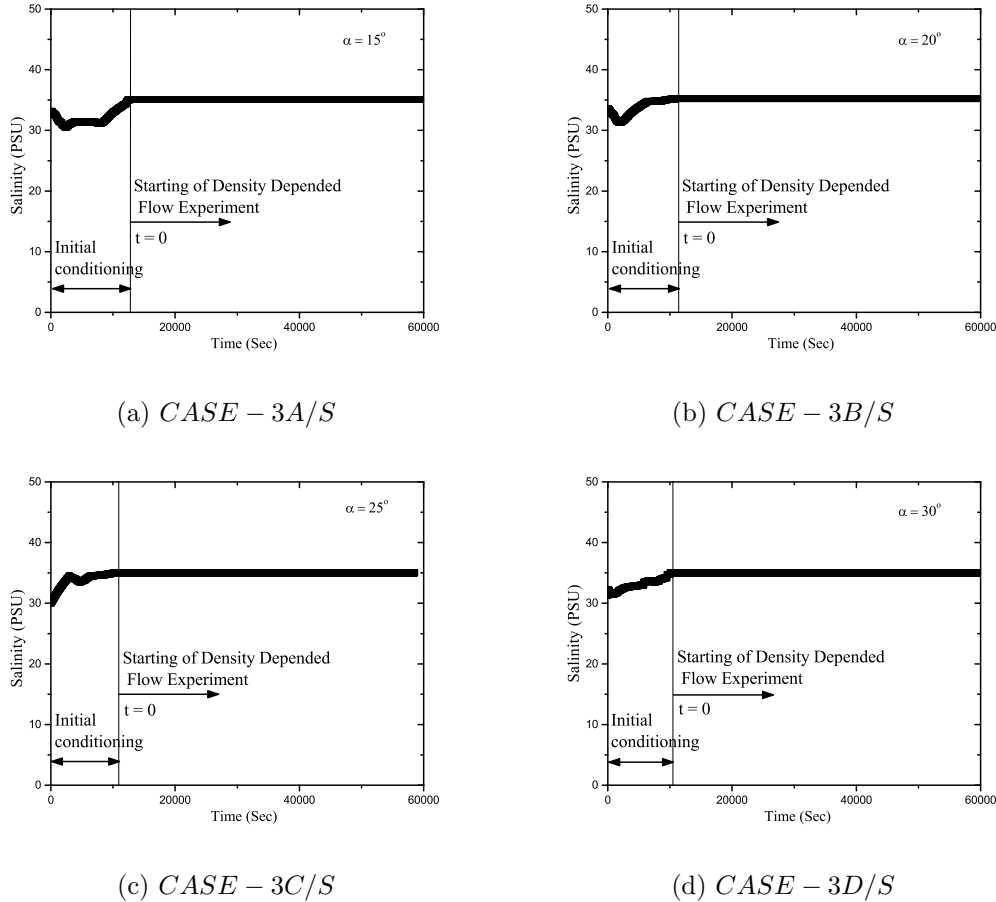


Figure 4.6: Observed Time Varying Salinity Profiles at Saltwater Reservoir (Zone - A)

#### 4.1.2 Numerical Simulation Model

The laboratory-scale experiments and the numerical simulation model produced a series of data sets (pressure head and concentration) at different time levels. Numerical simulations in two-dimensional vertical cross-sections were performed using the finite-element-based model FEFLOW (Diersch, 2013). The governing equations for variably saturated flow and transport are presented in *Section 3.2*. Unstructured finite element mesh of different sizes was utilized to discretize the *Sand Box Model* for four cases. A Mesh convergence study was performed with finer and coarser spatial discretizations. The optimal element size varies from 0.001 m to 0.004 m. Initial and boundary conditions were specified as per the *Sub-section 3.2.1*. Details of boundary conditions are shown in Figure 4.7. The flow and transport simulations were performed with a longitudinal dispersivity value of 0.004 m (of the order of the average grain diameter). The transverse dispersivity value was assumed to be 1/10 of the longitudinal dispersivity Welty and Gelhar (1994). Molecular diffusion, fluid viscosity, and the relative permeability function values were assigned on the basis of commonly reported estimates appearing in the

literature (Liu et al., 2016). The effective diffusivity (the product of free water diffusivity and tortuosity) of the *Rhodamine B* was numerically fitted. The difference in diffusion coefficients for salt constituents and *Rhodamine B* was neglected. Thus *Rhodamine B* was safely used to delineate the saltwater region within the porous media. The individual cases were calibrated against the experimental results by varying the parameters. Numerical parameter values are present in Table 4.2.

Table 4.2: Numerical Parameters Used for Experiments with Single Layered Porous Media Under Static Saltwater Side Boundary Condition

Parameters	Symbols	Value	Unit
Horizontal Length	L	3.1	m
Domain thickness	H	1.0	m
Porosity	$\epsilon$	0.35	-
Saltwater level	$h_f$	0.66	m
Freshwater density	$\rho_0$	1000	$kg/m^3$
Saltwater density	$\rho_s$	1025	$kg/m^3$
Saltwater concentration	$C_s$	35	$kg/m^3$
Longitudinal dispersivity	$\beta_L$	0.004	m
Transverse dispersivity	$\beta_T$	0.0004	m
Molecular diffusion coefficient	$D$	$10^{-9}$	$m^2/s$
Density Ratio	$\chi$	0.025	-
Hydraulic conductivity	K	600	m/d

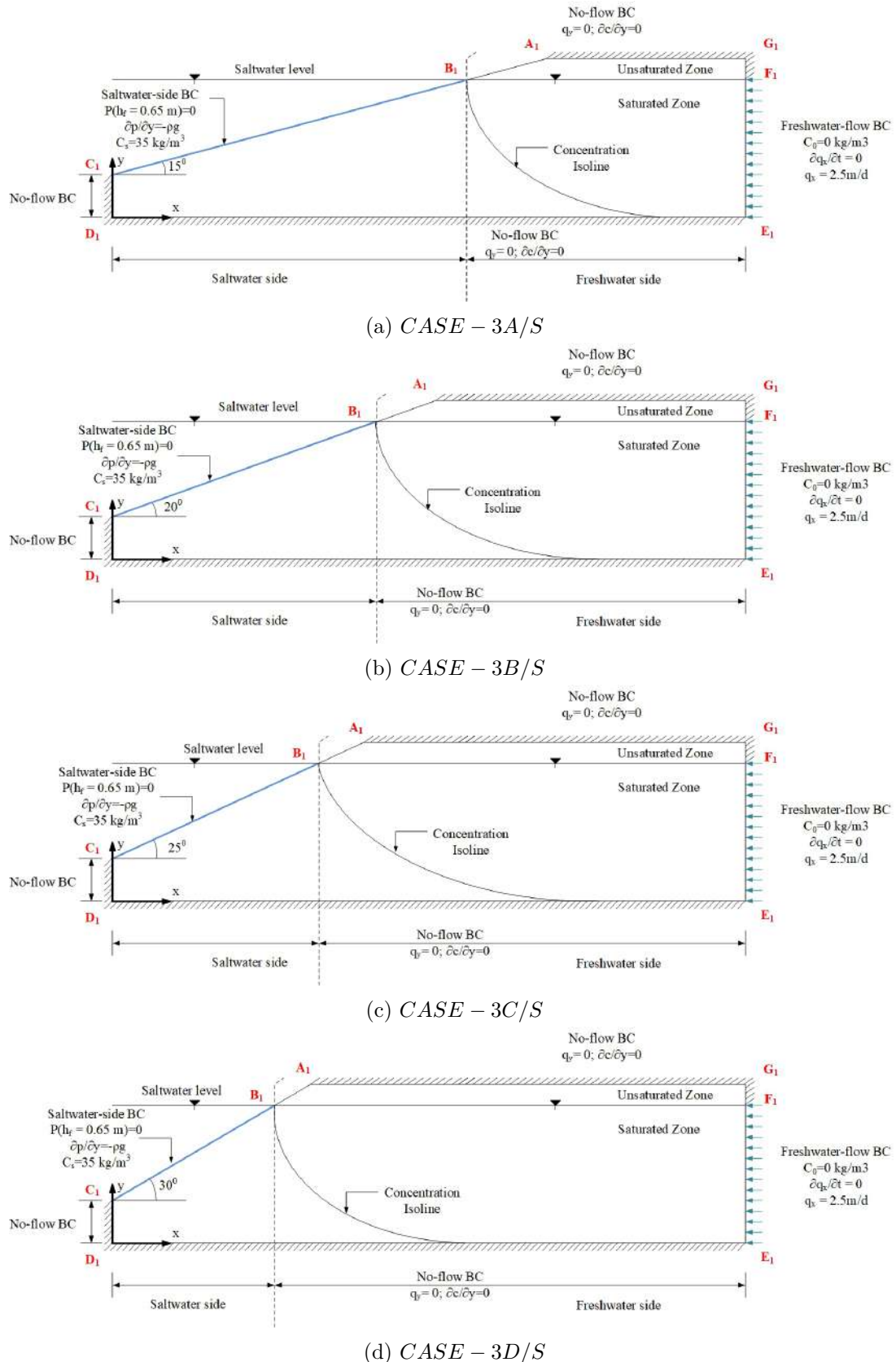


Figure 4.7: Boundary Conditions Used in Numerical Simulation for Experiments with Single Layered Porous Media Under Static Saltwater Side Condition

### 4.1.3 G-Channel Based Image Analysis

Instantaneous movement of saltwater was visually captured at an interval of 2 s by a Digital Single-Lens Reflex (DSLR) camera (Nikon d5100) placed centrally in front of the *Sand Box Model (Zone B)*. Lighting arrangements were kept the same as *CASE – 1/S* and *CASE – 2/S*. A virtual green rectangular box was utilized as a reference frame for the experimental images (Figures 4.2, 4.3, 4.4, 4.5). Portions of the experimental images were used as raw images (input) for further analysis. In the beginning, the captured images were cropped to fit the virtual green rectangular box. Raw images corresponding to all-time periods ( $\mathbf{Im}_{\text{Raw}}|_t$ ) were aligned with respect to a common coordinate system. Saltwater-freshwater interface movement information was extracted at a particular time by comparing the image with the reference image ( $\mathbf{Im}_{\text{Raw}}|_{t_0}$ ).

Experimental images contained colour information (pixel level) of i) unsaturated sand, ii) saturated sand, ii) *Rhodamine B* (tracer) mixed saltwater, iv) saltwater mixed sand. A robust image analysis technique was utilized for extraction of concentration gradient information. Image ( $\mathbf{Im}_{\text{Raw}}|_t$ ) corresponding to a particular time ( $t$ ) stores colour (R-G-B) information (Figure 3.6) in pixels ( $p_y \times p_x \times 3$ ). A colour can be regarded as a mixture of basic colours, viz. Red (R), Green (G), Blue (B) with different Digital Number (DN) values (between 0-255). Individual images can be decomposed into three different 2D ( $p_y \times p_x$ ) matrices ( $\mathbf{Im}_{\text{Raw}}^R|_t$ ,  $\mathbf{Im}_{\text{Raw}}^G|_t$ ,  $\mathbf{Im}_{\text{Raw}}^B|_t$ ) corresponding to Red, Green and Blue colours, respectively. The basic image analysis technique, proposed in *Section 3.3*, utilized difference between Red and Green DN values for extracting concentration gradient information. In-depth image analysis revealed that same DN value difference corresponds to multiple combinations of Red and Green channel values. Comparative analysis of different channels (R-G-B) showed that DN value standard deviation was maximum for Green Channel (G-Channel). Modeling of G Channel ( $\mathbf{Im}_t^G$ ) as a spatial process revealed physically consistent pattern near saltwater boundary corresponding to different pixel locations. However, variation in spatial pattern within the intermediate domain required a special attention. The proposed algorithm identifies spatial patterns on the basis of threshold DN value differences (between  $t$  and  $t_0$ ). This was achieved by G-channel matrix subtraction ( $\mathbf{Im}_t^G = \mathbf{Im}_{\text{Raw}}^G|_t - \mathbf{Im}_{\text{Raw}}^G|_{t_0}$ ). A typical instantaneous and reference images ( $p_y = 243 \times p_x = 800$ ) are shown in Figure 4.8b and Figure 4.8a, respectively. Figure 4.8c shows the output of G-Channel matrix subtraction.

Pixel level information (DN value difference) obtained from G-channel matrix subtraction was utilized for identification of concentration isolines. Line joining

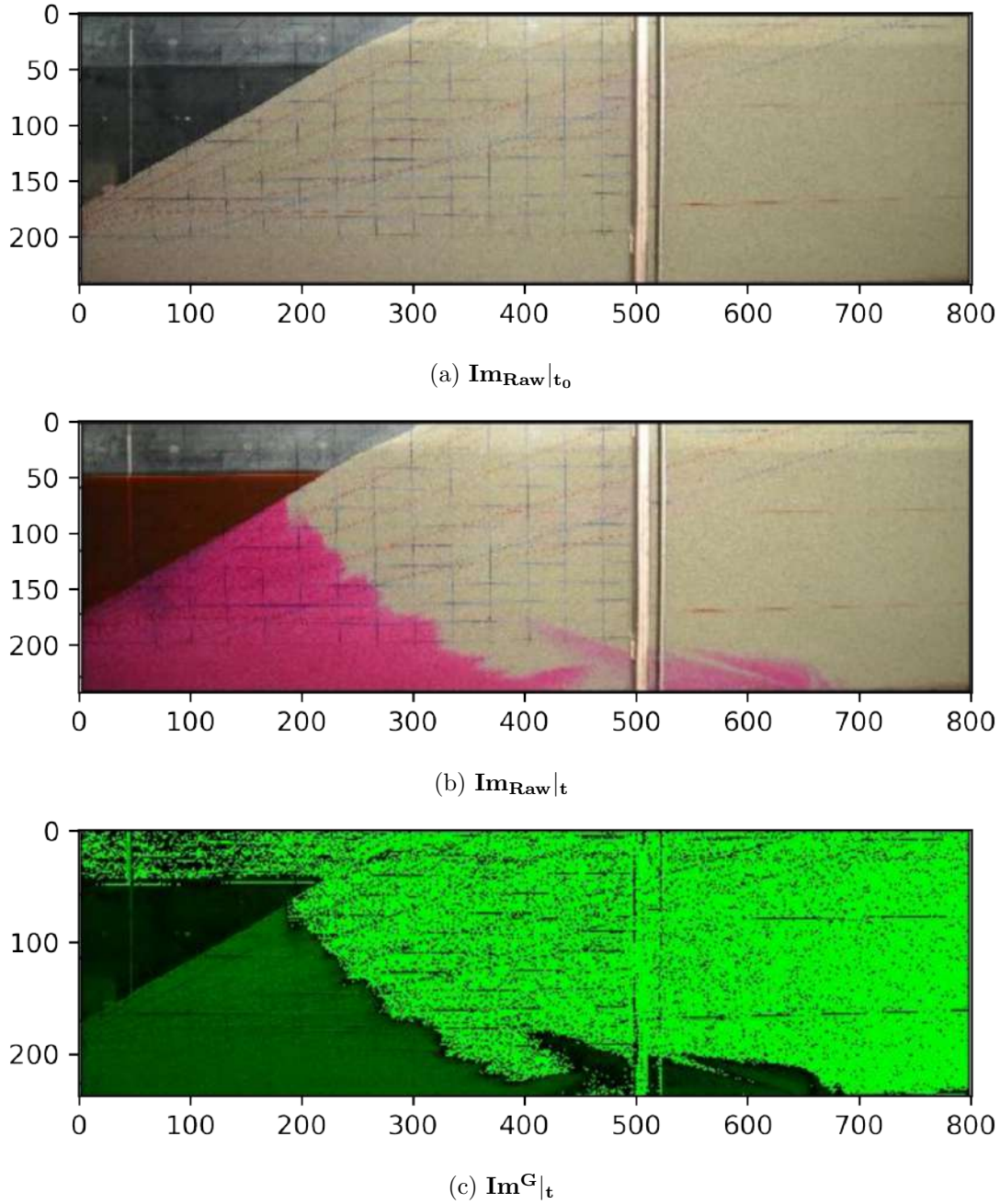


Figure 4.8: Detailed Steps of G-Channel Matrix Subtraction

pixels with equal threshold DN level showed too much variation. Figure 4.9a shows raw saltwater-freshwater interface. Statistical mean value cannot be utilized for filtering out fluctuations. Winsorized statistical mean is less sensitive to outliers. It eliminates an equal amount of both extremes and 10% to 25% values are replaced (Hastings et al., 1947). Saltwater-freshwater interface fluctuations were filtered (Figure 4.9b) by using 10% Winsorized Mean ( $\mathcal{WM}$ ) based on neighbouring pixels of  $i$  ( $\dots, \mathbf{Im}_t^G|_{i-1,j}, \mathbf{Im}_t^G|_{i,j}, \mathbf{Im}_t^G|_{i+1,j}, \dots$ ) present at level  $j$ . The framework utilized threshold DN values ( $DN_{Max}$  and  $DN_{Min}$ ) corresponding to maximum and minimum concentration levels ( $c_{Max}$  and  $c_{Min}$ ). Thresholds were fixed based on image statistics. For pixels (Set  $\mathbb{Z}_{SWB}$ ) corresponding to saltwater

boundary maximum concentration value ( $c_{Max}$ ) was specified. Similarly, 0.5 concentration isoline value ( $c_{Min}$ ) was specified for the pixels (Set  $\mathbb{Z}_{SFI}$ ) present in saltwater-freshwater interface. Concentration gradient information ( $\mathbf{Im}_{\mathbf{Grad}}^c$ ) for intermediate zone was obtained from an order statistics based linear interpolation method. Given two sets of concentration information points ( $DN_{Max}, c_{Max}$ ) and ( $DN_{Min}, c_{Min}$ ), a linear polynomial can be constructed as

$$\ell(\mathbf{Im}_{\mathbf{t}}^G|_{i, j}) = \frac{\mathbf{Im}_{\mathbf{t}}^G|_{i, j} - DN_{Min}}{DN_{Max} - DN_{Min}} c_{Max} + \frac{\mathbf{Im}_{\mathbf{t}}^G|_{i, j} - DN_{Max}}{DN_{Min} - DN_{Max}} c_{Min} \quad (4.1)$$

$\ell(\mathbf{Im}_{\mathbf{t}}^G|_{i, j})$  interpolates the concentration ( $c$ ) value for pixel ( $i, j$ ) in intermediate zone. Concentration gradient information matrix can be calculated as

$$\mathbf{Im}_{\mathbf{Grad}}^c|_{i, j} = \ell(\mathbf{Im}_{\mathbf{t}}^G|_{i, j}) \quad (4.2)$$

Figure 4.9c shows derived concentration distribution within the saltwater wedge within the porous media. The proposed G-Channel Based Image Analysis framework is presented in Algorithm 1. A python code was written to implement the proposed algorithm.

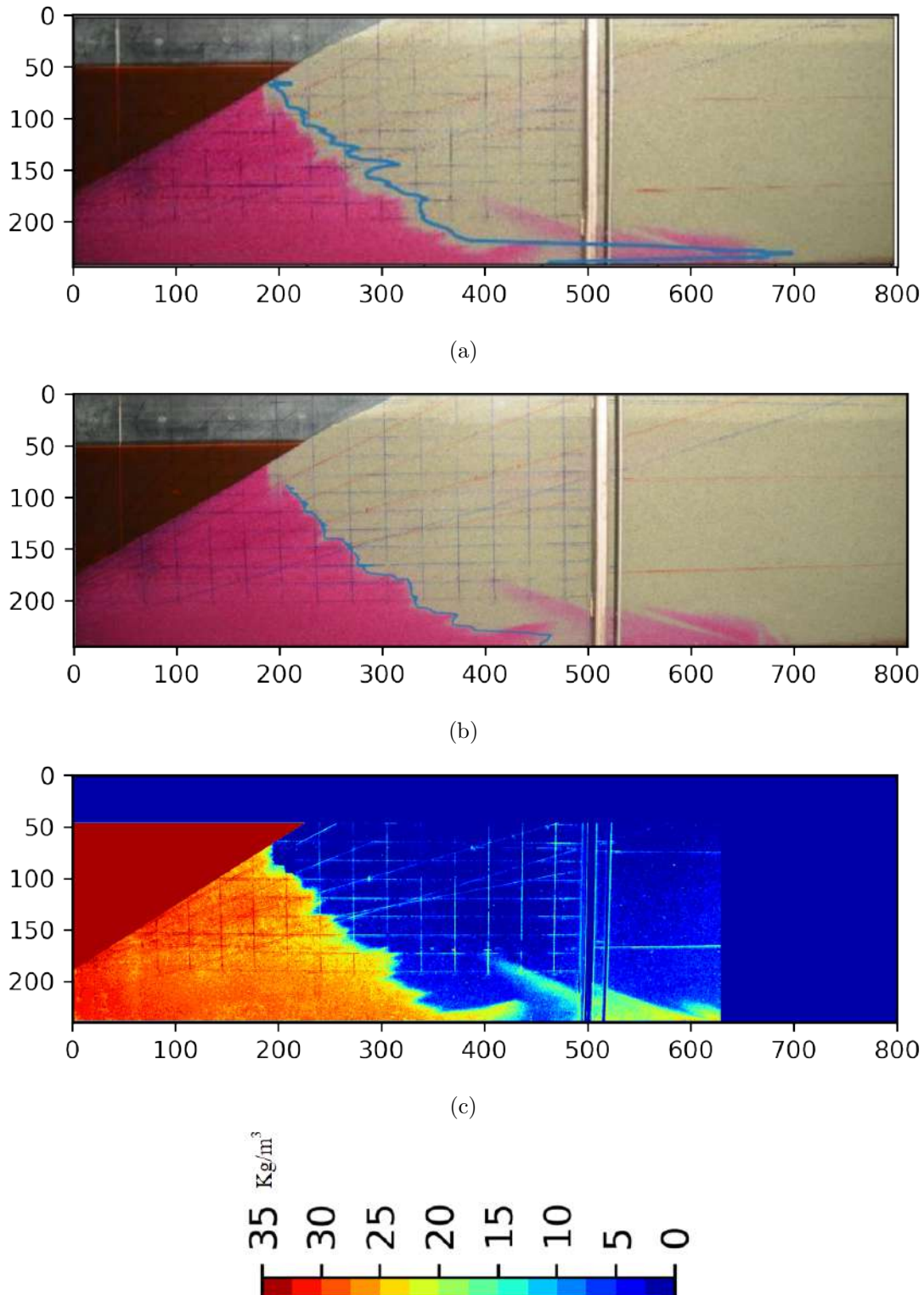


Figure 4.9: Detailed Steps of G-Channel Based Image Analysis: (a) Identification of Saltwater-Freshwater Interface, (b) Filtered Saltwater-Freshwater Interface Obtained from 10% Winsorized Mean , (c) Concentration Distribution

**Algorithm 1:** G-Channel Based Image Analysis

---

**Input:**  $\mathbf{Im}_{\text{Raw}}|_{t_0}$ ,  $\mathbf{Im}_{\text{Raw}}|_t$   
**Output:**  $\mathbf{Im}_{\text{Grad}}^c$

**1** Reference Image Decomposition  
**2**  $\mathbf{Im}_{\text{Raw}}|_{t_0} \rightarrow [\mathbf{Im}_{\text{Raw}}^R|_{t_0}, \mathbf{Im}_{\text{Raw}}^G|_{t_0}, \mathbf{Im}_{\text{Raw}}^B|_{t_0}]$   
**3** while  $t < T_{\text{max}}$  do  
**4**   | Image Decomposition  
**5**   |  $\mathbf{Im}_{\text{Raw}}|_t \rightarrow [\mathbf{Im}_{\text{Raw}}^R|_t, \mathbf{Im}_{\text{Raw}}^G|_t, \mathbf{Im}_{\text{Raw}}^B|_t]$   
**6**   | G-channel Matrix Subtraction  
**7**   |  $\mathbf{Im}_t^G \leftarrow \mathbf{Im}_{\text{Raw}}^G|_t - \mathbf{Im}_{\text{Raw}}^G|_{t_0}$   
**8**   | for  $j=1$  to  $p_y$  do  
**9**   |   | for  $i=1$  to  $p_x$  do  
**10**   |   |   | Winsorized Mean Calculation  
**11**   |   |   |  $\mathcal{WM} \leftarrow \text{WinsorizedM}(\dots, \mathbf{Im}_t^G|_{i-1,j}, \mathbf{Im}_t^G|_{i,j}, \mathbf{Im}_t^G|_{i+1,j}, \dots)$   
**12**   |   |   | Saltwater Boundary Identification  
**13**   |   |   | if  $\mathcal{WM} > \text{DN}_{\text{Max}}$  then  
**14**   |   |   |   |  $\mathbb{Z}_{\text{SWB}} \leftarrow (i, j)$   
**15**   |   |   |   | break  
**16**   |   |   | end  
**17**   |   | end  
**18**   |   | for  $i=1$  to  $p_x$  do  
**19**   |   |   | Winsorized Mean Calculation  
**20**   |   |   |  $\mathcal{WM} \leftarrow \text{WinsorizedM}(\dots, \mathbf{Im}_t^G|_{i-1,j}, \mathbf{Im}_t^G|_{i,j}, \mathbf{Im}_t^G|_{i+1,j}, \dots)$   
**21**   |   |   | Saltwater-Freshwater Interface Identification  
**22**   |   |   | if  $\mathcal{WM} < \text{DN}_{\text{Min}}$  then  
**23**   |   |   |   |  $\mathbb{Z}_{\text{SFI}} \leftarrow (i, j)$   
**24**   |   |   |   | break  
**25**   |   |   | end  
**26**   |   | end  
**27**   | end  
**28**   | Concentration for Saltwater Boundary  
**29**   | for each  $(i, j) \in \mathbb{Z}_{\text{SWB}}$  do  
**30**   |   |  $\mathbf{Im}_{\text{Grad}}^c|_{i,j} \leftarrow c_{\text{Max}}$   
**31**   | end  
**32**   | Concentration for Saltwater-Freshwater Interface  
**33**   | for each  $(i, j) \in \mathbb{Z}_{\text{SFI}}$  do  
**34**   |   |  $\mathbf{Im}_{\text{Grad}}^c|_{i,j} \leftarrow c_{\text{Min}}$   
**35**   | end  
**36**   | Concentration for Intermediate Zone  
**37**   | for  $j=1$  to  $p_y$  do  
**38**   |   | for  $i=1$  to  $p_x$  do  
**39**   |   |   | if  $(i, j) \notin \mathbb{Z}_{\text{SWB}}$  and  $(i, j) \notin \mathbb{Z}_{\text{SFI}}$  then  
**40**   |   |   |   |  $\mathbf{Im}_{\text{Grad}}^c|_{i,j} = \ell(\mathbf{Im}_t^G|_{i,j})$   
**41**   |   |   | end  
**42**   |   | end  
**43**   | end  
**44** end while

---

#### 4.1.4 Results and Discussion

Saltwater-freshwater interface dynamics in the single layer was studied for four different beach slopes ( $\alpha = 15^\circ, 20^\circ, 25^\circ, 30^\circ$ ) under static saltwater water level condition. The study quantified the influence of beach slope on saltwater dynamics in porous media. Laboratory-Scale numerical simulations were also utilized to assess the consistency of the experimental results.

Physical experiments, numerical simulations, experimental image analysis, and analytical solutions were utilized for comprehensive analysis. Time-varying saltwater intrusion flow pattern from experiments, G-Channel based image analysis and numerical simulations (0.5-concentration isoline) are shown in Figures 4.10, 4.11, 4.12, 4.13. Saltwater-freshwater interface and concentration distribution were analyzed corresponding to  $t = 600\text{ s}$ ,  $t = 2100\text{ s}$ ,  $t = 7320\text{ s}$ ,  $t = 25800\text{ s}$ . Saltwater-freshwater interfaces are clearly visible for the *CASE – 3A/S*, *CASE – 3B/S*, *CASE – 3C/S*, *CASE – 3D/S*. Reasonable match of experiment, image analysis and numerical simulation results were obtained for all the cases. Due to the diffusive nature of the saltwater-freshwater interface, the only visual matching technique was utilized. Interface toe location was used as the key matching parameter. Numerically simulated interface toe location reasonably matched with the experimental one.

Fingering effect is prominent in *CASE – 3A/S* for  $15^\circ$  slope. Effect is still visible for *CASE – 3B/S* for  $20^\circ$  slope. The initial saltwater fingering effect reduces with the increase in beach slope. However, the numerical simulation results captured the local fingering effect partially. This was due to the scale (mesh size) considered during the numerical simulations. Finer mesh would give a better fingering effect. However, the finer mesh was not used as our focus was on the developed saltwater-freshwater interface. The saltwater intrusion occurred rapidly, i.e., the size of the saltwater wedge increases, for flatter slopes (*CASE – 3A/S*). Thus saltwater-freshwater interface intruded less in *CASE – 3D/S*. Both experimental and numerical solutions showed similar trends. Moreover, the time required to reach the quasi-steady condition was less in *CASE – 3A/S*. It increases with the increase in beach slope. The overall influence of slope is evident from the aforementioned analysis.

#### 4.1. STATIC DENSITY HEAD EFFECT

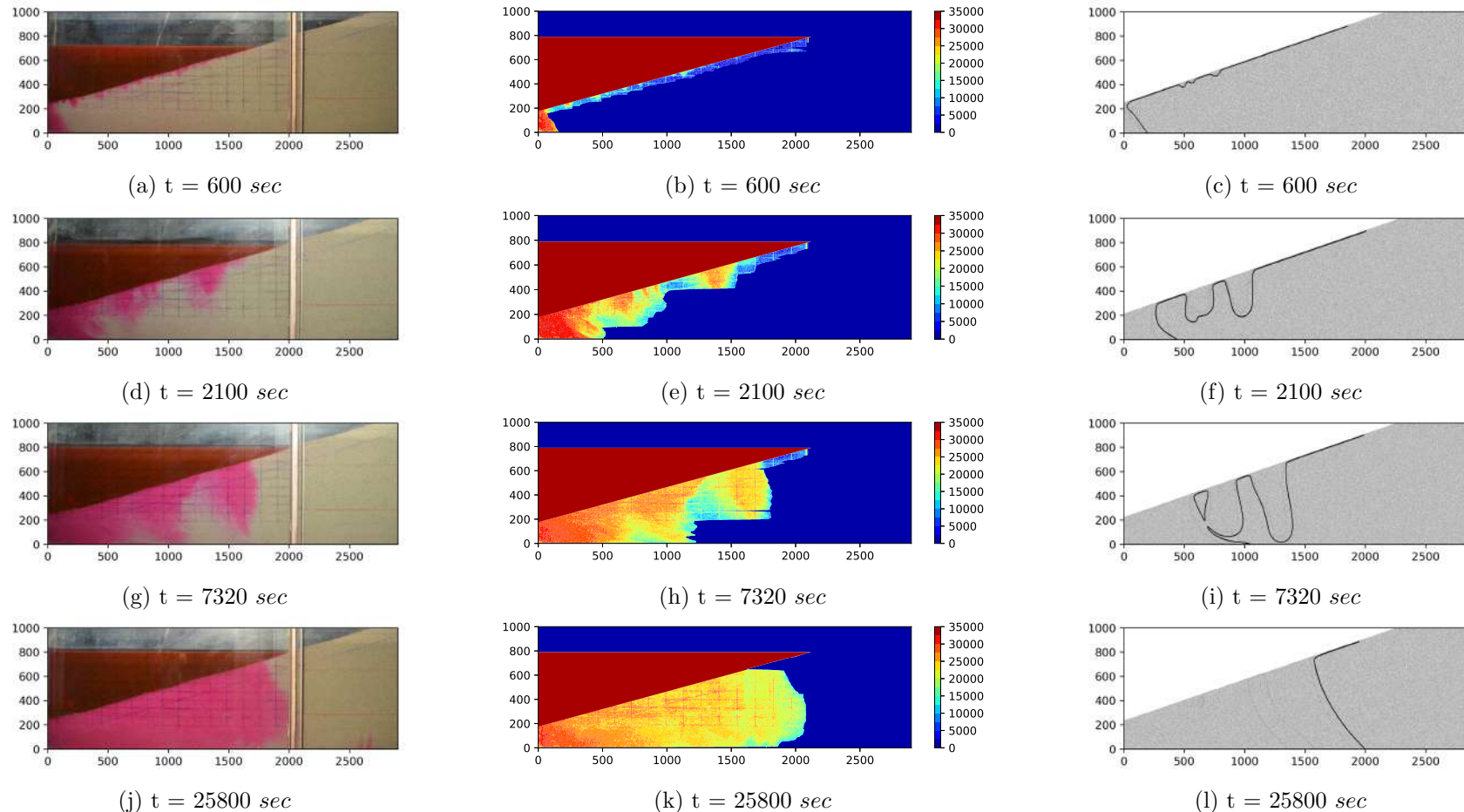


Figure 4.10: Development of Saltwater Wedge with Time in *CASE - 3A/S* [First Column: Experimental Images; Second Column: Output of G-Channel Based Image Analysis; Third Column: Numerical Simulation (0.5-Concentration Isoline), The Color Maps Indicate Concentration]. All dimensions are in mm.

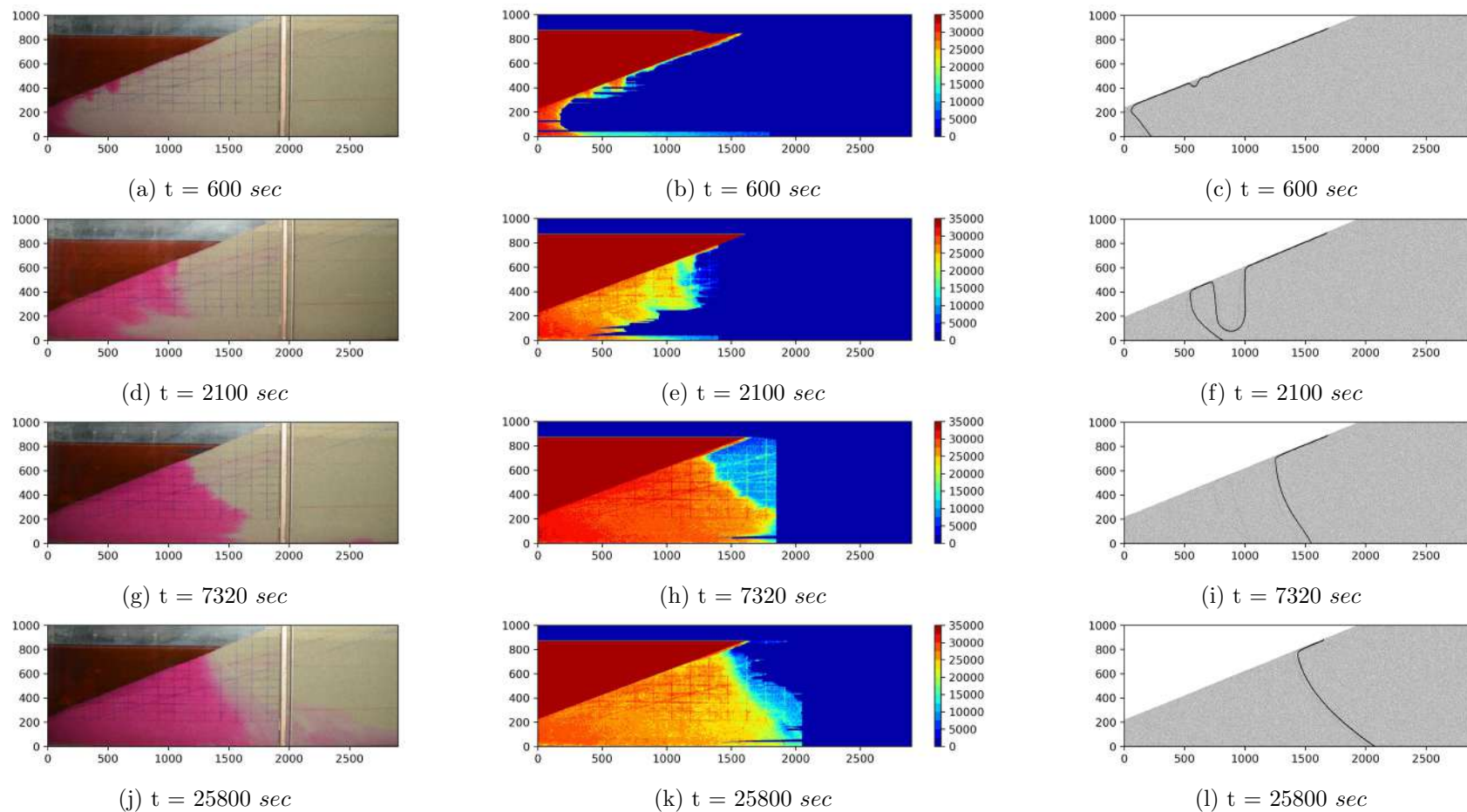


Figure 4.11: Development of Saltwater Wedge with Time in *CASE - 3B/S* [First Column: Experimental Images; Second Column: Output of G-Channel Based Image Analysis; Third Column: Numerical Simulation (0.5-Concentration Isoline), The Color Maps Indicate Concentration]. All dimensions are in mm.

#### 4.1. STATIC DENSITY HEAD EFFECT

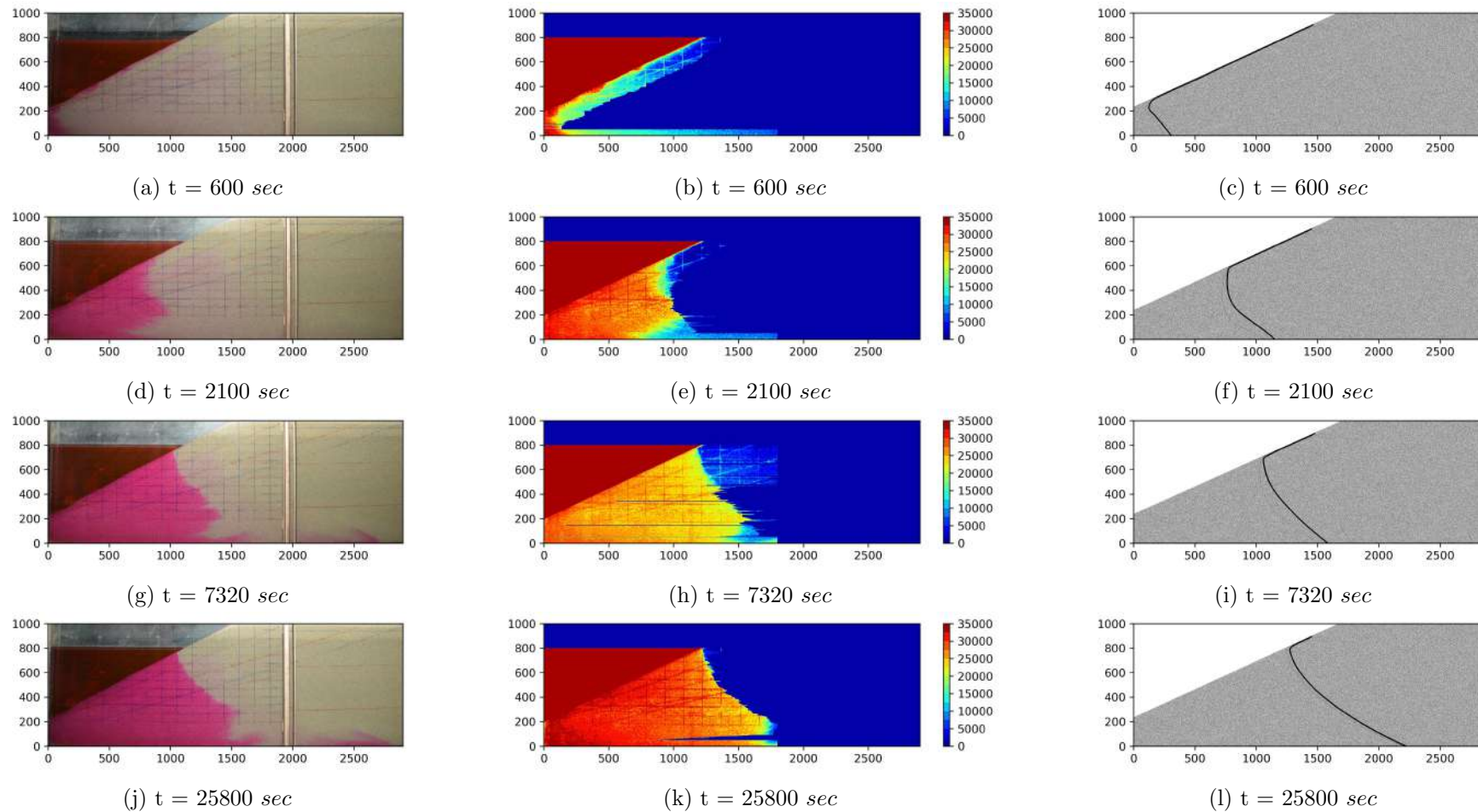


Figure 4.12: Development of Saltwater Wedge with Time in *CASE - 3C/S* [First Column: Experimental Images; Second Column: Output of G-Channel Based Image Analysis; Third Column: Numerical Simulation (0.5-Concentration Isoline), The Color Maps Indicate Concentration]. All dimensions are in mm.

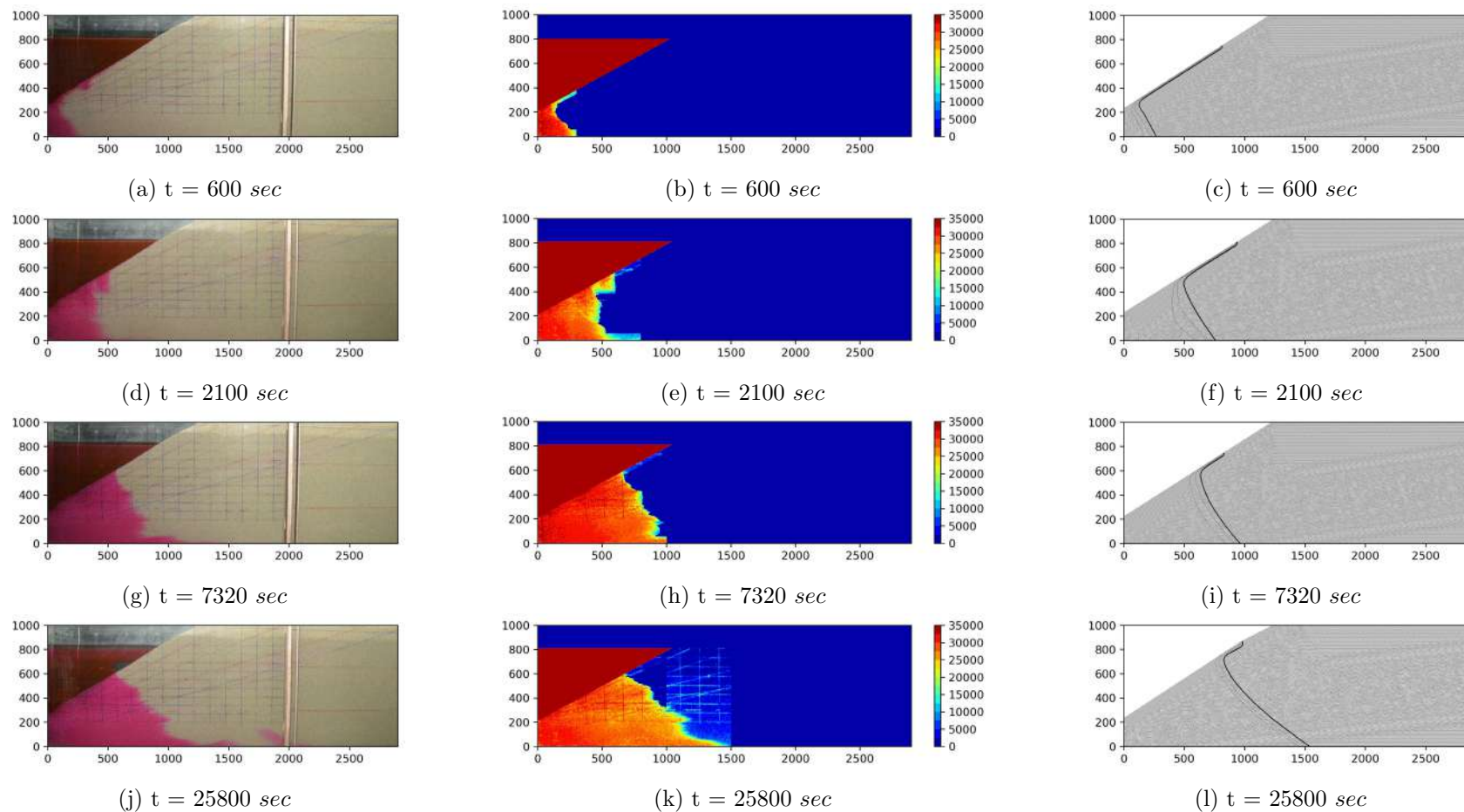


Figure 4.13: Development of Saltwater Wedge with Time in *CASE - 3D/S* [First Column: Experimental Images; Second Column: Output of G-Channel Based Image Analysis; Third Column: Numerical Simulation (0.5-Concentration Isoline), The Color Maps Indicate Concentration]. All dimensions are in mm.

Further numerically simulated and experimental (Pore Water Pressure Measurement) hydraulic head values were plotted to check the consistency of the obtained results. Figure 4.14 shows the plots corresponding to *CASE – 3A/S*, *CASE – 3B/S*, *CASE – 3C/S*, and *CASE – 3D/S* with a 0.5 cm band on both sides. The outlier clusters corresponding to different pressure transducers are visible from the plots. Spatial location of pressure transducers (*PS1*, *PS2*, *PS3*, *PS4*, *PS5*, *PS6*) were fixed with respect to *Sand Box Model* for cases. In *CASE – 3A/S* all the pressure transducers showed a good match except *PS2*. This was due to the boundary effect as *PS2* was located very near to the sloping boundary (15°). In *CASE – 3B/S* outlier clusters were corresponding to pressure transducers *PS3*, *PS5*, *PS6*. Pressure transducer *PS5* was located below the junction of saltwater level and beach face (20°). Thus some effect of submarine groundwater discharge (SGD) was present. Deviation in *PS6* was due to the freshwater boundary effect. This overestimation was due to the marginal rise of the water level near the right boundary. In *CASE – 3C/S* all the pressure transducers showed good match except *PS2* and *PS4*. Some effect of submarine groundwater discharge (SGD) was present in *PS4* (25°). Similarly, effect of submarine groundwater discharge (SGD) was present in *PS3* for *CASE – 3D/S*.

Comparative analysis was performed with saltwater-freshwater interface corresponding to 50%-salinity line from FEFLOW and processed images (G-Channel Based Image Analysis). Saltwater-freshwater interface toe location ( $l_T$ ) and submarine groundwater discharge gap ( $\zeta_0$ ) were determined analytically (Equations 3.9 and 3.10), numerically and experimentally. The analytical (Van der Veer, 1977) values of  $l_T$  and  $\zeta_0$  are 863 mm and 564 mm, respectively. The FEFLOW simulations underpredict the  $\zeta_0$  compared to the experimental value (Tables 4.3) for all the cases. SGD gap ( $\zeta_0$ ) decreases with an increase in beach slope. Figures 4.15 show saltwater-freshwater interface variations with beach slope.

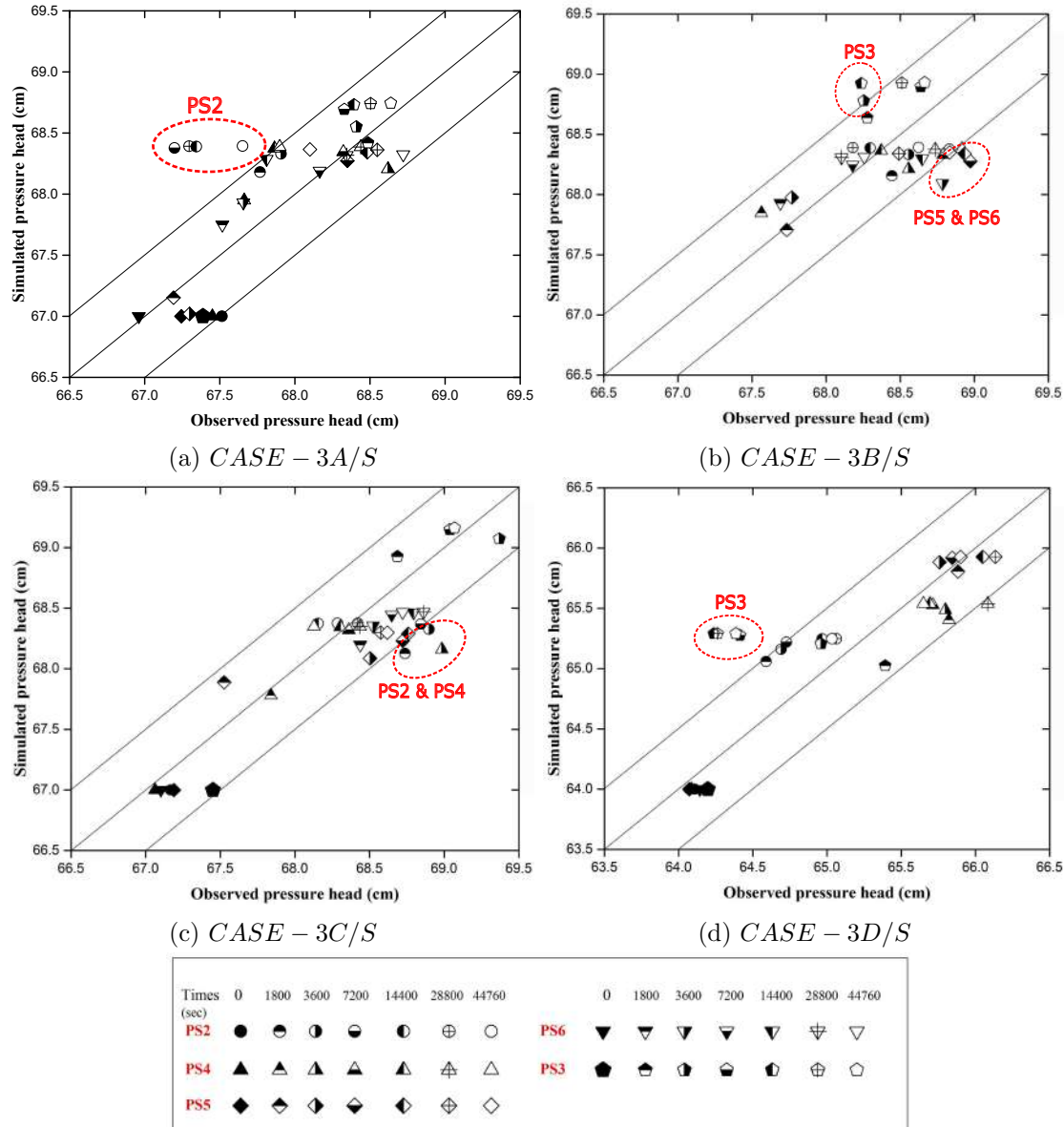


Figure 4.14: Comparison Between Time Varying Observed and Numerically Simulated Pressure Head Data

Table 4.3: Submarine Groundwater Discharge (SGD) Gap and Saltwater-Freshwater Interface Toe Length for Experiments with Single Layered Porous Media Under Static Saltwater Side Boundary Condition

Case	Slope	Sand	$\zeta_o$ (mm)	$\ell_T$ (mm)	$\zeta_o$ (mm)	$\ell_T$ (mm)	$\zeta_o$ -FEFLOW /
			Expt	Expt	FEFLOW	FEFLOW	$\zeta_o$ -Expt
CASE - 3A/S	15 <sup>0</sup>	IS Sand Grade I $d_{50}=1.12$ mm	452.7	443.28	298.21	408.93	0.658
CASE - 3B/S	20 <sup>0</sup>	IS Sand Grade I $d_{50}=1.12$ mm	288.81	540.80	284.78	543.02	0.986
CASE - 3C/S	25 <sup>0</sup>	Coarse Sand $d_{50}=1.12$ mm	245.82	699.28	220.30	639.44	0.896
CASE - 3D/S	30 <sup>0</sup>	Coarse Sand $d_{50}=1.12$ mm	241.79	816.75	188.06	609.51	0.777
Avg= 0.82							

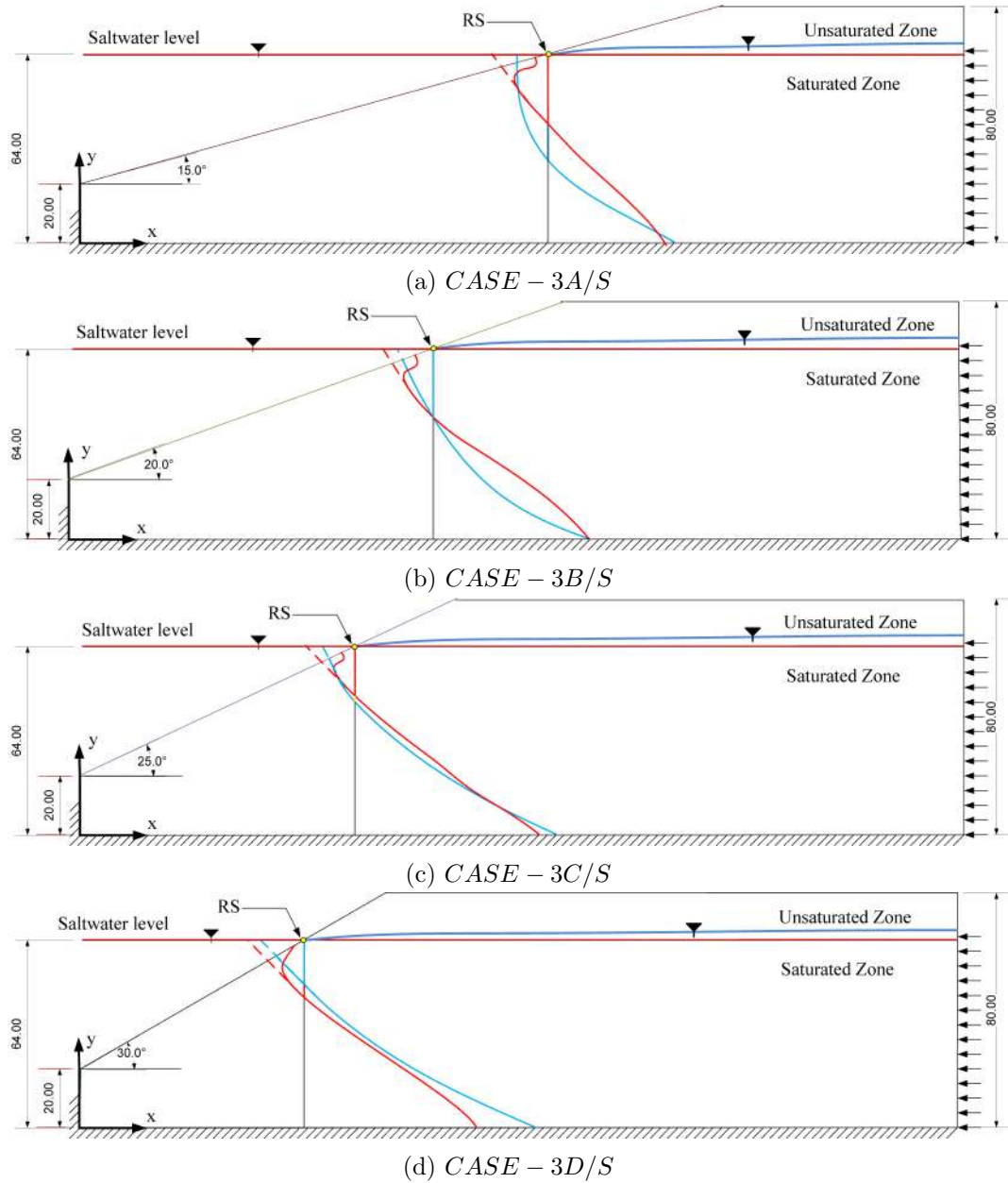


Figure 4.15: Saltwater-freshwater Interface for Experiments with Single Layered Porous Media Under Static Saltwater Side Boundary Condition (Red Line: FEFLOW Simulation Results; Blue Line: Experimental Results Obtained from G-Channel Based Image Analysis)

SGD flow path was identified by using the tracer injection technique. *Malachite Green* (external tracer) was injected under density neutral conditions (without externally generated buoyancy) at different locations through a tube-like setup within the porous media. The tracer experiments were started after attaining the quasi-steady state condition and continued till the tracer reached the intersection point of saltwater level and sloping beach face. Time-varying images of the tracer experiments are shown in Figure 4.16. It is evident that SGD particles move along the SWI zone and rise in the upward direction (up to the intersection point).

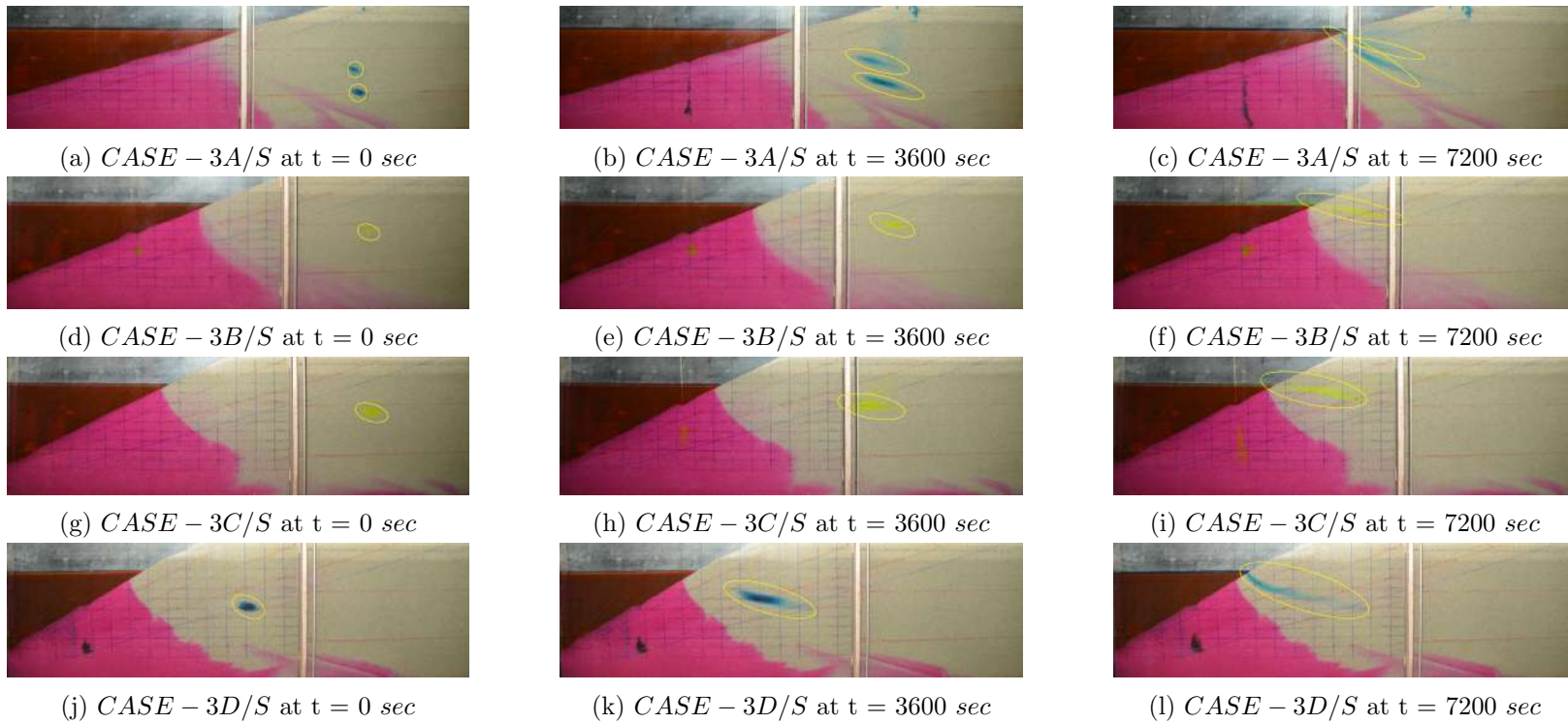


Figure 4.16: SGD Flow Pathways for Experiments with Single Layered Porous Media Under Static Saltwater Side Boundary Condition

## 4.2 Influence of Beach Slope on Saltwater Movement in Single Layer Under Tidal Condition

Tides are important oceanic forces acting on coastal aquifers. The static saltwater level represents the average of tidal oscillations. Water varies between High Saltwater Level (HSL) and Low Saltwater Level (LSL) during rising and falling tide, respectively. In a tidal cycle, the saltwater level drops below the freshwater level during falling tide. This leads to a phase-averaged saltwater circulation within the saltwater wedge. Upper saline plume (USP) emerges as a result of the circulation process. Moreover, freshwater discharge (Li et al., 1999; Moore et al., 2008; Robinson et al., 2007a, 2018; Yu et al., 2019b) occurs as submarine groundwater discharge (SGD) through the region between USP and the saltwater wedge. SGD depends on freshwater flux coming from the inland side (Watson et al., 2010). Walther et al. (2017) performed numerical experiments with sloping beach face. However, no study is available on the quantification of beach slope effect on coastal aquifers. The current study focused on quantifying beach slope effect in single layer unconfined aquifer under tidal conditions through laboratory and numerical experiments. The laboratory experiments were carried out with Grade I (1-2 mm) Indian Standard Sand (IS: 650-1991) with varying beach slopes to understand the saltwater dynamics in single (homogeneous) layered porous media under tidal saltwater boundary conditions. Laboratory experiments were conducted in *Sand Box Model* under controlled initial and boundary conditions. The experimental configurations are presented in Table 4.4. The flow circulation study in the freshwater zone was also performed.

### 4.2.1 Experimental Method

The schematic diagram of the experimental setup is shown in Figure 4.17. It included three components i) Two Dimensional *Sand Box Model* (3.1 m length  $\times$  1.0 m high  $\times$  0.020 m wide), ii) Tidal Mechanism, iii) Pressure Transducers (*PS1* to *PS6*) with Data Acquisition System. Both freshwater and saltwater reservoirs were available at both ends. The right side freshwater reservoir was utilized to supply freshwater flux from the inland boundary. The left side saltwater reservoir was connected to the *Tidal Mechanism* with Oscillating saltwater column (Figure 4.17b). The water level in the saltwater reservoir was maintained through an overflow outlet located on the left boundary of the *Sand Box Model*.

Four different beach slopes, 15°, 20°, 25°, and 30° were considered for cases *CASE-3A/T*, *CASE-3B/T*, *CASE-3C/T* and *CASE-3D/T*, respectively.

Table 4.4: Configurations for Experiments with Single Layered Porous Media Under Tidal Saltwater Side Boundary Condition

Cases	Beach Slope	Sand	Stratification	Tidal/ Static	Remarks
<i>CASE – 3A/T</i>	$15^0$	Grade I IS sand $d_{50} = 1.12 \text{ mm}$	No	Tidal	-
<i>CASE – 3B/T</i>	$20^0$	Grade I IS Sand $d_{50} = 1.12 \text{ mm}$	No	Tidal	-
<i>CASE – 3C/T</i>	$25^0$	Grade I IS Sand $d_{50} = 1.12 \text{ mm}$	No	Tidal	-
<i>CASE – 3D/T</i>	$30^0$	Grade I IS Sand $d_{50} = 1.12 \text{ mm}$	No	Tidal	-

The saturated freshwater flow was allowed (for 2-3 days) through the intermediate zone (*Zone-B*) to get a stabilized aquifer equivalent formation. All of the following steps were performed before starting the experiments:

1. Preparation of the saltwater solution with *Rhodamine B*.
2. Valve connecting the *Tidal Mechanism* was opened.
3. Bottom outlets were closed.
4. The aquifer was saturated up to a height of  $0.65 \text{ m}$  with freshwater.
5. Continuous supply of freshwater in *ZoneC* was ensured with a peristaltic pump (  $120 \text{ rpm}$ , equivalent to  $6.00 \text{ m/d}$ ).
6. The outlet valve of *ZoneA* placed at a  $0.65 \text{ m}$  was opened to maintain the water level.
7. Pressure transducers were connected and calibrated.
8. Camera was started in self capturing mode ( $2 \text{ s}$  interval) along with the lighting arrangements.

A *Tidal Mechanism* was designed to impose a periodic oscillation boundary conditions at left side of the *Sand Box Model* (Figure 4.17b). It produces suction pressure in both directions between saltwater reservoir (forward) to oscillating saltwater column (backward). The *Controller System* operates Rotodyne DC motor in the forward and backward directions for a fixed period to create a tidal wave.

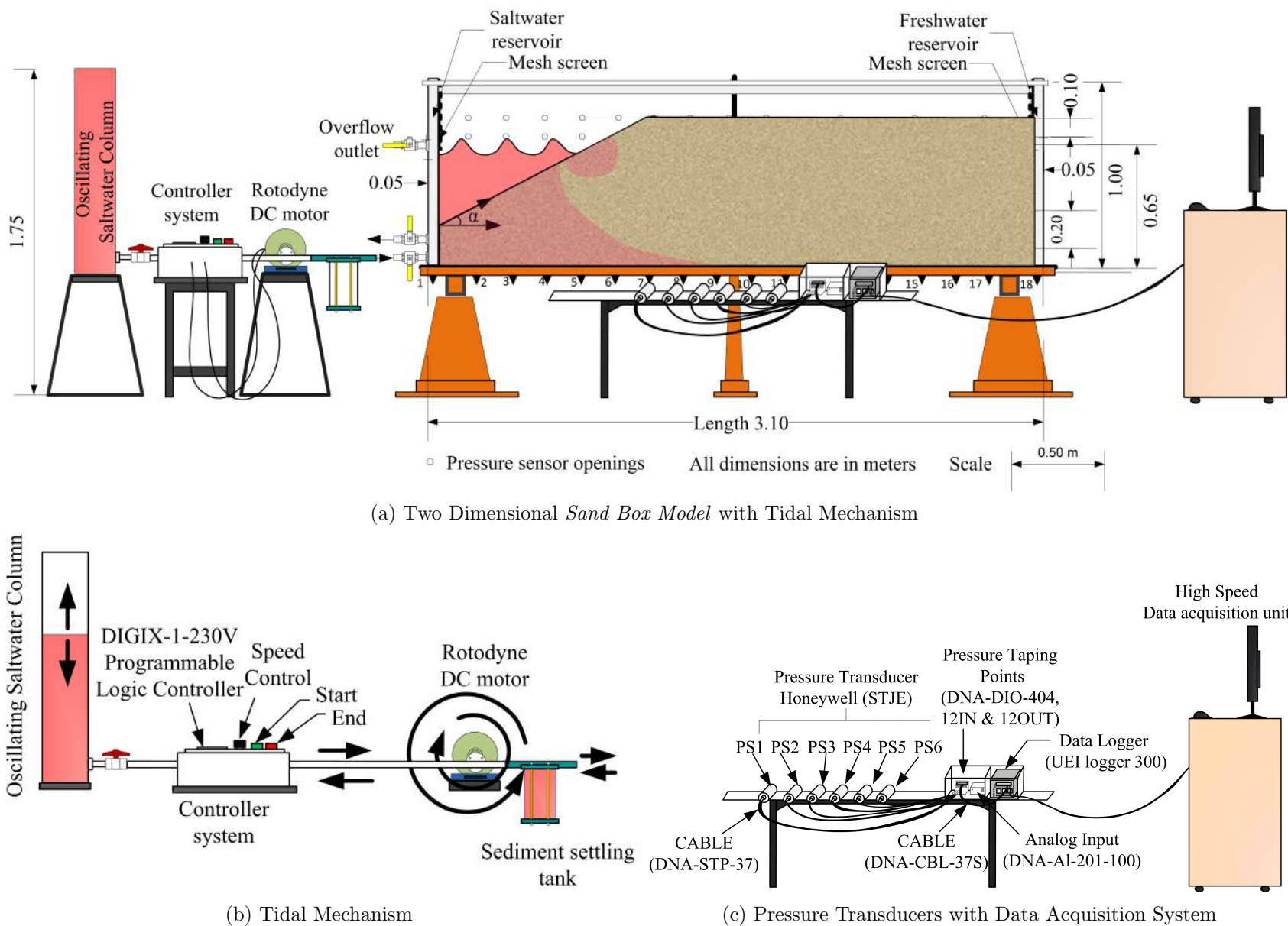


Figure 4.17: Schematic Representation Experimental Setup with Single Layered Porous Media Under Tidal Saltwater Side Boundary Condition

Six pressure transducers ( $PS_1$  to  $PS_6$ ) were connected to the back side glass wall of the *Sand Box Model*. The pressure values were recorded (sampling frequency: 20 Hz) through the data acquisition system (Figure 4.17c). The salinity of the saltwater solution was monitored using the CTD Diver. Approximately 35000 mg/l saltwater concentration was maintained in *Zone A* after initial period (Figures 4.18a, 4.18b, 4.18c, and 4.18d). The pressure measurements for density dependent experiments were recorded only after stabilisation of the salinity measurements. Figure 4.18 shows the starting point for different experimental cases. The experiments (*CASE-3A/T*, *CASE-3B/T*, *CASE-3C/T*, *CASE-3D/T*) were continued until 18 h to 20 h (time required to achieve a quasi-steady condition).

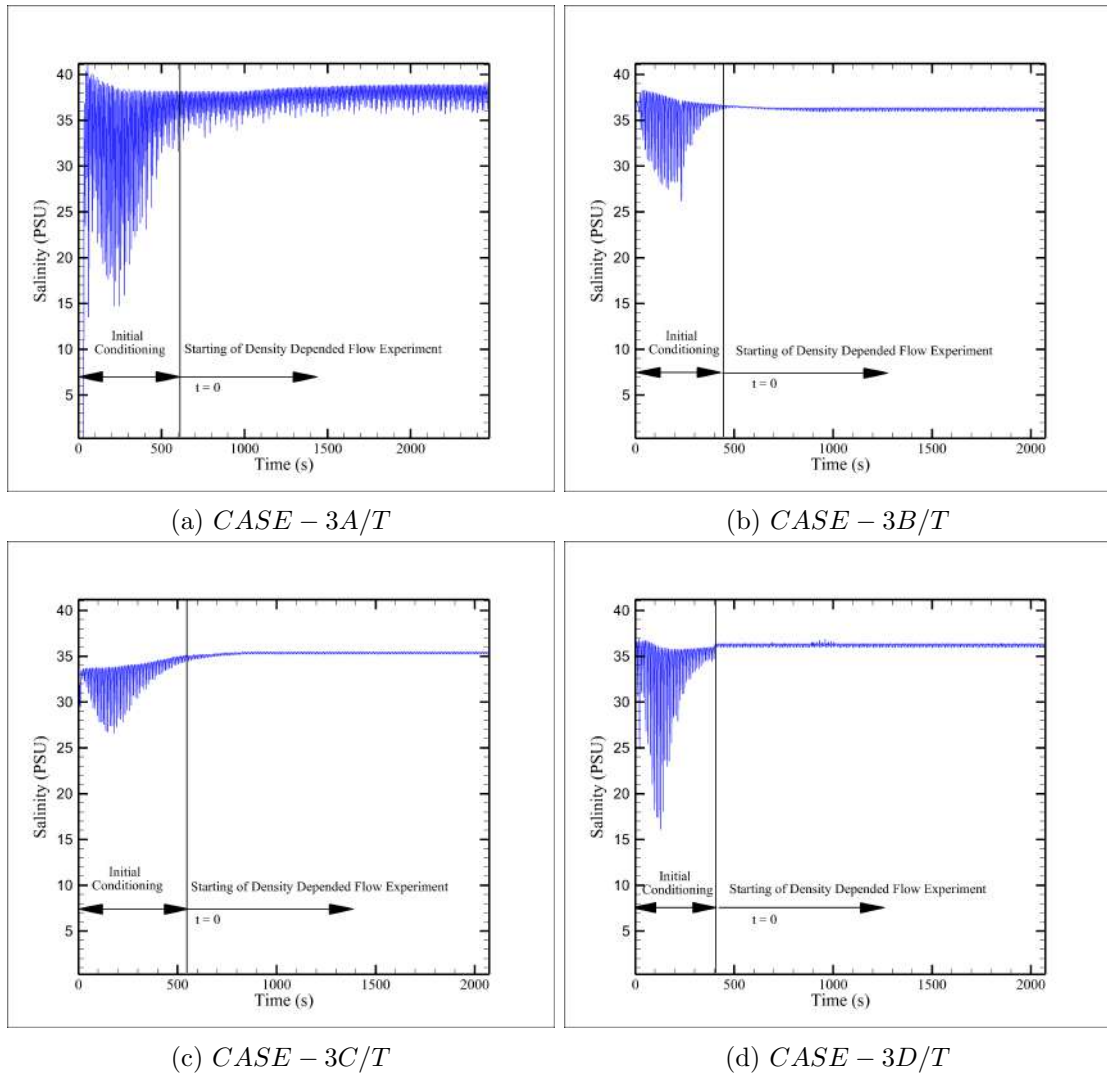


Figure 4.18: Observed Time Varying Salinity Profiles at Saltwater Reservoir (*Zone - A*)

## 4.2.2 Numerical Simulation Model

Numerical simulation model FEFLOW (Diersch, 2013) was utilized to get pressure head and concentration information for two-dimensional vertical cross-section at different time levels. Mesh convergence study was performed to determine optimal unstructured finite element mesh of different sizes (case dependent) for the *Sand Box Model*. The optimal element size varied from 0.001  $m$  to 0.004  $m$ . Peclet number criterion ( $Pe_m = \Delta L/\alpha L < 4$ ) for numerical stability was followed while discretizing the case specific model domains with triangular mesh (Diersch, 2013). Details of boundary conditions are shown in Figure 4.19.

### 4.2.2.1 Initial and Boundary Conditions

The laboratory-based physical model equivalent numerical domain (*CASE – 3A/T*, *CASE – 3B/T*, *CASE – 3C/T*, *CASE – 3D/T*), and relevant boundary conditions are shown in Figure 4.19. Initial conditions for all cases were specified in terms of head and concentration values. In the beginning, the domain was saturated with freshwater at constant flux from the right side (freshwater concentration). Initial conditions were specified in accordance with the boundary conditions by running the simulation model under quasi-steady-state conditions (without saltwater). Along the saltwater-side boundary ( $B_1 – C_1$ ) time-varying equivalent freshwater head condition was applied. Concentration boundary conditions were assigned from the starting point (after stabilization of conductivity values as shown in Figure 4.18) of the experiments. Initial free surface in porous media or water table ( $B_1 – F_1$ ) was identified from the quasi-steady-state run. Two types of boundary conditions were assigned i) Dirichlet Boundary and ii) Neumann Boundary.

#### *Dirichlet Boundary Condition*

Time varying saltwater head equivalent boundary condition was specified along sloping boundary ( $B_1 – C_1$ ). Actual tidal water levels were specified as Dirichlet Condition.

Individual nodes along the boundary were identified for specification of flow and concentration Dirichlet boundary conditions. A seepage face boundary was adopted up to the point where the saltwater level meets the sloping beach face. A constant mass concentration was applied for the boundary nodes below the saltwater surface. Above the saltwater surface, two cases were considered (Shoushtari et al., 2015): i) atmospheric pressure was specified for the saturated nodes corresponding to the previous time step, and ii) no-flow condition was specified for the unsaturated nodes. Specified constant concentration (saltwater, 35000  $mg/l$ )

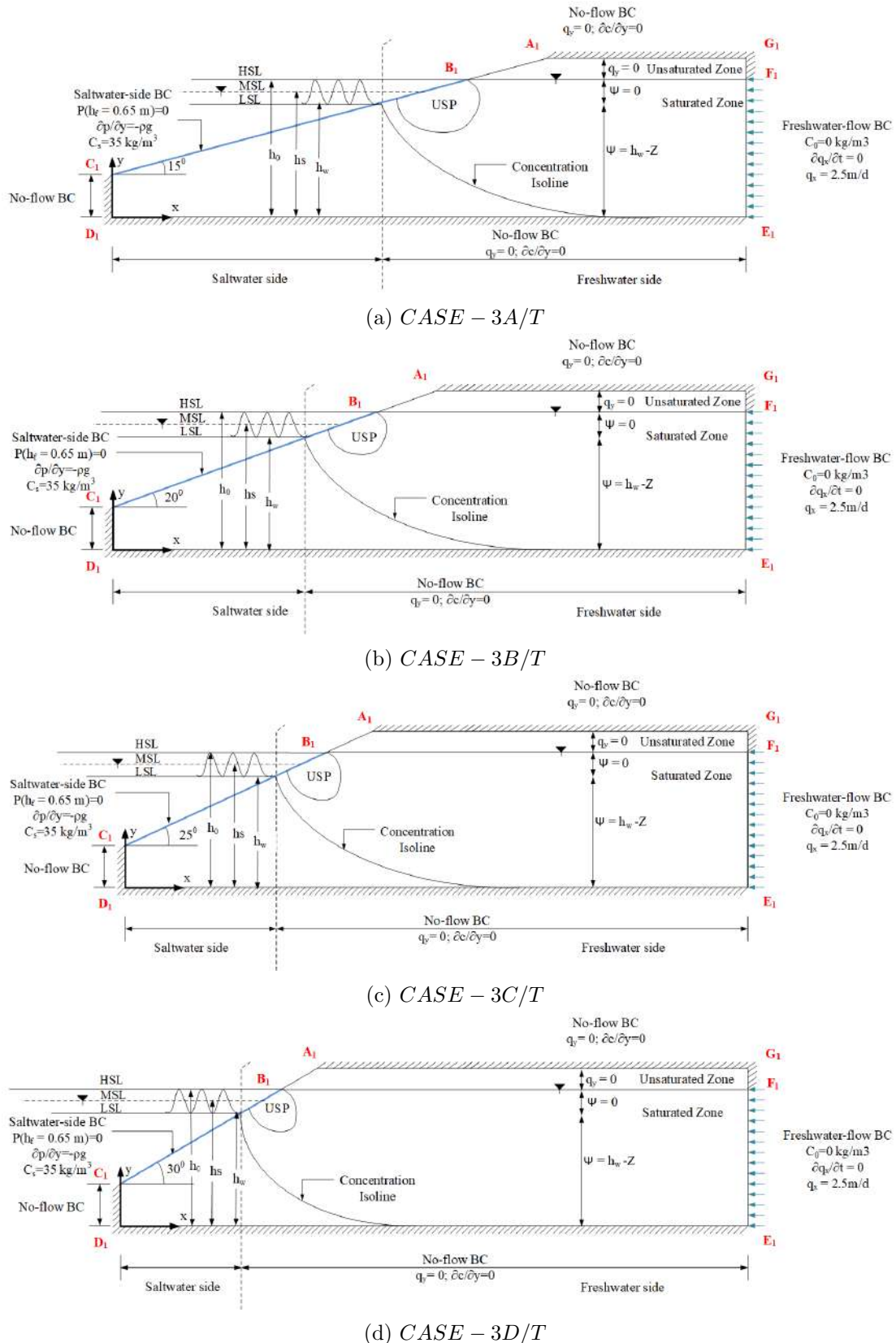


Figure 4.19: Boundary Conditions Used in Numerical Simulation for Experiments with Single Layered Porous Media Under Tidal Saltwater Side Condition.

condition was applied along the sloping boundary for all saturated nodes. Zero concentration level was specified for all unsaturated nodes.

### Neumann Boundary Condition

Freshwater flow from the right side ( $E_1 - F_1$ ) was specified as a Neumann flux type boundary condition. The peristaltic pump was used for creating the freshwater flux boundary condition. Top boundary ( $G_1 - A_1$ ), bottom boundary ( $D_1 - E_1$ ), vertical face in saltwater side boundary ( $C_1 - D_1$ ), and top vertical face in right side boundary ( $F_1 - G_1$ ) were specified with zero Neumann condition for flow and mass transport (concentration). The model was then calibrated against the experimental results using the physical parameters as shown in Table 4.5.

Table 4.5: Numerical Parameters Used for Experiments with Single Layered Porous Media Under Tidal Saltwater Side Boundary Condition

Parameters	Symbols	Value	Unit
Horizontal Length	L	3.1	m
Domain thickness	H	1.0	m
Porosity	$\epsilon$	0.385	-
Saltwater level	$h_f$	0.66	m
Freshwater density	$\rho_0$	1000	kg/m <sup>3</sup>
Saltwater density	$\rho_s$	1025	kg/m <sup>3</sup>
Saltwater concentration	$C_s$	35	kg/m <sup>3</sup>
Longitudinal dispersivity	$\beta_L$	0.004	m
Transverse dispersivity	$\beta_T$	0.0004	m
Molecular diffusion coefficient	$D$	$10^{-9}$	$m^2/s$
Density Ratio	$\chi$	0.025	-
Hydraulic conductivity	K	600	$m/d$

### 4.2.3 G-Channel Based Image Analysis

Experimental images were analysed as per the *G-Channel Based Image Analysis* framework presented in Algorithm 1 (*Subsection 4.1.3*).

### 4.2.4 Results and Discussion

Saltwater-freshwater interface dynamics in the single layer was studied for four different beach slopes ( $\alpha = 15^\circ, 20^\circ, 25^\circ, 30^\circ$ ) under tidal saltwater water level condition. Tidal experiments, viz, *CASE – 3A/T*, *CASE – 3B/T*, *CASE – 3C/T*, *CASE – 3D/T* were considered for quantification of influence of beach slope. Moreover, numerical simulations were also performed. The prominent fingering effect

was not visible for any case under tidal conditions. Due to tidal water level variation, two separate saltwater zones were visible for all cases. The first saltwater zone was similar to the saltwater wedge visible under static saltwater boundary conditions. The second zone, also known as *Upper Saline Plume*, extended between High Saltwater Level (HSL) and Low Saltwater Level (LSL). Submarine groundwater discharge (SGD) occurred through the intermediate zone between the saltwater wedge and USP. The zones are clearly visible in Figures 4.20, 4.21, 4.22, 4.23 for Saltwater-freshwater interfaces are clearly visible for *CASE – 3A/T*, *CASE – 3B/T*, *CASE – 3C/T*, *CASE – 3D/T*, respectively. The tidal oscillations changed the hydraulic gradient across the sloping beach face. This hydraulic gradient change generated circulating saltwater flow (in a clockwise direction) within porous media in the inter-tidal zone. This circulating flow resulted in the formation of the USP. The USP expanded with time and moved in a downward direction. Finally, a deformed elliptic-shaped USP was observed under quasi-steady-state conditions.

Saltwater-freshwater interface and concentration distribution were analyzed corresponding to  $t = 600\text{ s}$ ,  $t = 2100\text{ s}$ ,  $t = 7320\text{ s}$ ,  $t = 25800\text{ s}$ . Reasonable match of the experiment, image analysis, and numerical simulation results were obtained for all the cases. As observed in static cases (*CASE – 3A/S*, *CASE – 3B/S*, *CASE – 3C/S*, *CASE – 3D/S*) saltwater intrusion occurs rapidly for flatter slopes (*CASE – 3A/T*). The size of the saltwater wedge was minimum in *CASE – 3D/T*. Comparative analysis showed that saltwater intrusion length (Toe length) decreases with increasing beach slope. Further, saltwater intrusion length decreases under tidal condition (*CASE – 3A/T*, *CASE – 3B/T*, *CASE – 3C/T*, *CASE – 3D/T*) compared to static condition (*CASE – 3A/S*, *CASE – 3B/S*, *CASE – 3C/S*, *CASE – 3D/S*). Both experimental and numerical solutions showed similar trends. The overall time required to reach a quasi-steady condition was more in *CASE – 3A/T* compared to *CASE – 3A/S*. A similar trend was also observed for other slopes ( $20^\circ$ ,  $25^\circ$ ,  $30^\circ$ ). However, *CASE – 3D/T* was continued for a maximum time among all the tidal cases to achieve a quasi-steady-state condition. The overall influence of slope is evident from these analyses.

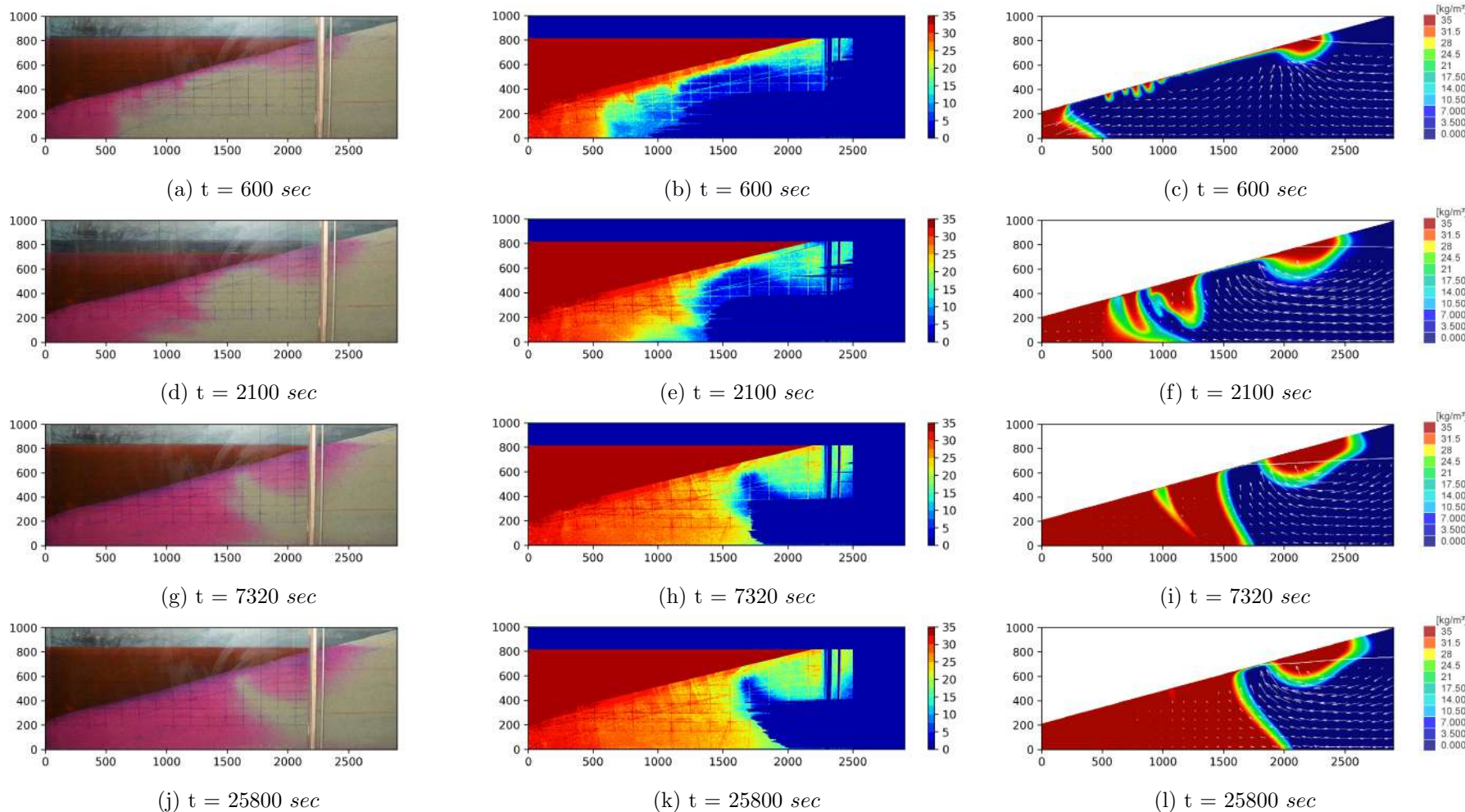


Figure 4.20: Development of Saltwater Wedge with Time in *CASE - 3A/T* [First Column: Experimental Images; Second Column: Output of G-Channel Based Image Analysis; Third Column: Numerical Simulation, The Color Maps Indicate Concentration]. All dimensions are in mm.

## 4.2. SINGLE LAYER UNDER TIDAL CONDITION

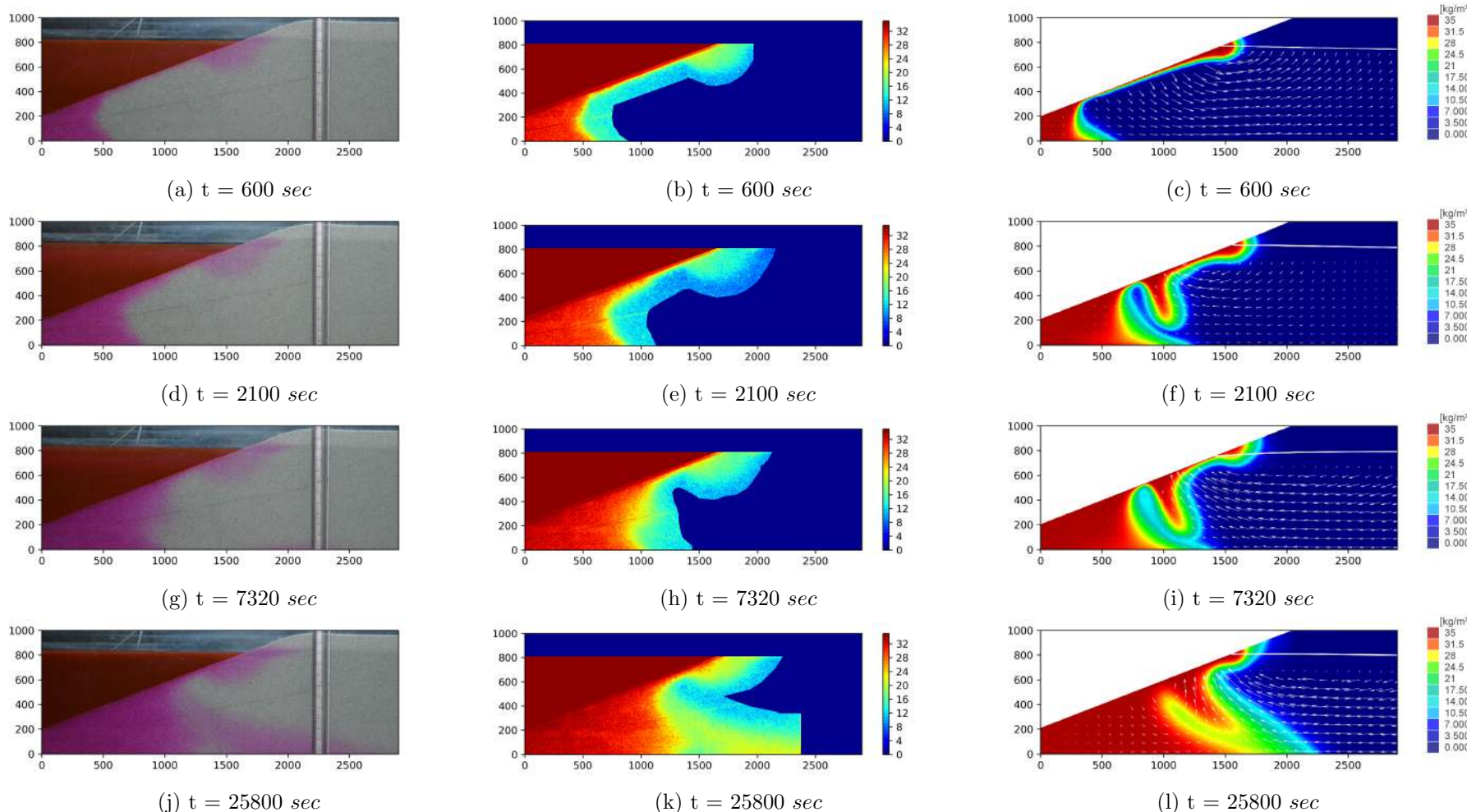


Figure 4.21: Development of Saltwater Wedge with Time in *CASE - 3B/T* [First Column: Experimental Images; Second Column: Output of G-Channel Based Image Analysis; Third Column: Numerical Simulation, The Color Maps Indicate Concentration]. All dimensions are in mm.

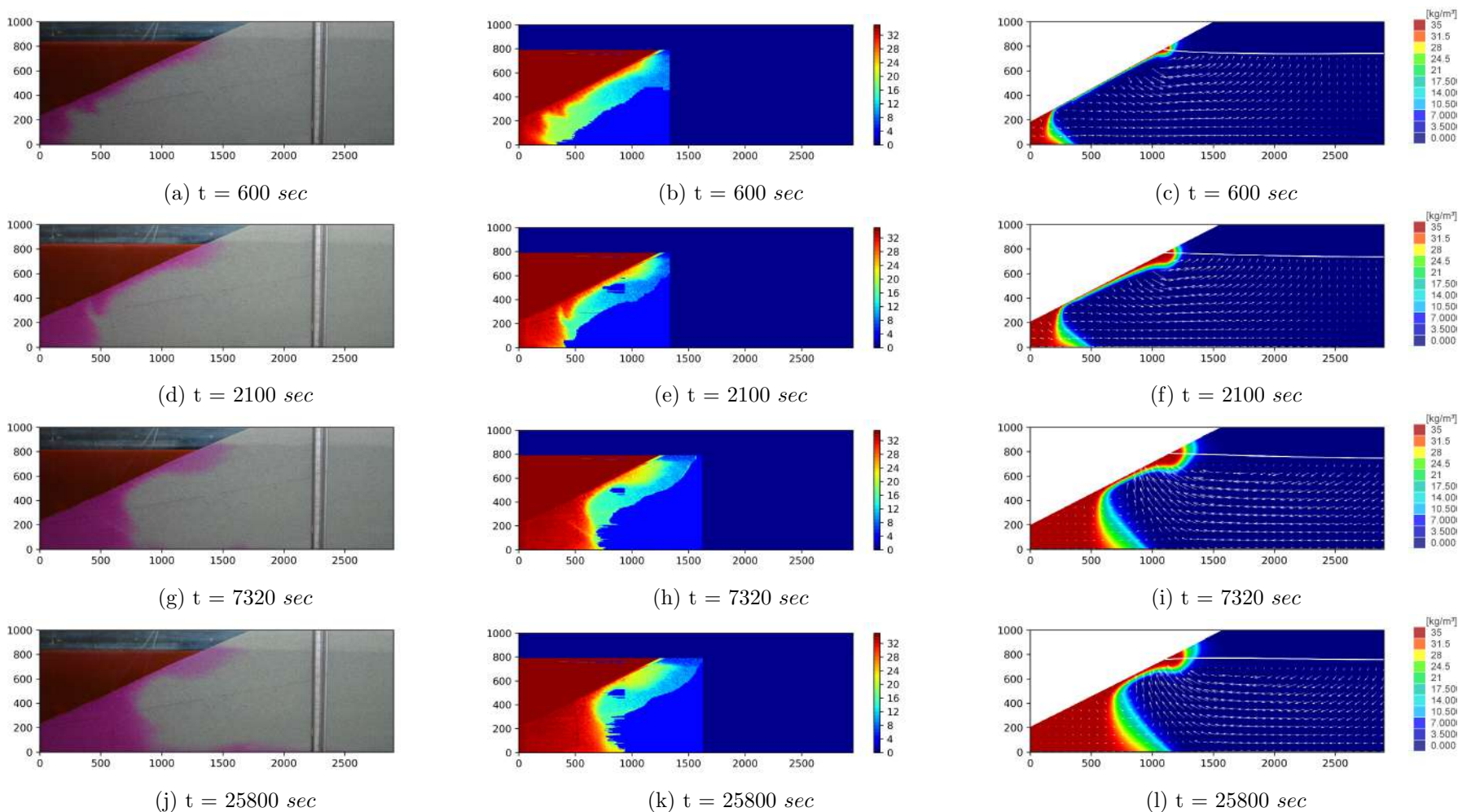


Figure 4.22: Development of Saltwater Wedge with Time in *CASE - 3C/T* [First Column: Experimental Images; Second Column: Output of G-Channel Based Image Analysis; Third Column: Numerical Simulation, The Color Maps Indicate Concentration]. All dimensions are in mm.

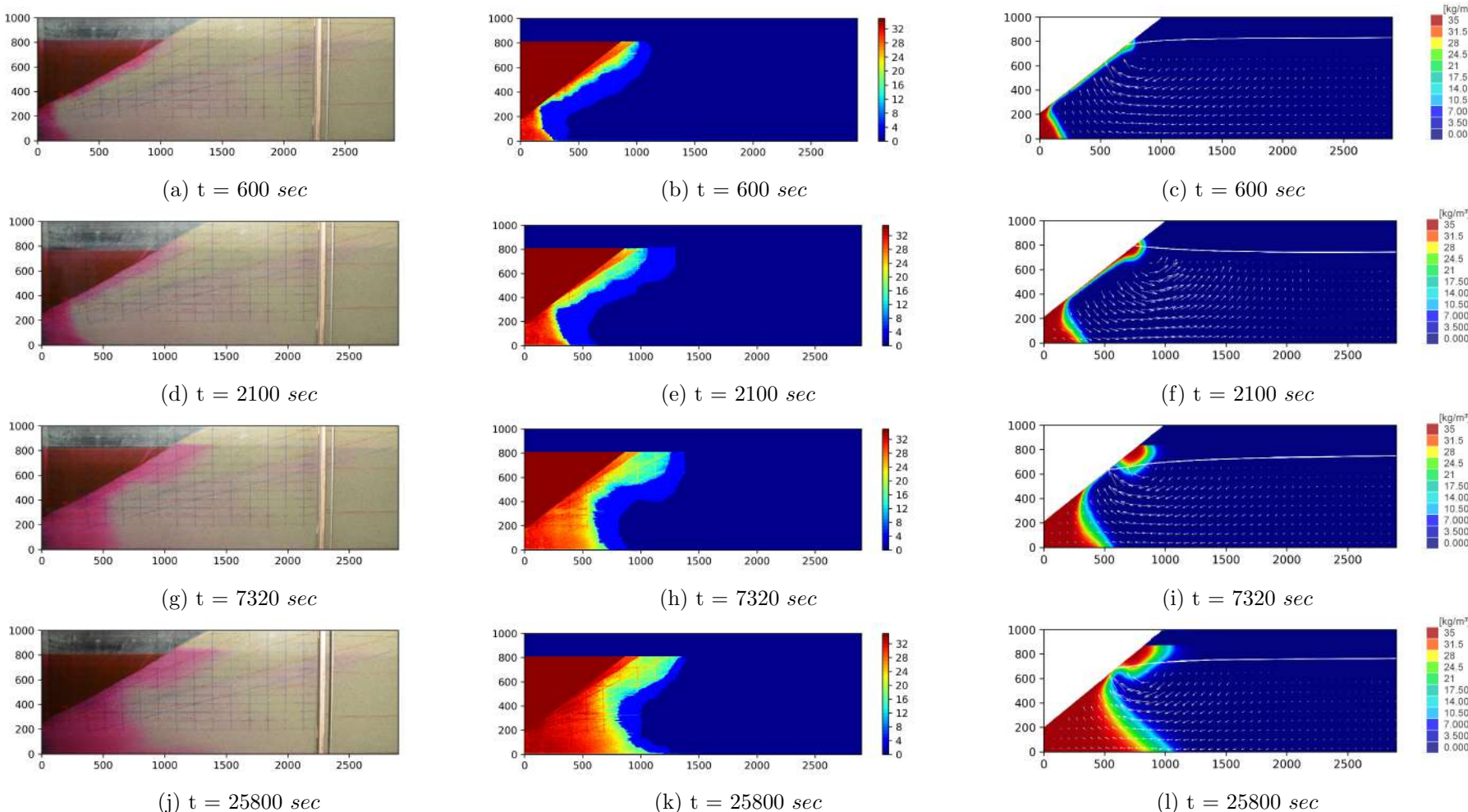


Figure 4.23: Development of Saltwater Wedge with Time in *CASE - 3D/T* [First Column: Experimental Images; Second Column: Output of G-Channel Based Image Analysis; Third Column: Numerical Simulation, The Color Maps Indicate Concentration]. All dimensions are in mm.

Numerically simulated and experimental (Pore Water Pressure Measurement) hydraulic head values were plotted in Figure 4.24 with 1 cm band on both sides. Unlike static water level condition, the outlier clusters are corresponding to different time periods for different slopes. No outliers are visible for *CASE – 3A/T*. However, outlier cluster are corresponding to time level 1800 s, 3600 s, 44760 s for *CASE – 3B/T*, *CASE – 3C/T*, *CASE – 3D/T*, respectively. Time varying head values for *CASE – 3A/T*, *CASE – 3B/T*, *CASE – 3C/T*, *CASE – 3D/T* are shown in Figure 4.25.

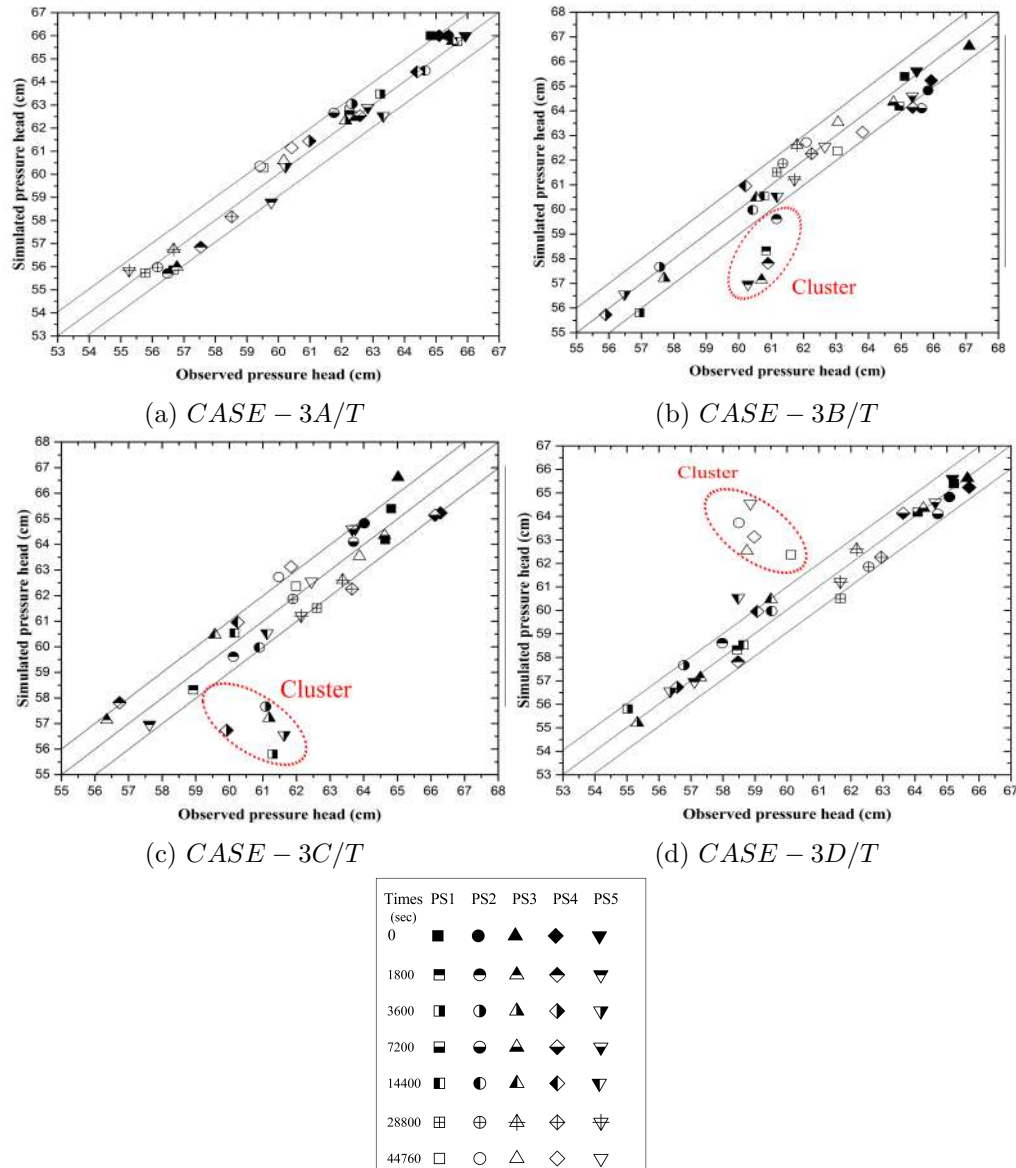


Figure 4.24: Comparison Between Time Varying Observed and Numerically Simulated Pressure Head Data

Processed experimental images (G-Channel Based Image Analysis) and numerically simulated saltwater-freshwater interface (50%-salinity line) were compared. The analytical (Van der Veer, 1977) values of  $l_T$  and  $\zeta_0$  are 863 mm and 564 mm,

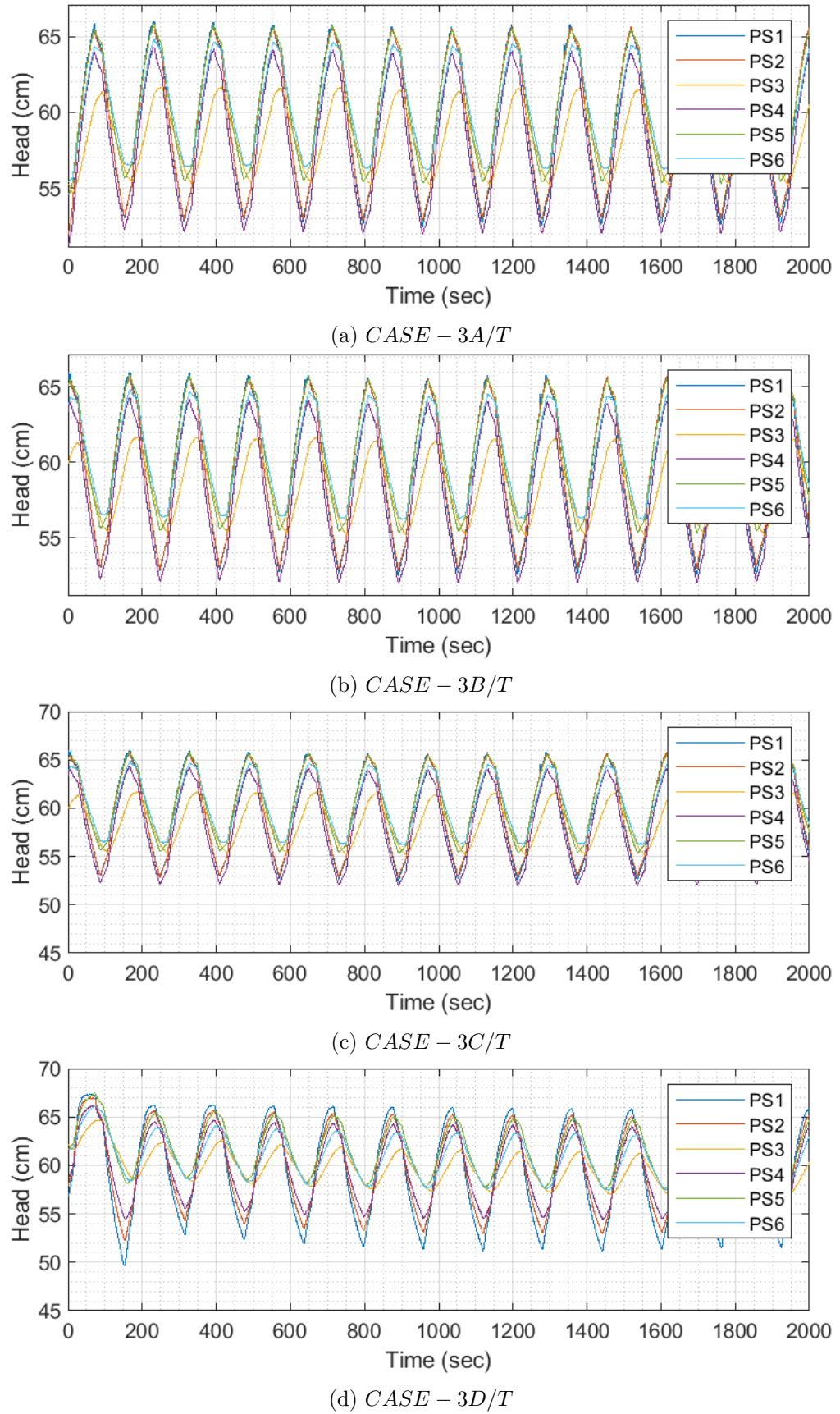


Figure 4.25: Observed Time Varying Pore-Water Pressure Head

respectively. The FEFLOW simulations underpredict the  $\zeta_0$  compared to the ex-

perimental value (Tables 4.6) for all the cases. The overall decreasing pattern was observed for the SGD gap ( $\zeta_0$ ) with the increase in beach slope. However, an increase in  $\zeta_0$  value was observed in tidal case (e.g., *CASE – 3A/T*) when compared to static one (e.g., *CASE – 3A/S*) with the same beach slope. Figure 4.26 shows saltwater-freshwater interface variations with beach slope.

*Rhodamine B* was utilized as the saltwater tracer. In tracer injection technique *Methyl Orange* was used as a neutral density tracer. The tracer without salt was injected in the freshwater zone to identify the SGD flow path under quasi-steady-state conditions. The tracer movement was captured until it reached the top of the saltwater surface. Figure 4.26 shows the SGD flow paths (tracer flow paths) for *CASE – 3A/T*, *CASE – 3B/T*, *CASE – 3C/T*, and *CASE – 3D/T*. Freshwater particles move along the saltwater-freshwater interface. Particles get discharged to the saltwater region through the intermediate zone of the saltwater wedge and USP.

Table 4.6: Submarine Groundwater Discharge (SGD) Gap and Saltwater-Freshwater Interface Toe Length for Experiments with Single Layered Porous Media Under Tidal Saltwater Side Boundary Condition

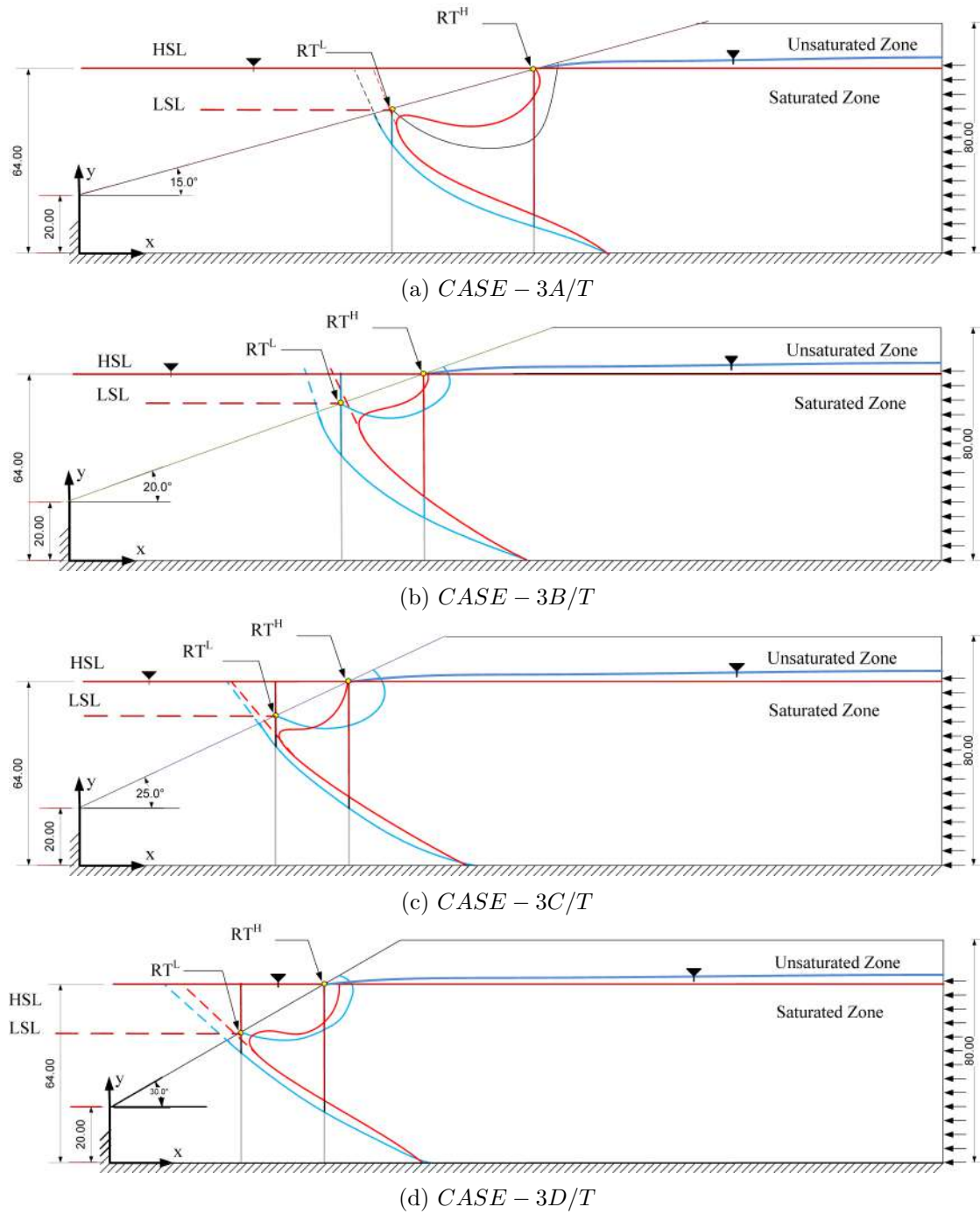


Figure 4.26: Saltwater-freshwater Interface for Experiments with Single Layered Porous Media Under Tidal Saltwater Side Boundary Condition (Red Line: FEFLOW Simulation Results; Blue Line: Experimental Results Obtained from G-Channel Based Image Analysis)

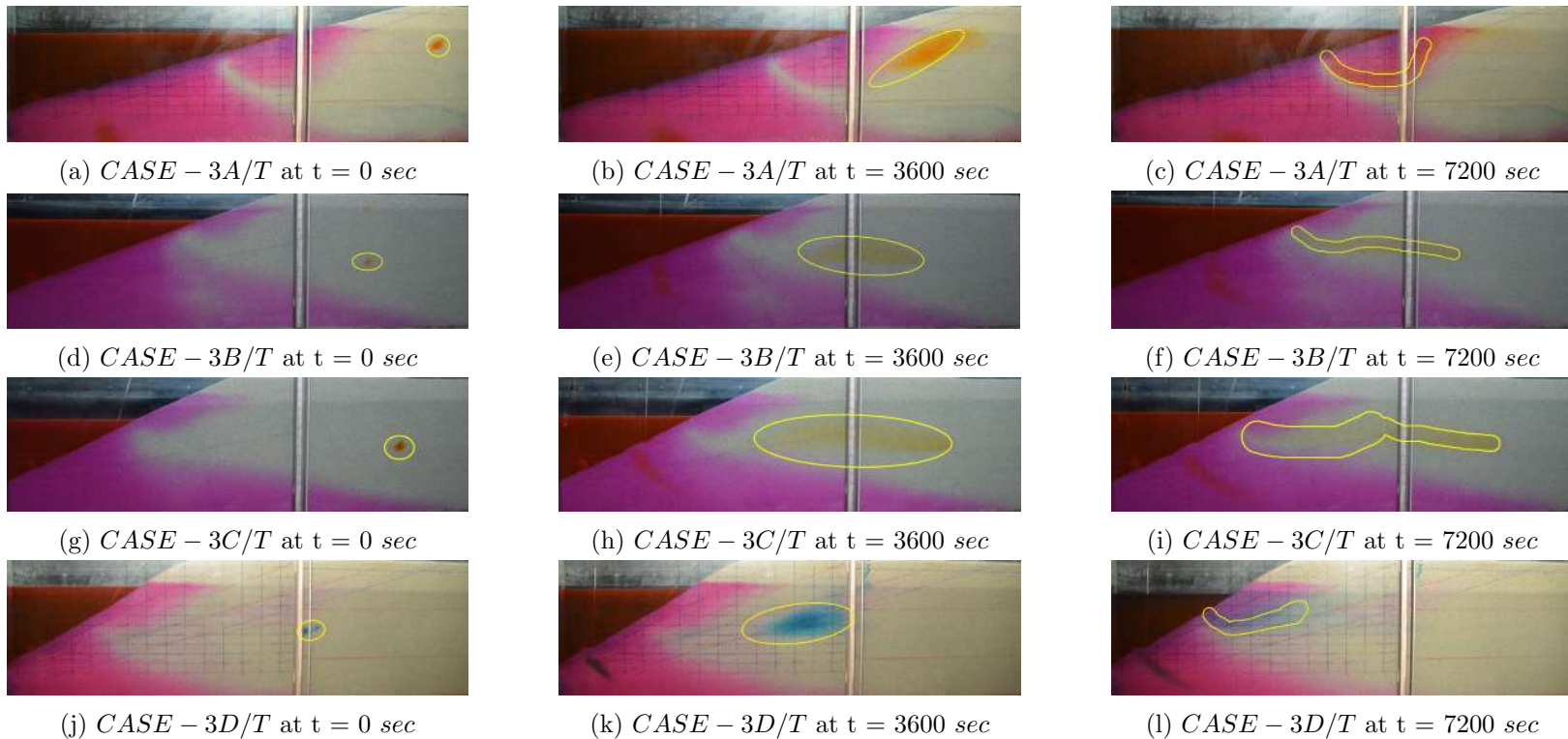


Figure 4.27: SGD Flow Pathways for Experiments with Single Layered Porous Media Under Tidal Saltwater Side Boundary Condition

### 4.3 Summary

The current Chapter included the physical experiments, numerical simulations, and image analysis for the single-layered (Grade-I IS Sand) sloping beach under static and tidal saltwater boundary conditions. A G-Channel-based image analysis technique was proposed for experimental images. A comprehensive analysis was performed to quantify the influence of sloping beaches on saltwater dynamics in porous media. The next Chapter presents quantification of the influence of beach slope on saltwater dynamics in stratified porous media.

# Chapter 5

## Influence of Beach Slope on Saltwater Movement in Multi-Layered Porous Media Under Static and Tidal Conditions

### 5.0 Overview

The previous Chapter covered the influence of beach slope on saltwater dynamics in single-layered porous media under static and tidal saltwater boundary conditions. Heterogenous formation alters the flow dynamics over various length scales (Simmons et al., 2001; Houben and Post, 2017). The multilayered structures are the most commonly encountered forms of subsurface heterogeneity. Process complexity increases due to intra and inter-layer mass transfer in multilayered porous media. Distinct flow patterns and saltwater-freshwater interfaces can be seen when compared to single-layered porous media. A better understanding of flow dynamics in multilayered porous media is required for controlling saltwater intrusion. Previous saltwater intrusion studies (Ketabchi et al., 2014; Liu et al., 2014; Dose et al., 2014; Mehdizadeh et al., 2014, 2017; Strack and Ausk, 2015) considered stratified representation to simulate subsurface heterogeneous conditions. Numerous experimental investigations (Abdoulhalik and Ahmed, 2017b; Strack and Ausk, 2015) showed that layered heterogeneity affects the saltwater-freshwater interface toe location. The steady-state saltwater-freshwater interface was mostly studied in the context of multiple permeable layers. Few studies considered the effects of low permeability layer on saltwater dynamics (Lu et al.,

2013; Abdoulhalik and Ahmed, 2017b, a). Dagan and Zeitoun (1998b, a) examined the effects of heterogeneity on the shape of the saltwater-freshwater interface in horizontally layered aquifers with randomly distributed hydraulic conductivity. It was observed that uncertainty in predicting toe location increases without including the stratification information. Held et al. (2005) observed similar results. Moreover, the geometry and position of the toe location are directly related to the degree of heterogeneity of the aquifer. However, saltwater dynamics in sloping beach stratified porous media (with the thin low permeability layer) were not studied with/without tidal conditions. The relative position and thickness of the stratified porous layers significantly affect the density-dependent flow. The current study focuses on the quantification of the impact of beach slope variation on saltwater-freshwater interface movement in

stratified porous media (both confined and unconfined configuration) under static and tidal saltwater side boundary conditions. Physical experiment, numerical analysis, image analysis, and analytical solution were utilized for quantitative and qualitative analysis.

## 5.1 Experimental Details

The laboratory experiments were carried out to understand the influence of beach slope on saltwater dynamics in multilayered porous media (3 layered configuration including low-permeability strata) under static and tidal saltwater side boundary conditions. Grade-I Indian Standard Sand (1-2 mm) was used as the aquifer material for both unconfined (Top) and confined (Bottom) layers. Bentonite was used as the aquitard material for the low permeable layer (middle). Three-layered porous media was placed in the *Zone B* of *Sand Box Model*. The thickness of the top, middle and bottom layers were 34 cm, 4 cm, 34 cm, respectively. Six pressure transducers (*PS1* in saltwater zone; *PS2*, *PS3*, *PS4*, *PS6* in confined zone; *PS5* in unconfined zone) were utilized for pressure measurements. Experiments were conducted with four different beach slopes under static and tidal saltwater side boundary conditions.

### 5.1.1 Experiments with Static Saltwater Side Boundary Condition

The experimental setup for static saltwater side boundary condition is shown in Figure 5.1. The experimental configurations are presented in Table 5.1. The laboratory experiments were performed as per the framework presented in *Section 3.1*. Saltwater salinity (35 PSU) was maintained in *Zone A* of the *Sand Box Model* after

initial period (Figures 5.2a, 5.2b, 5.2c, and 5.2d). The static experiments were continued until 12 h to 14 h (time required to achieve a quasi-steady condition).

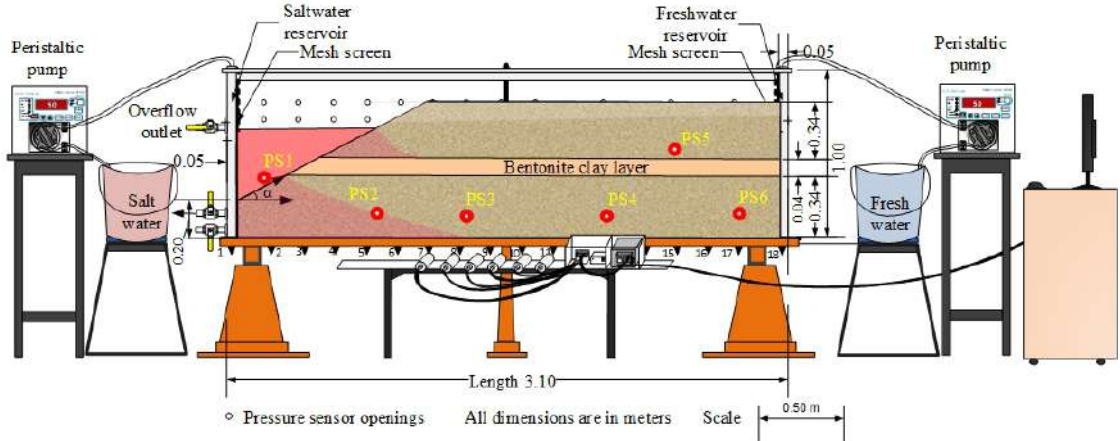


Figure 5.1: Schematic Representation Experimental Setup with Multilayered Porous Media Under Static Saltwater Side Boundary Condition

Table 5.1: Configurations for Experiments with Multilayered Porous Media Under Static Saltwater Side Boundary Condition

Cases	Beach Slope	Sand	Stratification	Tidal/Static	Remarks
Grade I IS Sand					
<i>CASE - 4A/S</i>	$15^0$	$(d_{50}=1.12 \text{ mm})$	Yes	Static	-
40 mm clay layer					
Grade I IS Sand					
<i>CASE - 4B/S</i>	$20^0$	$(d_{50}=1.12 \text{ mm})$	Yes	Static	-
40 mm clay layer					
Grade I IS Sand					
<i>CASE - 4C/S</i>	$25^0$	$(d_{50}=1.12 \text{ mm})$	Yes	Static	-
40 mm clay layer					
Grade I IS Sand					
<i>CASE - 4D/S</i>	$30^0$	$(d_{50}=1.12 \text{ mm})$	Yes	Static	-
40 mm clay layer					

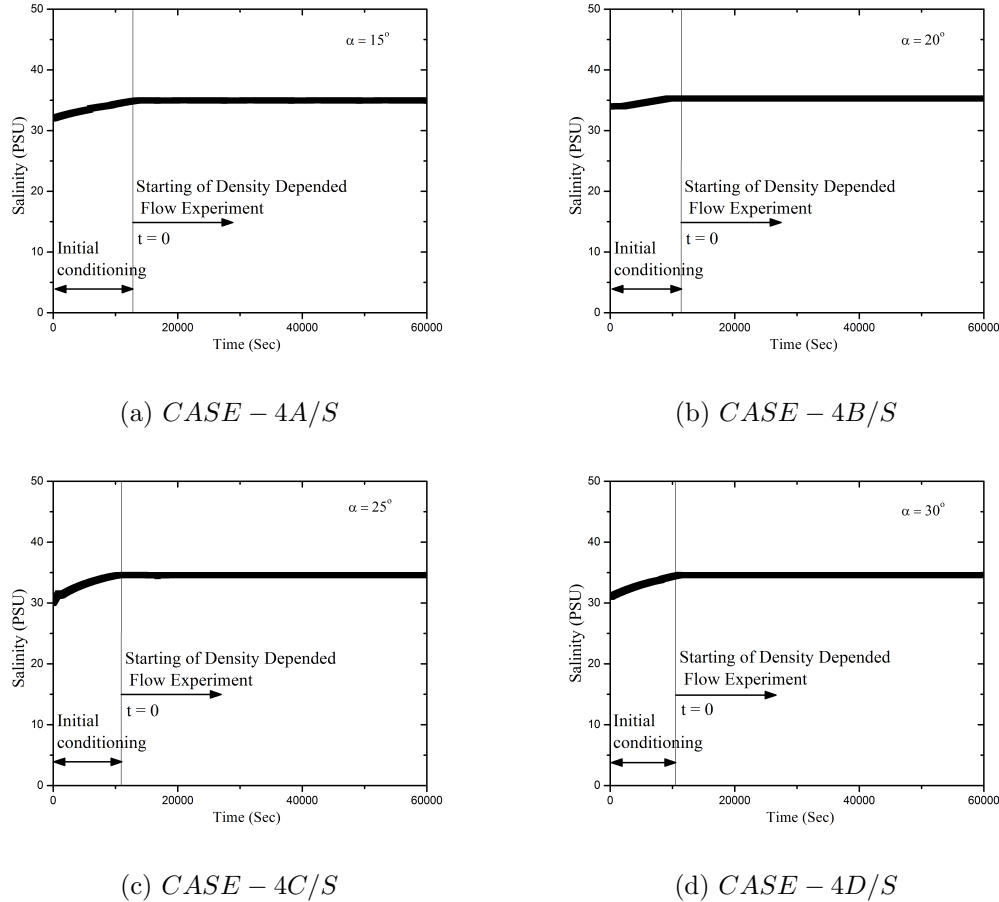


Figure 5.2: Observed Time Varying Salinity Profiles at Saltwater Reservoir (*Zone - A*)

### 5.1.2 Experiments with Tidal Saltwater Side Boundary Condition

The experimental setup for tidal saltwater side boundary condition is shown in Figure 5.3. The experimental configurations are presented in Table 5.2. The laboratory experiments were performed as per the framework presented in *Subsection 4.2.1*. Saltwater salinity (35 PSU) was maintained in *ZoneA* of the *Sand Box Model* after initial period (Figures 5.4a, 5.4b, 5.4c, and 5.4d). The tidal experiments were continued until 18 h to 20 h (time required to achieve a quasi-steady condition).

## 5.2 Numerical Modelling Method

FEFLOW (Diersch, 2013) based numerical simulation models were used to validate the experimental results (pressure head and concentration) at different time levels. Conceptualized as two-dimensional vertical cross-section was used simulations. The variably density flow and transport equations are provided in *Section 3.2*. Unstructured finite element mesh (as per Peclet number criterion) of

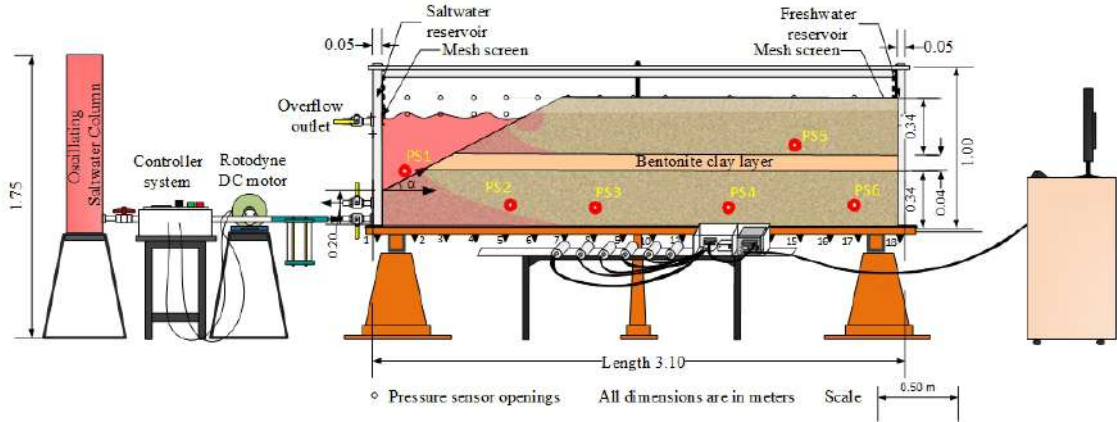


Figure 5.3: Schematic Representation Experimental Setup with Multilayered Porous Media Under Tidal Saltwater Side Boundary Condition

Table 5.2: Configurations for Experiments with Multilayered Porous Media Under Tidal Saltwater Side Boundary Condition

Cases	Beach Slope	Sand	Stratification	Tidal/Static	Remarks
Grade I IS Sand					
<i>CASE - 4A/T</i>	$15^0$	$(d_{50}=1.12 \text{ mm})$	Yes	Tidal	-
40 mm clay layer					
Grade I IS Sand					
<i>CASE - 4B/T</i>	$20^0$	$(d_{50}=1.12 \text{ mm})$	Yes	Tidal	-
40 mm clay layer					
Grade I IS Sand					
<i>CASE - 4C/T</i>	$25^0$	$(d_{50}=1.12 \text{ mm})$	Yes	Tidal	-
40mm clay layer					
Grade I IS Sand					
<i>CASE - 4D/T</i>	$30^0$	$(d_{50}=1.12 \text{ mm})$	Yes	Tidal	-
40mm clay layer					

different sizes were used to discretize the *Sand Box Model*. A Mesh convergence study was also performed.

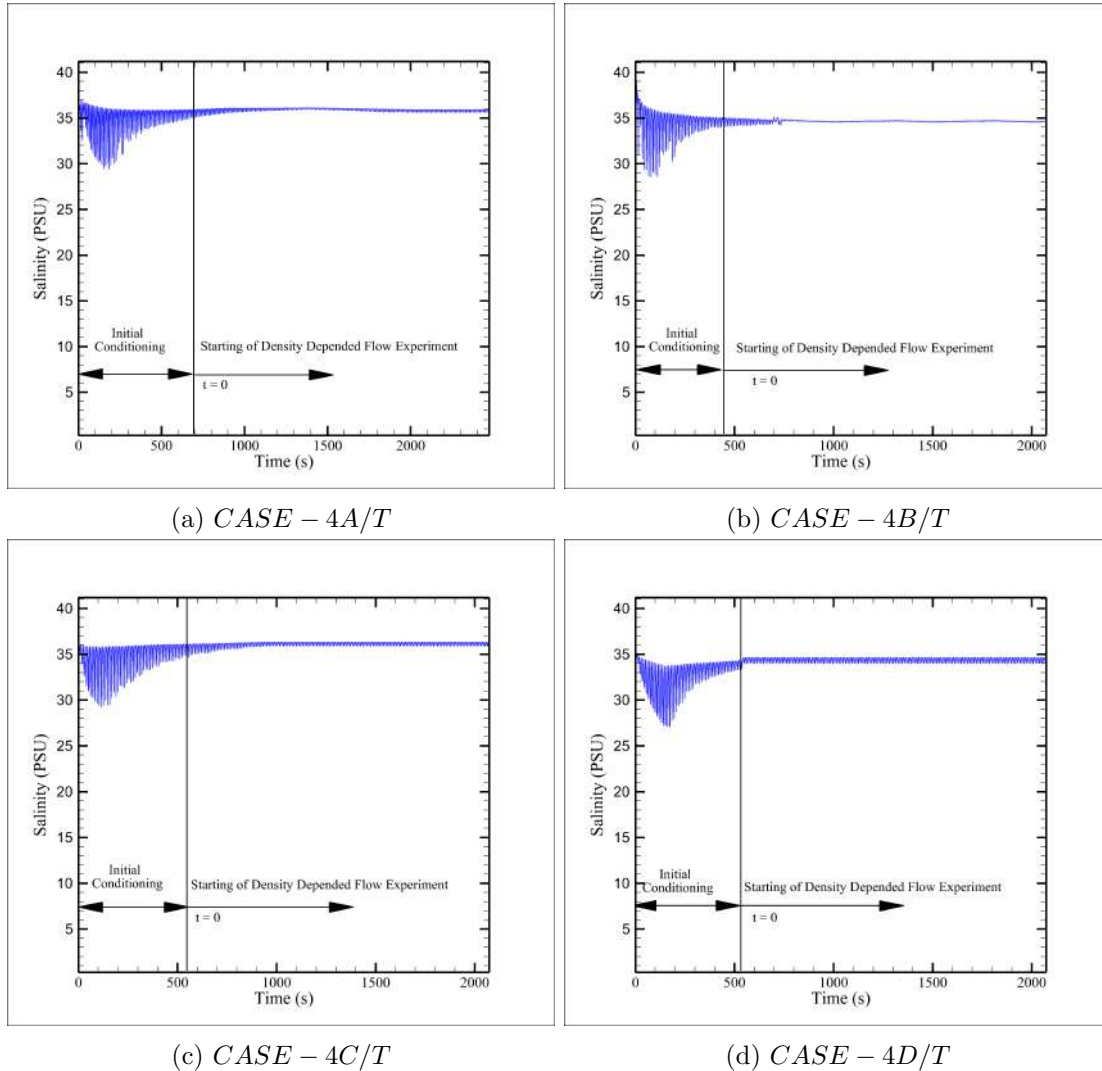


Figure 5.4: Observed Time Varying Salinity Profiles at Saltwater Reservoir (*Zone - A*)

### 5.2.1 Numerical Simulations with Static Saltwater Side Boundary Condition

The laboratory-based physical model equivalent numerical domains (*CASE - 4A/S*, *CASE - 4B/S*, *CASE - 4C/S* and *CASE - 4D/S*), and relevant boundary conditions are shown in Figure 5.5. Initial conditions were specified for head and concentration values from quasi-steady conditions without saltwater intrusion. Along the saltwater-side boundary ( $B_2 - F_2$ ), an equivalent static freshwater head condition was applied. Concentration boundary conditions were assigned from the starting point (after stabilization of salinity values) of the experiments. Initial free surface in porous media or water table ( $B_2 - I_2$ ) was identified from the quasi-steady-state run. Two types of boundary conditions were applied i) Dirichlet Boundary and ii) Neumann Boundary.

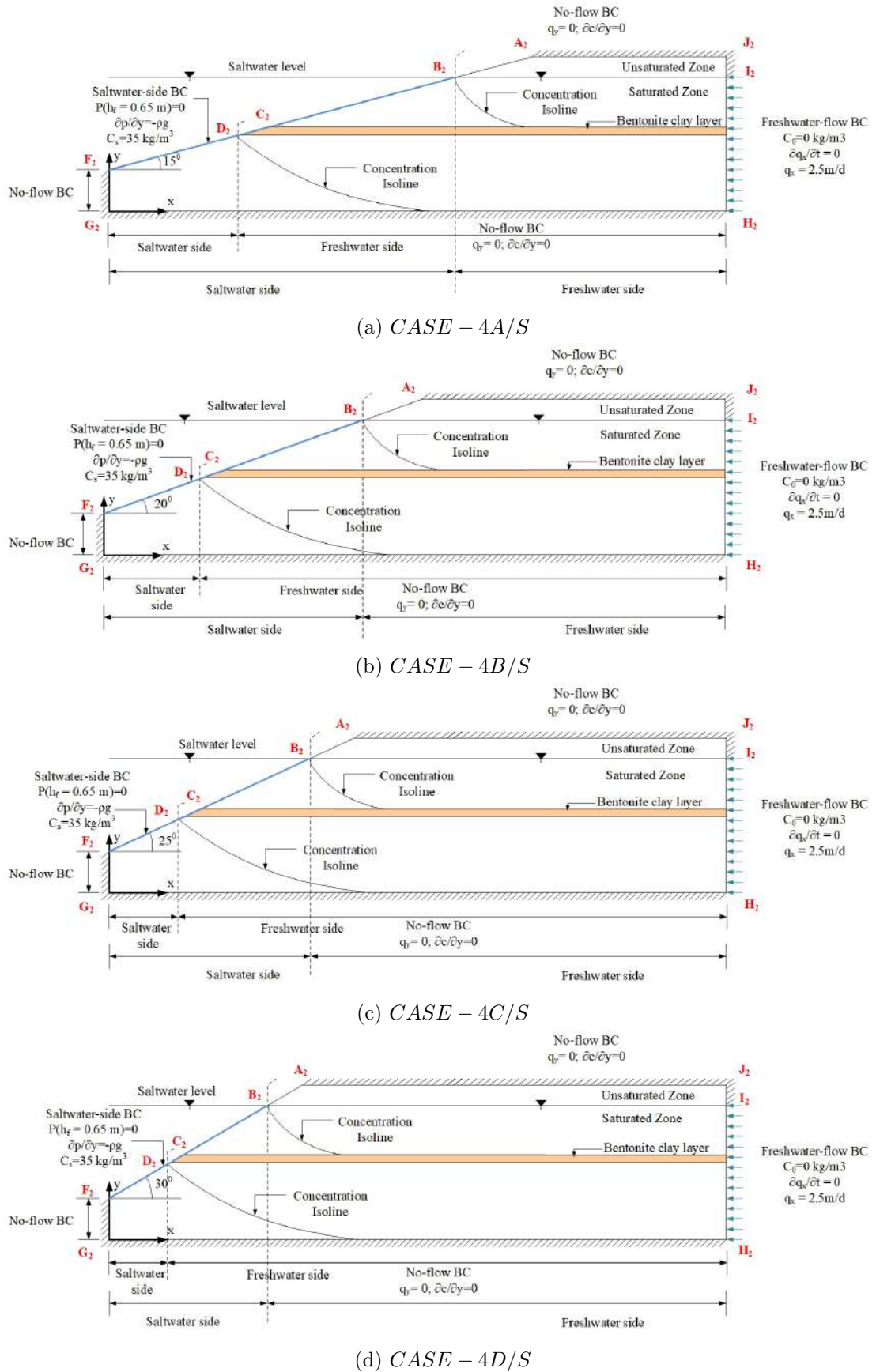


Figure 5.5: Boundary Conditions Used in Numerical Simulation for Experiments with Multilayered Porous Media Under Static Saltwater Side Condition

### 5.2.1.1 Dirichlet Boundary Condition

The saltwater head equivalent hydrostatic boundary condition was specified along the sloping boundary ( $B_2 - F_2$ ). Specified constant concentration (saltwater, 35000 mg/l) condition was applied along the sloping boundary. Individual nodes along the boundary were identified for specification of flow and concentration Dirichlet boundary conditions.

### 5.2.1.2 Neumann Boundary Condition

Freshwater flow from the right side ( $H_2 - I_2$ ) was specified as a Neumann flux type boundary condition. The peristaltic pump was used for creating the freshwater flux boundary condition. Top boundary ( $J_2 - A_2$ ), bottom boundary ( $G_2 - H_2$ ), vertical face in saltwater side boundary ( $F_2 - G_2$ ), and top vertical face in right side boundary ( $I_2 - J_2$ ) were specified with zero Neumann condition for flow and mass transport (concentration).

## 5.2.2 Numerical Simulations with Tidal Saltwater Side Boundary Condition

The laboratory based physical model equivalent numerical domains (*CASE – 4A/T*, *CASE – 4B/T*, *CASE – 4C/T* and *CASE – 4D/T*), and relevant boundary conditions are shown in Figure 5.6. Initial conditions were specified same as for *CASE – 4A/S*, *CASE – 4B/S*, *CASE – 4C/S* and *CASE – 4D/S*. Two types of boundary conditions were assigned i) Dirichlet Boundary and ii) Neumann Boundary.

### 5.2.2.1 Dirichlet Boundary Condition

Time-varying saltwater head equivalent boundary condition was specified along the sloping boundary ( $B_2 - F_2$ ). Individual nodes along the boundary were identified for specification of flow and concentration Dirichlet boundary conditions. Boundary conditions were assigned as per *Subsubsection 4.2.2.1* for saturated/unsaturated nodes identified during a particular tidal cycle.

### 5.2.2.2 Neumann Boundary Condition

The Neumann boundary conditions were specified as per *Subsubsection 5.2.1.2*.

Individual models under static and tidal saltwater boundary conditions were calibrated against the experimental results using the physical parameters as presented in Table 5.3.

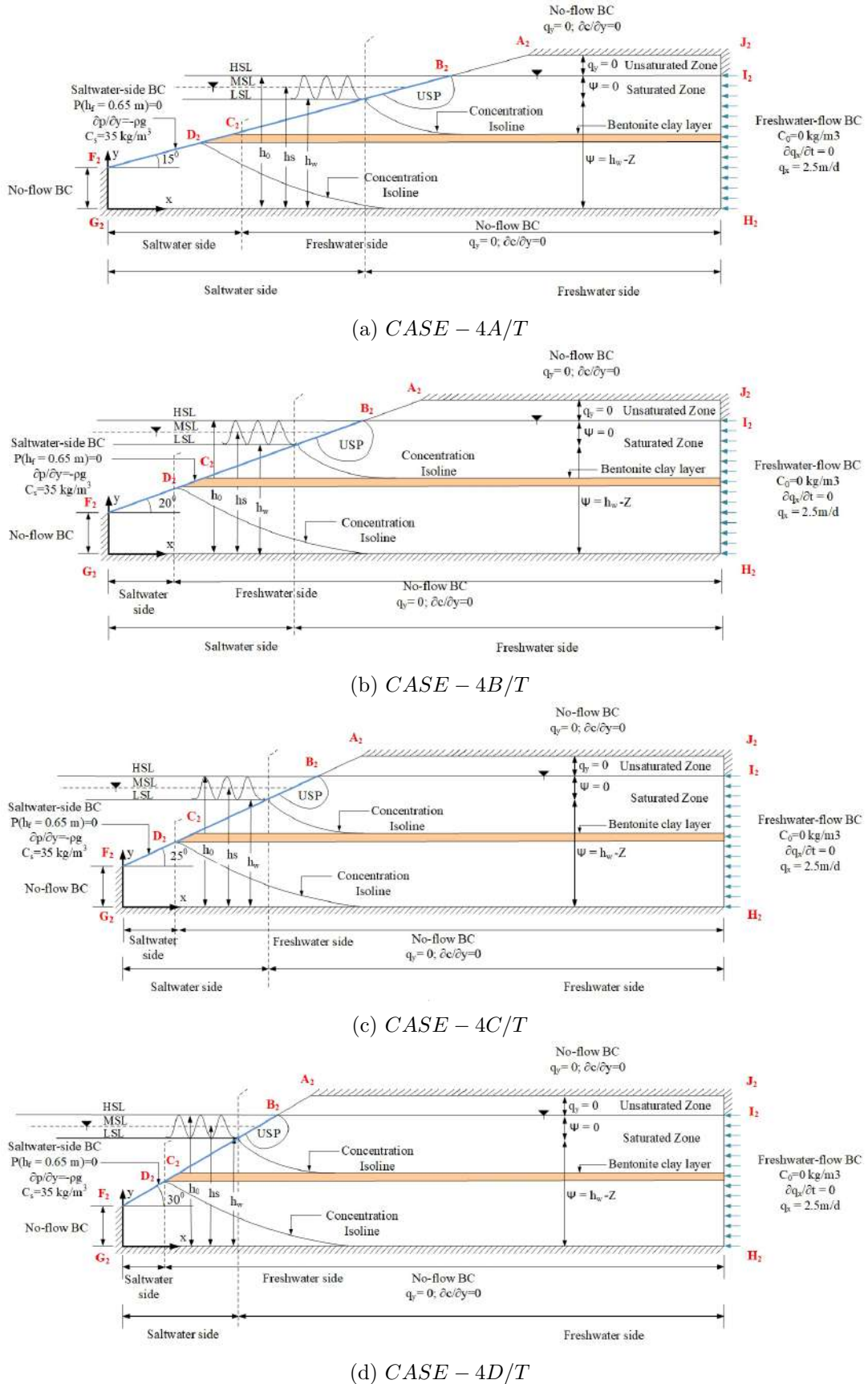


Figure 5.6: Boundary Conditions Used in Numerical Simulation for Experiments with Multilayered Porous Media Under Tidal Saltwater Side Condition

Table 5.3: Numerical Parameters Used for Experiments with Multilayered Porous Media Under Static and Tidal Saltwater Side Boundary Conditions

Parameters	Symbols	Value	Unit
Horizontal Length	L	3.1	m
Domain thickness	H	1.0	m
Porosity	$\epsilon$	0.385	-
Saltwater level	$h_f$	0.66	m
Freshwater density	$\rho_0$	1000	$kg/m^3$
Saltwater density	$\rho_s$	1025	$kg/m^3$
Saltwater concentration	$C_s$	35	$kg/m^3$
Longitudinal dispersivity	$\beta_L$	0.004	m
Transverse dispersivity	$\beta_T$	0.0004	m
Molecular diffusion coefficient	$D$	$10^{-9}$	$m^2/s$
Density Ratio	$\chi$	0.025	-
Hydraulic conductivity(IS Sand)	$K_s$	600	$m/d$
Hydraulic conductivity(Bentonite)	$K_B$	0.00004	$m/d$

### 5.3 G-Channel Based Image Analysis

Experimental images were analysed as per the *G-Channel Based Image Analysis* framework presented in Algorithm 1 (*Subsection 4.1.3*).

### 5.4 Results and Discussion

Saltwater-freshwater interface dynamics in multilayered porous media was studied experimentally and numerically for four different beach slopes ( $\alpha = 15^\circ, 20^\circ, 25^\circ, 30^\circ$ ) under static (*CASE – 4A/S, CASE – 4B/S, CASE – 4C/S, CASE – 4D/S*) and tidal (*CASE – 4A/T, CASE – 4B/T, CASE – 4C/T, CASE – 4D/T*) saltwater side boundary conditions. Physical experiments, numerical simulations, experimental image analysis, and analytical solutions were utilized for quantitative analysis. Time-varying saltwater intrusion patterns for static experiments, G-Channel based image analysis and numerical simulations (0.5-concentration isole) are shown in Figures 5.7, 5.8, 5.9, 5.10. Saltwater-freshwater interface and concentration distribution were analyzed corresponding to  $t = 600\text{ s}$ ,  $t = 2100\text{ s}$ ,  $t = 7320\text{ s}$ ,  $t = 25800\text{ s}$ . Reasonable match of the experiment, image analysis, and numerical simulation results were obtained for all the cases. Fingering effect was prominent in unconfined layer(*CASE – 4A/S*) for flatter slope ( $15^\circ$ ). However,

a reduction in the fingering effect was observed with the increase in beach slope. A minimal effect was observed in the confined layer. It was also observed that the scale effect dominates the fingering effect, e.g., a larger effect was present in the case of *CASE – 3A/S* when compared to *CASE – 4A/S*. Saltwater intrudes rapidly in an unconfined layer compared to a confined one. No specific trend was observed with respect to the size of the saltwater wedge, both in the case of unconfined and confined layers. This may be due to the scale effect, as some specific trends were observed in single-layered configurations. The time required to reach the quasi-steady condition was less in the case of a flatter slope (*CASE – 4A/S*). It increases with the increase in beach slope.

Time varying saltwater intrusion patterns for tidal condition are shown in Figures 5.11, 5.12, 5.13, 5.14. Prominent fingering effect was not visible for any case under tidal condition. Under tidal action both saltwater wedge and *Upper Saline Plume* were visible for unconfined layer. Only saltwater wedge was observed in confined layer. Submarine groundwater discharge (SGD) occurred through the intermediate zone between the saltwater wedge and USP. The zones are clearly visible in Figures 5.11, 5.12, 5.13, 5.14 for *CASE – 4A/T*, *CASE – 4B/T*, *CASE – 4C/T*, *CASE – 4D/T*, respectively. As observed in static cases (*CASE – 4A/S*, *CASE – 4B/S*, *CASE – 4C/S*, *CASE – 4D/S*) saltwater intrusion occurs rapidly in unconfined layer compared to confined layers. Saltwater wedge size increases for flatter slopes (*CASE – 4A/T*). Size of saltwater wedge was minimum in *CASE – 4D/T*. Comparative analysis showed that saltwater intrusion length (Toe length) decreases with increasing beach slope. Further, saltwater intrusion length decreases under tidal condition (*CASE – 4A/T*, *CASE – 4B/T*, *CASE – 4C/T*, *CASE – 4D/T*) compared to static condition (*CASE – 4A/S*, *CASE – 4B/S*, *CASE – 4C/S*, *CASE – 4D/S*). Overall time required to reach a quasi-steady condition was more in *CASE – 4A/T* compared to *CASE – 4A/S*. Similar trend was also observed for other slopes ( $20^\circ$ ,  $25^\circ$ ,  $30^\circ$ ). However, *CASE – 4D/T* was continued for maximum time among all the tidal cases to achieve a quasi-steady state condition.

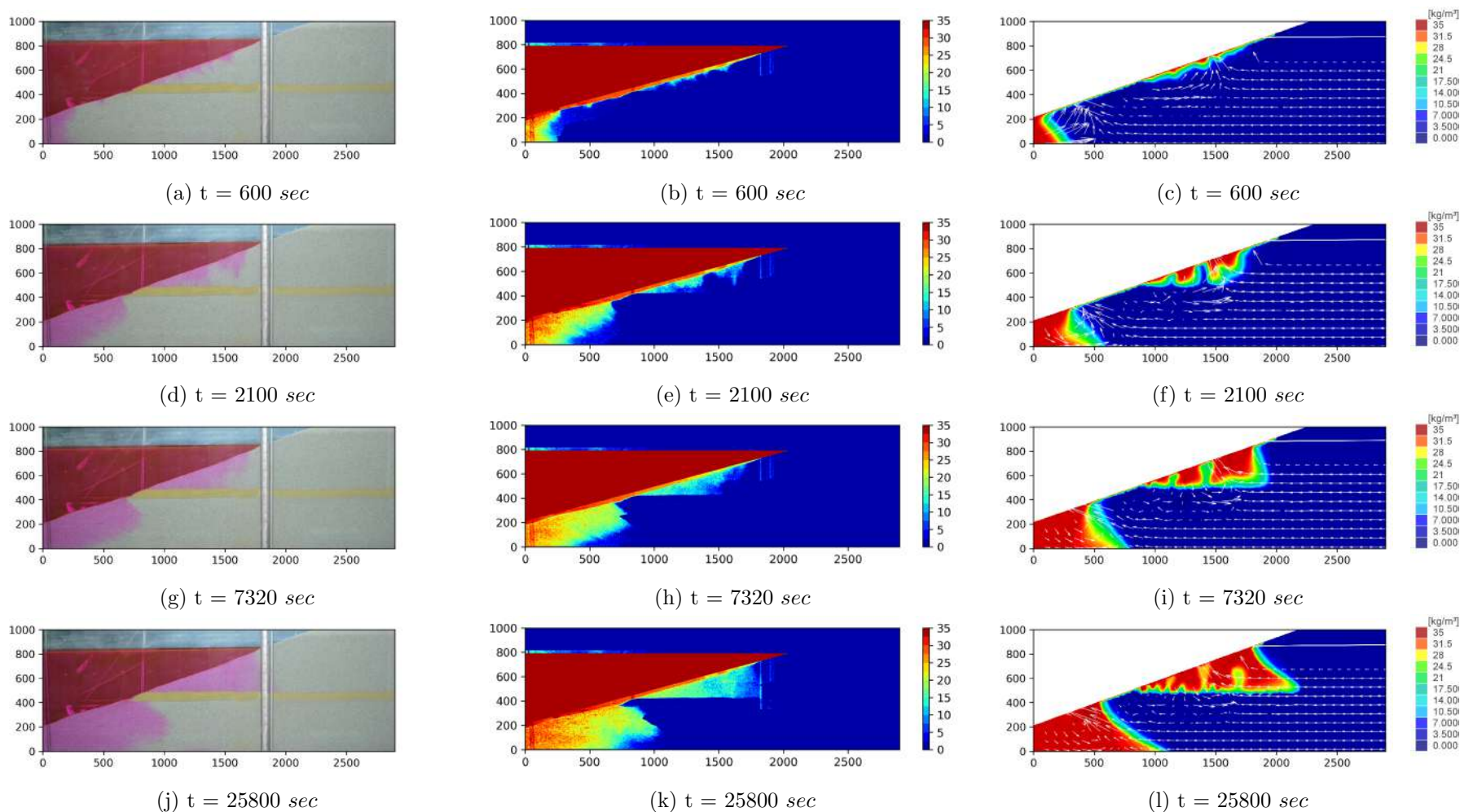


Figure 5.7: Development of Saltwater Wedge with Time in *CASE - 4A/S* [First Column: Experimental Images; Second Column: Output of G-Channel Based Image Analysis; Third Column: Numerical Simulation, The Color Maps Indicate Concentration]. All dimensions are in  $\text{mm}$ .

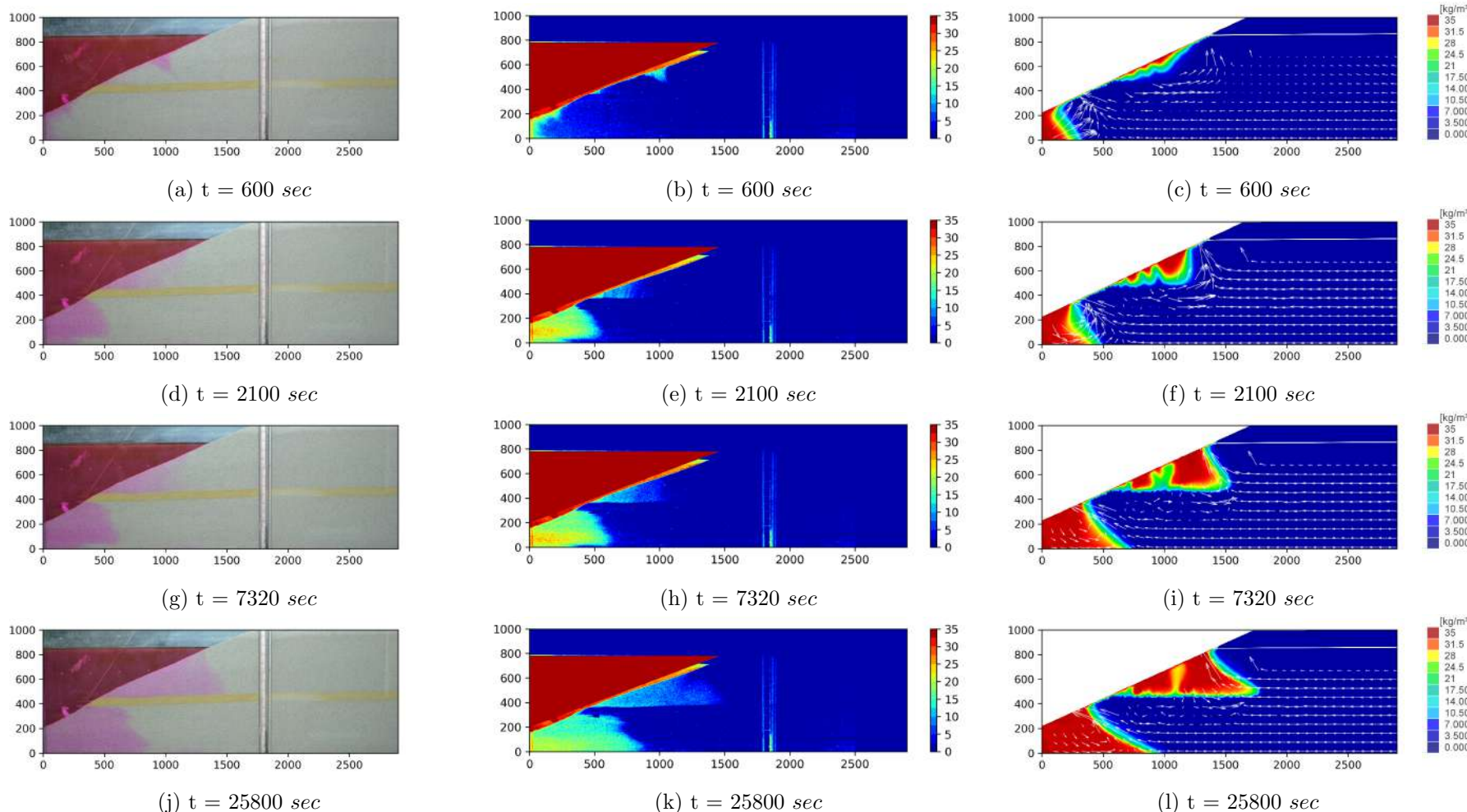


Figure 5.8: Development of Saltwater Wedge with Time in *CASE - 4B/S* [First Column: Experimental Images; Second Column: Output of G-Channel Based Image Analysis; Third Column: Numerical Simulation, The Color Maps Indicate Concentration]. All dimensions are in mm.

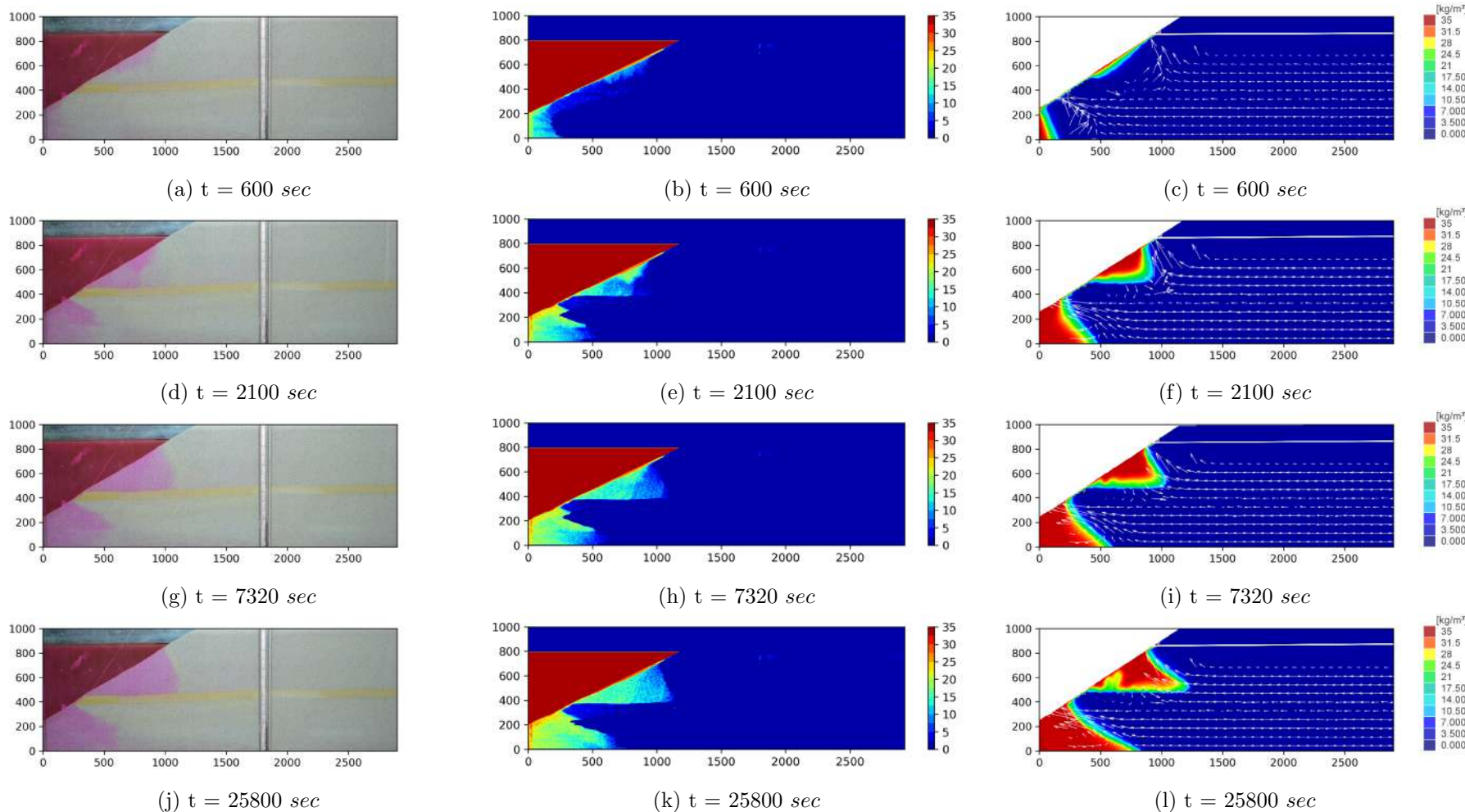


Figure 5.9: Development of Saltwater Wedge with Time in *CASE - 4C/S* [First Column: Experimental Images; Second Column: Output of G-Channel Based Image Analysis; Third Column: Numerical Simulation, The Color Maps Indicate Concentration]. All dimensions are in mm.

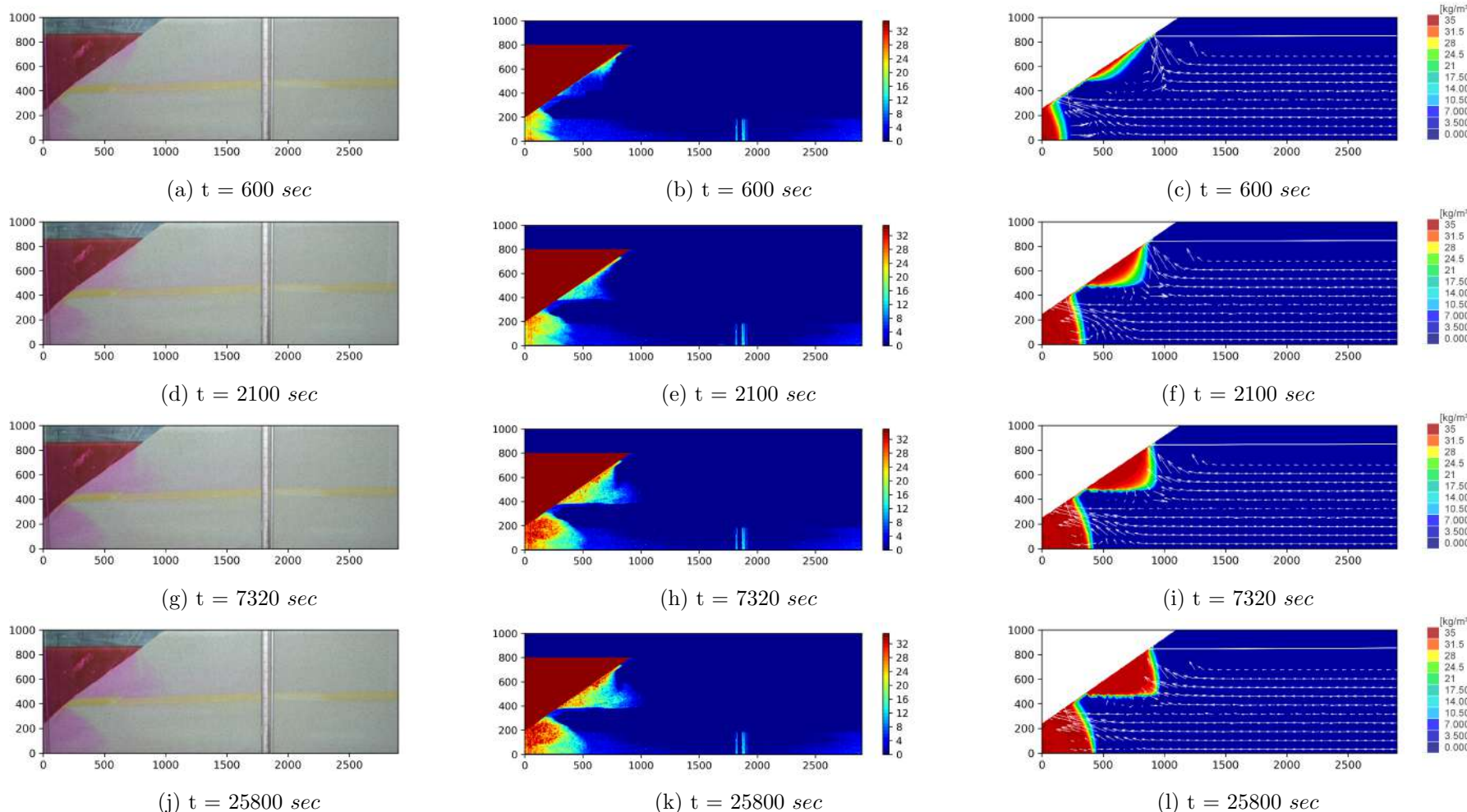


Figure 5.10: Development of Saltwater Wedge with Time in *CASE - 4D/S* [First Column: Experimental Images; Second Column: Output of G-Channel Based Image Analysis; Third Column: Numerical Simulation, The Color Maps Indicate Concentration]. All dimensions are in mm.

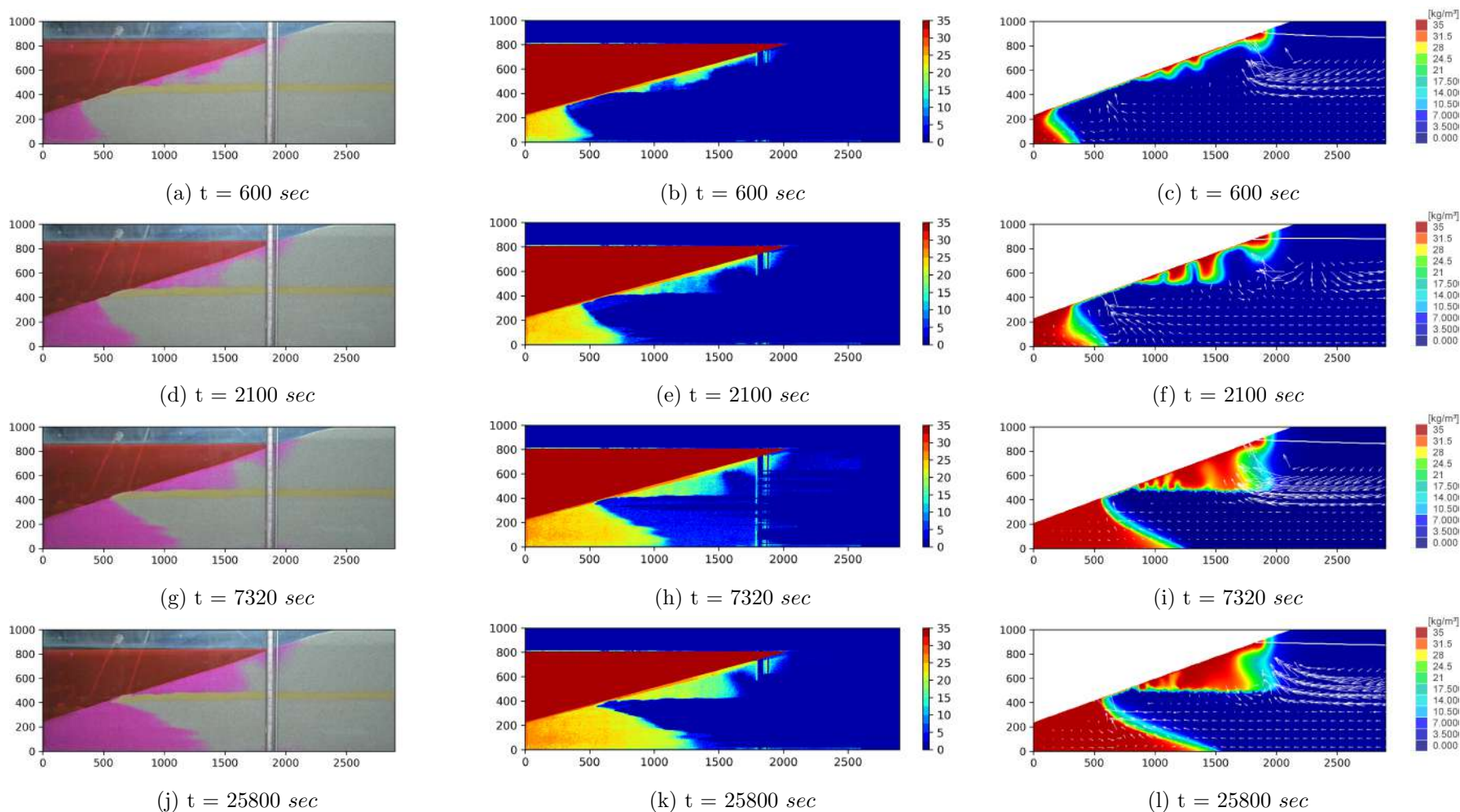


Figure 5.11: Development of Saltwater Wedge with Time in *CASE - 4A/T* [First Column: Experimental Images; Second Column: Output of G-Channel Based Image Analysis; Third Column: Numerical Simulation, The Color Maps Indicate Concentration]. All dimensions are in mm.

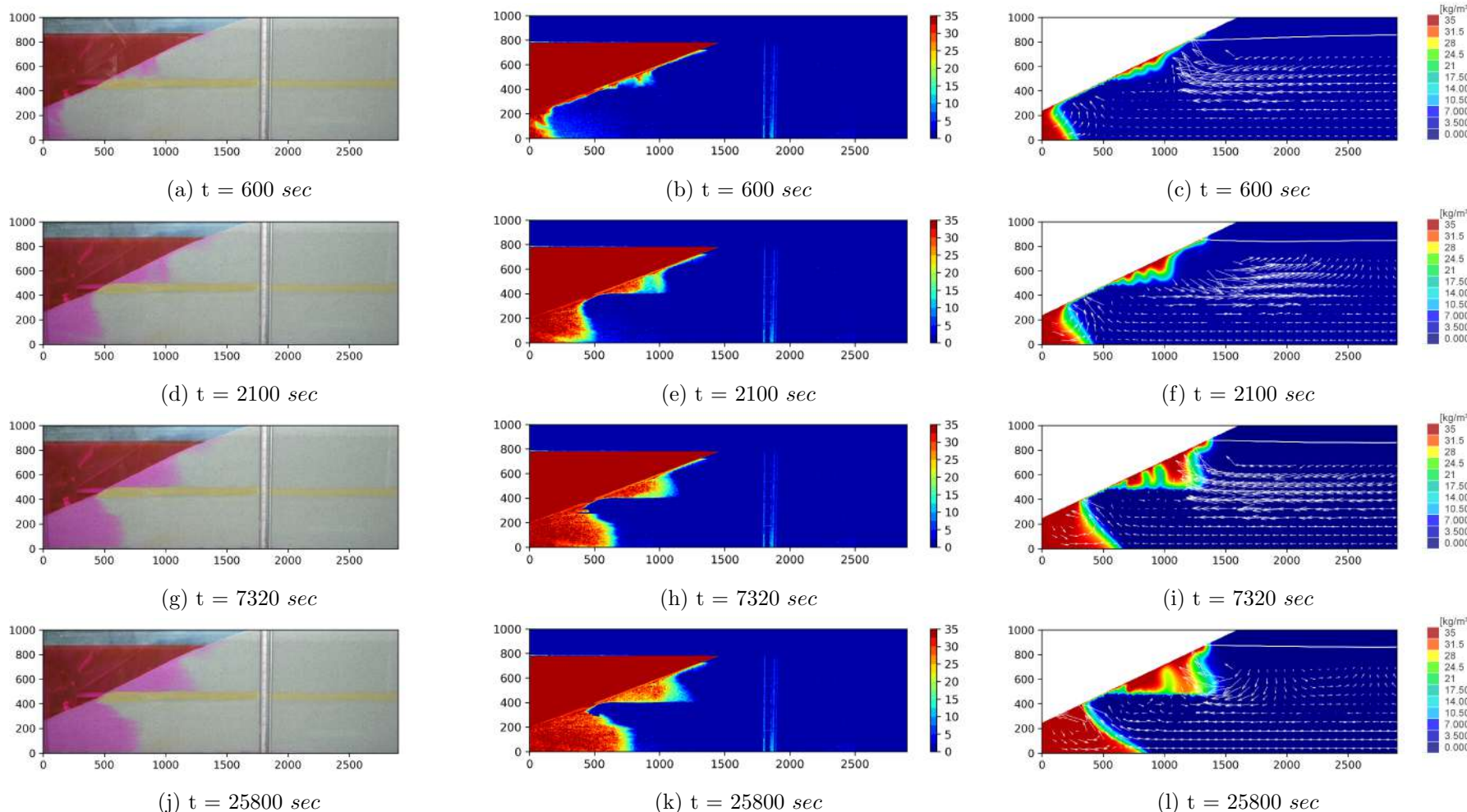


Figure 5.12: Development of Saltwater Wedge with Time in *CASE - 4B/T* [First Column: Experimental Images; Second Column: Output of G-Channel Based Image Analysis; Third Column: Numerical Simulation, The Color Maps Indicate Concentration]. All dimensions are in mm.

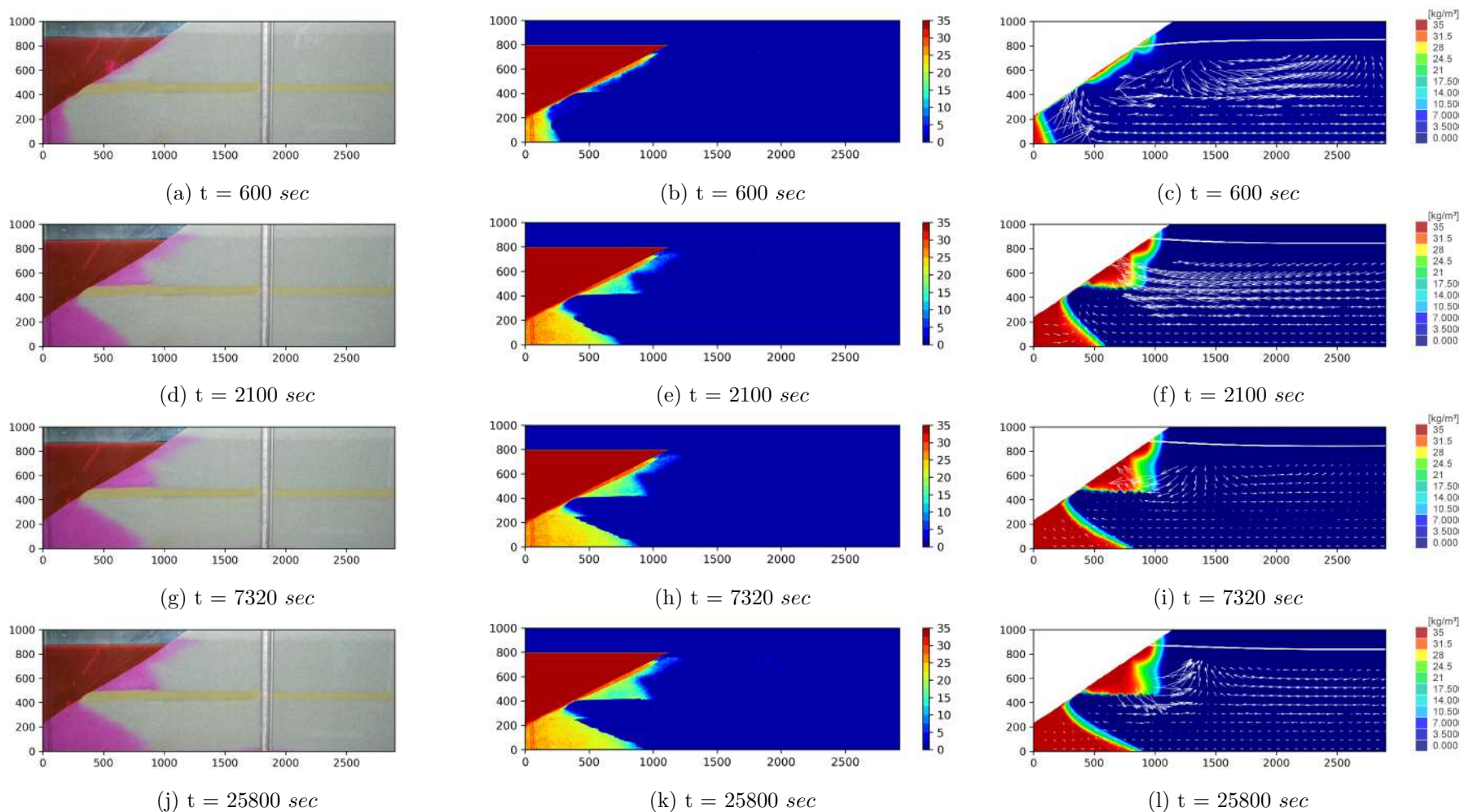


Figure 5.13: Development of Saltwater Wedge with Time in *CASE - 4C/T* [First Column: Experimental Images; Second Column: Output of G-Channel Based Image Analysis; Third Column: Numerical Simulation, The Color Maps Indicate Concentration]. All dimensions are in mm.

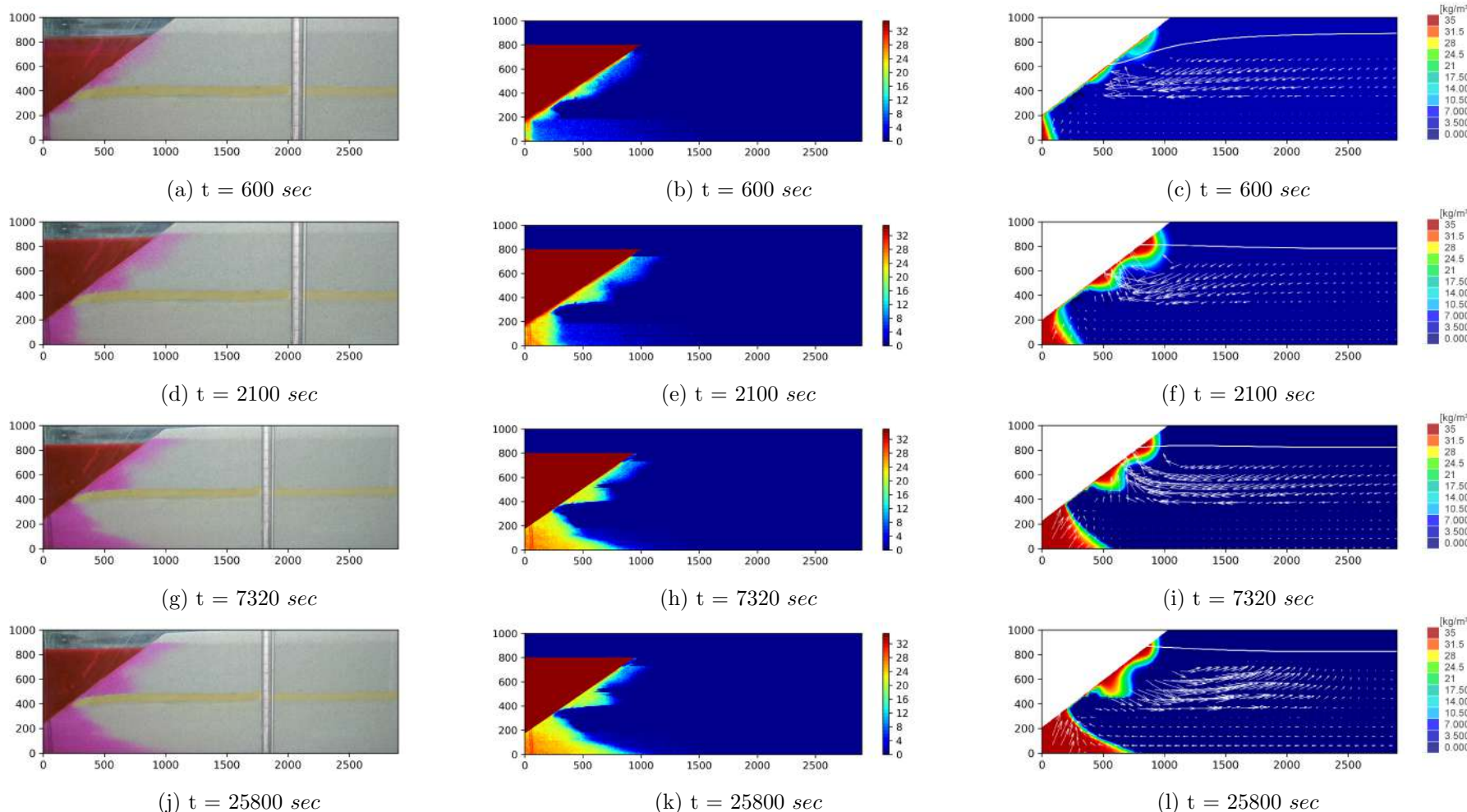


Figure 5.14: Development of Saltwater Wedge with Time in *CASE - 4D/T* [First Column: Experimental Images; Second Column: Output of G-Channel Based Image Analysis; Third Column: Numerical Simulation, The Color Maps Indicate Concentration]. All dimensions are in mm.

### 5.4.1 Pore Water Pressure Measurement

Numerical and experimental (Pore Water Pressure Measurement) hydraulic head values were plotted to check the consistency of the obtained results. Figure 5.15 shows the plots corresponding to *CASE-4A/S*, *CASE-4B/S*, *CASE-4C/S*, and *CASE-4D/S* with a 0.5 cm band on both sides. The outlier clusters corresponding to different pressure transducers are visible from the plots. Spatial location of pressure transducers (*PS1*, *PS2*, *PS3*, *PS4*, *PS5*, *PS6*) were fixed with respect to *Sand Box Model* for cases. In *CASE-4A/S* all the pressure transducers showed a good match except *PS4* (in the confined layer). This was due to the influence of submarine groundwater discharge (SGD). Similar effects were also observed in *PS4* and *PS3* for *CASE-4B/S* and *CASE-4D/S*, respectively. Deviation in *PS5* (unconfined layer) was due to the freshwater boundary effect in *CASE-4C/S*. This overestimation was due to the marginal rise of the water level near the right boundary.

Time varying experimental head values for *CASE-4A/T*, *CASE-4B/T*, *CASE-4C/T*, *CASE-4D/T* are shown in Figure 5.16. Numerical and experimental hydraulic head values were plotted in Figure 5.17 with 1 cm band on both sides. Submarine groundwater discharge (SGD) was observed for *PS4* in *CASE-4A/T*. Right side boundary effect was prominent in *PS6* (confined layer) for *CASE-4B/T*. Similar effect was also observed in *CASE-4C/T* and *CASE-4D/T* for *PS5* (unconfined layer).

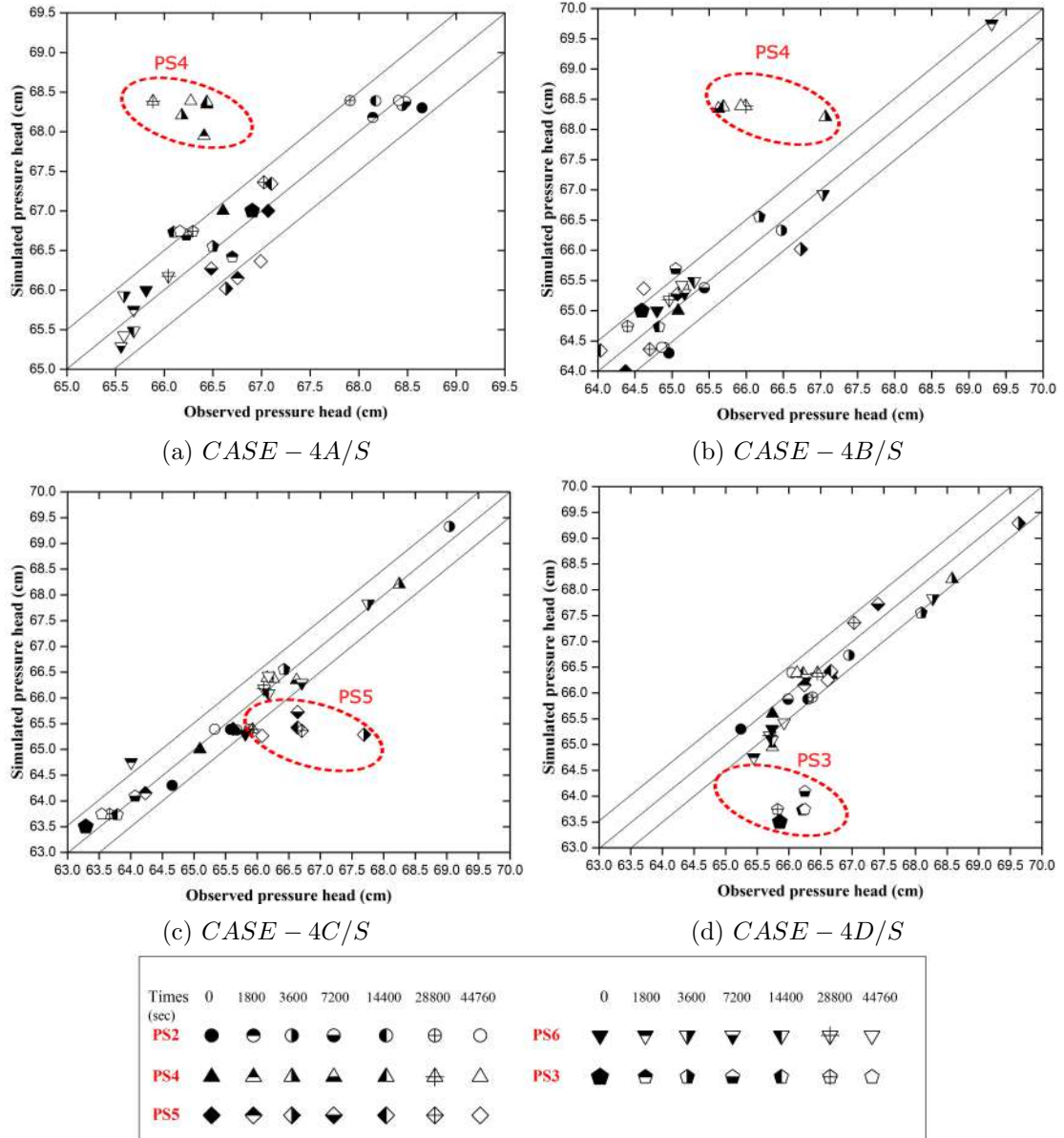


Figure 5.15: Comparison Between Time Varying Observed and Numerically Simulated Pressure Head Data

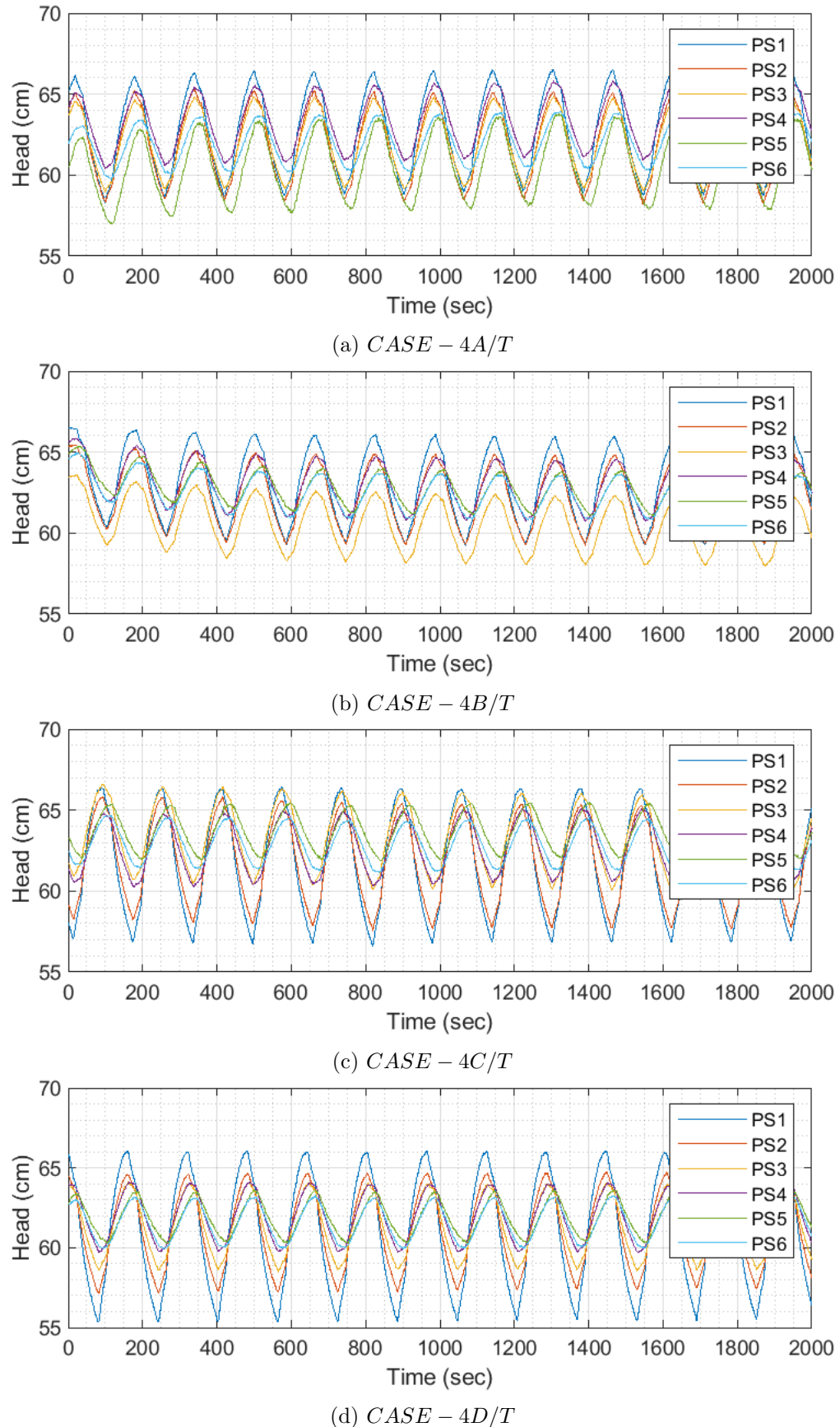


Figure 5.16: Observed Time Varying Pore-Water Pressure Head

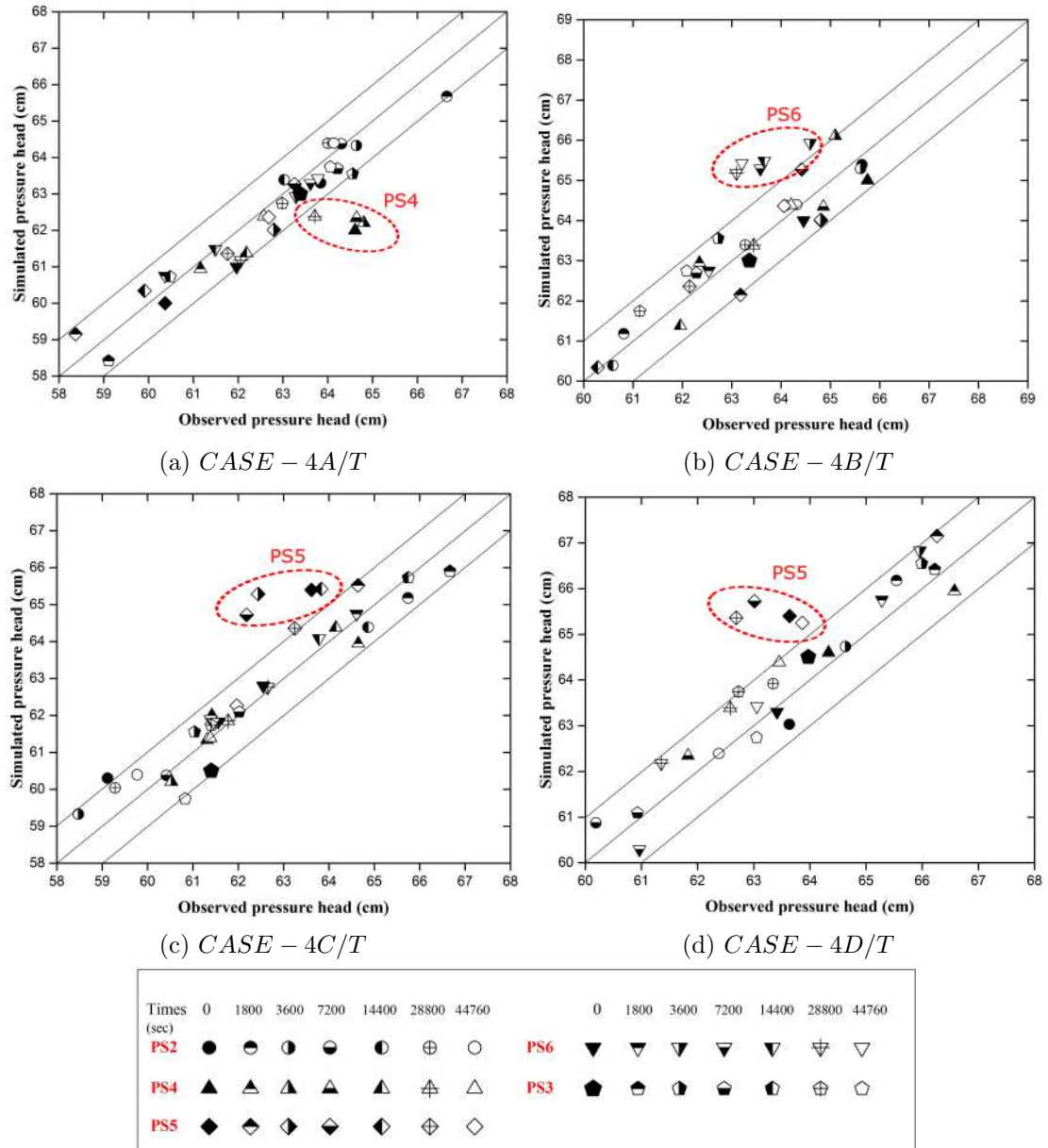


Figure 5.17: Comparison Between Time Varying Observed and Numerically Simulated Pressure Head Data

### 5.4.2 Comparison with Analytical Expression

Comparative analysis was performed with saltwater-freshwater interface corresponding to 50%-salinity line from FEFLOW and processed images (G-Channel Based Image Analysis). Saltwater-freshwater interface toe location ( $l_T$ ) and submarine groundwater discharge gap ( $\zeta_0$ ) were determined analytically (Equations 3.9 and 3.10), numerically and experimentally. The analytical (Van der Veer, 1977) values of  $l_T$  and  $\zeta_0$  for unconfined layer are 507 mm and 564 mm, respectively. The FEFLOW simulations underpredict the  $\zeta_0$  compared to the experimental value (Tables 5.4) under static saltwater side boundary condition (*CASE – 4A/S*, *CASE – 4B/S*, *CASE – 4C/S*, *CASE – 4D/S*). SGD gap ( $\zeta_0$ ) varies with beach slope for both unconfined and confined layers. Figure 5.18 shows saltwater-freshwater interface variations with beach slope under static saltwater side conditions.

The FEFLOW simulations under-predict the  $\zeta_0$  compared to the experimental value (Tables 5.5) for *CASE – 4A/T*, *CASE – 4B/T*, *CASE – 4C/T*, *CASE – 4D/T*. Overall increase in  $\zeta_0$  value was observed in tidal case (e.g., *CASE – 4A/T*) when compared to static one (e.g., *CASE – 4A/S*) with same beach slope. Figure 5.19 shows saltwater-freshwater interface variations with beach slope under tidal saltwater side condition.

Table 5.4: Submarine Groundwater Discharge (SGD) Gap and Saltwater-Freshwater Interface Toe Length for Experiments with Multilayered Porous Media Under Static Saltwater Side Boundary Condition

Case	Slope	layer	Sand	$\zeta_o$ (mm)	$\ell_T$ (mm)	$\zeta_o$ (mm)	$\ell_T$ (mm)	$\zeta_o$ -FEFLOW /
				Expt	Expt	FEFLOW	FEFLOW	$\zeta_o$ -Expt
CASE - 4A/S	$15^0$	Upper	Grade I IS Sand ( $d_{50}=1.12$ mm)	119.73	188.29	95.24	192.39	0.795
		Lower	4 cm Low Permeable Layer	68.02	1194.34	25.51	1015.15	0.375
CASE - 4B/S	$20^0$	Upper	Grade I IS Sand ( $d_{50}=1.12$ mm)	112.43	222.85	85.98	248.45	0.764
		Lower	4 cm thick Low Permeable Layer	72.75	560.94	40.62	457.83	0.558
CASE - 4C/S	$25^0$	Upper	Grade I IS Sand ( $d_{50}=1.12$ mm)	149.28	203.65	84.09	218.58	0.563
		Lower	4 cm thick Low Permeable Layer	57.63	425.83	51.96	370.37	0.901
CASE - 4D/S	$30^0$	Upper	Grade I IS sand ( $d_{50}=1.12$ mm)	76.53	298.94	69.91	323.11	0.913
		Lower	4 cm thick Low Permeable Layer	107.71	405.93	74.64	317.04	0.692

Avg= 0.69

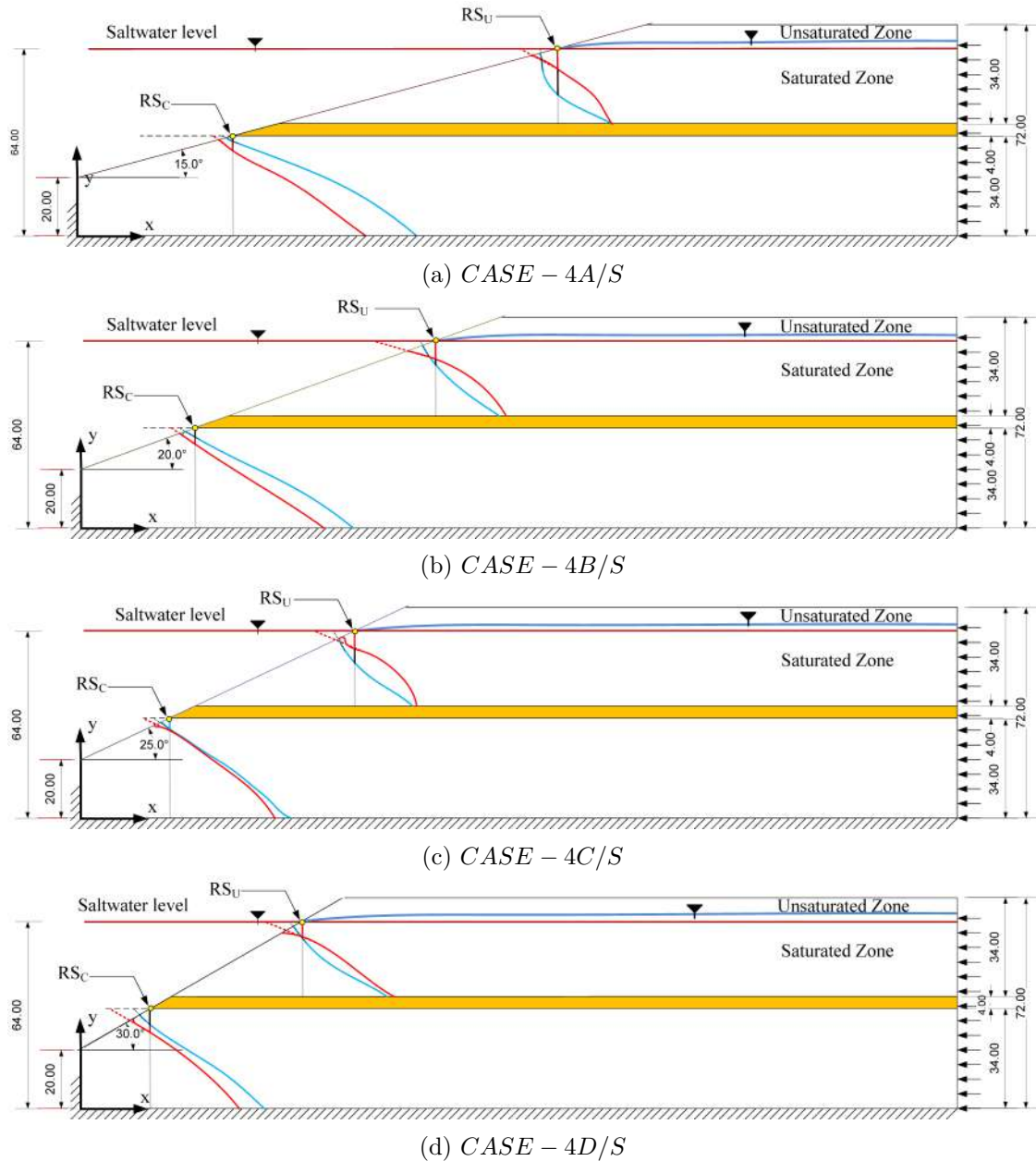


Figure 5.18: Saltwater-freshwater Interface for Experiments with Multilayered Porous Media Under Static Saltwater Side Boundary Condition (Red Line: FEFLOW Simulation Results; Blue Line: Experimental Results Obtained from G-Channel Based Image Analysis)

Table 5.5: Submarine Groundwater Discharge (SGD) Gap and Saltwater-Freshwater Interface Toe Length for Experiments with Multilayered Porous Media Under Tidal Saltwater Side Boundary Condition

Case	Slope	Layer	Sand	$\zeta_o$ (mm)	$\ell_T$ (mm)	$\zeta_o$ (mm)	$\ell_T$ (mm)	$\zeta_{o-FEFLOW}/\zeta_{o-Expt}$
				Expt	Expt	FEFLOW	FEFLOW	
<i>CASE - 4A/T</i>	$15^0$	Upper	Grade I IS Sand ( $d_{50}=1.12$ mm)	292	1798	97	1829	0.33
		Lower	4 cm thick Low Permeable Layer	45	1698	30	1695	0.66
<i>CASE - 4B/T</i>	$20^0$	Upper	Grade I IS Sand ( $d_{50}=1.12$ mm)	272	1342	163	1373	0.59
		Lower	4 cm thick Low Permeable Layer	104	972	94	969	0.90
<i>CASE - 4C/T</i>	$25^0$	Upper	Grade I IS Sand ( $d_{50}=1.12$ mm)	281	1063	201	1085	0.71
		Lower	4 cm thick Low Permeable Layer	139	841	96	839	0.69
<i>CASE - 4D/T</i>	$30^0$	Upper	Grade I IS Sand ( $d_{50}=1.12$ mm)	328	825	166	858	0.50
		Lower	4 cm thick Low Permeable Layer	125	630	122	484	0.97

Avg= 0.66

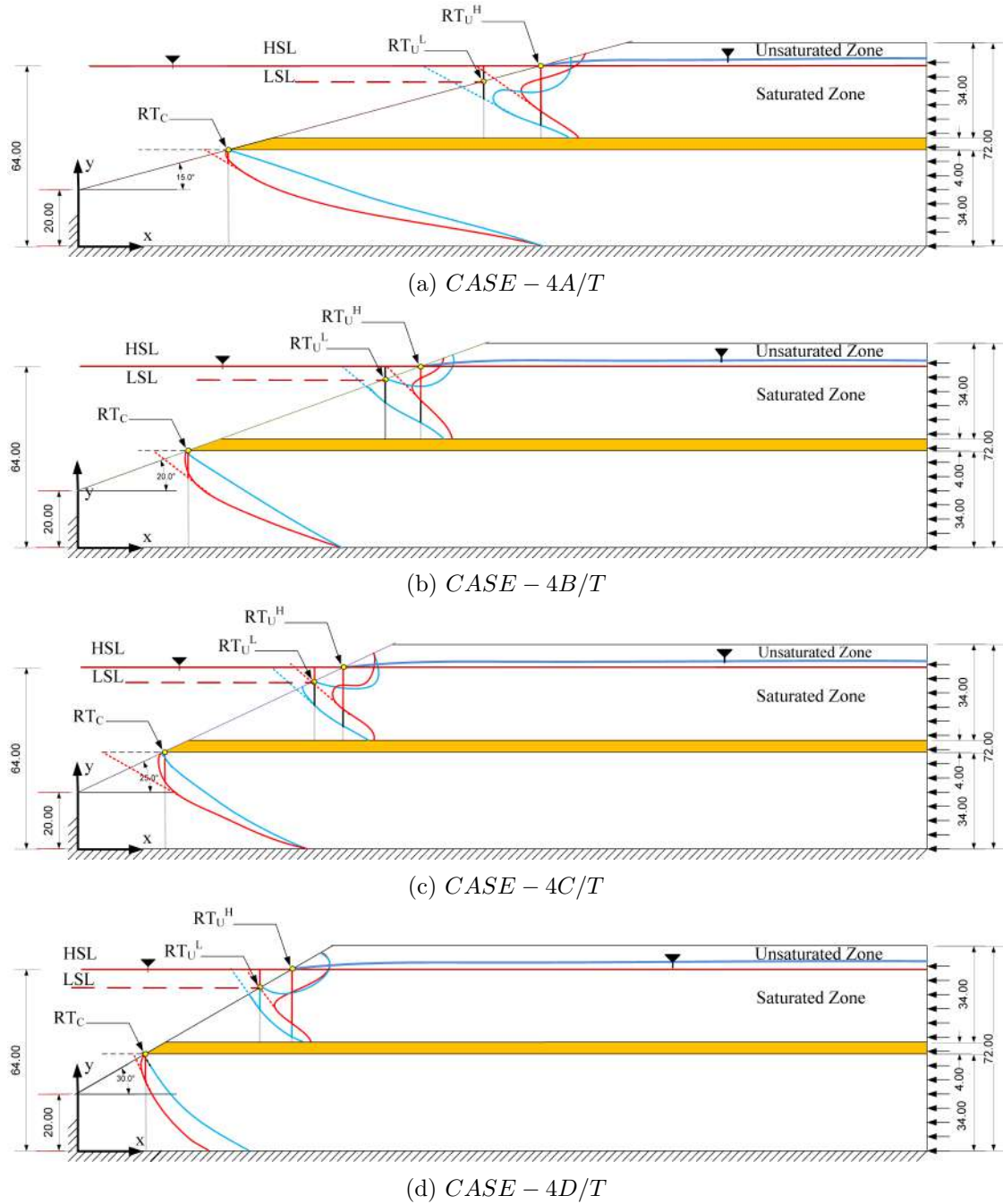


Figure 5.19: Saltwater-freshwater Interface for Experiments with Multilayered Porous Media Under Static Saltwater Side Boundary Condition (Red Line: FE-FLOW Simulation Results; Blue Line: Experimental Results Obtained from G-Channel Based Image Analysis)

### 5.4.3 Freshwater Flow Patterns

SGD flow pathways were identified by using the tracer injection technique. *Rhodamine B* was utilized as the saltwater tracer. *Methyl Orange* was utilized as the external tracer for both static and tidal conditions. The external tracer was injected at different locations through a tube-like setup under density neutral condi-

tions to minimize the externally generated buoyancy effect. The tracer experiments were started after attaining the quasi-steady state condition and continued till the tracer reached the saltwater surface. Time-varying images of the tracer experiments under static and tidal conditions are shown in Figure 5.20 and Figure 5.21, respectively. It is evident that SGD particles move along the saltwater-freshwater interface zone and rise upward to the intersection point in the unconfined layer for static cases. SGD Particles get discharged to the saltwater region through the intermediate zone of the saltwater wedge and USP for tidal cases.

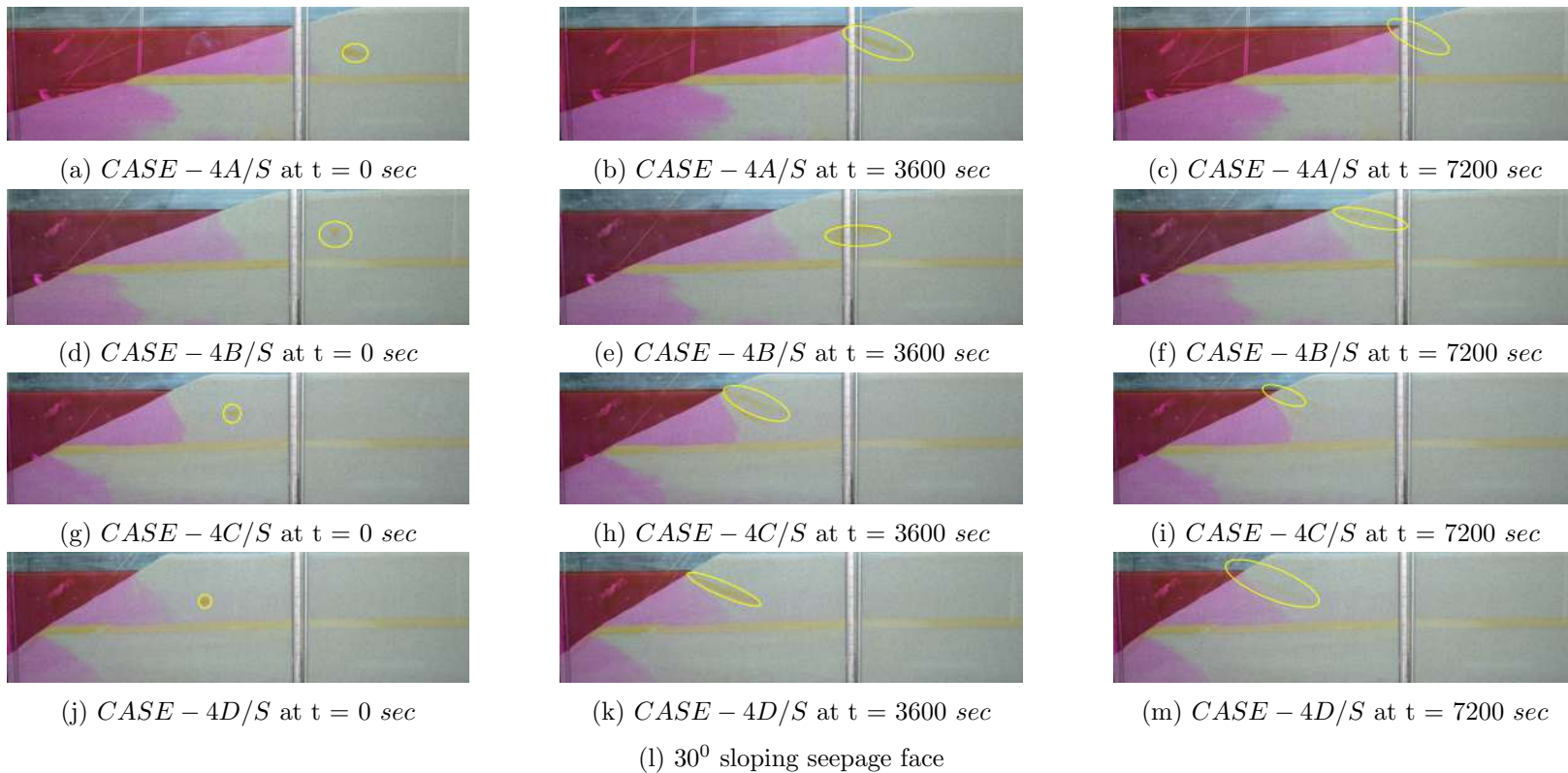


Figure 5.20: SGD Flow Pathways for Experiments with Multilayered Porous Media Under Static Saltwater Side Boundary Condition

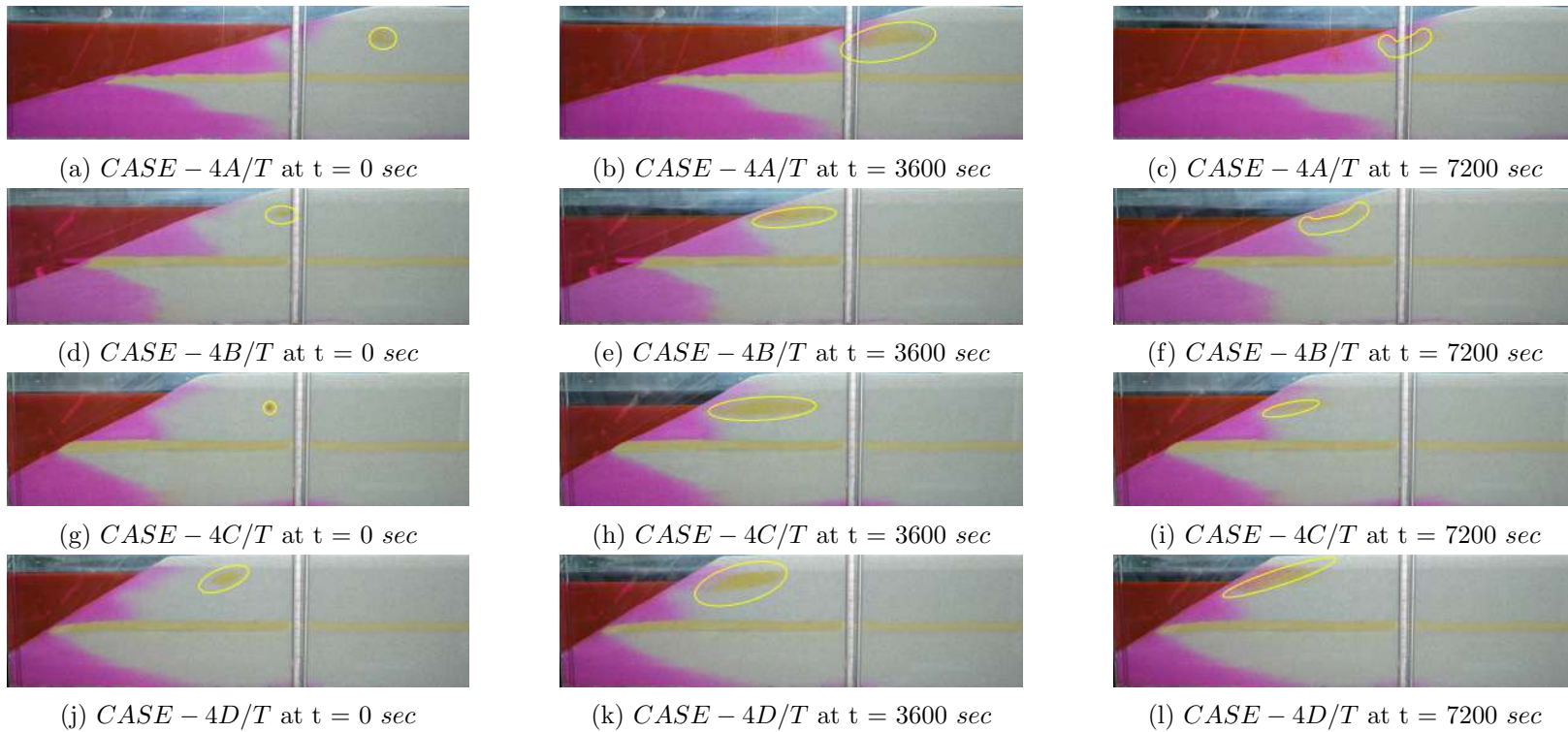


Figure 5.21: SGD Flow Pathways for Experiments with Multilayered Porous Media Under Tidal Saltwater Side Boundary Condition

## 5.5 Summary

The current Chapter included the physical experiments, numerical simulations, and image analysis for the multi-layered (Grade-I IS Sand) sloping beach under static and tidal saltwater boundary conditions. A comprehensive analysis was performed to quantify the influence of sloping beaches on saltwater dynamics in multi-layered porous media. The next Chapter presents a Dimensional Analysis of the single and multi-layered experiments under static and tidal saltwater side boundary conditions.

# Chapter 6

## Dimensional Analysis of Saltwater Intrusion Experiments

### 6.0 Overview

Dimensional analysis (DA) is a widely used technique to extract the inter-relationship of geometric, kinematic, and dynamic variables. DA identifies the non-dimensional parameter groups representing dependencies present in the system. These non-dimensional groups can be mathematically used to represent the approximate empirical relationship between the independent variable and dependent variables. The current chapter presents a detailed DA study to analyze the toe length and SGD gap. It also presents saltwater-fresh water interface stability analysis.

### 6.1 Buckingham $\Pi$ -Theorem

The Buckingham  $\Pi$ -theorem (Buckingham, 1914) was used to identify the non-dimensional parameter groups, given a functional relationship. It is based on the principle of dimensional homogeneity and requires incorporation of mechanistically relevant variables. Variables can be related as

$$\phi(\psi_1, \psi_2, \psi_3, \dots, \psi_n) = 0 \quad (6.1)$$

where  $n$  is the total number of variables. If  $m$  is the number of basic dimensions (Mass: M; Length: L; Time: T, usually 3), the Buckingham  $\Pi$ -theorem demands that  $n - m$  dimensionless groups of variables,  $\Pi$ -terms, can be related as

$$\varphi(\Pi_1, \Pi_2, \Pi_3, \dots, \Pi_{n-m}) = 0 \quad (6.2)$$

Individual  $\Pi$ -terms can be determined as

$$\begin{aligned}\Pi_1 &= (\psi_{r_1})^{\alpha_1^1} (\psi_{r_2})^{\alpha_2^1} \cdots (\psi_{r_m})^{\alpha_m^1} \psi_{e_1} \\ \Pi_2 &= (\psi_{r_1})^{\alpha_1^2} (\psi_{r_2})^{\alpha_2^2} \cdots (\psi_{r_m})^{\alpha_m^2} \psi_{e_2} \\ &\vdots = \vdots \\ \Pi_{n-m} &= (\psi_{r_1})^{\alpha_1^{n-m}} (\psi_{r_2})^{\alpha_2^{n-m}} \cdots (\psi_{r_m})^{\alpha_m^{n-m}} \psi_{e_{n-m}}\end{aligned}$$

where  $\psi_{e_1}, \psi_{e_2}, \dots, \psi_{e_{n-m}}$  are non-repeating variables (or dependent variables),  $\psi_{r_1}, \psi_{r_2}, \dots, \psi_{r_m}$  are repeating variables and  $\alpha_i^j$  represents integer exponent of  $i^{th}$  repeating variable for  $j^{th}$   $\Pi$  term.

The  $\Pi$  term containing the variable under consideration can be expressed in terms of other  $\Pi$  terms as

$$\Pi_k = C_k \prod_{i=1, i \neq k}^{n-m} \Pi_i^{\varsigma_i} \quad (6.3)$$

where index  $k$  corresponds to the term containing the variable under consideration,  $C_k$  is a real valued constant and  $\varsigma_i$  represents real valued exponent of  $i^{th}$   $\Pi$  term.  $C_k$  and  $\varsigma_i$  values can be estimated from regression analysis.

## 6.2 Single Layered Under Static Saltwater Boundary Condition

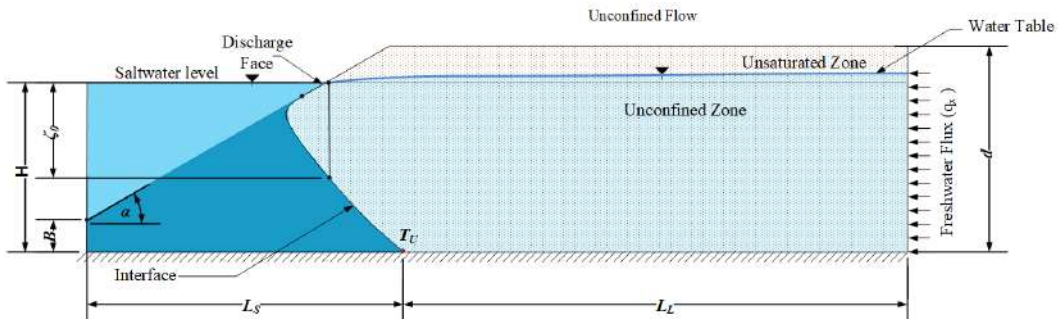


Figure 6.1: Single Layered Unconfined Aquifer Under Static Saltwater Side Boundary Condition

The saltwater-freshwater interface toe location ( $L_s$ ) and submarine groundwater discharge (SGD) gap ( $\zeta_0$ ) for a single-layered aquifer under static saltwater boundary condition depends on different physical parameters. The physical rela-

Table 6.1: Dimensional and Non-Dimensional Variables Used In Dimensional Analysis of Single Layered System Under Static Saltwater Side Boundary Condition

Variables	Symbols	Dimensions
Toe length of the saltwater interface	$L_S$	L
horizontal distance between-the coastline and the inland boundaries	$L_L$	L
Height of the model domain	H	L
Vertical saltwater depth	B	L
Vertical depth of the porous medium	d	L
Beach slope	$\alpha$	dimensionless
Specific discharge	$q_x$	$L^2 T^{-1}$
Porosity	$\epsilon$	dimensionless
Freshwater density	$\rho_0$	$M^1 L^{-3}$
Seawater density	$\rho_s$	$M^1 L^{-3}$
Longitudinal dispersivities	$\beta_L$	L
Transverse dispersivities	$\beta_T$	L
Density ratio	$\chi$	dimensionless
Hydraulic conductivity	$K$	$LT^{-1}$
Molecular diffusion coefficent	$D^*$	$L^2 T^{-1}$
Submarine groundwater discharge Gap	$\zeta_0$	L

tionship of  $L_S$  and other parameters was expressed as

$$L_S = \phi_1 (L_L, H, B, K, q_x, \rho_0, \rho_s, \beta_L, \beta_T, D^*, d, \zeta_0, \alpha, \epsilon, \chi) \quad (6.4)$$

where the parameters are defined in Table 6.1. Similarly, physical relationship of  $\zeta_0$  and other parameters was expressed as

$$\zeta_0 = \phi_2 (L_S, L_L, H, B, K, q_x, \rho_0, \rho_s, \beta_L, \beta_T, D^*, d, \alpha, \epsilon, \chi) \quad (6.5)$$

Same set of  $\Pi$  terms ( $n - m = 13$ ) were identified from Buckingham  $\Pi$ -Theorem for both Equation (6.4) and Equation (6.5) as the parameter set (total number of variables,  $n = 16$ ) was same. Total three fundamental dimensions are present ( $m = 3$ ). Thus,  $\Pi$  terms were expressed as

$$\varphi (\Pi_1, \Pi_2, \Pi_3, \Pi_4, \dots, \Pi_{13}) = 0 \quad (6.6)$$

where

$$\begin{aligned}
 \Pi_1 &= \frac{L_S}{d} \\
 \Pi_2 &= \frac{L_L}{d} \\
 \Pi_3 &= \frac{\rho_s}{\rho_0} \\
 \Pi_4 &= \frac{\beta_L}{d} \\
 \Pi_5 &= \frac{\beta_T}{d} \\
 \Pi_6 &= \frac{K_s d}{q_x} \\
 \Pi_7 &= \frac{D^*}{q_x} \\
 \Pi_8 &= \frac{\zeta_0}{d} \\
 \Pi_9 &= \alpha \\
 \Pi_{10} &= \epsilon \\
 \Pi_{11} &= \chi \\
 \Pi_{12} &= \frac{H}{d} \\
 \Pi_{13} &= \frac{B}{d}
 \end{aligned}$$

Toe location ( $L_S$ ) and submarine groundwater discharge (SGD) gap ( $\zeta_0$ ) was expressed as

$$\frac{L_S}{d} = C_1 \prod_{i=1, i \neq 1}^{n-m} \Pi_i^{\zeta_i} \quad (6.7)$$

and

$$\frac{\zeta_0}{d} = C_8 \prod_{i=1, i \neq 8}^{n-m} \Pi_i^{\zeta_i} \quad (6.8)$$

Both numerical simulation and experimental results were utilized to obtain the functional Equations (6.7) and (6.8). Variations in  $\Pi_1$ ,  $\Pi_2$ ,  $\Pi_4$ ,  $\Pi_8$  and  $\Pi_9$  were considered (Table 6.2 and Table 6.4).

Numerical  $L_S$  value can be explicitly calculated as

$$L_S = 10^{35.164} \left( \frac{L_L}{d} \right)^{-61.6} \left( \frac{\zeta_0}{d} \right)^{1.973} (\alpha)^{42.83} d \quad (6.9)$$

Similarly, experimental  $L_{SExp}$  value can be calculated as

$$L_{SExp} = 2.418 \left( \frac{L_L}{d} \right)^{-0.480} \left( \frac{\zeta_0}{d} \right)^{-0.063} (\alpha)^{-0.188} d \quad (6.10)$$

It is evident that the average ratio of Experimental to Numerical Toe Length is 0.79 (Table 6.2). Ratios are showing incensing trend with an increase in slope.

Table 6.2: Numerical Toe Length Calculation for Single Layered System Under Static Saltwater Side Boundary Condition

CASES	$\frac{L_L}{d}$	$\frac{\zeta_0}{d}$	$\alpha$	$L_S$	$L_S$	$L_{SExp}$	$\frac{L_{SExp}}{L_S}$
	[-]	[-]	[rad]	[m]	[mm]	[mm]	[-]
CASE - 3A/S	1.400	0.397	0.261	2.732	2732	2083	0.76
CASE - 3B/S	1.710	0.379	0.349	2.421	2421	1814	0.74
CASE - 3C/S	1.985	0.293	0.436	2.146	2146	1690	0.78
CASE - 3D/S	2.265	0.250	0.523	1.866	1866	1608	0.86

Avg= 0.79

Table 6.3: Experimental Toe Length Calculation for Single Layered System Under Static Saltwater Side Boundary Condition

CASES	$\frac{L_L}{d}$	$\frac{\zeta_0}{d}$	$\alpha$	$L_{SExp}$	$L_{SExp}$
	[-]	[-]	[rad]	[m]	[mm]
CASE - 3A/S	1.354	0.602	0.261	2.083	2083
CASE - 3B/S	1.713	0.384	0.349	1.814	1814
CASE - 3C/S	1.905	0.326	0.436	1.690	1690
CASE - 3D/S	1.988	0.250	0.523	1.608	1608

Numerical  $\zeta_0$  and experimental  $\zeta_{0Exp}$  can be calculated as

$$\zeta_0 = 10^{-17.82} \left( \frac{L_S}{d} \right)^{0.506} \left( \frac{L_L}{d} \right)^{31.22} (\alpha)^{-21.70} d \quad (6.11)$$

and

$$\zeta_{0Exp} = 10^{6.02} \left( \frac{L_S}{d} \right)^{-15.7} \left( \frac{L_L}{d} \right)^{-7.54} (\alpha)^{2.95} d. \quad (6.12)$$

It is evident that the average ratio of Experimental to Numerical SGD Gap is 0.95 (Table 6.4). Ratios are showing incensing trend with an increase in slope.

Table 6.4: Numerical SGD Gap Calculation for Single Layered System Under Static Saltwater Side Boundary Condition

CASES	$\frac{L_S}{d}$	$\frac{L_L}{d}$	$\alpha$	$\zeta_0$	$\zeta_0$	$\zeta_{0Exp}$	$\frac{\zeta_0}{\zeta_{0Exp}}$
	[-]	[-]	[rad]	[m]	[mm]	[mm]	[-]
CASE - 3A/S	2.732	1.400	0.261	0.397	397	602	0.66
CASE - 3B/S	2.421	1.710	0.349	0.378	378	384	0.98
CASE - 3C/S	2.146	1.985	0.436	0.293	293	326	0.89
CASE - 3D/S	1.866	2.265	0.523	0.321	321	250	1.28

Avg= 0.95

Table 6.5: Experimental SGD Gap Calculation for Single Layered System Under Static Saltwater Side Boundary Condition

CASES	$\frac{L_S}{d}$	$\frac{L_L}{d}$	$\alpha$	$\zeta_{0Exp}$	$\zeta_{0Exp}$
	[-]	[-]	[rad]	[m]	[mm]
CASE - 3A/S	2.777	1.354	0.261	0.602	602
CASE - 3B/S	2.418	1.713	0.349	0.384	384
CASE - 3C/S	2.226	1.905	0.436	0.326	326
CASE - 3D/S	2.144	1.988	0.523	0.250	250

### 6.3 Layered Porous Media Under Static Saltwater Boundary Condition

In layered porous media configuration, confined and unconfined layer specific parameters ( $d_u$ ,  $d_c$ ,  $K_s$ ,  $K_B$ ) were considered. A summary of the dimensionless ratios for layered configuration are presented in Table 6.6.

The saltwater-freshwater interface toe location and submarine groundwater discharge (SGD) gap were individually determined for both unconfined and confined layers under static saltwater boundary conditions. The  $\Pi$  terms obtained in the single-layered case are applicable for both confined and unconfined layers. However, variations were considered only for three  $\Pi$  terms.

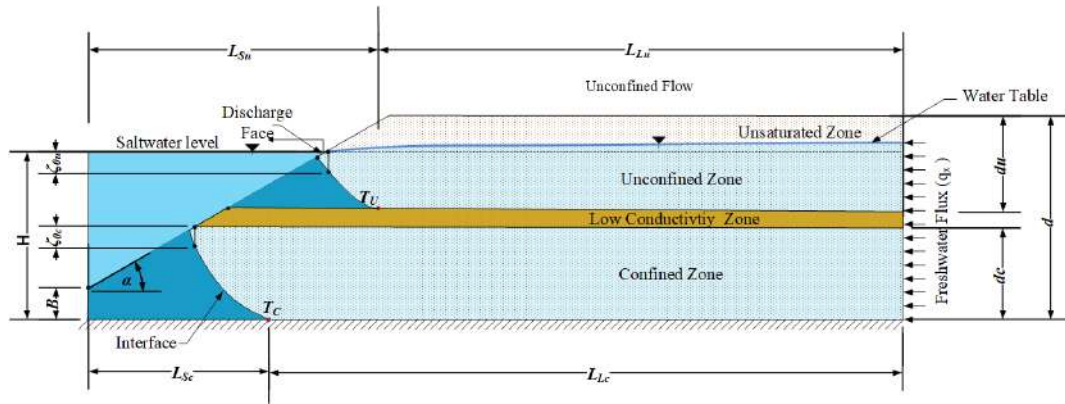


Figure 6.2: Multilayered Aquifer Under Static Saltwater Side Boundary Condition

Table 6.6: Dimensional and Non-Dimensional Variables Used In Dimensional Analysis of Multilayered System Under Static Saltwater Side Boundary Condition

Variables	Symbols	Dimensions
Toe length of the saltwater interface	$L_S$	L
horizontal distance between-the coastline and the inland boundaries	$L_L$	L
Height of the model domain	H	L
Vertical saltwater depth	B	L
Beach slope	$\alpha$	dimensionless
Specific discharge	$q_x$	$L^2 T^{-1}$
Porosity	$\epsilon$	dimensionless
Freshwater density	$\rho_0$	$M^1 L^{-3}$
Seawater density	$\rho_s$	$M^1 L^{-3}$
Longitudinal dispersivities	$\beta_L$	L
Transverse dispersivities	$\beta_T$	L
Density ratio	$\chi$	dimensionless
Hydraulic conductivity(clean sand)	$K_s$	$LT^{-1}$
Hydraulic conductivity(bentonite clay)	$K_B$	$LT^{-1}$
Molecular diffusion coefficent	$D^*$	$L^2 T^{-1}$
Submarine groundwater discharge Gap	$\zeta_0$	L
Vertical depth of the unconfined layer	$d_u$	L
Vertical depth of the confined layer	$d_c$	L

Toe lengths for unconfined and confined layers can be expressed as

$$\frac{L_{S_u}}{d_u} = \varphi_{1u} \left( \frac{L_L}{d_u}, \frac{\zeta_0}{d_u}, \alpha \right) \quad (6.13)$$

and

$$\frac{L_{S_c}}{d_c} = \varphi_{1c} \left( \frac{L_L}{d_c}, \frac{\zeta_0}{d_c}, \alpha \right) \quad (6.14)$$

where the relevant parameters are defined in Table 6.6. Similarly, submarine groundwater discharge gap for unconfined and confined layers can be expressed as

$$\frac{\zeta_0}{d_u} = \varphi_{2u} \left( \frac{L_S}{d_u}, \frac{L_L}{d_u}, \alpha \right) \quad (6.15)$$

and

$$\frac{\zeta_0}{d_c} = \varphi_{2c} \left( \frac{L_S}{d_c}, \frac{L_L}{d_c}, \alpha \right) \quad (6.16)$$

Both numerical simulation and experimental results were utilized to obtain the functional relationships.

### 6.3.1 Unconfined Layer Under Static Condition

Numerical and experimental toe length ( $L_{S_u}$  and  $L_{S_{uExp}}$ ) under static saltwater boundary for an unconfined layer can be explicitly calculated as

$$L_{S_u} = 5.54 \left( \frac{L_L}{d_u} \right)^{4.44} \left( \frac{\zeta_0}{d_u} \right)^{3.50} (\alpha)^{3.288} d_u \quad (6.17)$$

and

$$L_{S_{uExp}} = 1.178 \left( \frac{L_L}{d_u} \right)^{0.100} \left( \frac{\zeta_0}{d_u} \right)^{-0.142} (\alpha)^{-0.945} d_u. \quad (6.18)$$

It is evident that the average ratio of Experimental to Numerical Toe Length is 0.98 (Table 6.7).

Table 6.7: Numerical Toe Length Calculation for Unconfined Layer Under Static Saltwater Side Boundary Condition

CASES	$\frac{L_L}{d_u}$ [-]	$\frac{\zeta_0}{d_u}$ [-]	$\alpha$ [rad]	$L_{S_u}$ [m]	$L_{S_u}$ [mm]	$L_{S_{uExp}}$ [mm]	$\frac{L_{S_{uExp}}}{L_{S_u}}$ [-]
CASE - 4A/S	2.98	0.279	0.261	1.885	1885	1880	0.99
CASE - 4B/S	2.51	0.250	0.349	1.511	1511	1486	0.98
CASE - 4C/S	2.02	0.247	0.436	1.191	1191	1176	0.98
CASE - 4D/S	1.67	0.202	0.523	1.118	1118	1094	0.97

Avg = 0.98

Table 6.8: Experimental Toe Length Calculation for Unconfined Layer Under Static Saltwater Side Boundary Condition

CASES	$\frac{L_L}{d_u}$ [-]	$\frac{\zeta_0}{d_u}$ [-]	$\alpha$ [rad]	$L_{S_{uExp}}$ [m]	$L_{S_{uExp}}$ [mm]
CASE - 4A/S	3.585	0.350	0.261	1.880	1880
CASE - 4B/S	4.744	0.329	0.349	1.486	1486
CASE - 4C/S	5.655	0.438	0.436	1.176	1176
CASE - 4D/S	5.897	0.223	0.523	1.094	1094

Similarly, numerical and experimental submarine groundwater discharge gap ( $\zeta_{0u}$  and  $\zeta_{0uExp}$ ) under static saltwater boundary for unconfined layer can be explicitly calculated as

$$\zeta_{0u} = 0.279 \left( \frac{L_S}{d_u} \right)^{0.25} \left( \frac{L_L}{d_u} \right)^{0.247} (\alpha)^{0.202} d_u \quad (6.19)$$

and

$$\zeta_{0uExp} = 3.174 \left( \frac{L_S}{d_u} \right)^{-7.018} \left( \frac{L_L}{d_u} \right)^{0.707} (\alpha)^{-6.636} d_u. \quad (6.20)$$

It is evident that the average ratio of Experimental to Numerical SGD Gap is 0.75 (Table 6.9).

Table 6.9: Numerical SGD Gap Calculation for Unconfined Layer Under Static Saltwater Side Boundary Condition

Cases	$\frac{L_S}{d_u}$ [-]	$\frac{L_L}{d_u}$ [-]	$\alpha$ [rad]	$\zeta_{0u}$ [m]	$\zeta_{0u}$ [mm]	$\zeta_{0uExp}$ [mm]	$\frac{\zeta_{0u}}{\zeta_{0uExp}}$ [-]
CASE - 4A/S	5.544	3.57	0.261	0.095	95	119	0.79
CASE - 4B/S	4.444	4.67	0.349	0.085	85	112	0.75
CASE - 4C/S	3.502	5.61	0.436	0.084	84	149	0.56
CASE - 4D/S	3.288	5.82	0.523	0.069	69	76.5	0.90

Avg= 0.75

Table 6.10: Experimental SGD Gap Calculation for Unconfined Layer Under Static Saltwater Side Boundary Condition

CASES	$\frac{L_S}{d_u}$ [-]	$\frac{L_L}{d_u}$ [-]	$\alpha$ [rad]	$\zeta_{0_{uExp}}$ [m]	$\zeta_{0_{uExp}}$ [mm]
CASE - 4A/S	5.529	3.585	0.261	0.119	119
CASE - 4B/S	4.370	4.744	0.349	0.112	112
CASE - 4C/S	3.458	5.655	0.436	0.149	149
CASE - 4D/S	3.217	5.897	0.523	0.076	76

### 6.3.2 Confined Layer Under Static Condition

Numerical and experimental toe length ( $L_{S_c}$  and  $L_{S_{cExp}}$ ) under static saltwater boundary for confined layer can be explicitly calculated as

$$L_{S_c} = 10^{7.09} \left( \frac{L_L}{d_c} \right)^{-7.645} \left( \frac{\zeta_0}{d_c} \right)^{-0.697} (\alpha)^{2.389} d_c \quad (6.21)$$

and

$$L_{S_{cExp}} = 0.0029 \left( \frac{L_L}{d_c} \right)^{1.851} \left( \frac{\zeta_0}{d_c} \right)^{1.041} (\alpha)^{-3.151} d_c. \quad (6.22)$$

It is evident that the average ratio of Experimental to Numerical Toe Length is 0.87 (Table 6.11).

Table 6.11: Numerical Toe Length Calculation for Confined Layer Under Static Saltwater Side Boundary Condition

CASES	$\frac{L_L}{d_c}$ [-]	$\frac{\zeta_0}{d_c}$ [-]	$\alpha$ [rad]	$L_{S_c}$ [m]	$L_{S_c}$ [mm]	$L_{S_{cExp}}$ [mm]	$\frac{L_{S_c}}{L_{S_{cExp}}}$ [-]
CASE - 4A/S	6.12	0.073	0.261	1.015	1015	1194	0.85
CASE - 4B/S	6.57	0.117	0.349	0.856	856	968	0.88
CASE - 4C/S	7.09	0.150	0.436	0.688	688	743	0.92
CASE - 4D/S	7.43	0.217	0.523	0.570	570	658	0.86

Avg= 0.87

Similarly, numerical and experimental submarine groundwater discharge gap ( $\zeta_{0_c}$  and  $\zeta_{0_{cExp}}$ ) under static saltwater boundary for confined layer can be explicitly calculated as

$$\zeta_{0_c} = 10^{3.801} \left( \frac{L_S}{d_c} \right)^{1.372} \left( \frac{L_L}{d_c} \right)^{-4.455} (\alpha)^{1.722} d_c \quad (6.23)$$

Table 6.12: Experimental Toe Length Calculation for Confined Layer Under Static Saltwater Side Boundary Condition

CASES	$\frac{L_L}{d_c}$	$\frac{\zeta_0}{d_c}$	$\alpha$	$L_{S_{uExp}}$	$L_{S_{uExp}}$
	[-]	[-]	[rad]	[m]	[mm]
CASE - 4A/S	5.602	0.735	0.261	1.194	1194
CASE - 4B/S	6.267	1.176	0.349	0.968	968
CASE - 4C/S	6.929	1.500	0.436	0.743	743
CASE - 4D/S	7.179	2.176	0.523	0.658	658

and

$$\zeta_{0_{cExp}} = 10^{7.87} \left( \frac{L_S}{d_c} \right)^{-2.968} \left( \frac{L_L}{d_c} \right)^{-8.518} (\alpha)^{-0.412} d_c. \quad (6.24)$$

It is evident that the average ratio of Experimental to Numerical SGD Gap is 0.82 (Table 6.13).

Table 6.13: Numerical SGD Gap Calculation for Confined Layer Under Static Saltwater Side Boundary Condition

CASES	$\frac{L_S}{d_c}$	$\frac{L_L}{d_c}$	$\alpha$	$\zeta_{0_c}$	$\zeta_{0_c}$	$\zeta_{0_{cExp}}$	$\frac{\zeta_{0_c}}{\zeta_{0_{cExp}}}$
	[-]	[-]	[rad]	[m]	[mm]	[mm]	[-]
CASE - 4A/S	2.985	6.129	0.261	0.298	298	452	0.65
CASE - 4B/S	2.517	6.570	0.349	0.284	284	288	0.98
CASE - 4C/S	2.023	7.091	0.436	0.220	220	245	0.89
CASE - 4D/S	1.676	7.438	0.523	0.188	188	241	0.78

Avg= 0.82

Table 6.14: Experimental SGD Gap Calculation for Confined Layer Under Static Saltwater Side Boundary Condition

CASES	$\frac{L_S}{d_c}$	$\frac{L_L}{d_c}$	$\alpha$	$\zeta_{0_{cExp}}$	$\zeta_{0_{cExp}}$
	[-]	[-]	[rad]	[m]	[mm]
CASE - 4A/S	3.511	5.602	0.261	0.452	452
CASE - 4B/S	2.847	6.267	0.349	0.288	288
CASE - 4C/S	2.185	6.929	0.436	0.245	245
CASE - 4D/S	1.935	7.179	0.523	0.241	241

Few other  $\Pi$ -terms can be formed based on numerical and experimental model details, e.g., *Peclet number (Pe)* (Voss and Souza, 1987) depends on the mesh size

(or, discretization) used in the numerical model. It can be expressed as

$$Pe = \frac{\Delta L}{\beta_L} \quad (6.25)$$

where  $\Delta L$  [L] is the mesh size. Ideally, the  $Pe$  value should be less than 4. Initially, a coarse mesh of 1.09 cm size was used corresponding to a  $Pe$  value of 10.9. A mesh-convergence study was conducted for different mesh sizes. Finally a mesh of 0.38 cm size ( $Pe = 3.8$ ) was adopted. Less than 1% variation in results was observed when compared with the coarse mesh size.

Buoyancy forces (i.e., water density variations), advective forces (i.e., resulting from boundary head differences), and dispersion directly influence the saltwater-freshwater interface toe length. Abarca et al. (2007) used two nondimensional parameters, namely, mixed-convection ratio ( $MCR$ ) and Peclet number( $Pe$ ) to characterise the advective-dispersive processes.

$$MCR = \frac{q_f}{K_s \chi} \quad (6.26)$$

where  $q_f$  [L/T] is the freshwater Darcy velocity ( $q_f = q_x/h_f$ ). A higher  $MCR$  value indicates the relative dominance of advective force over the buoyancy force. It was observed that toe length decreases with the increasing  $MCR$  value, i.e., in the presence of dominant advective force.

Under steady-state condition  $Pe$  can be defined as (Abarca et al., 2007)

$$Pe = \frac{D^* \epsilon + \beta_g q_f}{q_x} \quad (6.27)$$

where  $\beta_g$  [L] is the geometric mean of dispersivity, i.e.,  $\sqrt{\beta_L \beta_T}$ . Dispersion is more dominant relative to advection with higher values of  $Pe$ . The toe length is shorter for higher  $Pe$  values.

Density-dependent flows were also characterized by the stability of fluid interfaces. The fluid interface was of irregular shape. The saltwater-fresh water interface moved at a faster rate in the vertical direction compared to the numerical simulation. It was due to the combined effect of hydraulic conductivity, longitudinal dispersivity, and transverse dispersivity. Rayleigh number and Peclet number were utilized to characterize the density-dependent flow through porous media.

List (1965) analyzed the stability for a density-stratified horizontal flow in an infinite saturated homogeneous porous medium. The occurrence of instabilities may be related to two Rayleigh numbers (Wooding, 1963) as given below

$$R_a^*|_L = \frac{\kappa g \Delta \rho L}{\epsilon \mu D_L}, \quad (6.28)$$

$$R_a^*|_T = \frac{\kappa g \Delta \rho H}{\epsilon \mu D_T}, \quad (6.29)$$

$$D_L = V_{in} \alpha_L, \quad (6.30)$$

$$D_T = V_{in} \alpha_T, \quad (6.31)$$

where  $\kappa$  is the permeability of the porous medium,  $g$  is the acceleration due to gravity,  $\Delta \rho$  is the density difference between the two fluids,  $L$  is the characteristic length,  $\mu$  is the dynamic viscosity of the fluid,  $D_L$  is the longitudinal dispersion coefficient,  $D_T$  is the transverse dispersion coefficient and  $H$  is the width of the medium. The value of  $R_a^*$  was around 50000 for experiments under static saltwater side condition. It was concluded in Oostrom et al. (1991) that the transition from stable to unstable plume occurs between  $R_a^* = 150$  to 250 or 750 depending on  $D_T$  calculation procedure. According to these criteria, the current set of flow and transport experiments appeared to be stable. In current modeling, neither artificial disturbances nor numerical errors were introduced. Therefore, such instabilities were not observed in the numerical results.

## 6.4 Parameters Under Tidal Condition

The analysis under saltwater side tidal boundary condition was performed with 6 model geometry parameter ( $L_L$ ,  $L_S$ ,  $\alpha$ ,  $H$ ,  $B$ ,  $d$ ), 6 fluid-aquifer parameters ( $K$ ,  $\epsilon$ ,  $\beta_L$ ,  $\beta_T$ ,  $\rho_s$ ,  $\rho_0$ ), and 2 tidal parameters ( $A$  and  $\omega$ ). On the basis of the small amplitude groundwater wave theory, tide-induced groundwater head fluctuations in the aquifer ( $h$ ) can be described by

$$h(x, t) = A e^{-kx} \cos(\omega t - kx) \quad (6.32)$$

where  $k$  ( $m^{-1}$ ) is inverse of tidal propagation distance( $\lambda$ ). It can be explicitly calculated as (Nielsen, 1990; Li et al., 2004)

$$k = \sqrt{\frac{\epsilon \omega}{2K_s B}} = \frac{1}{\lambda} \quad (6.33)$$

Saltwater intrusion dynamics in single layered system under tidal condition can be characterized by 10 non-dimensional parameter groups (Smith, 2004; Robinson et al., 2007b) as provided in Table 6.15.

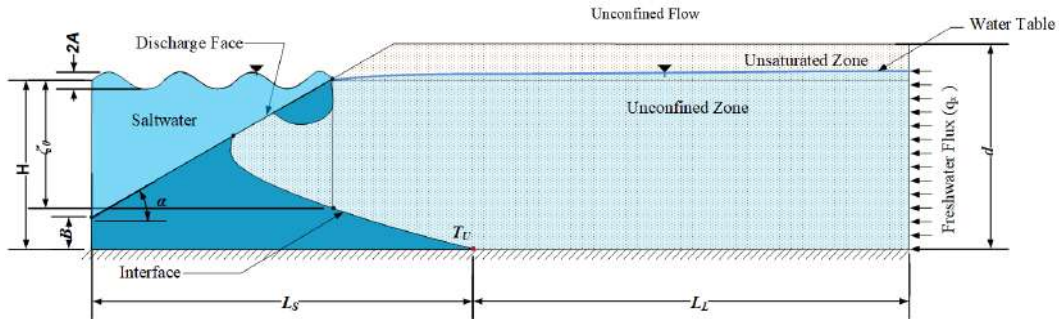


Figure 6.3: Single Layered Unconfined Aquifer Under Tidal Saltwater Side Boundary Condition

Table 6.15: Non-Dimensional Variables Used In Dimensional Analysis of Single Layered System Under Tidal Saltwater Side Boundary Condition

Parameter	Description
$L_L^* = L_L \sqrt{\frac{\epsilon \omega}{2K_s B}}$	Ratio of landward aquifer extent to tidal propagation distance
$L_S^* = L_S \sqrt{\frac{\epsilon \omega}{2K_s B}}$	Ratio of extent saltwater side aquifer to tidal propagation distance
$B^* = \sqrt{\frac{\epsilon \omega B}{2K_s}}$	Ratio of saltwater side aquifer thickness to tidal propagation distance
$d^* = \frac{d}{B}$	Ratio of vertical saltwater depth to aquifer thickness
$\delta = \frac{A}{B}$	Ratio of tidal amplitude to saltwater side aquifer thickness
$\nabla = \frac{d-H}{L_L}$	Saltwater hydraulic gradient
$\epsilon$	Porosity
$\chi = \frac{\rho_s - \rho_0}{\rho_0}$	Relative density
$\alpha$	Beach slope
$\frac{\zeta_0}{d}$	Submarine groundwater discharge Gap

## 6.5 Single Layered Porous Media Under Tidal Saltwater Boundary Conditions

The saltwater-freshwater interface toe location and submarine groundwater discharge (SGD) gap were determined for the single-layered system under tidal saltwater boundary conditions. Saltwater-freshwater interface toe length and submarine groundwater discharge gap ( $\zeta_0$ ) can be expressed in functional form as

$$L_S^* = \varphi_{T1} (L_L^*, B^*, d^*, \delta, \nabla, \chi, \zeta_0/d, \alpha, \epsilon), \quad (6.34)$$

and

$$\frac{\zeta_0}{d} = \varphi_{T2} (L_S^*, L_L^*, B^*, d^*, \delta, \nabla, \chi, \alpha, \epsilon). \quad (6.35)$$

### 6.5.1 Toe Length for Tidal Condition

Toe length was determined based on variations of four non-dimensional parameters only. Both the numerical simulation and experimental results were utilized to obtain the functional relationships.

Numerical  $L_S$  and experimental  $L_{SExp}$  can be calculated as

$$L_S = 0.277 (\nabla)^{0.311} \left( \frac{\zeta_0}{d} \right)^{-5.965} (\alpha)^{-0.672} \sqrt{\frac{\epsilon \omega}{2K_s B}} \quad (6.36)$$

and

$$L_{SExp} = 10^{7.981} (\nabla)^{6.864} \left( \frac{\zeta_0}{d} \right)^{0.603} (\alpha)^{3.858} \sqrt{\frac{\epsilon \omega}{2K_s B}}. \quad (6.37)$$

It is evident that the average ratio of Experimental to Numerical Toe Length is 0.98 (Table 6.16).

Table 6.16: Numerical Toe Length Calculation for Single Layered System Under Tidal Saltwater Side Boundary Condition

CASES	$\nabla$	$\zeta_0/d$	$\alpha$	$L_S$	$L_S$	$L_{SExp}$	$L_S / L_{SExp}$
	[-]	[-]	[rad]	[m]	[mm]	[mm]	[-]
CASE - 3A/T	0.134	0.788	0.261	1.907	1907	1909	1
CASE - 3B/T	0.109	0.662	0.349	1.636	1636	1639	0.99
CASE - 3C/T	0.095	0.617	0.436	1.402	1402	1430	0.97
CASE - 3D/T	0.083	0.641	0.523	1.164	1164	1194	0.97

Avg= 0.98

Table 6.17: Experimental Toe Length Calculation for Single Layered System Under Tidal Saltwater Side Boundary Condition

CASES	$\nabla$	$\zeta_0/d$	$\alpha$	$L_{SExp}$	$L_{SExp}$
	[-]	[-]	[rad]	[m]	[mm]
CASE - 3A/T	0.134	0.612	0.261	1.909	1909
CASE - 3B/T	0.109	0.773	0.349	1.639	1639
CASE - 3C/T	0.095	0.678	0.436	1.430	1430
CASE - 3D/T	0.083	0.706	0.523	1.164	1164

### 6.5.2 Submarine Groundwater Discharge Gap for Tidal Condition

Numerical  $\zeta_0$  and experimental  $\zeta_{0Exp}$  can be calculated as

$$\zeta_0 = 1.904 (L_S^*)^{-0.063} (\nabla)^{0.860} (\alpha)^{-0.810} d \quad (6.38)$$

and

$$\zeta_{0Exp} = 10^{-13.221} (L_S^*)^{1.656} (\nabla)^{-11.37} (\alpha)^{-6.391} d. \quad (6.39)$$

The average ratio of Experimental to Numerical submarine groundwater discharge gap is 0.85 (Table 6.18).

## 6.6 Layered Porous Media Under Tidal Saltwater Boundary Conditions

In layered porous media configuration, confined and unconfined layer specific parameters ( $d_u$ ,  $d_c$ ,  $K_s$ ,  $K_B$ ) were considered. A summary of the dimensionless

Table 6.18: Numerical SGD Gap Calculation for Single Layered System Under Static Saltwater Side Boundary Condition

CASES	$L_S^*$ [-]	$\nabla$ [-]	$\alpha$ [rad]	$\zeta_0$ [m]	$\zeta_0$ [mm]	$\zeta_{0Exp}$ [mm]	$\zeta_0 / \zeta_{0Exp}$ [-]
CASE - 3A/T	0.134	0.788	0.261	0.631	631	490	0.77
CASE - 3B/T	0.109	0.662	0.349	0.530	530	619	0.85
CASE - 3C/T	0.094	0.617	0.436	0.494	494	543	0.90
CASE - 3D/T	0.082	0.641	0.523	0.513	513	565	0.90
							Avg= 0.85

Table 6.19: Experimental SGD Gap Calculation for Single Layered System Under Static Saltwater Side Boundary Condition

CASES	$L_S^*$ [-]	$\nabla$ [-]	$\alpha$ [rad]	$\zeta_{0Exp}$ [m]	$\zeta_{0Exp}$ [mm]
CASE - 3A/T	0.421	0.134	0.261	0.490	490
CASE - 3B/T	0.362	0.109	0.349	0.619	619
CASE - 3C/T	0.316	0.095	0.436	0.543	543
CASE - 3D/T	0.263	0.083	0.523	0.565	565

ratios for layered configuration are presented in Table 6.20.

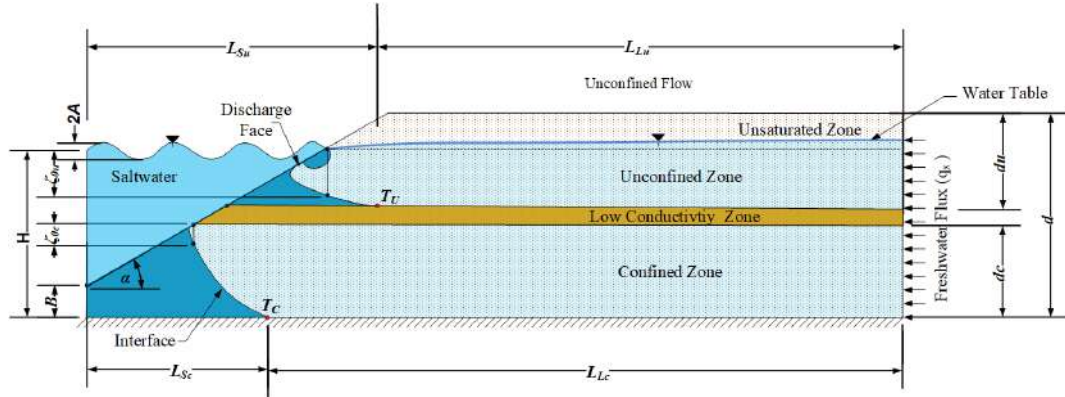


Figure 6.4: Multilayered System Under Tidal Saltwater Side Boundary Condition

Toe lengths for unconfined and confined layers can be expressed as

$$L_{S_u}^* = \varphi_{1u} (L_L^*, B^*, d^*, \delta, \nabla, \chi, \epsilon, \zeta_0/d, \alpha) \quad (6.40)$$

and

$$L_{S_c}^* = \varphi_{1c} (L_L^*, B^*, d^*, \delta, \nabla, \chi, \epsilon, \zeta_0/d, \alpha) \quad (6.41)$$

Table 6.20: Non-Dimensional Variables Used In Dimensional Analysis of Multilayered System Under Tidal Saltwater Side Boundary Condition

Parameter	Description
$L_{L_u}^* = L_L \sqrt{\frac{\epsilon \omega}{2K_s B}}$	Ratio of landward aquifer extent to tidal propagation distance for the unconfined layer
$L_{L_c}^* = L_L \sqrt{\frac{\epsilon \omega}{2K_s B}}$	Ratio of landward aquifer extent to tidal propagation distance for the confined layer
$L_{S_u}^* = L_S \sqrt{\frac{\epsilon \omega}{2K_s B}}$	Ratio of extent saltwater side aquifer to tidal propagation distance for the unconfined layer
$L_{S_c}^* = L_S \sqrt{\frac{\epsilon \omega}{2K_s B}}$	Ratio of extent saltwater side aquifer to tidal propagation distance for the confined layer
$B^* = \sqrt{\frac{\epsilon \omega B}{2K_s}}$	Ratio of saltwater side aquifer thickness to tidal propagation distance
$d^* = \frac{d}{B}$	Ratio of vertical saltwater depth to aquifer thickness
$\delta = \frac{A}{B}$	Ratio of tidal amplitude to saltwater side aquifer thickness
$\nabla = \frac{d-H}{L_L}$	Saltwater hydraulic gradient
$\epsilon$	Porosity
$\chi = \frac{\rho_s - \rho_0}{\rho_0}$	Relative density
$\alpha$	Beach slope
$\frac{\zeta_0}{d_u}$	SGD Gap of the unconfined layer
$\frac{\zeta_0}{d_c}$	SGD Gap of the confined layer

Similarly, submarine groundwater discharge gap for unconfined and confined layers can be expressed as

$$\frac{\zeta_0}{d_u} = \varphi_{2u} (L_S^*, L_L^*, B^*, d^*, \delta, \nabla, \chi, \epsilon, \alpha) \quad (6.42)$$

and

$$\frac{\zeta_0}{d_c} = \varphi_{2c} (L_S^*, L_L^*, B^*, d^*, \delta, \nabla, \chi, \epsilon, \alpha) \quad (6.43)$$

Both numerical simulation and experimental results were utilized to obtain the functional relationships.

### 6.6.1 Toe Length of Unconfined Layer Under Tidal Condition

Variations in four non-dimensional parameters ( $L_{S_u}^*$ ,  $\nabla$ ,  $\zeta_0/d$ ,  $\alpha$ ) were considered. Numerical  $L_{S_u}$  and experimental  $L_{S_{uExp}}$  can be calculated as

$$L_{S_u} = 0.0304 (\nabla)^{-0.383} \left( \frac{\zeta_0}{d_u} \right)^{0.014} (\alpha)^{-1.351} \sqrt{\frac{\epsilon\omega}{2K_s B}} \quad (6.44)$$

and

$$L_{S_{uExp}} = 0.045 (\nabla)^{-0.405} \left( \frac{\zeta_0}{d_u} \right)^{0.074} (\alpha)^{-1.54} \sqrt{\frac{\epsilon\omega}{2K_s B}}. \quad (6.45)$$

It is evident that the average ratio of Experimental to Numerical toe length is 0.97 (Table 6.21).

Table 6.21: Numerical Toe Length Calculation in Unconfined Layer Under Tidal Saltwater Side Boundary Condition

CASES	$\nabla$	$\zeta_0/d_u$	$\alpha$	$L_{S_u}$	$L_{S_u}$	$L_{S_{uExp}}$	$L_{S_u} / L_{S_{uExp}}$
	[-]	(m)	[rad]	[m]	[mm]	[mm]	[-]
CASE - 4A/T	0.131	0.858	0.261	1.829	1829	1798	0.98
CASE - 4B/T	0.100	0.80	0.349	1.373	1373	1342	0.97
CASE - 4C/T	0.083	0.591	0.436	1.085	1085	1063	0.97
CASE - 4D/T	0.080	0.488	0.523	858	858	825	0.96
							Avg= 0.97

Table 6.22: Experimental Toe Length Calculation in Unconfined Layer Under Tidal Saltwater Side Boundary Condition

CASES	$\nabla$	$\zeta_0/d_u$	$\alpha$	$L_{S_{uExp}}$	$L_{S_{uExp}}$
	[-]	[-]	[rad]	[m]	[mm]
CASE - 4A/T	0.636	0.285	0.261	1.798	1798
CASE - 4B/T	0.481	0.479	0.349	1.342	1342
CASE - 4C/T	0.403	0.826	0.436	1.063	1063
CASE - 4D/T	0.387	0.964	0.523	0.825	825

### 6.6.2 Submarine Groundwater Discharge Gap of Unconfined Layer Under Tidal Condition

Submarine groundwater discharge Gap in unconfined layer under tidal boundary condition was determined based on same set of non-dimensional parameters as used for toe length calculation. Numerical and experimental submarine groundwater discharge gap ( $\zeta_{0_u}$  and  $\zeta_{0_{uExp}}$ ) for unconfined layer can be explicitly calculated as

$$\zeta_{0_u} = 10^{107} (L_S^*)^{70.9} (\nabla)^{27.22} (\alpha)^{95.87} d_u \quad (6.46)$$

and

$$\zeta_{0_{uExp}} = 10^{17.89} (L_S^*)^{13.35} (\nabla)^{5.41} (\alpha)^{20.6} d_u. \quad (6.47)$$

It is evident that the average ratio of Experimental to Numerical submarine groundwater discharge gap is 0.53 (Table 6.23).

Table 6.23: Numerical SGD Gap Calculation in Unconfined Layer Under Tidal Saltwater Side Boundary Condition

CASES	$L_S^*$	$\nabla$	$\alpha$	$\zeta_{0_u}$	$\zeta_{0_u}$	$\zeta_{0_{uExp}}$	$\zeta_{0_u} / \zeta_{0_{uExp}}$
	[-]	[-]	[rad]	[m]	[mm]	[mm]	[-]
CASE - 4A/T	0.404	0.131	0.261	0.292	292	97	0.33
CASE - 4B/T	0.303	0.100	0.349	0.272	272	163	0.59
CASE - 4C/T	0.239	0.083	0.436	0.281	281	201	0.71
CASE - 4D/T	0.189	0.080	0.523	0.166	166	328	0.50

Avg= 0.53

Table 6.24: Experimental SGD Gap Calculation in Unconfined Layer Under Tidal Saltwater Side Boundary Condition

CASES	$L_S^*$	$\nabla$	$\alpha$	$\zeta_{0_{uExp}}$	$\zeta_{0_{uExp}}$
	[-]	[-]	[rad]	[m]	[mm]
CASE - 4A/T	0.397	0.636	0.261	0.097	97
CASE - 4B/T	0.296	0.481	0.349	0.163	163
CASE - 4C/T	0.234	0.403	0.436	0.281	281
CASE - 4D/T	0.182	0.387	0.523	0.328	328

### 6.6.3 Toe Length of Confined Layer Under Tidal Condition

Variations in four non-dimensional parameters ( $L_{S_c}^*$ ,  $\nabla$ ,  $\zeta_0/d_c$ ,  $\alpha$ ) were considered for toe length calculation in confined layer under tidal boundary condition. Numerical  $L_{S_c}$  and experimental  $L_{S_{cExp}}$  can be calculated as

$$L_{S_c} = 10^{-29.82} (\nabla)^{-22.14} \left( \frac{\zeta_0}{d_c} \right)^{0.569} (\alpha)^{-8.952} \sqrt{\frac{\epsilon\omega}{2K_s B}} \quad (6.48)$$

and

$$L_{S_{cExp}} = 0.019 (\nabla)^{-0.558} \left( \frac{\zeta_0}{d_c} \right)^{0.116} (\alpha)^{-1.859} \sqrt{\frac{\epsilon\omega}{2K_s B}}. \quad (6.49)$$

It is evident that the average ratio of Experimental to Numerical toe length is 0.93 (Table 6.25).

Table 6.25: Numerical Toe Length Calculation in Confined Layer Under Tidal Saltwater Side Boundary Condition

CASES	$\nabla$	$\zeta_0/d_c$	$\alpha$	$L_{S_c}$	$L_{S_c}$	$L_{S_{cExp}}$	$L_{S_c} / L_{S_{cExp}}$
	[-]	[-]	[rad]	[m]	[mm]	[mm]	[-]
CASE - 4A/T	0.076	0.132	0.261	1.695	1695	1698	0.99
CASE - 4B/T	0.071	0.305	0.349	0.969	969	972	0.99
CASE - 4C/T	0.066	0.408	0.436	0.839	839	841	0.99
CASE - 4D/T	0.063	0.426	0.523	0.484	484	630	0.76
							Avg = 0.93

Table 6.26: Experimental Toe Length Calculation in Confined Layer Under Tidal Saltwater Side Boundary Condition

CASES	$\nabla$	$\zeta_0/d_c$	$\alpha$	$L_{S_{cExp}}$	$L_{S_{cExp}}$
	[-]	[-]	[rad]	[m]	[mm]
CASE - 4A/T	0.407	0.088	0.261	1.698	1698
CASE - 4B/T	0.364	0.041	0.349	0.972	972
CASE - 4C/T	0.329	0.058	0.436	0.841	841
CASE - 4D/T	0.317	0.041	0.523	0.630	630

### 6.6.4 Submarine Groundwater Discharge Gap of Confined Layer Under Tidal Condition

Submarine groundwater discharge Gap in the confined layer under tidal boundary conditions was determined based on the same set of non-dimensional parameters as used for toe length calculation. Numerical and experimental submarine groundwater discharge gap ( $\zeta_{0c}$  and  $\zeta_{0cExp}$ ) for a confined layer can be explicitly calculated as

$$\zeta_{0c} = 10^{-19.978} (L_S^*)^{8.328} (\nabla)^{-23.01} (\alpha)^{1.981} d_c \quad (6.50)$$

and

$$\zeta_{0cExp} = 10^{14.79} (L_S^*)^{8.6} (\nabla)^{4.8} (\alpha)^{-16.0} d_c. \quad (6.51)$$

It is evident that the average ratio of Experimental to Numerical submarine groundwater discharge gap is 0.81 (Table 6.27).

Table 6.27: Numerical SGD Gap Calculation in Confined Layer Under Tidal Saltwater Side Boundary Condition

CASES	$L_S^*$	$\nabla$	$\alpha$	$\zeta_{0c}$	$\zeta_{0c}$	$\zeta_{0cExp}$	$\zeta_{0cExp} / \zeta_{0c}$
	[-]	[-]	[rad]	[m]	[mm]	[mm]	[-]
CASE - 4A/T	0.374	0.076	0.261	0.045	45	30	0.66
CASE - 4B/T	0.214	0.071	0.349	0.104	104	94	0.90
CASE - 4C/T	0.185	0.066	0.436	0.139	139	99	0.73
CASE - 4D/T	0.106	0.063	0.523	0.125	125	122	0.97

Avg= 0.81

Table 6.28: Experimental SGD Gap Calculation in Confined Layer Under Tidal Saltwater Side Boundary Condition

CASES	$L_S^*$	$\nabla$	$\alpha$	$\zeta_{0cExp}$	$\zeta_{0cExp}$
	[-]	[-]	[rad]	[m]	[mm]
CASE - 4A/T	0.375	0.407	0.261	0.030	30
CASE - 4B/T	0.214	0.364	0.349	0.094	94
CASE - 4C/T	0.185	0.329	0.436	0.099	99
CASE - 4D/T	0.106	0.317	0.523	0.122	122

## 6.7 Summary

Influencing non-dimensional parameters were identified during the dimensional analysis study. Equations were identified for both saltwater-freshwater interface toe location and submarine groundwater discharge gap under a) static/ tidal boundary condition and b) single layered/ multilayered systems. Numerical simulation results were compared with experimental ones as a ratio. It is evident that beach slope ( $\alpha$ ) directly affects the toe length and submarine groundwater discharge gap. The expressions presented are indicative. More experimental and field studies are required for further comments. The next chapter presents an overall summary, conclusions, and recommendations for future works.



# Chapter 7

## Overview and Conclusions

### 7.1 Overview

The major objective of the Thesis was to study the influence of beach slope and tidal conditions on saltwater dynamics in single and multilayered porous media. Experiments were performed in a *2D Sand Box Model* (longitudinal & vertical) to study the beach slope effect in both unconfined and confined aquifer configurations under tidal and non-tidal (static) conditions. Summary of the experimental cases for single and multilayered porous media are presented in Table 7.1 and Table 7.2, respectively. The cases *CASE – 1/S*, *CASE – 3A/S*, *CASE – 3B/S*, *CASE – 3C/S*, *CASE – 3D/S* were corresponding to single-layered porous media under static saltwater side boundary condition. The saltwater side boundary condition was changed to tidal one in *CASE – 3A/T*, *CASE – 3B/T*, *CASE – 3C/T*, *CASE – 3D/T*. The cases: *CASE – 2/S*, *CASE – 4A/S*, *CASE – 4B/S*, *CASE – 4C/S*, *CASE – 4D/S* were corresponding to multi-layered porous media under static saltwater side boundary condition. The saltwater side boundary condition was changed to tidal one in cases: *CASE – 4A/T*, *CASE – 4B/T*, *CASE – 4C/T*, *CASE – 4D/T*. Locally available *Clean Sand* was utilized as aquifer material in *CASE – 1/S* and *CASE – 2/S*. However, Grade-I IS Sand was used for all other cases. *Bentonite* was used for the low permeability layer. *Rohdamine B* was utilized as the saltwater tracer. Time-varying porewater pressure and images were captured during the experiments. A novel G-Channel-based image analysis technique was proposed to identify the saltwater-freshwater interface and concentration distribution within the porous media. Laboratory experiments were validated by FEFLOW based numerical models. Time-varying saltwater intrusion flow pattern from experiments, G-Channel based image analysis, and numerical simulations (0.5-concentration isoline) were utilized for comprehensive analysis. Reasonable match of the experiment, image analysis, and numerical

Table 7.1: Configurations for Experiments with Single Layered Porous Media Under Static and Tidal Saltwater Side Boundary Conditions

CASES	Beach Slope	Sand	Stratification	Saltwater Boundary Conditions
<i>CASE - 1/S</i>	$15^0$	Clean Sand ( $d_{50} = 1.024 \text{ mm}$ )	No	Static
<i>CASE - 3A/S</i>	$15^0$	Grade I IS Sand ( $d_{50}=1.12 \text{ mm}$ )	No	Static
<i>CASE - 3B/S</i>	$20^0$	Grade I IS Sand ( $d_{50}=1.12 \text{ mm}$ )	No	Static
<i>CASE - 3C/S</i>	$25^0$	Grade I IS Sand ( $d_{50}=1.12 \text{ mm}$ )	No	Static
<i>CASE - 3D/S</i>	$30^0$	Grade I IS Sand ( $d_{50}=1.12 \text{ mm}$ )	No	Static
<i>CASE - 3A/T</i>	$15^0$	Grade I IS Sand ( $d_{50}=1.12 \text{ mm}$ )	No	Tidal
<i>CASE - 3B/T</i>	$20^0$	Grade I IS Sand ( $d_{50}=1.12 \text{ mm}$ )	No	Tidal
<i>CASE - 3C/T</i>	$25^0$	Grade I IS Sand ( $d_{50}=1.12 \text{ mm}$ )	No	Tidal
<i>CASE - 3D/T</i>	$30^0$	Grade I IS Sand ( $d_{50}=1.12 \text{ mm}$ )	No	Tidal

simulation results were obtained for all the cases. Submarine groundwater discharge (SGD) pathways were identified through tracer injection technique for all the cases. Flow circulation mechanism in saltwater wedge was also identified in *CASE - 1/S*. Dimensional Analysis was performed for the identification of influencing non-dimensional parameters. Non-dimensional parameter-based equations were identified for saltwater-freshwater interface toe length ( $L_S$ ) and SGD Gap ( $\zeta_0$ ) calculation.

Table 7.2: Configurations for Experiments with Multilayered Porous Media Under Static and Tidal Saltwater Side Boundary Conditions

CASES	Beach Slope	Sand	Stratification	Saltwater Boundary Conditions
Clean Sand				
<i>CASE - 2/S</i>	$15^0$	$(d_{50} = 1.024 \text{ mm})$	Yes	Static
		30 mm clay layer		
		Grade I IS Sand		
<i>CASE - 4A/S</i>	$15^0$	$(d_{50}=1.12 \text{ mm})$	Yes	Static
		40 mm clay layer		
		Grade I IS Sand		
<i>CASE - 4B/S</i>	$20^0$	$(d_{50}=1.12 \text{ mm})$	Yes	Static
		40 mm clay layer		
		Grade I IS Sand		
<i>CASE - 4C/S</i>	$25^0$	$(d_{50}=1.12 \text{ mm})$	Yes	Static
		40 mm clay layer		
		Grade I IS Sand		
<i>CASE - 4D/S</i>	$30^0$	$(d_{50}=1.12 \text{ mm})$	Yes	Static
		40 mm clay layer		
		Grade I IS Sand		
<i>CASE - 4A/T</i>	$15^0$	$(d_{50}=1.12 \text{ mm})$	Yes	Tidal
		40 mm clay layer		
		Grade I IS Sand		
<i>CASE - 4B/T</i>	$20^0$	$(d_{50}=1.12 \text{ mm})$	Yes	Tidal
		40 mm clay layer		
		Grade I IS Sand		
<i>CASE - 4C/T</i>	$25^0$	$(d_{50}=1.12 \text{ mm})$	Yes	Tidal
		40 mm clay layer		
		Grade I IS Sand		
<i>CASE - 4D/T</i>	$30^0$	$(d_{50}=1.12 \text{ mm})$	Yes	Tidal
		40 mm clay layer		

## 7.2 Conclusions

The following conclusions can be inferred from the present Thesis:

- Experimental and numerical analyses showed that the movement rate and volume of the saltwater wedge (i.e., saltwater-freshwater interface toe length) decrease with the increase in beach slope (e.g.,  $\alpha = 15^\circ$  to  $\alpha = 30^\circ$ ). The saltwater intrusion occurred rapidly, i.e., the size of the saltwater wedge increases, for flatter slopes (*CASE – 3A/S*). Thus saltwater-freshwater interface intruded less in *CASE – 3D/S*. Both experimental and numerical solutions showed similar trends.
- Fingering effect is prominent in *CASE – 3A/S* for  $15^\circ$  slope. The initial saltwater fingering effect reduces with the increase in beach slope *CASE – 3D/S* for  $30^\circ$ . However, under tidal conditions finger effect was observed only in *CASE – 3A/T* for the flatter slope. This was due to the scale effect.
- The G-Channel (of R-G-B) based image analysis technique identified the saltwater-freshwater interface and concentration gradient from the experimental images. The 50% concentration isolines obtained from the numerical simulations matched the interfaces obtained from the image analysis. A narrow mixing zone was observed for the current set of experiments.
- Numerically simulated and transient porewater pressure head data quantified the time-varying saltwater movement in the porous medium. The pressure transducer placed near the right boundary showed an over-height condition (*PS6* in *CASE – 3B/S*). This was due to the marginal rise of the water level in the presence of freshwater flux.
- Tide significantly alters the seawater circulation pattern. In the case of the stratified porous medium, saltwater movement in the lower confined layer was slower than the movement in the upper unconfined layer for both tidal and static seaside conditions. However, intrusion length decreases under tidal conditions.
- Time required to reach the quasi-steady condition was less under static condition (e.g., *CASE – 3A/S*). It increases with the increase in beach slope for the single-layered experimental analysis under static boundary conditions. A similar trend was also observed for tidal conditions. However, a marginal rise in overall experimental time was seen in tidal cases and (e.g., *CASE – 3D/T*) compared to static one (e.g., *CASE – 3D/S*).

- Upper saline plume (USP) developed for all experimental cases for unconfined layer in single and multilayered systems under tidal saltwater side boundary conditions. The extent of the upper saline plume was dependent on the freshwater flux.
- Submarine groundwater discharge (SGD) gap ( $\zeta_0$ ) obtained from the physical experiments vary with slopes. The vertical SGD gap ( $\zeta_0$ ) decreases with an increase in beach face slope, whereas the SWI toe length increases. The ratio of experimental to analytical (Van der Veer, 1977) submarine groundwater discharge (SGD) gap ( $\zeta_0$ ) varied from 52% to 28% with the increase in beach slope ( $15^0$  to  $30^0$ ) for the single-layered system under static saltwater boundary condition. However, an increase (51% to 94%) in SWI toe length ratio (experimental to analytical) was observed for an increase in beach slope under similar conditions. Under the tidal condition, the SGD gap ratio decreased from 79% to 65% with the increase in slope ( $15^0$  to  $30^0$ ). Overall increase (30% to 43%) in SWI toe length ratio was observed for the increase in beach slope under similar conditions.
- Submarine groundwater discharge (SGD) flow pathways were identified by density neutral tracer injection technique for unconfined layer in single and multilayered systems. SGD particles move along the saltwater-freshwater interface zone and rise upward up to the intersection point of saltwater level and sloping beach face under static conditions. Particles get discharged to the saltwater region through the intermediate zone of the saltwater wedge and USP under tidal conditions.
- Dimensionless groups were identified for both tidal and non-tidal conditions. The saltwater-freshwater interface toe length and submarine groundwater discharge gap values were dependent on beach slope. Flow stability was determined on the basis of Rayleigh number ( $R_a^* = 150$  to  $250$  or  $750$ ).

A number of experiments were performed to quantify the influence of beach slope on saltwater dynamics in porous media. This study addressed some of the existing gaps in the available frameworks/ methodologies. The quantification framework should be applicable to other groundwater contaminant movement studies with minor modifications. In field situations, 2D Electrical Resistivity Tomography (ERT) data can be utilized in place of experimental images.

### 7.3 Recommendations for Future Work

The present study can be extended to the following to enhance the understanding of the tidal influence on coastal aquifers:

- The density-dependent experiments should be done for flatter beach slopes (less than  $10^0$ ) and Island aquifer systems (tidal condition on both sides).
- Length of the *Sand Box Model* should be increased to create an effective semi-infinite aquifer system.
- Number of pressure transducers should be increased to capture true  $2D$  variation.
- Introduction of tensiometer and soil moisture sensors would help in understanding the capillary effect.

# References

- Abarca, E., Carrera, J., Sánchez-Vila, X., and Dentz, M. (2007). Anisotropic dispersive henry problem. *Advances in Water Resources*, 30(4):913–926.
- Abarca, E. and Clement, T. P. (2009). A novel approach for characterizing the mixing zone of a saltwater wedge. *Geophysical Research Letters*, 36(6).
- Abdoulhalik, A., Abdelgawad, A. M., and Ahmed, A. A. (2020). Impact of layered heterogeneity on transient saltwater upconing in coastal aquifers. *Journal of Hydrology*, 581:124393.
- Abdoulhalik, A., Ahmed, A., and Hamill, G. (2017). A new physical barrier system for seawater intrusion control. *Journal of Hydrology*, 549:416–427.
- Abdoulhalik, A. and Ahmed, A. A. (2017a). The effectiveness of cutoff walls to control saltwater intrusion in multi-layered coastal aquifers: Experimental and numerical study. *Journal of environmental management*, 199:62–73.
- Abdoulhalik, A. and Ahmed, A. A. (2017b). How does layered heterogeneity affect the ability of subsurface dams to clean up coastal aquifers contaminated with seawater intrusion? *Journal of hydrology*, 553:708–721.
- Abdoulhalik, A. and Ahmed, A. A. (2018). Transient investigation of saltwater upconing in laboratory-scale coastal aquifer. *Estuarine, Coastal and Shelf Science*, 214:149–160.
- Adegoke, K. A. and Bello, O. S. (2015). Dye sequestration using agricultural wastes as adsorbents. *Water Resources and Industry*, 12:8–24.
- Aeby, P., Forrer, J., Flühler, H., and Steinmeier, C. (1997). Image analysis for determination of dye tracer concentrations in sand columns. *Soil Science Society of America Journal*, 61(1):33–35.
- Armanuos, A. M., Ibrahim, M. G., Mahmod, W. E., Takemura, J., and Yoshimura, C. (2019). Analysing the combined effect of barrier wall and freshwater injection countermeasures on controlling saltwater intrusion in unconfined coastal aquifer systems. *Water Resources Management*, 33(4):1265–1280.
- Ataie-Ashtiani, B., Volker, R., and Lockington, D. (1999). Numerical and experimental study of seepage in unconfined aquifers with a periodic boundary condition. *Journal of Hydrology*, 222(1-4):165–184.
- Bear, J. (1999). Conceptual and mathematical modeling. In *Seawater Intrusion in Coastal Aquifers—Concepts, Methods and Practices*, pages 127–161. Springer.

- Brooks, R. and Corey, A. (1964). Hydraulic properties of porous media. *hydrol. paper 3, colorado state univ., fort collins, co. Hydraulic properties of porous media. Hydrol. Paper No. 3. Colorado State Univ., Fort Collins, CO.*
- Buckingham, E. (1914). Physically similar systems. *Journal of the Washington Academy of Sciences*, 4(13):347–353.
- Cartwright, N., Nielsen, P., and Li, L. (2004). Experimental observations of watertable waves in an unconfined aquifer with a sloping boundary. *Advances in Water Resources*, 27(10):991–1004.
- Catania, F., Massabo, M., Valle, M., Bracco, G., and Paladino, O. (2008). Assessment of quantitative imaging of contaminant distributions in porous media. *Experiments in Fluids*, 44(1):167–177.
- Chang, S. W. and Clement, T. P. (2013). Laboratory and numerical investigation of transport processes occurring above and within a saltwater wedge. *Journal of contaminant hydrology*, 147:14–24.
- Cheng, A.-D. and Ouazar, D. (1999). Analytical solutions. In *Seawater intrusion in coastal aquifers—concepts, methods and practices*, pages 163–191. Springer.
- Chetia, M. and Sekharan, S. (2015). Evaluation of different laboratory procedures for determining suction–water content relationship of cohesionless geomaterials. *Journal of Materials in Civil Engineering*, 28(2):04015123.
- Dagan, G. and Zeitoun, D. (1998a). Free-surface flow toward a well and interface upconing in stratified aquifers of random conductivity. *Water resources research*, 34(11):3191–3196.
- Dagan, G. and Zeitoun, D. G. (1998b). Seawater-freshwater interface in a stratified aquifer of random permeability distribution. *Journal of Contaminant Hydrology*, 29(3):185–203.
- Dalai, C., Munusamy, S. B., and Dhar, A. (2020). Experimental and numerical investigation of saltwater intrusion dynamics on sloping sandy beach under static seaside boundary condition. *Flow Measurement and Instrumentation*, 75:101794.
- Dentz, M., Tartakovsky, D., Abarca, E., Guadagnini, A., Sanchez-Vila, X., and Carrera, J. (2006). Variable-density flow in porous media. *Journal of fluid mechanics*, 561:209–235.
- DHI-WASY (2010). Feflow finite element subsurface flow and transport simulation system - user's manual/reference manual/whitepapers. *Release 6.1, Tech. rep., DHI-WASY GmbH, Berlin, Germany.*, (Available from: [Http://www.feflow.info](http://www.feflow.info)(accessed November 2019)).
- Diersch, H.-J. and Kolditz, O. (2002). Variable-density flow and transport in porous media: approaches and challenges. *Advances in water resources*, 25(8-12):899–944.
- Diersch, H.-J. G. (2013). *FEFLOW: finite element modeling of flow, mass and heat transport in porous and fractured media*. Springer Science & Business Media.

- Dose, E. J., Stoeckl, L., Houben, G. J., Vacher, H., Vassolo, S., Dietrich, J., and Himmelsbach, T. (2014). Experiments and modeling of freshwater lenses in layered aquifers: steady state interface geometry. *Journal of hydrology*, 509:621–630.
- Durner, W. (1994). Hydraulic conductivity estimation for soils with heterogeneous pore structure. *Water resources research*, 30(2):211–223.
- Flowers, T. C. and Hunt, J. R. (2007). Viscous and gravitational contributions to mixing during vertical brine transport in water-saturated porous media. *Water resources research*, 43(1).
- Freeze, R. A. and Cherry, J. A. (1974). A. 1979. groundwater. *Prentice—Hall, Inc Englewood cliffs, New Jersey*, 604:215–227.
- Goswami, R. R. and Clement, T. P. (2007). Laboratory-scale investigation of saltwater intrusion dynamics. *Water Resources Research*, 43(4).
- Hassanzadeh, S. M. and Leijnse, A. (1995). A non-linear theory of high-concentration-gradient dispersion in porous media. *Advances in Water Resources*, 18(4):203–215.
- Hastings, C., Mosteller, F., Tukey, J. W., Winsor, C. P., et al. (1947). Low moments for small samples: a comparative study of order statistics. *The Annals of Mathematical Statistics*, 18(3):413–426.
- Held, R., Attinger, S., and Kinzelbach, W. (2005). Homogenization and effective parameters for the henry problem in heterogeneous formations. *Water resources research*, 41(11).
- Henry, H. R. (1960). Salt intrusion into coastal aquifers. Technical report.
- Henry, H. R. (1964). Effects of dispersion on salt encroachment in coastal aquifers, in " seawater in coastal aquifers". *US Geological Survey, Water Supply Paper*, 1613:C70–C80.
- Holzbecher, E. O. (1998). *Modeling density-driven flow in porous media: principles, numerics, software*. Springer Science & Business Media.
- Houben, G. and Post, V. E. (2017). The first field-based descriptions of pumping-induced saltwater intrusion and upconing. *Hydrogeology Journal*, 25(1):243–247.
- Jaeger, S., Ehni, M., Eberhardt, C., Rolle, M., Grathwohl, P., and Gauglitz, G. (2009). Ccd camera image analysis for mapping solute concentrations in saturated porous media. *Analytical and bioanalytical chemistry*, 395(6):1867.
- Jakovovic, D., Werner, A. D., de Louw, P. G., Post, V. E., and Morgan, L. K. (2016). Saltwater upconing zone of influence. *Advances in Water Resources*, 94:75–86.
- Jiao, C.-Y. and Hötzl, H. (2004). An experimental study of miscible displacements in porous media with variation of fluid density and viscosity. *Transport in porous media*, 54(2):125–144.

- Kang, P. K., Lee, J., Fu, X., Lee, S., Kitanidis, P. K., and Juanes, R. (2017). Improved characterization of heterogeneous permeability in saline aquifers from transient pressure data during freshwater injection. *Water Resources Research*, 53(5):4444–4458.
- Ketabchi, H., Mahmoodzadeh, D., Ataie-Ashtiani, B., Werner, A. D., and Simmons, C. T. (2014). Sea-level rise impact on fresh groundwater lenses in two-layer small islands. *Hydrological Processes*, 28(24):5938–5953.
- Kim, I. H. and Yang, J.-S. (2018). Prioritizing countermeasures for reducing seawater-intrusion area by considering regional characteristics using seawat and a multicriteria decision-making method. *Hydrological Processes*, 32(25):3741–3757.
- Kim, K.-Y., Chon, C.-M., and Park, K.-H. (2007). A simple method for locating the fresh water–salt water interface using pressure data. *Groundwater*, 45(6):723–728.
- Konz, M., Ackerer, P., Meier, E., Huggenberger, P., Zechner, E., and Gechter, D. (2008). On the measurement of solute concentrations in 2-d flow tank experiments. *Water Resources Research*, 45(2).
- Konz, M., Ackerer, P., Younes, A., Huggenberger, P., and Zechner, E. (2009a). Two-dimensional stable-layered laboratory-scale experiments for testing density-coupled flow models. *Water Resources Research*, 45(2).
- Konz, M., Younes, A., Ackerer, P., Fahs, M., Huggenberger, P., and Zechner, E. (2009b). Variable-density flow in heterogeneous porous media—laboratory experiments and numerical simulations. *Journal of contaminant hydrology*, 108(3–4):168–175.
- Kosugi, K. (1996). Lognormal distribution model for unsaturated soil hydraulic properties. *Water Resources Research*, 32(9):2697–2703.
- Kuan, W. K., Jin, G., Xin, P., Robinson, C., Gibbes, B., and Li, L. (2012). Tidal influence on seawater intrusion in unconfined coastal aquifers. *Water Resources Research*, 48(2).
- Kuan, W. K., Xin, P., Jin, G., Robinson, C. E., Gibbes, B., and Li, L. (2019). Combined effect of tides and varying inland groundwater input on flow and salinity distribution in unconfined coastal aquifers. *Water Resources Research*, 55(11):8864–8880.
- Lee, C.-H. and Cheng, R. T.-S. (1974). On seawater encroachment in coastal aquifers. *Water Resources Research*, 10(5):1039–1043.
- Li, L., Barry, D., Stagnitti, F., and Parlange, J.-Y. (1999). Submarine groundwater discharge and associated chemical input to a coastal sea. *Water Resources Research*, 35(11):3253–3259.
- Li, L., Barry, D. A., Jeng, D. S., and Prommer, H. (2004). Tidal dynamics of groundwater flow and contaminant transport in coastal aquifers. *Coastal aquifer management: Monitoring, modeling, and case studies*, pages 115–141.
- List, E. J. (1965). *The stability and mixing of a density-stratified horizontal flow in a saturated porous medium*. PhD thesis, California Institute of Technology.

- Liu, Y., Jiao, J. J., and Luo, X. (2016). Effects of inland water level oscillation on groundwater dynamics and land-sourced solute transport in a coastal aquifer. *Coastal Engineering*, 114:347–360.
- Liu, Y., Mao, X., Chen, J., and Barry, D. A. (2014). Influence of a coarse interlayer on seawater intrusion and contaminant migration in coastal aquifers. *Hydrological Processes*, 28(20):5162–5175.
- Llopis-Albert, C. and Pulido-Velazquez, D. (2014). Discussion about the validity of sharp-interface models to deal with seawater intrusion in coastal aquifers. *Hydrological Processes*, 28(10):3642–3654.
- Lu, C., Cao, H., Ma, J., Shi, W., Rathore, S. S., Wu, J., and Luo, J. (2019). A proof-of-concept study of using a less permeable slice along the shoreline to increase fresh groundwater storage of oceanic islands: Analytical and experimental validation. *Water Resources Research*, 55(8):6450–6463.
- Lu, C., Chen, Y., Zhang, C., and Luo, J. (2013). Steady-state freshwater–seawater mixing zone in stratified coastal aquifers. *Journal of Hydrology*, 505:24–34.
- Luyun Jr, R., Momii, K., and Nakagawa, K. (2011). Effects of recharge wells and flow barriers on seawater intrusion. *Groundwater*, 49(2):239–249.
- MacAllister, D., Jackson, M., Butler, A., and Vinogradov, J. (2018). Remote detection of saline intrusion in a coastal aquifer using borehole measurements of self-potential. *Water Resources Research*, 54(3):1669–1687.
- Manickam, O. and Homsy, G. (1995). Fingering instabilities in vertical miscible displacement flows in porous media. *Journal of Fluid Mechanics*, 288:75–102.
- Mehdizadeh, S. S., Karamalipour, S. E., and Asoodeh, R. (2017). Sea level rise effect on seawater intrusion into layered coastal aquifers (simulation using dispersive and sharp-interface approaches). *Ocean & Coastal Management*, 138:11–18.
- Mehdizadeh, S. S., Katabchi, H., Ghoroqi, M., and Hasanzadeh, A. K. (2020). Experimental and numerical assessment of saltwater recession in coastal aquifers by constructing check dams. *Journal of Contaminant Hydrology*, page 103637.
- Mehdizadeh, S. S., Werner, A. D., Vafaie, F., and Badaruddin, S. (2014). Vertical leakage in sharp-interface seawater intrusion models of layered coastal aquifers. *Journal of Hydrology*, 519:1097–1107.
- Mehnert, E. and Jennings, A. A. (1985). The effect of salinity-dependent hydraulic conductivity on saltwater intrusion episodes. *Journal of Hydrology*, 80(3-4):283–297.
- MOEFCC (2017). Database on Coastal States of India. *Website of Ministry of Environment Forest and Climate Change website*.
- Moore, W. S., Sarmiento, J. L., and Key, R. M. (2008). Submarine groundwater discharge revealed by  $^{228}\text{Ra}$  distribution in the upper atlantic ocean. *Nature Geoscience*, 1(5):309–311.
- Mualem, Y. (1976). A new model for predicting the hydraulic conductivity of unsaturated porous media. *Water resources research*, 12(3):513–522.

- Nakagawa, K., Momii, K., and Berndtsson, R. (2005). Saltwater intrusion in coastal aquifer comparison between the cip and moc simulation technique. *Environmental Modeling & Assessment*, 10(4):323–329.
- Nielsen, P. (1990). Tidal dynamics of the water table in beaches. *Water Resources Research*, 26(9):2127–2134.
- Oates, P. M. and Harvey, C. F. (2006). A colorimetric reaction to quantify fluid mixing. *Experiments in fluids*, 41(5):673–683.
- Olsson, Å. and Grathwohl, P. (2007). Transverse dispersion of non-reactive tracers in porous media: a new nonlinear relationship to predict dispersion coefficients. *Journal of contaminant hydrology*, 92(3-4):149–161.
- Oostrom, M., Dane, J., Güven, O., and Hayworth, J. (1992). Experimental investigation of dense solute plumes in an unconfined aquifer model. *Water Resources Research*, 28(9):2315–2326.
- Oostrom, M., Dane, J., Güven, O., Hayworth, J., and Hill, W. (1991). Concentration measurements in dense leachate plumes using a gamma radiation system. In *Symposium on Ground Water*, pages 287–292. ASCE.
- Oswald, S. and Kinzelbach, W. (2004). Three-dimensional physical benchmark experiments to test variable-density flow models. *Journal of Hydrology*, 290(1-2):22–42.
- Oswald, S. E., Spiegel, M. A., and Kinzelbach, W. (2007). Three-dimensional saltwater–freshwater fingering in porous media: contrast agent mri as basis for numerical simulations. *Magnetic resonance imaging*, 25(4):537–540.
- Oz, I., Shalev, E., Yechieli, Y., and Gvirtzman, H. (2015). Saltwater circulation patterns within the freshwater–saltwater interface in coastal aquifers: Laboratory experiments and numerical modeling. *Journal of Hydrology*, 530:734–741.
- Pearl, Z., Magaritz, M., and Bendel, P. (1993). Nuclear magnetic resonance imaging of miscible fingering in porous media. *Transport in porous media*, 12(2):107–123.
- Pinder, G. F. and Cooper Jr, H. H. (1970). A numerical technique for calculating the transient position of the saltwater front. *Water Resources Research*, 6(3):875–882.
- Post, V. E. A. and Werner, A. D. (2017). Coastal aquifers: Scientific advances in the face of global environmental challenges.
- Reilly, T. E. and Goodman, A. S. (1985). Quantitative analysis of saltwater–freshwater relationships in groundwater systems—a historical perspective. *Journal of Hydrology*, 80(1-2):125–160.
- Richards, J. A. and Richards, J. (1999). *Remote sensing digital image analysis*, volume 3. Springer.
- Robinson, C., Gibbes, B., Carey, H., and Li, L. (2007a). Salt-freshwater dynamics in a subterranean estuary over a spring-neap tidal cycle. *Journal of Geophysical Research: Oceans*, 112(C9).

- Robinson, C., Li, L., and Prommer, H. (2007b). Tide-induced recirculation across the aquifer-ocean interface. *Water Resources Research*, 43(7).
- Robinson, C. E., Xin, P., Santos, I. R., Charette, M. A., Li, L., and Barry, D. A. (2018). Groundwater dynamics in subterranean estuaries of coastal unconfined aquifers: Controls on submarine groundwater discharge and chemical inputs to the ocean. *Advances in water resources*, 115:315–331.
- Robinson, G., Hamill, G., and Ahmed, A. A. (2015). Automated image analysis for experimental investigations of salt water intrusion in coastal aquifers. *Journal of Hydrology*, 530:350–360.
- Sabatini, D. A. and Austin, T. A. (1991). Characteristics of rhodamine wt and fluorescein as adsorbing ground-water tracers. *Groundwater*, 29(3):341–349.
- Schincariol, R. A. and Schwartz, F. W. (1990). An experimental investigation of variable density flow and mixing in homogeneous and heterogeneous media. *Water Resources Research*, 26(10):2317–2329.
- Schincariol, R. A., Schwartz, F. W., and Mendoza, C. A. (1994). On the generation of instabilities in variable density flow. *Water Resources Research*, 30(4):913–927.
- Schotting, R., Moser, H., and Hassanzadeh, S. (1999). High-concentration-gradient dispersion in porous media: experiments, analysis and approximations. *Advances in Water Resources*, 22(7):665–680.
- Schotting, R. J., Moser, H., and Hassanzadeh, S. M. (1997). High-concentration-gradient dispersion in porous media: experiments, analysis and approximations. *Modelling, Analysis and Simulation [MAS]*, (R 9734).
- Shen, Y., Xin, P., and Yu, X. (2020). Combined effect of cutoff wall and tides on groundwater flow and salinity distribution in coastal unconfined aquifers. *Journal of Hydrology*, 581:124444.
- Shi, L., Cui, L., Park, N., and Huyakorn, P. S. (2011). Applicability of a sharp-interface model for estimating steady-state salinity at pumping wells—validation against sand tank experiments. *Journal of contaminant hydrology*, 124(1-4):35–42.
- Shi, W., Lu, C., Ye, Y., Wu, J., Li, L., and Luo, J. (2018). Assessment of the impact of sea-level rise on steady-state seawater intrusion in a layered coastal aquifer. *Journal of hydrology*, 563:851–862.
- Shoushtari, S. M. H. J., Cartwright, N., Perrochet, P., and Nielsen, P. (2015). Influence of hysteresis on groundwater wave dynamics in an unconfined aquifer with a sloping boundary. *Journal of Hydrology*, 531:1114–1121.
- Simmons, C. T., Fenstemaker, T. R., and Sharp Jr, J. M. (2001). Variable-density groundwater flow and solute transport in heterogeneous porous media: approaches, resolutions and future challenges. *Journal of Contaminant Hydrology*, 52(1-4):245–275.
- Simmons, C. T. and Narayan, K. A. (1997). Mixed convection processes below a saline disposal basin. *Journal of Hydrology*, 194(1-4):263–285.

- Simmons, C. T., Pierini, M., and Hutson, J. (2002). Laboratory investigation of variable-density flow and solute transport in unsaturated-saturated porous media. *Transport in Porous Media*, 47(2):215–244.
- Simpson, M. and Clement, T. (2003). Theoretical analysis of the worthiness of henry and elder problems as benchmarks of density-dependent groundwater flow models. *Advances in Water Resources*, 26(1):17–31.
- Simpson, M. J. and Clement, T. P. (2004). Improving the worthiness of the henry problem as a benchmark for density-dependent groundwater flow models. *Water Resources Research*, 40(1).
- Smith, A. J. (2004). Mixed convection and density-dependent seawater circulation in coastal aquifers. *Water Resources Research*, 40(8).
- Souza, W. R. and Voss, C. I. (1987). Analysis of an anisotropic coastal aquifer system using variable-density flow and solute transport simulation. *Journal of Hydrology*, 92(1-2):17–41.
- Sriapai, T., Walsri, C., Phueakphum, D., and Fuenkajorn, K. (2012). Physical model simulations of seawater intrusion in unconfined aquifer. *Songklanakarin Journal of Science & Technology*, 34(6).
- Stoeckl, L., Walther, M., and Graf, T. (2016). A new numerical benchmark of a freshwater lens. *Water Resources Research*, 52(4):2474–2489.
- Strack, O. (1976). A single-potential solution for regional interface problems in coastal aquifers. *Water Resources Research*, 12(6):1165–1174.
- Strack, O. and Ausk, B. (2015). A formulation for vertically integrated groundwater flow in a stratified coastal aquifer. *Water Resources Research*, 51(8):6756–6775.
- Swartz, C. H. and Schwartz, F. W. (1998). An experimental study of mixing and instability development in variable-density systems. *Journal of Contaminant Hydrology*, 34(3):169–189.
- Van der Veer, P. (1977). Analytical solution for steady interface flow in a coastal aquifer involving a phreatic surface with precipitation. *Journal of Hydrology*, 34(1-2):1–11.
- Van Genuchten, M. T. (1980). A closed-form equation for predicting the hydraulic conductivity of unsaturated soils. *Soil science society of America journal*, 44(5):892–898.
- Volker, R. and Rushton, K. (1982). An assessment of the importance of some parameters for seawater intrusion in aquifers and a comparison of dispersive and sharp-interface modelling approaches. *Journal of Hydrology*, 56(3-4):239–250.
- Voss, C. I. and Souza, W. R. (1987). Variable density flow and solute transport simulation of regional aquifers containing a narrow freshwater-saltwater transition zone. *Water Resources Research*, 23(10):1851–1866.
- Walther, M., Graf, T., Kolditz, O., Liedl, R., and Post, V. (2017). How significant is the slope of the sea-side boundary for modelling seawater intrusion in coastal aquifers? *Journal of Hydrology*, 551:648–659.

- Watson, S., Barry, D., Schotting, R., and Hassanzadeh, S. (2002). Validation of classical density-dependent solute transport theory for stable, high-concentration-gradient brine displacements in coarse and medium sands. *Advances in Water Resources*, 25(6):611–635.
- Watson, T. A., Werner, A. D., and Simmons, C. T. (2010). Transience of seawater intrusion in response to sea level rise. *Water Resources Research*, 46(12).
- Welty, C. and Gelhar, L. W. (1994). Evaluation of longitudinal dispersivity from nonuniform flow tracer tests. *Journal of Hydrology*, 153(1-4):71–102.
- Werner, A. D., Bakker, M., Post, V. E., Vandenbohede, A., Lu, C., Ataie-Ashtiani, B., Simmons, C. T., and Barry, D. A. (2013). Seawater intrusion processes, investigation and management: recent advances and future challenges. *Advances in Water Resources*, 51:3–26.
- Werner, A. D., Jakovovic, D., and Simmons, C. T. (2009). Experimental observations of saltwater up-coning. *Journal of Hydrology*, 373(1-2):230–241.
- Werth, C. J., Zhang, C., Brusseau, M. L., Oostrom, M., and Baumann, T. (2010). A review of non-invasive imaging methods and applications in contaminant hydrogeology research. *Journal of contaminant hydrology*, 113(1-4):1–24.
- Wooding, R. (1963). Convection in a saturated porous medium at large rayleigh number or peclet number. *Journal of Fluid Mechanics*, 15(4):527–544.
- Wooding, R., Tyler, S. W., and White, I. (1997). Convection in groundwater below an evaporating salt lake: 1. onset of instability. *Water Resources Research*, 33(6):1199–1217.
- Wu, H., Lu, C., Yan, M., and Werner, A. D. (2020). Expanding freshwater lenses adjacent to gaining rivers through vertical low-hydraulic-conductivity barriers: Analytical and experimental validation. *Water Resources Research*, 56(2):e2019WR025750.
- Yu, X., Xin, P., and Lu, C. (2019a). Seawater intrusion and retreat in tidally-affected unconfined aquifers: Laboratory experiments and numerical simulations. *Advances in Water Resources*, 132:103393.
- Yu, X., Xin, P., Wang, S. S., Shen, C., and Li, L. (2019b). Effects of multi-constituent tides on a subterranean estuary. *Advances in Water Resources*, 124:53–67.
- Zhang, B., Zheng, X., Zheng, T., Xin, J., Sui, S., and Zhang, D. (2019). The influence of slope collapse on water exchange between a pit lake and a heterogeneous aquifer. *Frontiers of Environmental Science & Engineering*, 13(2):20.
- Zhang, Q., Volker, R., and Lockington, D. (2001). Influence of seaward boundary condition on contaminant transport in unconfined coastal aquifers. *Journal of Contaminant Hydrology*, 49(3-4):201–215.
- Zhang, Q., Volker, R. E., and Lockington, D. A. (2002). Experimental investigation of contaminant transport in coastal groundwater. *Advances in Environmental Research*, 6(3):229–237.

- Zhou, Y., Lim, D., Cupola, F., and Cardiff, M. (2016). Aquifer imaging with pressure waves—evaluation of low-impact characterization through sandbox experiments. *Water Resources Research*, 52(3):2141–2156.
- Zinn, B., Meigs, L. C., Harvey, C. F., Haggerty, R., Peplinski, W. J., and von Schwerin, C. F. (2004). Experimental visualization of solute transport and mass transfer processes in two-dimensional conductivity fields with connected regions of high conductivity. *Environmental science & technology*, 38(14):3916–3926.